

Caractérisation et modélisation des matériaux magnétiques pour les dispositifs de conversion électromagnétique de l'énergie

Rapport de synthèse

Soutenue le 7 décembre 2015

pour l'obtention d'une

Habilitation à Diriger des Recherches

(spécialité Génie Electrique)

présentée par

Abdelkader Benabou

Composition du jury

- Rapporteurs :* KEDOUS-LEBOUC Afef - Directrice de Recherche au CNRS
HAMEYER Kay - Professeur à l'Université d'Aix-la-Chapelle (RWTH - Allemagne)
TAKORABET Nouredine - Professeur à l'Université de Lorraine
- Examineurs :* CLÉNET Stéphane - Professeur à Arts et Métiers ParisTech
MARCHAND Claude - Professeur à l'Université Paris-Sud
ROGER Daniel - Professeur à l'Université d'Artois
SADOWSKI Nelson - Professeur à l'Université de Santa Catarina (UFSC - Brésil)
TOUNZI Abdelmounaim - Professeur à l'Université Lille1
- Invité :* MIPO Jean-Claude - Ingénieur de recherche, Valeo Electrical System

Contents

Partie I	Dossier individuel	1
1	Curriculum Vitae	3
2	Activités pédagogiques	3
2.1	Responsabilités pédagogiques	3
2.2	Activités d'enseignement	4
3	Activités liées à la recherche	5
3.1	Responsabilités d'intérêt collectif	5
3.2	Responsabilités de recherche et valorisation	6
3.3	Bilan comptable en recherche	6
3.4	Résumé des activités de recherche	7
3.5	Liste des publications	16
Partie II	Synthesis of the work	27
Main introduction		29
Chapter 1	Some basics on magnetic materials	31
1.1	Definition of the magnetic quantities of interest	31
1.2	Diamagnetism	32
1.3	Paramagnetism	32
1.4	Ferromagnetism	34
1.4.1	Weiss theory	34
1.4.2	Ferrimagnetism	36
1.4.3	Anisotropy	36
1.4.4	Magnetic domains	38

1.4.5	Magnetization process	41
1.5	Ferromagnetic materials	45
1.5.1	Soft magnetic materials	46
1.5.2	Hard magnetic materials	51
1.6	Conclusion	54
Chapter 2 Material characterization		57
2.1	Standard techniques	57
2.1.1	Principle	57
2.1.2	Ring core technique	59
2.1.3	Epstein frame	59
2.1.4	Single Sheet Tester	60
2.1.5	Discussion and limits	60
2.2	Specific approaches	62
2.2.1	Cutting effect on stator teeth of slinky stators	62
2.2.2	Electrical conductivity in non-trivial geometries	65
2.2.3	Identification procedure for low permeability magnetic materials	68
2.2.4	Magnetization loss in permanent magnets	77
2.2.5	Magnetic characterization in High Frequency for EMI filters . .	80
Chapter 3 Materials and numerical modelling		85
3.1	General context of the numerical modelling	85
3.1.1	Mathematical model	85
3.1.2	Formulations	87
3.1.3	Accounting for the non-linear magnetic behaviour	90
3.2	Magnetic behaviour	91
3.2.1	Single-valued approximation	91
3.2.2	Preisach model	91
3.2.3	Jiles-Atherton model	96
3.2.4	Magnetization loss model for permanent magnets	103
3.3	Iron loss models	107
3.3.1	Analytical loss models	111
3.3.2	Minor loops surface response model	112
3.4	Probabilistic approach	114
3.4.1	Context and definitions	114

3.4.2	Illustration with the iron loss variability modelling	118
Chapter 4	Magnetic material characterization and applications	123
4.1	Conventional applications	123
4.1.1	Three phase transformer and inrush current	123
4.1.2	Study of the stray load losses in an induction motor	127
4.2	Non-conventional applications	131
4.2.1	Hysteresis motor	131
4.2.2	Study of a magneto-rheological brake	137
4.2.3	Magnetization loss in permanent magnets	145
Chapter 5	Conclusion and perspectives	151
5.1	Conclusion	151
5.2	Perspectives	152
5.2.1	Improvement and development of material models	152
5.2.2	Impact of the manufacturing process	153
Bibliography		157

Part I

Dossier individuel

1 Curriculum Vitae

Etat civil

Nom : Benabou
 Prénom : Abdelkader
 Date de naissance : 1^{er} janvier 1976
 e-mail : abdelkader.benabou@univ-lille1.fr

Situation actuelle

Je suis actuellement Maître de Conférences à l'Université Lille 1, affecté à l'Ecole Polytechnique Universitaire de Lille (Polytech'Lille) et membre du Laboratoire d'Electrotechnique et d'Electronique de Puissance de Lille (L2EP). J'y effectue mes activités de recherche au sein de l'équipe Optimisation et Méthodes Numériques (OMN), tout en étant bénéficiaire d'une prime d'excellence scientifique depuis 2009.

Emplois dans la fonction publique

Depuis 2004 : Maître de Conférences à l'Université Lille 1 (Polytech'Lille)
 2003-2004 : ATER à l'Université Lille 1 (Polytech'Lille) et au L2EP
 2002-2003 : ATER à l'Université Lille 1 (U.F.R. d'IEEA) et au L2EP

Diplômes universitaires

1999-2002 : Thèse de Doctorat en Génie Électrique de l'Université Lille 1
"Etude et caractérisation du phénomène d'hystérésis magnétique en vue d'une implantation dans un code de calcul éléments finis"
 Thèse soutenue devant le jury composé de:
 J.P. HAUTIER Président
 A. KEDOUS-LEBOUC Rapporteure
 J.P. MASSON Rapporteur
 J.A. MELKEBEEK Examineur
 F. PIRIOU Directeur de Thèse
 S. CLÉNET Examineur

1998-1999 : DEA Sciences des Matériaux - Université Lille 1
 1996-1998 : Licence et Maîtrise de Physique - Université Lille 1
 1994-1996 : DEUG Sciences de la Matière option Physique - Université Lille 1

2 Activités pédagogiques

2.1 Responsabilités pédagogiques

A Polytech'Lille

Depuis 2006 : Responsable de la filière "Systèmes Autonomes" en 4^{ieme} et 5^{ieme} années du département Informatique Microélectronique Automatique (IMA) et du tronc commun en 5^{ieme} année (depuis 2009).

- : Responsable de l'option "Electronique de Puissance" en 4^{ieme} et 5^{ieme} années du département IMA (2006-2009).
- Depuis 2004 : Responsable de la salle de travaux pratiques et référent au sein du
 - : pôle EEI (Electronique Electrotechnique Instrumentation) pour la gestion et l'achat de matériel pédagogique en électrotechnique.
- 2012-2014 : Membre de la Commission Pédagogique Ecole.
- 2010-2014 : Membre du Jury Ecole.
- 2009 et 2013 : Participation aux groupes de travail pour la refonte de la maquette IMA en 2009 et la mise en place de celle de la formation par apprentissage IMA-2A en 2013.

2.2 Activités d'enseignement

De **1999 à 2002**, en parallèle de ma thèse, j'ai effectué des vacances à l'École Centrale de Lille. Les enseignements dispensés en 1^{ere} année d'école d'ingénieurs, sous forme de travaux pratiques, avaient pour thèmes les machines électriques et l'électronique de puissance.

Durant l'année universitaire **2002-2003**, j'ai été nommé ATER à l'Université Lille 1 (U.F.R. d'IEEA) où j'ai assuré des enseignements en électrotechnique (TD et TP), électronique de puissance (TD et TP), en physique pour le génie électrique (TD et TP, avec création d'un TP) et en analyse numérique (TP). J'ai également été amené à encadrer un projet de Maîtrise.

L'année universitaire suivante, en **2003-2004**, toujours ATER à l'Université Lille1, j'ai été affecté à Polytech'Lille. Les enseignements dispensés étaient principalement orientés en électrotechnique et électronique de puissance, notamment en TP, TD et Tutorat pour les 3^{ieme} et 4^{ieme} années. J'ai aussi encadré des projets en 4^{ieme} et 5^{ieme} années. Enfin, le suivi (fonctionnement, matériel...) de la salle de TP Electrotechnique m'a été confié au cours de cette année.

Depuis ma nomination en **septembre 2004** en tant que Maître de Conférences à Polytech'Lille, j'ai naturellement continué à dispenser les enseignements de TD, TP et Tutorat en électrotechnique et électronique de puissance pour les 3^{ieme} et 4^{ieme} années ainsi que l'encadrement de projets en 4^{ieme} et 5^{ieme} années. J'ai souvent été amené à faire évoluer les énoncés et contenus des TD et TP, mais aussi à créer de nouveaux sujets pour les tutorats en électrotechnique et électronique de puissance. Dès **2006**, j'ai pris en charge (Cours et TD) un module sur les moteurs électriques dispensé au sein du département Construction Mécanique (CM) de Polytech'Lille. Depuis **2008**, je suis responsable d'un module transversal optionnel sur les Energies Renouvelables qui est proposé en 5^{ieme} année à tous les départements de Polytech'Lille. Par ailleurs, suite à la réforme de la maquette IMA en **2009** et à la création de la formation par apprentissage IMA-2A en **2013**, j'ai pu introduire un module 5^{ieme} année sur la conception et éco-conception de systèmes électriques. J'assure aussi, depuis **2013**, des TD d'électromagnétisme pour les élèves en Parcours des Écoles d'Ingénieurs Polytechniques (PeiP) qui ont vocation à intégrer l'une des écoles du réseau Polytech. Enfin, depuis la rentrée **2015**, j'interviens dans le master Véhicule Intelligent Electrique (VIE) qui est en partenariat entre l'U.F.R. d'IEEA et

Polytech'Lille.

Par ailleurs, dès **2006**, j'ai été sollicité pour effectuer des enseignements au sein de l'U.F.R. d'IEEA, notamment en 2^{ième} année de Licence ESEA (TD sur les propriétés des matériaux pour le génie électrique), en 3^{ième} année de Licence d'Ingénierie en Génie Electrique (TD de physique pour le génie électrique), en Master Recherche Génie Electrique (TD d'électromagnétisme) et en projets encadrés en 1^{ière} année de Master Automatique et Systèmes Electriques. A l'extérieur de l'Université Lille 1, depuis **2009**, j'interviens sur les matériaux magnétiques au sein du mastère Ingénierie des Véhicules Electriques (IVE) co-accrédité par Arts et Métiers ParisTech, l'Ecole Nationale Supérieure de Techniques Avancées et Mines ParisTech.

En plus des activités d'enseignement classiques, un certain nombre de responsabilités m'ont été confiées au sein du département IMA. Les premières, dès **2004**, ont été la prise en main de la salle de TP afin d'en assurer un fonctionnement optimal (matériel et occupation). Parallèlement, j'ai été naturellement le référent électrotechnique au sein du pôle EEI (Electronique Electrotechnique Instrumentation) de l'école afin d'assurer la gestion et l'achat du matériel pédagogique dédié aux enseignements d'électrotechnique. J'ai rapidement été amené à prendre, de **2006** à **2009**, la responsabilité de l'option *Electronique de Puissance* en 4^{ième} et 5^{ième} années, responsabilité qui est devenue, depuis **2009**, celle de la filière *Systèmes Autonomes*, toujours en 4^{ième} et 5^{ième} années, avec en sus le tronc commun de 5^{ième} année. Ce changement est lié à la réforme de la maquette IMA qui a conduit au regroupement des options Electronique de Puissance et Automatique sous l'appellation *Systèmes Autonomes*. Par la suite, j'ai intégré le *Jury Ecole* de **2010** à **2014** et la *Commission Pédagogique Ecole* de **2012** à **2014**. J'ai également été impliqué dans les groupes de travail mis en place lors de la réforme de maquette IMA en **2009** et aussi lors de la création de la formation par apprentissage IMA-2A en **2013**.

3 Activités liées à la recherche

3.1 Responsabilités d'intérêt collectif

Au L2EP

- Depuis 2004 : - Responsable de la Commission Communication et Webmaster du site web du L2EP (<http://l2ep.univ-lille1.fr>)
 - Responsable de la Commission Elections (organisation des élections du Conseil de Laboratoire et du Directeur)
 - Missions diverses: rédaction du règlement intérieur du laboratoire en 2009 et mise à jour des statuts du laboratoire en 2013.
- 2004-2008 : Membre élu au Conseil de Laboratoire (collège Enseignants-Chercheurs).
- 2001-2004 : Membre élu au Conseil de Laboratoire (collège Doctorants).

A l'Université Lille 1 et à l'extérieur

- Depuis 2008 : Membre élu du vivier 63^{ième} section de l'Université Lille 1.
- Membre des comités de sélection pour les postes:
- MCF-1751 en 2015 (*vice-président*)

- MCF-0012 en 2012
 - MCF-0350 en 2010 (*vice-président*)
- 2010 : Membre extérieur du comité de sélection pour le poste MCF-0211 à l'Université d'Artois.

3.2 Responsabilités de recherche et valorisation

Au L2EP

Depuis 2004 : Responsable de la plateforme *Caractérisation des Matériaux Magnétiques* du L2EP. Mise en place et gestion des moyens expérimentaux dédiés.

- Depuis 2006 : Membre des comités d'organisation pour les conférences internationales:
- COMPUMAG 2019 (co-chairman de l'Editorial Board)
 - EPE 2013
 - EPNC 2008
 - NUMELEC 2006

Activités d'expertise

- Relecture d'articles pour des revues internationales:
 - IEEE Transactions on Magnetics
 - International Journal for Computation and Mathematics in Electrical Engineering (COMPEL)
 - International Journal of Applied Electromagnetics and Mechanics (IJAEM)
 - ...
- Relecture de communications pour les conférences internationales COMPUMAG, CEFC, EPNC ...
- Chairman de sessions posters pour les conférences internationales COMPUMAG 2009 et CEFC 2014.
- Expertise de dossiers ANRT pour des thèses CIFRE.

3.3 Bilan comptable en recherche

Encadrements

- De 2007 à aujourd'hui: encadrement de 9 Thèses (5 à 50% et 4 à 33%) dont 6 ont été soutenues.
- De 2005 à aujourd'hui: encadrement de 8 Master Recherche (6 à 100% et 2 à 50% avec d'autres laboratoires).

Publications

- 39 publications dans des revues internationales référencées, dont:
 - 13 IEEE Transactions on Magnetics
 - 10 International Journal for Computation and Mathematics in Electrical Engineering (COMPEL)
 - 4 International Journal of Applied Electromagnetics and Mechanics (IJAEM)
 - 3 Journal of Magnetism and Magnetic Materials
 - 2 IEEE Transactions on Power Electronics
 - ...
- 52 communications dans des conférences internationales avec comité de lecture, dont:
 - 11 COMPUMAG
 - 8 EPNC
 - 7 ISEF
 - 4 CEFC
 - 4 SMM
 - 4 ISEM
 - ...

3.4 Résumé des activités de recherche

3.4.1 Contexte

Environnement

Mes activités de recherche au L2EP se déroulent, depuis 2004, au sein de l'équipe *Modélisation* dont les objectifs de recherche sont le développement de modèles et méthodes numériques pour la modélisation fine des systèmes électromagnétiques en basse fréquence. Depuis le 1^{er} janvier 2015, les équipes Modélisation et Optimisation se sont regroupées pour former l'équipe *Outils et Méthodes Numériques*. Les objectifs de recherche de l'équipe Optimisation étant le développement de méthodologies de conception et d'optimisation des dispositifs électriques, la nouvelle équipe ainsi formée possède les compétences pour la conception optimale et l'étude des dispositifs électromagnétiques dans leur environnement. Naturellement, au vu du titre de ce rapport de synthèse, j'interviens sur les aspects caractérisation et modélisation des matériaux magnétiques.

Les problématiques abordées sont, de façon non exhaustive, la caractérisation et modélisation des matériaux magnétiques, le développement de formulations électromagnétiques, les couplages multi-physiques, l'optimisation multi-disciplinaires, multi-niveaux et multi-échelles, la prise en compte des incertitudes, le développement de méthodes numériques ...

L'ensemble des travaux est capitalisé dans une plateforme logicielle commune regroupant le code de calcul par éléments finis *code_Carmel*¹ et le code d'optimisation *Sophémis*.

Le laboratoire est partenaire du projet MEDEE², projet phare de la région Nord-Pas de Calais, comprenant 10 sous-projets couvrant les thématiques de machines et systèmes électriques jusqu'aux process industriels. Je suis impliqué dans le sous-projet MEDEE 2, intitulé "*Diagnostic électromagnétique par modélisation numérique*", par l'encadrement de 3 thèses, dont deux ont été soutenues et une est en cours.

Par ailleurs, après plusieurs années de collaboration fructueuse avec EDF R&D, les membres de l'ancienne équipe Modélisation et une partie des chercheurs du groupe Themis de EDF ont mis en place, depuis le 1^{er} janvier 2006, le LAMEL³, un laboratoire commun entre les deux entités de recherche.

Collaborations internationales

Depuis 2002 l'équipe est régulièrement partenaire international dans le programme belge PAI (Pôles d'Attraction Interuniversitaires) qui est l'équivalent de l'agence nationale pour la recherche. L'implication de l'équipe se fait dans les actions en lien avec la modélisation en électromagnétisme et dans lesquelles on retrouve les universités de Gand, Liège et KU Leuven. Dans ce cadre, j'ai participé aux phases V (2002-2006) et VI (2007-2011), notamment dans les thématiques liées à la modélisation de la loi de comportement des matériaux magnétiques. Ces travaux ont donné lieu à une publication commune en revue [RICL-35] et à une thèse, celle de Francisc Bölöni, que j'ai co-encadrée et qui faisait partie de la phase VI du PAI.

Par ailleurs, suite à un accord CAPES/COFECUB avec le Brésil de 2002 à 2008, des liens particuliers ont été établis avec le GRUCAD de l'*Universidade Federale de Santa Catarina* (UFSC) du Brésil. Dans ce cadre, j'ai effectué un séjour de deux semaines dans ce laboratoire. Les travaux de recherche menés dans ce cadre, et concernant la partie modélisation des matériaux magnétiques, ont débouché sur trois publications communes en revues [RICL-31, RICL-32, RICL-34] et quatre communications à des conférences internationales [CICL-39, CICL-40, CICL-43, CICL-45]. Cette collaboration s'est poursuivie au-delà du cadre du projet initial avec d'autres publications communes suite aux séjours de chercheurs brésiliens au L2EP et surtout avec la mise en place de deux thèses en cotutelle, entre l'Université Lille 1 et l'UFSC, dont celle de Juliana-Luisa Müller que j'ai co-encadrée.

Plus récemment, depuis 2015, une collaboration a débuté avec l'Université Louvain-la-Neuve en Belgique. Le laboratoire a accueilli un Professeur invité de cette université et des travaux ont été initiés sur la thématique du calcul de la force magnétique dans les codes éléments finis en électromagnétisme. A cette occasion, j'ai contribué à la mise en place d'un dispositif expérimental de mesure de la force magnétique pour la validation des calculs. Ces travaux ont donné lieu à une communication dans une conférence internationale [CICL-7].

¹Code Avancé de Recherche en Modélisation Electromagnétique

²Maitrise Énergétique des Entraînements Électriques.

³Laboratoire Avancé de Modélisation du Matériel Electrique.

Collaboration nationales et locales

Au niveau de la communauté nationale en génie électrique, j'ai participé au GDR ME²MS⁴ (2002-2006) dans la thématique « Matériaux » en lien avec la modélisation de l'hystérésis magnétique. Ces travaux ont donné lieu à une communication commune dans une conférence nationale [CNCL-7]. Plus récemment, dans le cadre du projet MEDEE 2, l'une des opérations concernait la mise en place d'un dispositif expérimental, en lien avec la thèse de Juliana-Luisa Müller, au LSEE à Béthune. Les travaux de modélisation de la thèse ont ainsi pu être validés avec des mesures faites au LSEE et une publication commune en revue internationale a été réalisée [RICL-16].

Très tôt, dès 2006, des collaborations avec des laboratoires hors génie électrique ont été initiées. On peut citer les travaux, dans le cadre d'un master recherche commun (Francisc Bölöni), portant sur l'usinage sous champ magnétique avec le MSMP (ex LMPF) d'Arts et Métiers Châlons-en-Champagne. Ces travaux ont plus récemment fait l'objet d'une publication commune en revue internationale [RICL-12]. De la même façon en 2009, également dans le cadre d'un master recherche commun (Inigo Cappelán-Perez) [CNCL-4], une étude a été faite avec le MSMP (ex LMPGM) d'Arts et Métiers Lille pour la reconstruction de la loi de comportement de matériaux magnétiques composites à partir d'imagerie au microscope électronique.

Plus récemment, une collaboration plus étroite a été mise en place avec des laboratoires dans les domaines des matériaux et des procédés de fabrication, à savoir les laboratoires MSMP d'Arts et Métiers Lille (depuis 2012) et LCFC d'Arts et Métiers Metz (depuis 2014). Cette collaboration s'est établie sur la problématique de l'impact des procédés de fabrication sur les propriétés des matériaux magnétiques. Deux thèses, dont une que je co-encadre (Marc Borsenberger), sont en cours avec ces laboratoires.

Enfin, localement, des travaux portant sur l'impact de la fatigue sur les propriétés magnétiques des tôles ont fait l'objet d'un master recherche commun (Fatima Elarab) en 2015 avec le laboratoire matériaux UMET de l'Université Lille 1.

3.4.2 Thématiques de recherches

Mes activités concernent la caractérisation et la modélisation des propriétés des matériaux magnétiques utilisés pour la fabrication des dispositifs de conversion électromagnétique de l'énergie. Ces matériaux sont au cœur de la conversion de l'énergie et leurs propriétés sont déterminantes pour les performances de ces dispositifs. Dans ce cadre, ces activités de recherche sont principalement axées sur les thématiques *pertes fer* et *loi de comportement magnétique*, et ce, en termes de modélisation et de caractérisation expérimentale. L'objectif est de disposer de modèles de matériaux pouvant être intégrés, entre autres, dans *code_Carmel* afin de disposer d'un outil d'étude et d'investigation des dispositifs électrotechniques fiable et précis. Ces travaux sont menés en partie dans le cadre de collaborations avec les sociétés Valeo Equipements Electriques et EDF R&D.

Modélisation de la loi de comportement magnétique

Les modèles de représentation de l'hystérésis, phénomène fortement non-linéaire et dis-

⁴Maîtrise de l'Energie Electrique du Matériau au Système

sipatif accompagnant le processus d'aimantation des matériaux ferromagnétiques, ont fait initialement l'objet de mes travaux dans ce domaine, en particulier pour les matériaux *doux*. Les modèles étudiés permettent de représenter le comportement dynamique dans la gamme de fréquences industrielles de fonctionnement des dispositifs électrotechniques [RICL-35, RICL-38]. Les phénomènes vectoriels et harmoniques (cycles mineurs) ont également été abordés pour le développement de ces modèles [RICL-9, RICL-26, RICL-29, RICL-30]. Ceux-ci ont été implémentés dans des codes de calcul par éléments finis, notamment dans *code_Carmel* [RICL-31, RICL-32], et validés avec l'expérience [RICL-23, RICL-24, RICL-27].

Dans les systèmes de conversion de l'énergie, on retrouve également des matériaux ferromagnétiques *durs*, à savoir les aimants permanents. Ceux-ci peuvent subir des contraintes de fonctionnement intenses, notamment à cause des pertes par courants induits dues à la combinaison d'harmoniques spatiales et temporelles dans le champ d'excitation. Ces pertes engendrent un échauffement des aimants pouvant conduire à une perte, partielle ou totale, de leur aimantation permanente. Ainsi, dans le cadre de la thèse de Radu Frăţilă, des modèles de désaimantation des aimants ont été développés et implémentés dans *code_Carmel* [RICL-14]. Un dispositif expérimental spécifique a été développé pour valider cette implémentation numérique [CICL-12].

Par ailleurs, les outils de modélisation numérique intègrent des modèles de matériaux déterministes, identifiés notamment à partir de données expérimentales faites sur des matériaux bruts. Dans le cadre des travaux de thèse de Rindra Ramarotafika, l'intérêt d'une approche probabiliste a été démontré suite, par exemple, à un procédé de fabrication modifiant les propriétés des matériaux de façon non homogène d'une pièce à l'autre. En effet, il a été observé un coefficient de dispersion important sur les pertes d'un lot de stators enroulés, censément identiques, et une approche probabiliste unifiée a été proposée pour la modélisation de la loi de comportement magnétiques et des pertes [RICL-8, RICL-11, RICL-15].

On notera que, dans ces activités, le développement des modèles de matériaux se fait toujours dans l'objectif d'une intégration dans le code de calcul par éléments finis. Dans ce contexte, il est nécessaire de construire le modèle afin qu'il soit implémentable de façon relativement aisée. Il doit également présenter des caractéristiques en termes de mémoire et de temps de calcul acceptables puisque la méthode des éléments finis peut être très coûteuse sur ces mêmes critères dès lors qu'un dispositif complexe est étudié.

Caractérisation des matériaux

Le développement des modèles de matériaux va de pair avec la caractérisation expérimentale desdits matériaux. Le recours aux données expérimentales permet de construire les modèles en passant par une étape d'identification qui est elle-même, le plus souvent, cruciale pour la fiabilité du modèle une fois celui-ci exploité. On peut ainsi noter que, selon la méthode d'identification retenue (un même modèle pouvant être identifié selon différentes techniques), les données expérimentales requises ne sont pas nécessairement les mêmes. Dans ces conditions, le dispositif expérimental doit parfois être modifié pour fournir les mesures adéquates. De plus, même s'il s'agit d'une finalité dans la démarche de modélisation précise des dispositifs électromagnétiques, la caractérisation experimen-

tale ne doit pas être exclusivement dédiée à l'identification des modèles. En effet, elle est aussi une étape nécessaire pour l'investigation et la compréhension du comportement du matériau, notamment pour juger de la pertinence de prise en compte d'un paramètre donné dans un modèle.

Dans ce contexte, l'activité de caractérisation des matériaux magnétiques, qui était principalement associée à l'identification des modèles de matériaux [RICL-7], notamment dans les thèses de Mircea Frăţilă et Jalal Cheaytani [RICL-7, RICL-4], s'est progressivement orientée vers de l'investigation des propriétés des matériaux dans des contextes bien précis, tel que celui de l'impact des procédés de fabrication [RICL-17] ou l'étude des propriétés de poudres magnétiques [CICL-24]. Naturellement, des limites sont très vite apparues du fait de l'inadéquation des techniques standard pour réaliser certaines études, en particulier dans le cadre de la thèse de Laure Arbenz où une technique spécifique a été développée [RICL-3, CICL-2]. Dans ce travail, la détermination non destructive de la conductivité électrique, sur des échantillons à géométrie complexe, est réalisée par une méthodologie alliant la mesure expérimentale et la modélisation numérique. De la même façon, dans les thèses de Radu Frăţilă, pour l'étude de la démagnétisation des aimants [RICL-6], et de Carlos Cuellar, pour la construction et l'identification d'un modèle de noyaux magnétiques en haute fréquence pour la CEM [RICL-5], il a été nécessaire de mettre en place des dispositifs et protocoles expérimentaux adaptés.

Exploitation des modèles

Dans la démarche de développement des modèles de matériaux, il est primordial de valider les travaux sur des cas représentatifs de la réalité de fonctionnement des dispositifs électromagnétiques. Cette validation est le plus souvent réalisée sur des cas tests simples en même temps que l'étape d'implémentation des modèles dans les outils numériques [RICL-22, RICL-23]. Les modèles de matériaux développés ont été exploités dans des études beaucoup plus industrielles, comme celles portant sur les pertes fer et supplémentaires dans les motorisations performantes dans le cadre des thèses de Mircea Frăţilă et Jalal Cheaytani.

Mais l'exploitation des outils a aussi permis l'étude de systèmes moins conventionnels. C'est notamment le cas de deux études, l'une portant sur la modélisation d'un moteur à hystérésis [RICL-36] et l'autre ayant trait à un frein magnéto-rhéologique [RICL-21]. Ces deux études ont mis en évidence l'intérêt de modèles plus fins pour investiguer des fonctionnements et comportements qui n'auraient pu être analysés par des outils conventionnels incluant des lois de comportements univoques.

Impact des procédés

Depuis quelques années, et la thèse de Rindra Ramarotafika, mon activité de recherche s'est élargie à l'étude de l'impact, sur les propriétés des matériaux magnétiques, des procédés de fabrication des dispositifs électromagnétiques. Ces procédés, en plus de dégrader les propriétés des matériaux, peuvent conduire à une dispersion de ces mêmes propriétés au sein d'un ensemble d'échantillons issus de la même chaîne de fabrication. Pour cela, des campagnes de caractérisation expérimentales conséquentes sont nécessaires pour l'identification des modèles qui eux-mêmes doivent reposer sur une démarche d'identification de nature statistique. Ce type de travaux a été en particulier mené dans

le cadre de la thèse de Rindra Ramarotafika où, comme indiqué précédemment, une méthodologie d'identification a été proposée pour la représentation probabiliste de la loi de comportement magnétique et des pertes fer [RICL-8, RICL-11, RICL-15] de stators de enroulés. De la même façon, les travaux de Laure Arbenz sont orientés sur la caractérisation des propriétés électromagnétiques locales de pièces ferromagnétiques massives, notamment les rotors à griffes d'alternateurs. Ces pièces sont forgées à chaud et l'inhomogénéité de la microstructure (due aux paramètres du procédé de fabrication) nécessite d'avoir une approche locale pour la représentation fine des propriétés d'une telle pièce dans un modèle numérique. Les travaux actuels visent à mettre en place les techniques expérimentales adaptées aux objectifs de l'étude [CICL-2, CICL-9]. Une thèse a récemment démarré, celle de Marc Borsenberger, en collaboration avec un laboratoire ayant des compétences dans le domaine des procédés de fabrication (LCFC) afin d'étudier plus en détail les différentes étapes du procédé et leurs impacts respectifs sur les propriétés électromagnétiques de l'acier.

On notera qu'il existe très peu d'études, ou alors très parcellaires, dans le domaine de l'impact des procédés sur les propriétés électromagnétiques et les performances des dispositifs de conversion de l'énergie. La motivation de ces travaux est donc de contribuer à la mise en place de méthodologies, modèles et techniques de caractérisation permettant de développer à terme des outils de conception prenant en compte le processus complet des contraintes physiques mises en jeu lors de la fabrication d'un dispositif (découpe, forgeage, déformation ...) et lors du fonctionnement (température, contrainte mécanique ...).

3.4.3 Partenariats industriels

Le génie électrique étant une discipline appliquée, en particulier dans le domaine de la conversion de l'énergie électrique, il est naturel que les interactions avec le monde industriel soient fortes. Dans l'équipe, deux industriels (Valeo Equipements Electriques et EDF R&D) sont en partie "pourvoyeurs" de problématiques qui, bien qu'industrielles, n'en nécessitent pas moins de réaliser des développements en recherche.

Dans ce cadre, le laboratoire commun LAMEL mis en place pour le développement conjoint de *code_Carmel*, a permis de mettre en oeuvre un certain nombre de travaux de thèses (Juliana-Luisa Müller, Mircea Frăţilă, Jalal Cheaytani) pour le développement et l'application des modèles de matériaux.

De la même façon, l'équipe et Valeo Equipements Electriques sont partenaires de longue date avec de nombreuses thèses en partenariat, comme celle de Laure Arbenz sur la caractérisation électromagnétique locale des aciers massifs. Cet échange s'est encore beaucoup plus accentué depuis 2014 avec notamment le projet PSPC⁵ "Lowco2motion+", dans lequel je co-encadre la thèse de Marc Borsenberger. Ce projet d'envergure, qui contribue fortement au développement de la thématique sur l'impact des procédés de fabrication, offre aussi l'opportunité de travailler avec des laboratoires d'autres disciplines (matériaux, procédés de fabrication) comme le MSMP et le LCFC.

⁵Projets Structurants des Pôles de Compétitivité

3.4.4 Liste des encadrements

Encadrements de thèses

- **Francisc Bölöni** (encadrement à 50%)

"Contribution à la modélisation déterministe et stochastique du phénomène de pull-in dans les MEMS à actionnement électrostatique".

Thèse soutenue le 10 novembre 2010 devant le jury composé de:

Mr. Jean-Louis COULOMB	Président - Rapporteur
Mr. Yvan LEFEVRE	Rapporteur
Mr. Michel HECQUET	Examineur
Mr. Jan MELKEBEEK	Examineur
Mr. Nicolas TIERCELIN	Examineur
Mr. Abdelkader BENABOU	Examineur
Mr. Abdelmounaïm TOUNZI	Directeur de Thèse

Publications associées à la thèse:

[RICL-19, RICL-25] et [CICL-15, CICL-35]

- **Juliana-Luisa Müller** (encadrement à 33%)

"Contribution à la modélisation de tests de diagnostic de courts-circuits entre tôles dans les stators de turboalternateurs".

Thèse soutenue le 16 mai 2012 devant le jury composé de:

Mr. Nelson SADOWSKI	Président
Mr. Javad FOULADGAR	Rapporteur
Mr. Renato Cardoso MESQUITA	Rapporteur
Mr. Mauricio Valencia Ferreira DA LUZ	Examineur
Mr. Patrick DULAR	Examineur
Mr. Abdelkader BENABOU	Examineur
Mr. Francis PIRIOU	Directeur de Thèse
Mr. João Pedro Assumpção BASTOS	Co-Directeur de Thèse
Mr. Jean-Yves ROGER	Invité
Mr. Mario Célio CONTIN	Invité

Publications associées à la thèse:

[RICL-16] et [CICL-23, CICL-28, CICL-34]

- **Rindra Ramarotafika** (encadrement à 50%)

"Modélisation stochastique de la variabilité des propriétés magnétiques des matériaux ferromagnétiques: application sur des stators de machines électriques".

Thèse soutenue le 13 septembre 2012 devant le jury composé de:

Mr. Alain IOST	Président
Mme Afef KEDOUS-LEBOUC	Rapporteuse
Mr. Laurent DANIEL	Rapporteur
Mr. Luc DUPRÉ	Examinateur
Mr. Kay HAMEYER	Examinateur
Mr. Abdelkader BENABOU	Examinateur
Mr. Stéphane CLÉNET	Directeur de Thèse
Mr. Jean Claude MIPO	Invité

Publications associées à la thèse:

[RICL-8, RICL-10, RICL-11, RICL-15, RICL-17] et [CICL-16, CICL-17, CICL-19, CICL-25, CICL-26]

- **Mircea Frăţilă** (encadrement à 50%)

"Contribution à la prise en compte des pertes fer dans la modélisation des machines électriques par éléments finis".

Thèse soutenue le 19 décembre 2012 devant le jury composé de:

Mr. Hamid BEN AHMED	Président
Mr. Anouar BELAHCEN	Rapporteur
Mr. Daniel MATT	Rapporteur
Mme. Marie-Ange RAULET	Examinatrice
Mr. Frédéric GILLON	Examinateur
Mr. Daniel ROGER	Examinateur
Mr. Abdelkader BENABOU	Examinateur
Mr. Abdelmounaïm TOUNZI	Directeur de Thèse
Mr. Maxime DESSOUDE	Invité

Publications associées à la thèse:

[RICL-7, RICL-9, RICL-10] et [CICL-14, CICL-18, CICL-19, CICL-26, CICL-27]

- **Carlos Cuellar** (encadrement à 35%)

"HF characterization and modeling of magnetic materials for the passive components design of EMI filters".

Thèse soutenue le 07 octobre 2013 devant le jury composé de:

Mr. François COSTA	Président
Mme Marie-Ange RAULET	Rapporteuse
Mr. Flavio CANAVERO	Rapporteur
Mr. Abdelkader BENABOU	Examinateur
Mr. Xavier MARGUERON	Examinateur
Mr. Nadir IDIR	Directeur de Thèse
Mr. Houmam MOUSSA	Invité

Publications associées à la thèse:

[RICL-1, RICL-2, RICL-5] et [CICL-4, CICL-11, CICL-21]

- **Radu Frățilă** (encadrement à 50%)

"Modélisation numérique de la perte d'aimantation d'aimants permanents sous les contraintes magnétique et thermique rencontrées dans les dispositifs électriques".

Thèse soutenue le 28 mars 2014 devant le jury composé de:

Mr. Mohamed El Hadi ZAÏM	Président
Mr. Anouar BELAHCEN	Rapporteur
Mr. Jean-Paul YONNET	Rapporteur
Mr. Christophe ESPANET	Examineur
Mr. Abdelkader BENABOU	Examineur
Mr. Abdelmounaïm TOUNZI	Directeur de Thèse
Mr. Jean-Claude MIPO	Invité

Publications associées à la thèse:

[RICL-6, RICL-14] et [CICL-12, CICL-13, CICL-22]

- **Jalal Cheytani** (encadrement à 50%)

"Calcul par éléments finis des pertes supplémentaires dans les motorisations performantes".

Thèse sous la direction de A. Tounzi (L2EP) - Soutenance prévue début 2016.

Publications associées à la thèse:

[CICL-1, CICL-8, CICL-10]

- **Laure Arbenz** (encadrement à 50%)

"Caractérisation et modélisation des propriétés électromagnétiques des aciers doux de rotors à griffes".

Thèse sous la direction de S. Clénet (L2EP) - Soutenance prévue début 2016.

Publications associées à la thèse:

[RICL-3], [CICL-2, CICL-9] et [CNCL-1, CNCL-3]

- **Marc Borsenberger** (encadrement à 40%)

Thèse sous la direction de R. Bigot (LCFC) - Soutenance prévue début 2018.

Encadrements de master

- **Fatima Elarab** (2015)

co-encadrement avec le laboratoire UMET-Université Lille 1

"Etude de l'influence de chargements mécaniques cycliques sur les propriétés magnétiques de l'acier Fe3%Si".

- **Hicham Elaroussi** (2014)
"Influence du champ magnétique sur les procédés d'usinage".
- **Alfonso Ayensa-Jimenez** (2010)
"Caractérisation électrique et magnétique d'une poudre de magnétite".
Publication associée: [CICL-24]
- **Carlos Cuellar** (2010)
"Caractérisation et modélisation haute fréquence des matériaux ferrites des filtres CEM". Carlos Cuellar a poursuivi en thèse au laboratoire.
- **Inigo Cappelán-Perez** (2009)
co-encadrement avec le laboratoire MSMP-Arts et Métiers Lille
"Reconstruction de la loi de comportement magnétique macroscopique d'un SMC à partir d'imagerie au microscope".
Publication associée: [CNCL-4]
- **Diallo Souaibou** (2008)
"Modélisation d'un transformateur triphasé et calcul des pertes associées".
- **Francisc Bölöni** (2006)
"Techniques hybrides de production de champs magnétiques".
Francisc Bölöni a poursuivi en thèse au laboratoire.
- **Hichem Azli** (2005)
"Etude éléments finis de systèmes électrotechniques avec prise en compte de l'hystérésis vectoriel".

3.5 Liste des publications

- **Revue Internationale avec Comité de Lecture**

- [RICL-1] "High Frequency Behavioral Ring Core Inductor Model", Carlos Cuellar, Nadir Idir, Abdelkader Benabou, IEEE Transactions on Power Electronics, à paraître.
- [RICL-2] "High frequency current probes for common-mode impedance measurements of power converters under operating conditions", Carlos Cuellar, Abdelkader Benabou, Nadir Idir, Xavier Margueron, EPE Journal, Vol. 24, No. 4, 2015.
- [RICL-3] "Characterization of the Local Electrical Properties of Electrical Machine Parts with non-Trivial Geometry", Laure Arbenz, Abdelkader Benabou, Stéphane Clénet, Jean-Claude Mipo, Pierre Faverolle, International Journal of Applied Electromagnetics and Mechanics, Vol. 48, No. 2-3, pages 201-206, 2015.
- [RICL-4] "End-Region Leakage Fluxes and Losses Analysis of Cage Induction Motors Using 3-D Finite-Element Method", Jalal Cheaytani, Abdelkader Benabou, Abdelmounaïm Tounzi, Maxime Dessoude, Loïc Chevallier, Thomas Henneron, IEEE Transactions on Magnetics, Vol. 51, No. 3, 2015.

- [RICL-5] "Characterization and modeling of hysteresis for magnetic materials used in EMI filters of power converters", Carlos Cuellar, Abdelkader Benabou, Nadir Idir, IEEE Transactions on Power Electronics, Vol. 29, No. 9, pages 4911-4920, 2014
- [RICL-6] "A Combined experimental and Finite Element Analysis method for the estimation of eddy-current loss in NdFeB magnets", Radu Fratila, Abdelkader Benabou, Abdelmounaïm Tounzi, Jean-Claude Mipo, Sensors Journal, Vol. 14, Special Issue, 2014.
- [RICL-7] "Calculation of iron loss in Solid Rotor Induction Machine using FEM", Mircea Fratila, Abdelkader Benabou, Abdelmounaïm Tounzi, Maxime Dessoude, IEEE Transactions on Magnetics, Vol. 50, No. 2, 2014.
- [RICL-8] "Stochastic Jiles-Atherton model accounting for soft magnetic material variability", Rindra Ramarotafika, Abdelkader Benabou, Stéphane Clénet, COMPEL: The International Journal for Computation and Mathematics in Electrical and Electronic Engineering, Vol. 32, No. 5, pages 1679-1691, 2013.
- [RICL-9] "Improved iron loss calculation for non-centered minor loops", Mircea Fratila, Abdelkader Benabou, Abdelmounaïm Tounzi, Maxime Dessoude, COMPEL: The International Journal for Computation and Mathematics in Electrical and Electronic Engineering, Vol. 32, No. 4, 2013.
- [RICL-10] "Stochastic post processing calculation of iron losses -Application to a PMSM", Mircea Fratila, Rindra Ramarotafika, Abdelkader Benabou, Stéphane Clénet, Abdelmounaïm Tounzi, COMPEL: The International Journal for Computation and Mathematics in Electrical and Electronic Engineering, Vol. 32, No. 4, 2013.
- [RICL-11] "Stochastic modelling of anhysteretic magnetic curve using random interdependant coefficients", Rindra Ramarotafika, Abdelkader Benabou, Stéphane Clénet, International Journal of Applied Electromagnetics and Mechanics, Vol. 43, No. 1-2, pages 151-159, 2013.
- [RICL-12] "Analytical modeling to predict the cutting behavior of ferromagnetic steels: A coupled magnetic-mechanical approach", Ali Mkaddem, Abdelkader Benabou, Mohamed El Mansori, Stéphane Clénet, International Journal of Solids and Structures, Vol. 50, No. 13, pages 2078-2086, 2013.
- [RICL-13] "Nonlinear Proper Generalized Decomposition Method Applied to the Magnetic Simulation of a SMC Microstructure", Thomas Henneron, Abdelkader Benabou, Stéphane Clénet, IEEE Transactions on Magnetics, Vol. 48, No. 11, 2012.
- [RICL-14] "Nonlinear Modeling of Magnetization Loss in Permanent Magnets", Radu Fratila, Abdelkader Benabou, Abdelmounaïm Tounzi, Jean Claude Mipo, IEEE Transactions on Magnetics, Vol. 48, No. 11, pages 2957-2960, 2012.

- [RICL-15] "Stochastic Modeling of Soft Magnetic Properties of Electrical Steels: Application to Stators of Electrical Machines", Rindra Ramarotafika, Abdelkader Benabou, Stéphane Clénet, IEEE Transactions on Magnetics, Vol. 48, No. 10, pages 2573-2584, 2012.
- [RICL-16] "Interlaminar short circuit detection: modeling and measurement", Juliana-Luisa Müller, Raphael Romary, Abdelkader Benabou, Thomas Henneron, Francis Piriou, J-P Bastos, J-Y Roger, COMPEL: The International Journal for Computation and Mathematics in Electrical and Electronic Engineering, Vol. 31, No. 5, 2012.
- [RICL-17] "Experimental Characterization of the Iron Losses Variability in Stators of Electrical Machines", Rindra Ramarotafika, Abdelkader Benabou, Stéphane Clénet, J-C Mipo, IEEE Transactions on Magnetics, Vol. 48, No. 4, pages 1629-1632, 2012.
- [RICL-18] "Adaptive Method for Non-Intrusive Spectral Projection – Application on a Stochastic Eddy Current NDT Problem", Karim Beddek, Stéphane Clénet, Olivier Moreau, Valentin Costan, Yvonnick LE Menach, Abdelkader Benabou, IEEE Transactions on Magnetics, Vol. 48, No. 2, pages 759-762, 2012.
- [RICL-19] "Stochastic Modeling of the Pull-In Voltage in a MEMS Beam Structure", Francisc Boloni, Abdelkader Benabou, Abdelmounaïm Tounzi, IEEE Transactions on Magnetics, Vol. 47, No. 5, pages 974-977, 2011.
- [RICL-20] "Evaluation of the Perturbation Method for Iterative Calculations in 2D Finite Element Analysis", Benoit Daussy, Damien Laval, Abdelkader Benabou, Abdelmounaïm Tounzi, Studies in Applied Electromagnetics and Mechanics: Computer Field Models of Electromagnetic Devices, Vol. 34, pages 285-291, 2010.
- [RICL-21] "Finite Element Modeling of the Hysteresis Effect in a Magnetorheological Brake", Richard Demersseman, Abdelkader Benabou, Stéphane Clénet, Betty Lemaire-Semail, Studies in Applied Electromagnetics and Mechanics: Computer Field Models of Electromagnetic Devices, Vol. 34, pages 756-762, 2010.
- [RICL-22] "Hysteresis Phenomenon Implementation in FIT: Validation with Measurements", Julien Korecki, Abdelkader Benabou, Yvonnick Le Menach, Jean-Pierre Ducreux, Francis Piriou, IEEE Transactions on Magnetics, Vol. 46, No. 8, pages 3285-3288, 2010.
- [RICL-23] "Transformer Inrush Currents Taking Into Account Vector Hysteresis", Jean Viane Leite, Abdelkader Benabou, Nelson Sadowski, IEEE Transactions on Magnetics, Vol. 46, No. 8, pages 3237-3240, 2010.
- [RICL-24] "Three-Phase Transformer Modelling Using the Vector Hysteresis Model and Including the Eddy Current and the Anomalous Losses", Mauricio Valencia

Ferreira Da Luz, Jean Vianeï Leite, Abdelkader Benabou, Nelson Sadowski, IEEE Transactions on Magnetics, Vol. 46, No. 8, pages 3201-3204, 2010.

- [RICL-25] "Comparison of pull-in voltage in MEMS using 3D FEM and analytical approach", Francisc Boloni, Abdelkader Benabou, Abdelmounaïm Tounzi, The International Journal for Computation and Mathematics in Electrical and Electronic Engineering, Vol. 29, No. 6, 2010.
- [RICL-26] "Minor Loops Calculation with a Modified Jiles-Atherton Hysteresis Model", Jean Vianeï Leite, Nelson Sadowski, Patrick Kuo-Peng, Abdelkader Benabou, Journal of Microwaves, Optoelectronics and Electromagnetic Applications, Vol. 8, No. 1, 2009.
- [RICL-27] "Finite Element Three-Phase Transformer Modeling Taking Into Account a Vector Hysteresis Model", Jean Vianeï Leite, Abdelkader Benabou, Nelson Sadowski, Mauricio V. Ferreira Da Luz, IEEE Transactions on Magnetics, Vol. 45, No. 3, pages 1716-1719, 2009.
- [RICL-28] "Electromagnetic modelling of short circuited coreplates", Jean-Yves Roger, Emmanuel Vrignaud, Thomas Henneron, Abdelkader Benabou, Jean-Pierre Ducreux, The International Journal for Computation and Mathematics in Electrical and Electronic Engineering, Vol. 28, No. 3, pages 762-771, 2009.
- [RICL-29] "Accurate minor loops calculation with a modified Jiles-Atherton hysteresis model", Jean Vianeï Leite, Abdelkader Benabou, Nelson Sadowski, The International Journal for Computation and Mathematics in Electrical and Electronic Engineering, Vol. 28, No. 3, pages 741-749, 2009.
- [RICL-30] "Minor loops modelling with a modified Jiles-Atherton model and comparison with the Preisach model", Abdelkader Benabou, Jean Vianeï Leite, Stéphane Clénet, C. Simao, N. Sadowski, Journal of Magnetism and Magnetic Materials, Vol. 320, No. 20, pp. 1034-1038, 2008.
- [RICL-31] "Implementation of a Vector Hysteresis Model in 2D Finite Element Analysis: Study of a RSST with Anisotropic Sample", Jean Vianeï Leite, Abdelkader Benabou, Nelson Sadowski, Stéphane Clénet, Yvonnick Le Menach, International Journal of Applied Electromagnetics and Mechanics, Vol. 28, No. 1-2, pp. 41-47, 2008.
- [RICL-32] "Implementation of an Anisotropic Vector Hysteresis Model In a 3D Finite Element Code", Jean Vianeï Leite, Abdelkader Benabou, Nelson Sadowski, Stéphane Clénet, J.P.A. Bastos, Francis Piriou, IEEE Transactions on Magnetics, Vol. 44, No. 6, pp. 918-921, 2008.
- [RICL-33] "Permanent magnets modelling for dynamic applications", Abdelkader Benabou, Samuel Georges, Stéphane Clénet, Journal of Magnetism and Magnetic Materials, Vol. 320, No. 6, pp. 830-835, 2008.

- [RICL-34] "Analysis of a rotational single sheet tester using 3D Finite Element model taking into account hysteresis effect", Jean Viane Leite, Abdelkader Benabou, Pedro Armando Da Silva, Nelson Sadowski, Thomas Henneron, Stéphane Clénet, P. Kuo-Peng, Francis Piriou, N.J. Batistela, COMPEL: The International Journal for Computation and Mathematics in Electrical and Electronic Engineering, Vol. 26, No. 4, pp. 1037-1048, 2007.
- [RICL-35] "Inclusion of a stress-dependent Preisach model in 2D FE calculations", Abdelkader Benabou, Lode Vandenbossche, Johan Gyselinck, Stéphane Clénet, Luc Dupré, Patrick Dular, COMPEL: The International Journal for Computation and Mathematics in Electrical and Electronic Engineering, Vol. 25, No. 1, pp. 81-90, 2006.
- [RICL-36] "Modelling of a hysteresis motor using the Jiles-Atherton model", Abdelkader Benabou, Lounas Bouaziz, Stéphane Clénet, European Physical Journal Applied Physics, Vol. 29, No. 3, pp. 259-265, 2005.
- [RICL-37] "Comparison of the Preisach and Jiles-Atherton models to take hysteresis phenomenon into account in Finite Element Analysis", Abdelkader Benabou, Stéphane Clénet, Francis Piriou, COMPEL: The International Journal for Computation and Mathematics in Electrical and Electronic Engineering, Vol. 23, No. 3, pages 825-834, 2004.
- [RICL-38] "Adaptation of the Frequency Dependent Jiles-Atherton Model with B as entry variable", Abdelkader Benabou, Stéphane Clénet, Francis Piriou, International Journal of Applied Electromagnetics and Mechanics, Vol. 19, No. 1-4, pages 187-191, 2004.
- [RICL-39] "Comparison of Preisach and Jiles-Atherton models to take into account hysteresis phenomenon for finite element analysis", Abdelkader Benabou, Stéphane Clénet, Francis Piriou, Journal of Magnetism and Magnetic Materials, Vol. 261, No. 1-2, pages 139-160, 2003.

• **Conférences Internationales avec Comité de Lecture**

- [CICL-1] "Loss analysis of surface-mounted permanent magnet synchronous motor due to carrier harmonics using 3D-FEM", Jalal Cheaytani, Abdelkader Benabou, Abdelmounaïm Tounzi, Maxime Dessoude, ISEF 2015, Valence, Espagne, 09-2015.
- [CICL-2] "Characterization of the local incremental permeability of a ferromagnetic plate based on a four needles technique", Laure Arbenz, Abdelkader Benabou, Stéphane Clénet, Jean-Claude Mipo, Pierre Faverolle, SMM 2015, Sao Paulo, Brésil, 09-2015.

- [CICL-3] "Iron loss computation of a hybrid excitation synchronous generator", Maxime Ployard, Aymen Ammar, Juliana Iamamura, Dan Ilea, Frédéric Gillon, Abdelkader Benabou, ISEF 2015, Valence, Espagne, 09-2015.
- [CICL-4] "High Frequency Model of Ferrite and Nanocrystalline Ring Core Inductors", Carlos Cuellar, Nadir Idir, Abdelkader Benabou, 17th European conference on power electronics and applications (EPE 2015), 08-2015.
- [CICL-5] "Iron loss evaluation on a hybrid synchronous generator using FEM", Juliana Iamamura, Maxime Ployard, Frédéric Gillon, Abdelkader Benabou, Daniel Laloy, Aymen Ammar, Compumag 2015, Montreal, Canada, 07-2015.
- [CICL-6] "Eddy current computation in 2D-FEM for permanent magnet loss calculation", Walid Boughanmi, Thomas Henneron, Abdelkader Benabou, Abdelmounaim Tounzi, Mohammed-El-Hadi Zaim, Compumag 2015, Montreal, Canada, 07-2015.
- [CICL-7] "Finite Element Implementation and Experimental Validation of 2D/3D Magnetic Force formulae", Walid Boughanmi, François Henrotte, Abdelkader Benabou, Yvonnick Le-Menach, Compumag 2015, Montreal, Canada, 07-2015.
- [CICL-8] "Finite-Element Investigation on Zig-Zag Flux in Squirrel Cage Induction Machines", Jalal Cheaytani, Abdelkader Benabou, Abdelmounaim Tounzi, Maxime Dessoude, International Conference on Electrical Machines (ICEM2014), 9-2014.
- [CICL-9] "Characterization of the local electrical properties of electrical machine parts with non-trivial geometry", Laure Arbenz, Abdelkader Benabou, Stéphane Clenet, Jean-Claude Mipo, Pierre Faverolle, 2dm , Turin, Italy, 09-2014.
- [CICL-10] "End-region leakage fluxes and losses analysis of cage induction motors using 3-D finite element method", Jalal Cheaytani, Abdelkader Benabou, Abdelmounaim Tounzi, Maxime Dessoude, Conference on Electromagnetic field computation (CEFC 2014), Annecy, France, 5-2014.
- [CICL-11] "High frequency current probes for common-mode impedance measurements of power converters under operating conditions", Carlos Cuellar, Nadir Idir, Abdelkader Benabou, Xavier Margueron, EPE'13-ECCE Europe, Lille, France, 9-2013.
- [CICL-12] "Calculation and measurement of eddy-current loss in NdFeB Magnet", Radu Fratila, Abdelkader Benabou, Abdelmounaim Tounzi, J-C Mipo, ISEF 2013, Ohrid, Macedonia, 9-2013.
- [CICL-13] "Nonlinear magnetization loss in sintered NdFeB magnet due to eddy current heat dissipation", Radu Fratila, Abdelkader Benabou, Abdelmounaim Tounzi, J-C Mipo, Compumag 2013, Budapest, Hungary, 7-2013.

- [CICL-14] "Calculation of Iron loss in Solid Rotor Induction Machine using FEM", Mircea Fratila, Abdelkader Benabou, Abdelmounaïm Tounzi, Maxime Dessoude, Compumag 2013, Budapest, Hungary, 7-2013.
- [CICL-15] "Impact of the material and geometry uncertainties on the pull-in voltage in a MEMS beam structure", Abdelkader Benabou, Francisc Boloni, Abdelmounaïm Tounzi, Stéphane Clénet, OIPE 2012, Ghant, Belgium, 9-2012.
- [CICL-16] "Stochastic modeling of anhysteretic magnetic curves using random inter-dependant coefficients", Rindra Ramarotafika, Abdelkader Benabou, Stéphane Clénet, OIPE 2012, Ghant, Belgium, 9-2012.
- [CICL-17] "Stochastic Jiles-Atherton model accounting for soft magnetic material variability", Rindra Ramarotafika, Abdelkader Benabou, Stéphane Clénet, IGTE 2012, Graz, Austria, 9-2012.
- [CICL-18] "Improved iron loss calculation for non-centered minor loops", Mircea Fratila, Abdelkader Benabou, Abdelmounaïm Tounzi, Maxime Dessoude, EPNC 2012, Pula, Croatie, 6-2012.
- [CICL-19] "Stochastic post processing calculation of iron losses -Application to a PMSM", Mircea Fratila, Rindra Ramarotafika, Abdelkader Benabou, Stéphane Clénet, Abdelmounaïm Tounzi, EPNC 2012, Pula, Croatie, 6-2012.
- [CICL-20] "Proper Generalized Decomposition method applied to the magnetic simulation of a SMC microstructure", Thomas Henneron, Abdelkader Benabou, Stéphane Clénet, Intermag 2012, Vancouver, Canada, 5-2012.
- [CICL-21] "Measurement Method of the Complex Magnetic Permeability of Ferrites in High Frequency", Carlos Cuellar, Wenhua Tan, Xavier Margueron, Abdelkader Benabou, Nadir Idir, IEEE Instrumentation and Measurement Technology Conference I2MTC12, 5-2012.
- [CICL-22] "Non-linear modeling of magnetization loss in permanent magnets", Radu Fratila, Abdelkader Benabou, Abdelmounaïm Tounzi, Jean-Claude Mipo, Intermag 2012, Vancouver, Canada, 5-2012.
- [CICL-23] "Interlaminar short-circuit detection: modeling of the El Cid test and comparison with the experiment", Juliana-Luisa Müller, R. Romary, Abdelkader Benabou, Thomas Henneron, Francis Piriou, J.P.A. Bastos, J-Y Roger, ISEF 2011, Madeira, Portugal, 9-2011.
- [CICL-24] "Determination of the electrical conductivity and magnetic permeability of magnetic powders", Abdelkader Benabou, Ayensa Jimenez, Stéphane Clénet, Olivier Moreau, ISEF 2011, Madeira, Portugal, 9-2011.
- [CICL-25] "Influence of the manufacturing process on magnetic properties of claw pole generator stators: B-H curve variability measurements", Rindra Ramarotafika, Abdelkader Benabou, Stéphane Clénet, ISEM 2011, Napoli, Italy, 9-2011.

- [CICL-26] "Investigation of the Numerical Error Influence in a 3D FE Post-Processing Iron Loss Calculation Procedure", Mircea Fratila, Abdelkader Benabou, Abdelmounaïm Tounzi, Rindra Ramarotafika, Maxime Dessoude, ISEM 2011, Napoli, Italy, 9-2011.
- [CICL-27] "Investigation of the Impact of Rotational Losses in a Three-Phase Transformer", Mircea Fratila, Abdelkader Benabou, Abdelmounaïm Tounzi, Maxime Dessoude, ISEF 2011, Madeira, Portugal, 9-2011.
- [CICL-28] "3D FE Modelling of Interlamination Short-circuits Taking into Account the Building Bar", Juliana-Luisa Müller, Abdelkader Benabou, Thomas Henneron, Francis Piriou, J.P.A. Bastos, J-Y Roger, Compumag 2011, Sydney, Australie, 7-2011.
- [CICL-29] "Proper adaptive method for Non-intrusive Spectral Projection – Application on Eddy Current Non Destructive Testing", Karim Beddek, Stéphane Clénet, Olivier Moreau, Valentin Costan, Yvonnick Le Menach, Abdelkader Benabou, Compumag 2011, Sydney, Australie, 7-2011.
- [CICL-30] "Experimental characterization of the iron losses variability in stators of electrical machines", Rindra Ramarotafika, Abdelkader Benabou, Stéphane Clénet, Jean Claude Mipo, SMM, Kos, Greece, 4-2011.
- [CICL-31] "Non-Linear Analytical Model of a Three Phase Transformer Based on 2D-FEM Identification of its Reluctances", Mircea Fratila, Abdelkader Benabou, Thomas Henneron, EPNC 2010, Essen, Germany, 6-2010.
- [CICL-32] "Statistical modeling of an anisotropic lamination stack", Adil Jarrah, Stéphane Clénet, Abdelkader Benabou, Rindra Ramarotafika, CEFC 2010, Chicago, USA, 5-2010.
- [CICL-33] "Stochastic Modeling of the Pull-In Voltage in a MEMS Beam Structure", Francisc Bölöni, Abdelkader Benabou, Abdelmounaïm Tounzi, CEFC 2010, Chicago, USA, 5-2010.
- [CICL-34] "Study of Different FEM Models to Analyze Homogenized Iron Lamination with Electrical Fault", Juliana-Luisa Müller, Abdelkader Benabou, Thomas Henneron, Francis Piriou, J.P.A. Bastos, J-Y. Roger, Compumag 2009, Florianopolis, Brasil, 11-2009.
- [CICL-35] "Force Computation in a MEMS Structure Using Adaptive Mesh Refinement", Francisc Boloni, Abdelkader Benabou, Guillaume Krebs, Abdelmounaïm Tounzi, Compumag 2009, Florianopolis, Brasil, 11-2009.
- [CICL-36] "Evaluation of the perturbation method for iterative calculations in 2D finite element analysis", Benoit Daussy, Damien Laval, Abdelkader Benabou, Abdelmounaïm Tounzi, ISEF 2009, Arras, France, 9-2009.

- [CICL-37] "Comparison between the Preisach model and a modified Jiles-Atherton hysteresis model for the minor loops representation", Jean Vianeite Leite, Nelson Sadowski, Abdelkader Benabou, Numelec 2008, Liège, Belgique, 12-2008.
- [CICL-38] "Calculation of the force exerted on an object penetrating a ferrofluid", Abdelkader Benabou, Stéphane Clénet, EPNC 2008, Lille, France, 7-2008.
- [CICL-39] "Accurate minor loops calculation with a modified Jiles-Atherton hysteresis model", Jean Vianeite Leite, Abdelkader Benabou, Nelson Sadowski, EPNC 2008, Lille, France, 7-2008.
- [CICL-40] "Finite Element Three-Phase Transformer Modeling Taking into Account a Vector Hysteresis Model", Jean Vianeite Leite, Abdelkader Benabou, Nelson Sadowski, Mauricio V. Luz, CEFC 2008, Athen, Greece, 5-2008.
- [CICL-41] "Measurement of magnetic losses in soft magnetic materials with harmonic induction", Charles Cyr, Fabrice Locment, Stéphane Clénet, Abdelkader Benabou, Philippe Viarouge, SMM 2007, Cardiff, UK, 9-2007.
- [CICL-42] "Implementation of a Vector Hysteresis Model in 2D Finite Element Analysis: Study of a RSST with Anisotropic Sample", Abdelkader Benabou, Nelson Sadowski, Yvonnick Le Menach, Stéphane Clénet, Pedro Armando Da Silva, ISEM 2007, Michigan, USA, 9-2007, Jean Vianeite Leite.
- [CICL-43] "Minor loops modelling with a modified Jiles-Atherton model and comparison with the Preisach Model", Abdelkader Benabou, Jean Vianeite Leite, Stéphane Clénet, C. Simao, Nelson Sadowski, SMM 2007, Cardiff, United Kingdom, 9-2007.
- [CICL-44] "Implementation of an Anisotropic Vector Hysteresis Model In a 3D Finite Element Code", Jean Vianeite Leite, Abdelkader Benabou, Nelson Sadowski, Stéphane Clénet, Joao Pedro A. Bastos, Francis Piriou, Compumag 2007, Aachen, Germany, 7-2007.
- [CICL-45] "Improvements in Jiles-Atherton Hysteresis Model to Take into Account Minor Loops", Jean Vianeite Leite, Abdelkader Benabou, C. Simao, Nelson Sadowski, HMM 2007, Naples, Italy, 6-2007.
- [CICL-46] "Study of Magnetic Induction Measurement Techniques in Rotational Single Sheet Tester", Pedro Armando Da Silva, Nelson Sadowski, Abdelkader Benabou, N.J. Batistela, J.P.A. Bastos, Stéphane Clénet, Francis Piriou, Compumag 2007, Aachen, Germany, 6-2007.
- [CICL-47] "Analysis of the shielding sheet distance influence in rotational single sheet tester", Pedro Armando Da Silva, Abdelkader Benabou, N.J. Batistela, Stéphane Clénet, Nelson Sadowski, J.P.A. Bastos, Numelec 2006, Lille, France, 12-2006.

- [CICL-48] "Analysis of a rotational single sheet tester using 3d finite element model taking into account hysteresis effect", Jean Vianei Leite, Abdelkader Benabou, Pedro Armando Da Silva, Nelson Sadowski, Thomas Henneron, Stéphane Clenet, Patrick Kuo-Peng, Francis Piriou, N.J. Batistela, EPNC 2006, Maribor, Slovenia, 6-2006.
- [CICL-49] "Inclusion of a stress-dependent Preisach model in 2D FE calculations", Abdelkader Benabou, Lode Vandenbossche, Johan Gyselinck, Stéphane Clenet, Luc Dupre, Patrick Dular, EPNC 2004, Poznan, Poland, 6-2004.
- [CICL-50] "Experimental determination of SMC material conductivity", Abdelkader Benabou, Stéphane Clenet, Francis Piriou, EMF 2003, Aachen, Germany, 10-2003.
- [CICL-51] "Adaptation of the Frequency Dependent Jiles-Atherton Model with B as entry variable", Abdelkader Benabou, Stéphane Clenet, Francis Piriou, ISEM 2003, Versailles, France, 5-2003.
- [CICL-52] "Comparison of the Preisach and Jiles-Atherton models to take hysteresis phenomenon into account in Finite Element Analysis", Abdelkader Benabou, Stéphane Clenet, Francis Piriou, EPNC 2002, Leuven, Belgium, 7-2002.

• Conférences Nationales avec Comité de Lecture

- [CNCL-1] "Etude par éléments finis de la méthode des quatre pointes pour la caractérisation des propriétés électromagnétiques d'une plaque épaisse", Laure Arbenz, Abdelkader Benabou, Stéphane Clenet, Jean-Claude Mipo, Pierre Faverolle, Numelec 2015, Saint-Nazaire, 06-2015.
- [CNCL-2] "Détermination des pertes harmoniques dans les aimants permanents. Cas des machines synchrones à aimants déposés", Mohamed Elhaddi Zaïm, Walid Boughanmi, Abdelkader Benabou, Abdelmounaim Tounzi, T.N.L. Dang, Numelec 2015, Saint-Nazaire, 06-2015.
- [CNCL-3] "Approche combinée expérimentale/numérique pour la mesure de la conductivité électrique locale avec minimisation de l'incertitude de mesure", Laure Arbenz, Abdelkader Benabou, Stéphane Clenet, Thierry Coorevits, Jean-Claude Mipo, Pierre Faverolle, SGE 2014, Cachan, France, 07-2014.
- [CNCL-4] "Détermination de la loi de comportement macroscopique des SMC à partir d'imagerie au MEB : étude de l'influence des conditions d'observation", Inigo Capellan-Perez, Abdelkader Benabou, Gildas Guillemot, Stéphane Clenet, MGE 2010, Montpellier, France, 8-2010, 8-2010.
- [CNCL-5] "Détermination de la contrainte seuil dans un liquide magnétorhéologique à l'aide d'un modèle EF 3D", Abdelkader Benabou, Stéphane Clenet, W. Na, MGE 2008, Toulouse, France, 5-2008.

- [CNCL-6] "Modélisation par éléments finis de capteurs de flux pour la caractérisation de l'hystérésis en champ tournant", Abdelkader Benabou, Thomas Henneron, Stéphane Clénet, Francis Piriou, MGE 2005, Lyon, France, 12-2005.
- [CNCL-7] "Modélisation de l'hystérésis magnétique des aciers électriques sous contrainte mécanique", Abdelkader Benabou, Yves Bernard, Florence Ossart, EF 2003, Gif-sur-Yvette, France, 12-2003.
- [CNCL-8] "Modélisation de l'hystérésis magnétique : étude d'un modèle atomique pour la description du ferromagnétisme", Abdelkader Benabou, JCGE 2003, Saint-Nazaire, France, 6-2003.
- [CNCL-9] "Etude de modèles d'hystérésis dynamiques en vue d'une implantation dans un code de calcul Eléments Finis", Abdelkader Benabou, Stéphane Clénet, Francis Piriou, MGE 2003, Grenoble, France, 4-2003.
- [CNCL-10] "Identification et optimisation des paramètres du modèle de Jiles-Atherton pour la modélisation de l'hystérésis magnétique", Abdelkader Benabou, JCGE 2001, Nancy, France, 11-2001.

Part II

Synthesis of the work

Main introduction

Magnetic materials are widely used in engineering applications, from small electric actuators to high energy conversion devices. In fact, their electromagnetic properties allow to design devices that can fulfil the actuation operation through electromagnetic interactions and/or the energy conversion involving both the mechanical and electrical energies. The performances of such devices are intrinsically linked to the physical properties of these materials, particularly their electrical conductivity and magnetic permeability. These properties are not only dependent on the composition and micro-structure of the materials but also on the external conditions (stress, temperature...) to which the materials can be subjected.

In that context, the main question that arises is related to the role of the researcher in the field of magnetic materials in electrical engineering. On the one hand, the material science explains and theorizes on the fundamental behaviour of magnetic materials and, on the other hand, there is the applied aspect of these materials in the design of electrical devices. The literature is abundant in experimental and/or modelling studies related to both aspects. In the scope of electrical machine study/design, researchers are mostly interested in fast and reliable models that will give a good estimation and, in the worst case, a global tendency of the electrical device operation. The role of the researcher in magnetic materials for electrical engineering is at the interface between the material science and the electrical engineering. The aim is finally to provide adequate material models, in the sense of the required accuracy, involved physical phenomena (the most significant ones for the targeted application) and ease of use (identification, numerical implementation, computation time). Moreover, in the actual context of increasing efficiency requirements, new leads in terms of research must be explored, such as the influence of the manufacturing of the end-product on the material properties. Such studies require then interactions with researchers in the field of the manufacturing processes.

This synthesis report is within the frame of such approach, trying to give an overview of my research activities during this last decade. It started during my PhD dedicated to the modelling of the magnetic hysteresis phenomenon for the purpose of implementation in finite element analysis. Then, as a member of the numerical modelling team of the L2EP, these activities have rapidly evolved in direct relation with the numerical modelling of electrical devices, with the material aspect as a contribution. This contribution is part of the modelling team approach that consists in the mastering of the whole chain of modelling, from the material to the real electrical device operation. In particular, a

"three-steps" approach is applied: the model construction, the implementation in the field calculation code and the experimental validation, along with the electrical device operation analysis.

More recently, my research interests on magnetic materials have been focused on an earlier stage than the direct study of electrical devices: the manufacturing process and its influence on the material properties. The common denominator is the characterization and modelling of these properties, two aspects that are intimately linked as they are required for the knowledge of the material behaviour as well as the model elaboration and identification.

The present report is divided into four chapters. The first chapter is dedicated to the basics of magnetic materials and their properties of interest for electrical devices. Then, in the second chapter, after a description of the principle of magnetic material characterization and the most common techniques, some specific experimental setups developed during my research activities are detailed. The third chapter presents my contribution in the development of magnetic material models and their implementation in numerical models based on the Finite Element method. The content is especially dedicated to the magnetic behaviour of soft magnetic materials and the magnetization loss in permanent magnets in a context of Finite Element implementation. An opening towards probabilistic modelling of material properties is also addressed. Finally, to emphasize the interest of the proposed approaches, some conventional and non-conventional study cases are developed in the last chapter.

1

Some basics on magnetic materials

In this chapter, basics of magnetic materials are described. In addition, the main notions and notations that are used in the report are also defined.

1.1 Definition of the magnetic quantities of interest

In the vacuum, the magnetic field \mathbf{H} is related to the magnetic flux density \mathbf{B} by the magnetic permeability $\mu_0 = 4\pi \cdot 10^{-7}$ such that $\mathbf{B} = \mu_0 \mathbf{H}$. Before considering the magnetism of matter, let us first define its origin. The magnetism of materials is linked to their atomic composition and property. In fact, in the same way as a macroscopic current flowing through a closed loop generates a magnetic moment, the motion of electrons is associated to an atomic magnetic moment. More precisely, this magnetic moment is the result of two types of the electron motion, the *orbital* and *spin*. The orbital is associated to the motion of the electron around the nucleus and the spin can be interpreted as the motion of the electron spinning around its own axis.

From these considerations, the magnetic moment of an atom is the vector sum of these two types of electronic moments. For a medium, without an external magnetic field, two cases can be distinguished:

- if the magnetic moments of each atom cancel each other, making the net permanent magnetic moment of this atom equal to zero, then the medium is defined as *diamagnetic*,
- for other cases, when the magnetic moments of each atom are partially cancelled or added, the medium is defined a *para-*, *ferro-* or *ferrimagnetic*.

Under an external magnetic field, the magnetization \mathbf{M} is defined to describe the reaction of the medium to the applied magnetic field \mathbf{H} . At the macroscopic scale, the magnetization \mathbf{M} of the elementary volume ∂v in a medium is given by:

$$\mathbf{M} = \frac{\partial \mathcal{M}}{\partial v} \quad (1.1)$$

where \mathcal{M} is the vector sum over all atomic magnetic moments in ∂v . The magnetization \mathbf{M} is introduced in the relationship between \mathbf{B} and \mathbf{H} such that:

$$\mathbf{B} = \mu_0(\mathbf{H} + \mathbf{M}) \quad (1.2)$$

One can define the magnetic polarisation of the medium by $\mathbf{J} = \mu_0\mathbf{M}$ and the magnetic susceptibility χ such that $\mathbf{M} = \chi\mathbf{H}$. The relationship (1.2) can be written under the form:

$$\mathbf{B} = \mu_0(1 + \chi)\mathbf{H} \quad (1.3)$$

As mentioned above, magnetic materials are classified in three groups: diamagnetic, paramagnetic and ferromagnetic. A short description of the two first groups is given hereafter. The ferromagnetic materials, that are of interest in the frame of the present work, will be further detailed.

1.2 Diamagnetism

From a practical point of view, a diamagnetic material exhibits a weak magnetism in the opposite direction of the applied magnetic field. The theory explains this behaviour by the reduction of the effective current of the electron orbit when an external magnetic field is applied. This produces a magnetic moment opposing the applied field.

The table 1.1 shows magnetic susceptibility values for some diamagnetic materials.

Table 1.1: Magnetic susceptibility for some diamagnetic material at room temperature.

Material	Susceptibility χ
Silicon	-1.2×10^{-6}
Copper	-1.08×10^{-6}
Lead	-1.4×10^{-6}

1.3 Paramagnetism

The paramagnetism is associated to the existence of a net magnetic moment carried by the atoms or molecules. In the absence of an external magnetic field, the magnetic moments are randomly oriented so that the magnetization of the material is zero. When a magnetic field is applied, the atomic magnetic moments tend to turn toward the direction of the applied field. In the case where no opposing force is acting on the magnetization, the magnetic moments would be all aligned and the material would exhibit a large magnetic moment in the same direction as the applied magnetic field. Nevertheless, the thermal agitation of the atoms opposes the magnetization process and the magnetic moments remain pointing at random. The resulting magnetization, in the magnetic field direction, is very small with a positive susceptibility.

In table 1.2, some magnetic susceptibility values are given for paramagnetic materials.

Table 1.2: Magnetic susceptibility for some paramagnetic material at room temperature.

Material	Magnetic susceptibility χ
Aluminium	$7, 7 \cdot 10^{-6}$
Tungstène	$3, 5 \cdot 10^{-6}$
Platine	$1, 2 \cdot 10^{-5}$

As previously described, the macroscopic properties of a paramagnetic material result from a collective behaviour at the microscopic scale. A brief description of the paramagnetism, in the classical theory, is presented hereafter. This classical theory will be further used to describe the ferromagnetic behaviour.

Let us consider a system constituted of magnetic moments \mathbf{m} without any interaction and which point at random in the absence of an external magnetic field. As previously mentioned, the resulting macroscopic magnetization is zero. But, when applying a magnetic field $\mathbf{B} = \mu_0 \mathbf{H}$, the potential energy associated to a magnetic moment is given by:

$$W_{para} = -\mathbf{m} \cdot \mathbf{B} = -mB \cos(\theta) \quad (1.4)$$

with θ the angle between \mathbf{m} and \mathbf{B} .

Globally, the magnetic moments will tend to align with the applied magnetic field. Supposing that they are free to re-orientate, and in a state of thermal equilibrium, the probability for a magnetic moment having the potential energy W_{para} can be obtained from the classical Boltzmann statistical approach. This probability is proportional to:

$$g(\theta) = e\left(-\frac{W_{para}}{kT}\right) \quad (1.5)$$

where k and T are, respectively, the Boltzmann constant and the temperature. The total potential energy can be written as the statistical average:

$$\langle W_{para} \rangle = -mB \langle \cos \theta \rangle = \frac{\int_{W_{min}}^{W_{max}} W_{para}(\theta) g(\theta) dW}{\int_{W_{min}}^{W_{max}} g(\theta) dW} \quad (1.6)$$

with W_{min} and W_{max} corresponding to the minimum and maximum energy states for, respectively, $\theta = 0$ and $\theta = \pi$. By applying the change of variable such that $dW = -mB \sin(\theta) d\theta$, the average magnetic moment is found to be proportional to:

$$\langle \cos \theta \rangle = \frac{\int_0^\pi \cos \theta g(\theta) \sin \theta d\theta}{\int_0^\pi g(\theta) \sin \theta d\theta} \quad (1.7)$$

Then, by applying the change of variables $x = \cos \theta$, $z = \frac{mB}{kT}$ and $dx = -\sin \theta d\theta$, equation (1.7) becomes:

$$\langle \cos \theta \rangle = \frac{\int_1^{-1} x e^{zx} dx}{\int_1^{-1} e^{zx} dx}$$

This integral can be calculated using the integral by parts:

$$\int_{-1}^1 x e^{zx} dx = \left[\frac{x}{z} e^{zx} \right]_{-1}^1 - \frac{1}{z} \int_{-1}^1 e^{zx} dx = \frac{e^z + e^{-z}}{z} - \frac{1}{z^2} (e^z - e^{-z})$$

one equation (1.7) finally becomes:

$$\langle \cos \theta \rangle = \frac{chz}{shz} - \frac{1}{z} = \coth z - \frac{1}{z} = L(z) \quad (1.8)$$

where $L(z)$ is the Langevin function.

The total magnetization for a set of independent magnetic moments, having a density N , is given by:

$$M = NmL(z) = Nm \left[\coth \left(\frac{\mu_0 m H}{kT} \right) - \frac{kT}{\mu_0 m H} \right] \quad (1.9)$$

From this expression, one can note that for a sufficiently large magnetic field and/or low temperature, i.e. $\frac{\mu_0 m H}{kT}$ is large, almost all the magnetic moments are aligned with the direction of \mathbf{H} and the magnetization M is $M \approx Nm = M_{sat}$, corresponding to the saturation magnetization. Nevertheless, under *normal* conditions, the quantity $\frac{\mu_0 m H}{kT}$ is small and a linear behaviour is observed.

In the context of energy conversion devices, the paramagnetic and diamagnetic materials are considered to behave like the vacuum and their magnetic behaviour law is considered to be $\mathbf{B} = \mu_0 \mathbf{H}$. The ferromagnetism being the main magnetic property on which rely the energy conversion, is described in detail hereafter.

1.4 Ferromagnetism

In the case of paramagnetism, at room temperature and without the presence of an external magnetic field, no macroscopic magnetization can be observed. Nevertheless, some media exhibit a spontaneous magnetization and other media are able to magnetize under a weak external magnetic field. For these cases, the Langevin theory is not able to describe this behaviour.

1.4.1 Weiss theory

In 1907, P. Weiss introduced the molecular field theory that accounts for the interactions between the magnetic moments in a paramagnetic solid. From this point, P. Weiss formulated the hypothesis that these interactions are responsible for the existence of a spontaneous magnetization in *ferromagnetic* solids in the absence of an external magnetic field. In fact, in a ferromagnetic material, nearby spins tend to align in the same direction in order to reduce the electrostatic energy of the electrons. This exchange interaction, associated to an exchange energy, explains the existence of magnetized substances.

The basic hypothesis of P. Weiss consists in formulating that the interactions between the magnetic moments give rise to a magnetic field \mathbf{H}_m that adds to the applied magnetic field \mathbf{H} . Moreover, this interaction magnetic field \mathbf{H}_m is supposed to be proportional

to the magnetization such that $\mathbf{H}_m = \alpha\mathbf{M}$. Then, the effective magnetic field that is experienced by a magnetic moment is:

$$\mathbf{H}_e = \mathbf{H} + \alpha\mathbf{M} \quad (1.10)$$

where α is a coefficient (*molecular field parameter*). The potential energy of a magnetic moment in a ferromagnetic medium becomes:

$$W_{ferro} = -\mathbf{m} \cdot \mathbf{B}_e = -m\mu_0(H + \alpha M) \cos(\theta) \quad (1.11)$$

In that context, the Langevin expression remains valid by replacing \mathbf{H} by \mathbf{H}_e . Then, for $z = \frac{m\mu_0(H + \alpha M)}{kT}$, the state equation of the Weiss ferromagnetism is obtained:

$$M = M_{sat} \left[\coth \left(\frac{m\mu_0(H + \alpha M)}{kT} \right) - \frac{kT}{m\mu_0(H + \alpha M)} \right] \quad (1.12)$$

One must note that the ferromagnetic medium has been considered ideal and, therefore, the magnetization curve $M(H)$ obtained from the expression (1.12) is the same whether the magnetic field H is increasing or decreasing. Such magnetic behaviour will be further described as the anhysteretic curve M_{an} in the following. Moreover, the parameter a is introduced such that $a = \frac{kT}{\mu_0 m}$ and the equation becomes:

$$M_{an} = M_{sat} \left[\coth \left(\frac{H + \alpha M}{a} \right) - \frac{a}{H + \alpha M} \right] \quad (1.13)$$

The parameter a being proportional to the temperature T , its influence can be drawn in figure 1.1. In the same way, the influence of the parameter α is reported in figure 1.2.

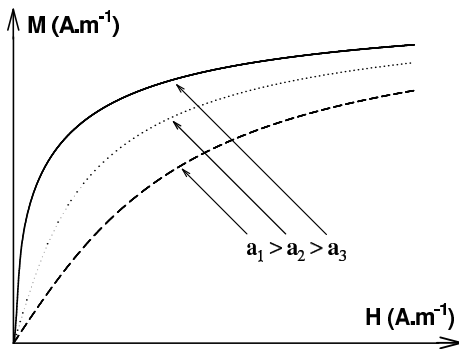


Figure 1.1: Influence of the parameter a .

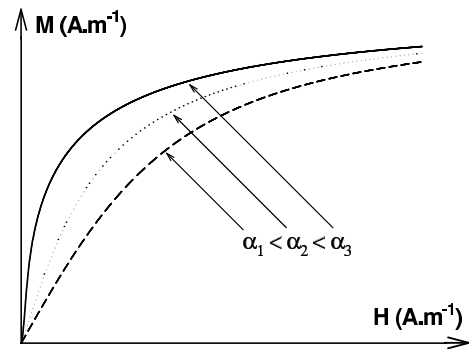


Figure 1.2: Influence of the parameter α .

One must also note that the ferromagnetic materials undergo a sharp transition in their properties at a given temperature, called the Curie temperature T_c . At this temperature, and above, the materials become paramagnetic. The process is reversible if the temperature drops below the temperature T_c . In energy conversion devices, most of the used ferromagnetic materials are based on iron alloys and, in a less extent, on cobalt and nickel. Some ferromagnetic materials are reported in table 1.3 with their respective Curie temperatures.

Table 1.3: Some ferromagnetic materials and their Curie temperature.

Material	T_c
Cobalt (Co)	1115° C
Iron (Fe)	770° C
Nickel (Ni)	358° C

1.4.2 Ferrimagnetism

Ferrimagnetism describes substances that can exhibit, like ferromagnetic substances, a spontaneous magnetization at room temperature. The ferrimagnetic substances of interest in this work are *ferrites* that are ionic compounds (double oxides of iron and another metal) and their magnetic properties depend on the magnetic ions of which they are constituted. The metal ions in a ferrite occupy two different crystallographic positions leading to a magnetic structure composed of two magnetic sub-lattices (called A and B in figure 1.3). The theoretical background for understanding the ferrimagnetism was proposed initially by L. Néel in 1948.

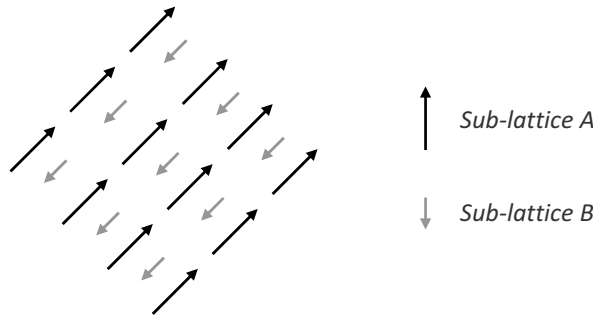


Figure 1.3: Illustration of ferrimagnetism with sub-lattices A and B

In fact, to describe the behaviour of ferrites, he showed that the exchange force acting between an ion located on the lattice A and an ion located on the lattice B is negative, as in the antiferromagnetic case. This results in a structure of ions spontaneously magnetized in two opposite directions, respectively on the A and B lattices. Moreover, in a ferrimagnetic material, the magnitudes of the sub-lattice magnetizations are different, i.e. the opposing magnetic moments do not cancel, leading then to a net spontaneous magnetization in the medium.

In electrical engineering, ferrimagnetic materials are mostly used for high frequency devices (filters, transformers, ...). These are commonly called ferrites and their composition is described by the general formula κOFe_2O_3 , where κ is a divalent ion such as Mn^{2+} , Fe^{2+} , Co^{2+} and Ni^{2+} .

1.4.3 Anisotropy

To describe the shape of the magnetization curve $M(H)$, i.e. how it changes from zero to the saturation M_{sat} , it is useful to mention the factors that affect the shape of the $M(H)$

curve. In particular, a factor that may strongly affect the shape of the $M(H)$ curve (and then the shape of the hysteresis loop as it will be described further) is the magnetic anisotropy. This means that the magnetic properties of a substance will depend on the direction in which they are measured. Two origins of anisotropy can be distinguished: the one intrinsic to the material (crystal anisotropy or *magnetocrystalline anisotropy*) and those induced (shape anisotropy, stress anisotropy, annealing, plastic deformation, ...). In the following, only the anisotropy intrinsic to the material will be briefly described in the case of iron.

The crystal structure of iron is cubic body-centered as illustrated in figure 1.4. If a disk sample of iron is cut parallel to a plane $\{110\}$ (see figure 1.4), the magnetization curves along the three main axes, namely *easy*, *medium* and *hard* axes, are very different as shown in figure 1.5.

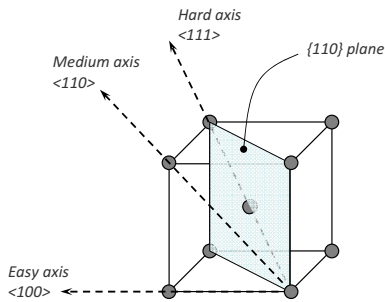


Figure 1.4: Cubic body-centered structure of iron

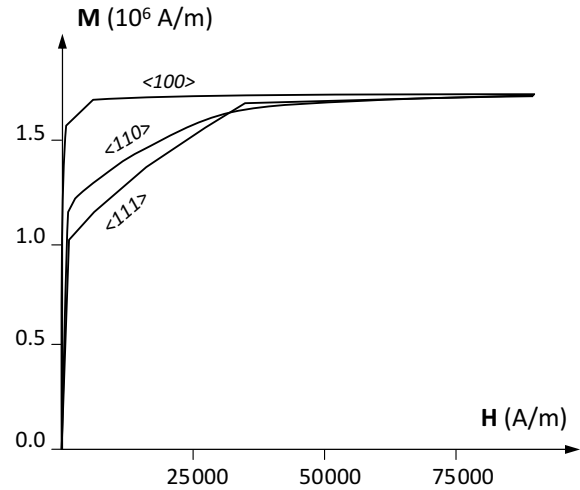


Figure 1.5: Magnetization curves for a single crystal of iron.

In its demagnetized state, the iron will be ideally structured in domains (this notion will be further introduced) that are spontaneously magnetized to saturation in the $\langle 100 \rangle$ directions. When magnetizing the sample along a different direction, the magnetic moments of the atoms will rotate if the external magnetic field is sufficiently high. In fact, as the crystal anisotropy is a force that tends to hold the magnetization along preferential crystallographic directions, the external magnetic field has to act against this force that is usually strong.

In terms of energy, the applied magnetic field must supply a work against the anisotropy and the energy stored in the crystal is called the anisotropy energy E_{ani} . For a cubic crystal, when the saturation magnetization M_{sat} is along a direction that makes angles θ_1 , θ_2 and θ_3 with the crystal axes, the anisotropy energy can be written:

$$E_{ani} = K_0 + K_1 (\alpha_1^2 \alpha_2^2 + \alpha_2^2 \alpha_3^2 + \alpha_3^2 \alpha_1^2) + K_2 (\alpha_1^2 \alpha_2^2 \alpha_3^2) + \dots \quad (1.14)$$

where $\alpha_i = \cos \theta_i$ with $i = \{1, 2, 3\}$ and K_0 , K_1 , K_2 are the anisotropy constants (in J/m^3) that depend on the material and temperature.

1.4.4 Magnetic domains

The molecular field theory introduced by P. Weiss is incomplete to explain the macroscopic behaviour of ferromagnetic substances, such as for the iron, that have no net magnetization in the absence of an external magnetic field. Weiss made the assumption that a ferromagnetic material, in its demagnetized state, is divided into small domains (*Weiss domains*) that are magnetized to saturation due to the strong coupling between the magnetic moments. Nevertheless, the directions of the domain magnetization are distributed such that the macroscopic magnetization is equal to zero.

The interface between two adjacent magnetic domains, called *domain wall*, was examined theoretically by F. Bloch in 1932 (*Bloch walls*). The domain wall is a region where the magnetization direction changes, i.e. the magnetic moments rotates from one direction to another over a distance of hundreds to thousands of Angström ($1\text{\AA}=10^{-10}m$).

1.4.4.1 Weiss domains

It has been shown that a ferromagnetic medium is constituted of magnetic moments that tend to be oriented in the same direction due to strong exchange forces. If there was only this kind of interaction, all the magnetic moments would be aligned and the resulting magnetic moment of the substance would be the saturation moment. But, two other energies, that oppose to the exchange energy between the magnetic moments, are also involved in the process : the *magnetostatic energy* and the *magnetocrystalline anisotropy energy*. As described in 1.4.3, this latter tends to align the magnetic moments along preferential directions. In the case of the magnetostatic energy, it results from interactions between the elementary magnetic moments over *long* distances within the ferromagnetic substance. Let us consider a parallelepiped single crystal sample, with its faces perpendicular to an easy magnetization axis, that is spontaneously magnetized at \mathbf{M}_{sat} (see figure 1.6). Due to the local divergence of the magnetization, volume magnetic charges will appear together with surface charges on the sample surface, and will create a demagnetizing magnetic field \mathbf{H}_d opposed to the magnetization \mathbf{M}_{sat} . In other words, this demagnetizing field is directly linked to the large dipolar field created outside the sample. The magnetostatic energy associated to the sample can be written [1]:

$$W_m = -\frac{\mu_0}{2} \int_V \mathbf{M}_{sat} \cdot \mathbf{H}_d \, dv \quad (1.15)$$

where V is the volume of the sample.

In figure 1.6, two domain configurations are illustrated. In the configuration (a), the exchange and anisotropy energies are minimised if the magnetic moments are aligned along the easy magnetization axis. But, the magnetostatic energy is large because the positive and negative magnetic poles are far from each other. As for the configuration (b), it allows to decrease the magnetostatic energy but the exchange energy increases as now there exist magnetic moments that are anti-parallel aligned at the interface between

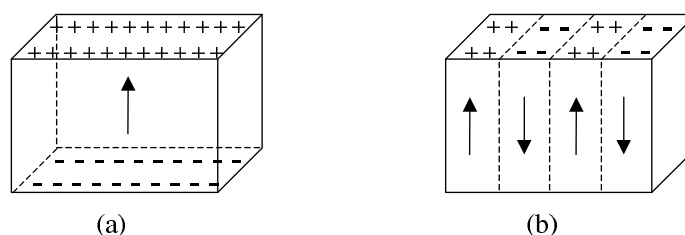


Figure 1.6: (a) Uniformly magnetized sample (b) Anti-parallel magnetized domains.

the domains. Moreover, the contribution of the anisotropy energy must also be taken into account as it tends to align the magnetic moments along specific directions of the crystal.

The competition of these different energies with opposite effects, will lead to the division of the sample into several Weiss domains. The domain structure is then not random and will obey to the physical principle of energy minimisation. The size of the domains depends on the considered ferromagnetic medium and, for a given medium, it will also depend on the shape and metallurgical quality. The order of magnitude for a Weiss domain is typically from hundreds of μm to several mm .

1.4.4.2 Bloch walls

The domain structure will lead to the creation of transitional regions between the domains where the magnetic moments have to rotate from one direction to the other. Let us first consider a 180° domain wall at the interface of two magnetic domains in which the magnetic moments are along the easy magnetization axis (see figure 1.7). The exchange energy for a pair of atoms i and j having the spin angular momentum $\hbar\mathbf{S}_i$ and $\hbar\mathbf{S}_j$ is:

$$E_{ex} = -2J_{ex}\mathbf{S}_i\mathbf{S}_j = -2JS_iS_j\cos(\phi) \quad (1.16)$$

where J_{ex} originates from the exchange effects calculation and is called the *exchange integral*, ϕ is the angle between the spins and $\hbar = \frac{h}{2\pi}$ is the reduced Planck constant ($h = 6.626 \times 10^{-34} J \cdot s$). Note that, for a ferromagnetic substance, the exchange integral J_{ex} is positive and the lowest energy state is obtained when the spins are parallel.

For a pair of atoms having the same spin S , the exchange energy becomes:

$$E_{ex} = -2JS^2\cos(\phi_{ij}) \quad (1.17)$$

If we consider a continuous model of atoms represented by n the number of atoms per unit cell and a the lattice parameter, the exchange energy can be written:

$$E_{ex} = -2A\cos\left(\frac{d\phi}{dx}\right) \quad (1.18)$$

where $A = \frac{nJS^2}{a}$ (in J/m) is the exchange stiffness and $\frac{d\phi}{dx}$ is the rate of change at which the magnetic moments are rotating in the wall. From the series expansion of the *cosinus* function, one can obtain the following expression of E_{ex} :

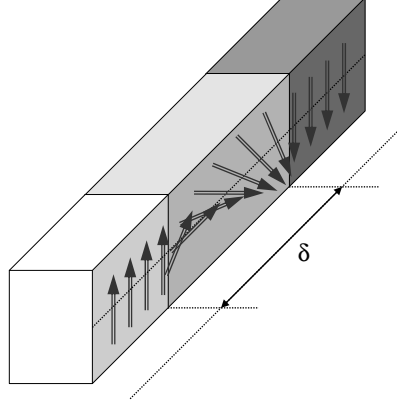


Figure 1.7: Magnetic moments rotating in a 180° Bloch wall.

$$E_{ex} = -2A + A \left(\frac{d\phi}{dx} \right)^2 \quad (1.19)$$

In this expression, if we consider the *cost* in term of energy for creating a domain wall, the constant term $-2A$ can be omitted as it does not depend on the angle. This expression shows that the rate of change of the magnetic moment orientation in the domain wall will be slow as it is less energy *consuming* than an abrupt change in the orientation of the magnetization. If we consider only the exchange energy, the domain wall length will grow without limit. In fact, the contribution to the global energy that acts to limit the length of the wall is the anisotropy energy E_K . The optimal length will be obtained from the minimization of the global energy, i.e. the sum of both energies E_{ex} and $E_K = f(\phi)$ integrated over the thickness of the wall:

$$W_{wall} = \int_{-\infty}^{\infty} (E_{ex} + E_K) dx = \int_{-\infty}^{\infty} \left(A \left(\frac{d\phi}{dx} \right)^2 + f(\phi) \right) dx \quad (1.20)$$

From this expression, it can be shown [2] that the energy (in J/m²) and effective length associated to a Bloch Wall in a material with uni-axial anisotropy, i.e. $E_K = K_{uni} \sin^2 \phi$, are:

$$W_{uni}^{180^\circ} = 4\sqrt{AK_{uni}} \quad (1.21)$$

$$\delta_{uni}^{180^\circ} = \pi \sqrt{\frac{A}{K_{uni}}} \quad (1.22)$$

In the same way, in a material such as the iron with cubic anisotropy and with a 90° domain wall in a {100} plane, i.e. $E_K = K_1 \sin^2 \phi \cos^2 \phi$, these quantities becomes :

$$W_{cubic}^{90^\circ} = 2\sqrt{AK_1} \quad (1.23)$$

$$\delta_{cubic}^{90^\circ} = \pi \sqrt{\frac{A}{K_1}} \quad (1.24)$$

In the case of iron, $K_1 = 4.2 \times 10^4 \text{ J/m}^3$ and A is calculated with $n = 2$ for body-centred cubic lattice, $J = 2.16 \times 10^{-21} \text{ J}$, $S = 1$, $a = 2.86 \times 10^{-10} \text{ m}$. The step angle between two successive magnetic moments in the 90° domain wall is about 0.6° and the length of the wall is $\delta_{cubic}^{90^\circ} \approx 430 \text{ \AA}$.

1.4.5 Magnetization process

Let us consider a ferromagnetic substance without the influence of an external magnetic field. As illustrated in figure 1.8-a, the magnetic domain structure is such that the magnetizations of the Weiss domains are oriented along easy magnetization axes and the macroscopic magnetization of the substance is zero. If now an external magnetic field is applied along an easy axis (the $[100]$ axis in this example), the process of magnetization consists in modifying the multi-domain structure into a single domain magnetized in the same direction as the applied field (see figures 1.8-b and 1.8-c). In fact, the magnetic domain having its magnetization in the same direction as the one of the external magnetic field, will grow at the expense of the other domains by *motion* of the domain walls, i.e. by the rotation of the magnetic moments.

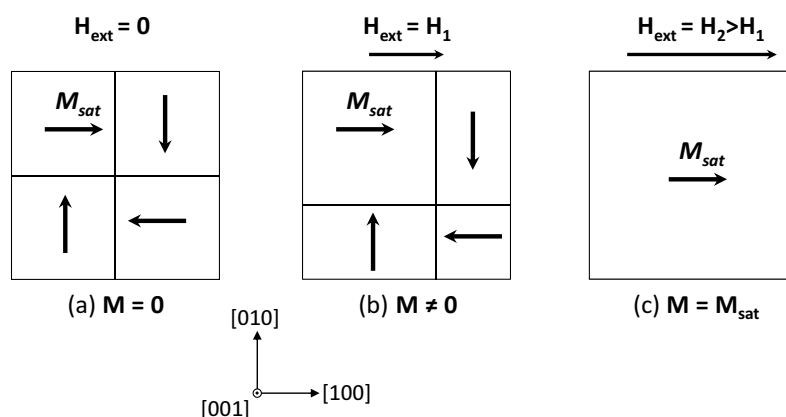


Figure 1.8: Magnetization process in a ferromagnetic medium.

Now, if we consider the case of an external magnetic field applied along a direction having an angle α with the $[100]$ axis (see figure 1.9-a), a similar magnetization process as the one described in figure 1.8 will occur in a first place. But, to align the magnetization with the applied field, the required magnetic field will be higher in order to overcome the anisotropy energy. This part of the magnetization process is associated to the rotation of the magnetization towards the applied magnetic field direction (see figure 1.9-b).

1.4.5.1 Domain wall motion

From now, it will be considered there is a *motion* of the domain walls when a magnetic field is applied. This motion is not smooth as it has been shown experimentally in 1919 by H. Barkhausen. In fact, the domain wall motion is rather discontinuous and irregular. The experiment, consisting in a search coil wound on a ferromagnetic sample, showed that during the magnetization process irregular spikes are observed on the electromotive

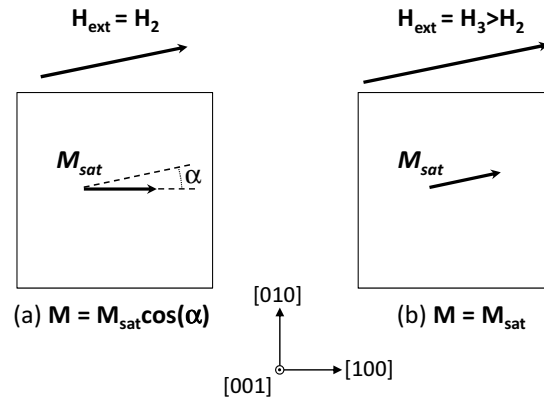


Figure 1.9: Magnetization rotation when the applied field is misaligned with an easy axis.

force induced in the search coil. These spikes are known as the *Barkhausen noise*. This effect is mainly due to the domain walls jumping from one position to another during the magnetization process.

Previously, the magnetization process has been described as the contribution of domain wall motion and domain magnetization rotation. Depending on the material composition and its micro-structure, these contributions are more or less important during the whole magnetization process. But, as a first approach, the magnetization curve can be arbitrary split into two main regions where each contribution is predominant (see figure 1.9): *domain wall motion region* beneath the knee of the curve and *domain rotation region* above this point.

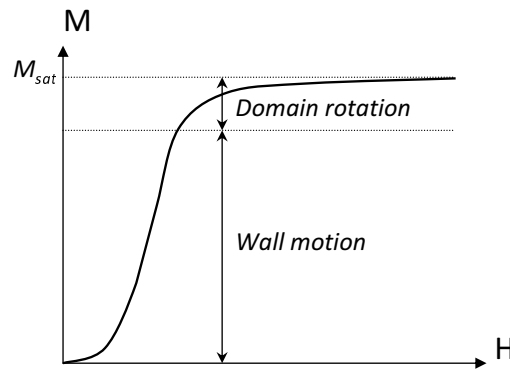


Figure 1.10: Magnetization curve divided into the wall motion and domain rotation regions.

Note that for pure domain rotation, the magnetization process is expected to be reversible whereas for the wall motion contribution, the process is irreversible as described in the following.

In fact, the motion of the domain walls is hindered by microscopic imperfections in the material. These imperfections are *inclusions* of different kinds and have a different magnetic behaviour from the surrounding material. For instance, there are impurities that can be non-magnetic (carbides, nitrides ...) and magnetic (cementite). Also, the imperfections can be related to micro-stresses due to dislocations (linear defect in the crystal lattice),

grain-boundaries and magnetostriction (interactions between domains and domain walls). Note that extrinsic conditions can also affect the domain wall motion, such as the plastic deformation for laminated materials and the surface roughness if the material is thin enough to have a single domain wall through the thickness.

All these imperfections will act as *pinning sites* within the material during the domain wall motion process. Then, from an energetic point of view, the imperfections act as *potential wells* for the domain walls. Moreover, this pinning phenomenon is the main contribution to the magnetization process giving rise to the hysteresis behaviour that will be described later.

1.4.5.2 Low field magnetization

The low field magnetization is usually considered as the one studied by Lord Rayleigh in 1887 and is called the *Rayleigh region*. The involved magnetic field is typically up to a few dozen of A/m . From the experiment, Rayleigh observed that for weak field regions (a few A/m), the magnetic permeability μ of the iron is constant whereas for high magnetic fields (up to $100A/m$) it increases linearly with the magnetic field. Thus, the magnetic permeability is:

$$\mu = \mu_i + \eta H \quad (1.25)$$

where η is the Rayleigh constant. Therefore, the magnetic behaviour $B = \mu H$ is written:

$$B = \mu_i H + \eta H^2 \quad (1.26)$$

Hysteresis loops in the Rayleigh region can be described by incorporating the parameters μ_i and η in the following expression:

$$B = (\mu_i + \eta H_{max}) H \pm \frac{\eta}{2} (H_{max}^2 - H^2) \quad (1.27)$$

where the plus and minus signs are, respectively, for the descending and ascending parts of the hysteresis loop. Nevertheless, this expression is limited to low magnetic fields and can not represent the whole magnetization process up to the saturation.

1.4.5.3 High field magnetization

For magnetic fields magnetizing the material outside the Rayleigh region, the magnetization process becomes strongly non-linear. As mentioned in section 1.4.5.1 and illustrated in figure 1.10, most of the changes in the magnetization are due to the domain wall motion (*Barkhausen jumps*) before reaching the saturation region where the magnetization rotates. This entire process is energetically dissipative and results in a magnetic hysteresis loop if the applied magnetic field is cycled. Moreover, the shape of this hysteresis loop varies widely from one kind of material to another.

Classically, in electrical engineering, the macroscopic hysteresis loop of a ferromagnetic material is defined as the magnetic flux density B versus the excitation field H

as illustrated in figure 1.11. One can obtain the $M(H)$ representation from the relation $B = \mu_0(H + M)$.

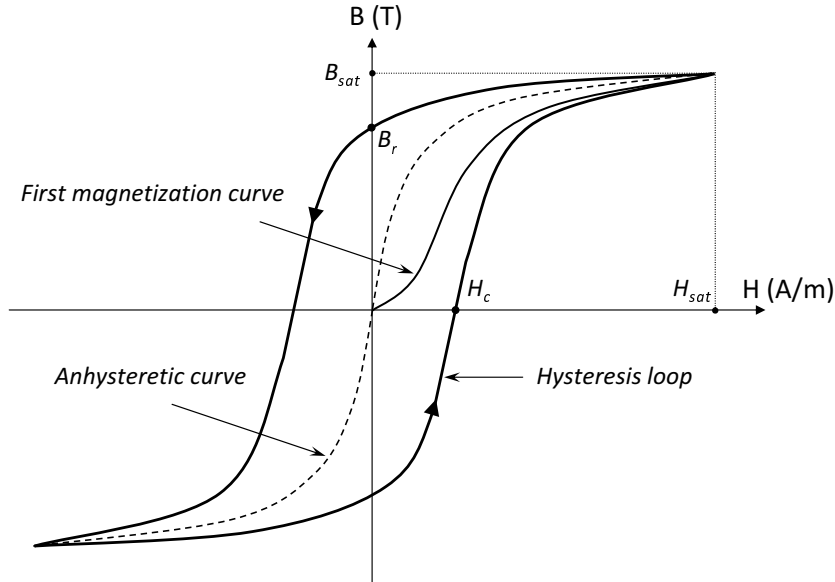


Figure 1.11: Hysteresis loop and anhysteretic curve.

In this figure, two behaviours are summarized. In the one hand, if the magnetization process is totally reversible, the behaviour is represented by the *anhysteretic curve* (in dashed line) meaning that no energy dissipation occurs during the magnetization process. This behaviour can be described by equation (1.12) obtained within the frame of the molecular field theory. On the other hand, as real magnetic materials are not perfect, the experimentally observed behaviour is depicted by the solids lines. If the material is initially demagnetized, the magnetic law $B(H)$ will follow the *first magnetization curve* with the increasing excitation field H , let say, up to the saturation point (B_{sat}, H_{sat}) . In this region, the material micro-structure tends to be single-domain and the magnetic moments are rotating towards the direction of the magnetic field. Now, if the magnetic field H decreases the magnetization curve $B(H)$ will follow a different path from the initial magnetization curve till it reaches the opposite (negative) magnetization state $(-B_{sat}, -H_{sat})$. This process will be repeated with a similar behaviour when the excitation field increases again up to the positive saturation, closing then the *magnetic hysteresis loop*. Note that, this process being dissipative, the path followed by the $B(H)$ curve during a cycle, or period, must follow the direction indicated by arrows in figure 1.11. Some particular points can be extracted from the hysteresis loop: the coercive field H_c , point at which the magnetic flux density is zero, and the remnant magnetic flux density B_r , point at which the magnetic field is zero.

Note that the term *hysteresis* comes from the Greek *husterêsis* that means *delay*. It is usually used to describe any system for which the response is delayed with regard to its excitation.

1.5 Ferromagnetic materials

Till this point, we have described the magnetization process leading to the magnetic hysteresis. Considering the ferromagnetic materials employed in the manufacturing of energy conversion devices, one can find a wide variety and disparity in the magnetic law from one material to another. The differences in the shape of the hysteresis loop are related to the composition and micro-structure of the material can be observed on some experimental parameters. These are, for the most noticeable, the saturation magnetic flux density B_{sat} , the remnant flux density B_r , the coercive field H_c and the area of the hysteresis loop W_{hyst} . In electrical engineering, a first classification of the ferromagnetic materials consists in distinguishing two groups: *soft* magnetic materials and *hard* magnetic materials. This classification can be represented in the $J_{sat} - H_c$ plane as illustrated in figure 1.12.

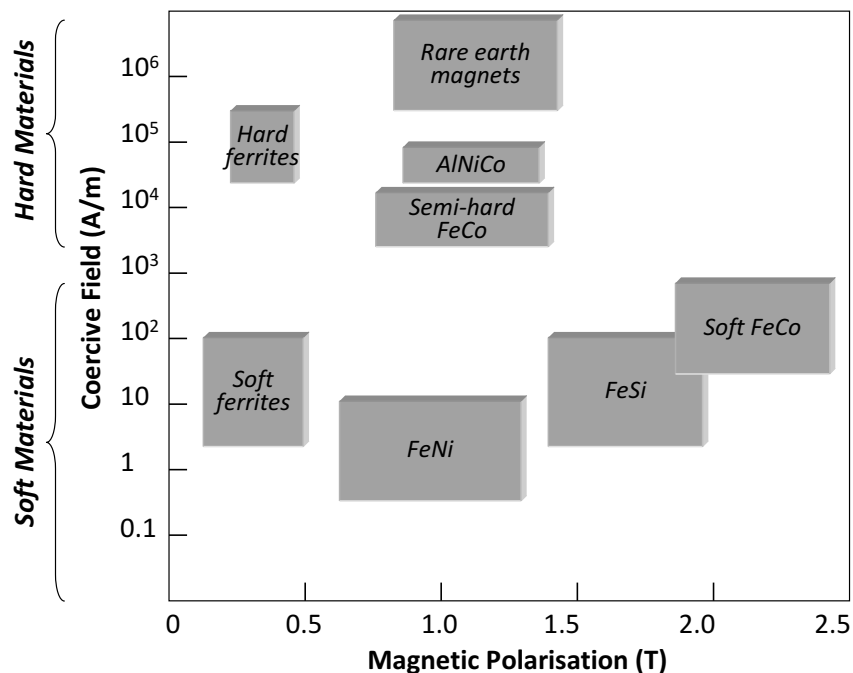


Figure 1.12: Classes of industrial magnetic materials [3].

- *Soft magnetic materials*

This group includes materials that are easy to magnetize, thanks to a high magnetic susceptibility, and easy to demagnetize, thanks to a low coercive field ($H_c \leq 10^2 A/m$). This kind of material is adapted for energy conversion devices (transformers, rotating electrical machines ...) where the magnetic flux amplification property is required. Therefore, electrical steel, made from iron alloys such as FeSi, are commonly used for these applications.

- *Hard magnetic materials*

In this group, the materials are rather difficult to magnetize and demagnetize due to their high coercivity ($H_c \geq 10^4 A/m$). These materials are used to create a permanent and constant magnetic field in a device and are often called "permanent

magnets". Their main property is to retain their magnetization against demagnetizing effects (external magnetic field, temperature ...), at least in the operating conditions of the energy conversion devices. The ability of these materials to store magnetic energy makes them adapted for the realization of excitation field sources.

Note that they also exist semi-hard magnetic materials that exhibit an intermediate coercive field.

1.5.1 Soft magnetic materials

In electrical engineering, electromagnetic energy conversion devices often involve time varying excitation fields. The magnetic materials constituting these devices are then subjected to energy losses. These are linked to Joule heating due to currents, induced by the magnetization variations, that take place over different spatial scales. Two main power loss sources can be distinguished: the hysteresis losses and the classical eddy current losses. These contributions are linked to, respectively, microscopic and macroscopic eddy currents. In fact, the domain wall motion are associated to eddy currents at the scale of the domain wall whereas the macroscopic eddy currents are linked to the bulk electrical conductivity.

1.5.1.1 General expression of the losses

Let us consider a period of an excitation field H that is applied to a ferromagnetic substance exhibiting a hysteresis behaviour. During the process, the energy stored in the material (required to magnetize and demagnetize) is larger than the energy restored by the material. The remaining excess energy is dissipated into heat form in the material. Moreover, this energy loss depends on the rate (or dynamic) of the excitation field. More specifically, the term *hysteresis losses* is associated to the energy loss in rate-independent conditions, in the so-called *quasi-static* conditions, and the term *dynamic losses* is associated to the energy loss in rate-dependent conditions when macroscopic eddy currents are involved or can not be neglected.

To realize a full sweep of the hysteresis loop, it can be shown that the required work (J/m^3) is:

$$W = \oint H.dB \quad (1.28)$$

Then, if a ferromagnetic material is subjected to a periodic excitation field with frequency f , the average volume power loss (W/m^3) is:

$$P_h = f \oint H.dB \quad (1.29)$$

In dynamic excitation conditions, the shape of the *apparent* hysteresis loop changes as additional eddy current losses are involved. As it will be further described, the term $\oint H.dB$ can be modified in order to account for these effects. In the following, a brief description of the physical origins of the losses is given for the *quasi-static* and *dynamic* operating conditions.

1.5.1.2 Hysteresis losses

Hysteresis, or quasi-static, losses are considered to be mainly linked to intrinsic physical characteristics of the material. Indeed, the hysteresis phenomenon, associated to these losses, can be described as the results of friction forces inside the material during the magnetization process. In fact, a representation of this phenomenon has been introduced by Néel and Lliboutry as an *opposition function* [4] that is linked to the imperfections in the magnetic material as mentioned in paragraph 1.4.5.1. It has also been shown that the existence of magnetic poles give rise to a demagnetizing field that opposes the applied one. Then, the delay in the magnetization M with regard to the excitation field H , in the static regime is mainly due to the existence, within the material, of a *blocking field* H_b induced by both previously described phenomena.

In figure 1.13, the evolution of the blocking field is given versus the position x of a domain wall in the material. This magnetic field opposes the motion of the domain walls that are then the location where the variations of the magnetostatic energy occur. Indeed, the domain walls collide with potential barriers that can be crossed only with the contribution of a supplementary energy provided by the external field. Then, the external field H must be greater than the local blocking field H_b at each domain wall in order to allow its motion.

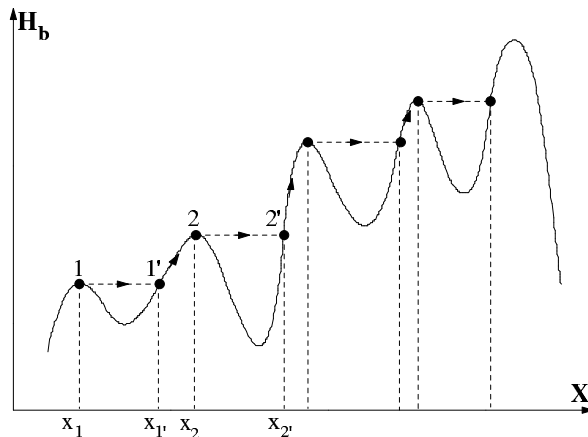


Figure 1.13: Blocking field H_b versus the position x of the domain wall with an increasing external field.

As explained in paragraph 1.4.5.1, the domain wall motion is discontinuous and irregular, with *jumps* from one pinning site to the other (*Barkhausen jumps*). These jumps also contribute to the losses that are the consequence of local microscopic eddy currents (figure 1.14) associated to local magnetic flux variations.

In figure 1.14, two domains, labelled 1 et 2, are considered with a 180° domain wall at the interface and subjected to an external magnetic field \mathbf{H} . The domain 2, with magnetization in the same direction as the external field, grows in volume by the jump of the domain wall and eddy currents appear to oppose the brutal magnetic flux variation. In the following paragraph, the model of a domain wall motion, proposed by C. Kittel [5], is presented.

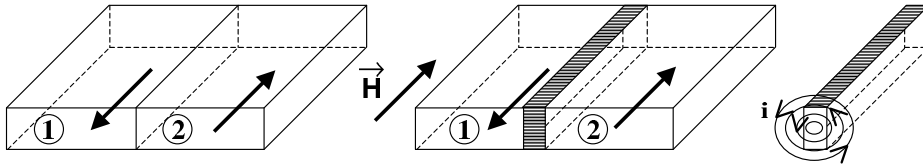


Figure 1.14: Local microscopic eddy currents resulting from the jump of a domain wall.

1.5.1.3 Domain wall dynamic

In 1950, H.J. Williams and C. Kittel [5] have considered a 180° domain wall separating two magnetic domains that constitute a closed magnetic circuit of thickness e and cut in a single FeSi crystal as illustrated in figure 1.15.

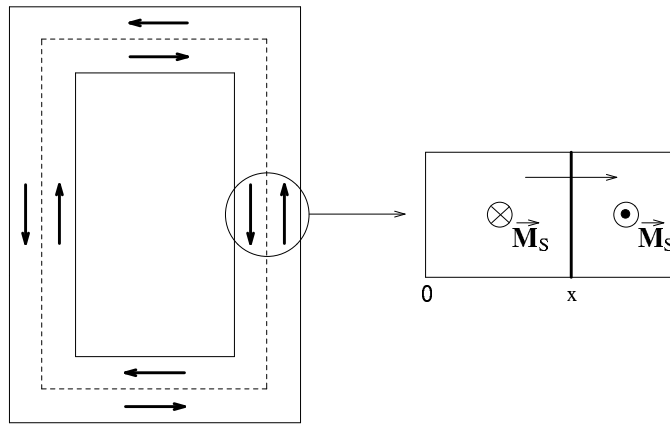


Figure 1.15: Magnetic circuit with two domains separated by a 180° wall.

They postulated that an electrically conductive ferromagnetic material, subjected to an external magnetic field, will experience a viscous friction. The origin of this friction force is linked to the eddy currents, consequence of the domain wall motion. The dynamic of the system can be written:

$$\begin{aligned} \frac{dx}{dt} &= \eta[H_{surf}(t) - H_0] \quad \text{si } H_{surf} > H_0 \\ &= \eta[H_{surf}(t) + H_0] \quad \text{si } H_{surf} < -H_0 \end{aligned} \quad (1.30)$$

where $H_{surf}(t)$ is the magnetic field on the surface of the system, H_0 is a threshold field and η is the domain wall mobility coefficient ($A^{-1} \cdot m^2 \cdot s^{-1}$). In the particular case where $0 < H_{surf} < H_0$, the domain wall remains steady. The magnetization state of the system is totally defined by the position x of the domain wall. The mobility coefficient η , that can be associated to the damping factor due to the eddy currents, is given by:

$$\eta = \frac{1}{2\mu_0 M_s \sigma G e} \quad (1.31)$$

where σ is the electrical conductivity and G is a constant such that $G = 0,1356$. The time variation of the total magnetization in the frame of width l is proportional to the time variation of the domain wall position (equation 1.30) and writes:

$$\frac{dM}{dt} = \frac{2M_s}{l} \frac{dx}{dt} \quad (1.32)$$

In the case of a Bloch wall in motion within a material composed of several Weiss domains, the involved phenomena are more complex. Nevertheless, the model of a single domain wall given by expression (1.30) can be generalized to the case of a domain wall subjected to the influence of other domain walls inside the magnetic system. The motion expression of such domain wall is then:

$$\frac{dx}{dt} = \eta[H(t) - H_b] \quad (1.33)$$

The threshold field H_0 of equation (1.30) is replaced by the blocking field H_b , introduced in the paragraph 1.5.1.2, such that the magnetic field $H(t)$ acting locally on the domain wall verifies:

$$\begin{aligned} H(t) &= H_{surf}(t) - H_i(t) \\ \text{et } H(t) &> H_b(x, t) \end{aligned} \quad (1.34)$$

The field $H_i(t)$ is due to localised eddy currents that are the consequence of the other domain walls motion constituting the magnetic system. Therefore, it can be shown that the rate of change of the surface magnetic field $H_{surf}(t)$ lead to a frictional force, similar to a viscous damping, that opposes the domain wall motion.

Nevertheless, it must be noted that in magnetic materials with a weak electrical conductivity, where no viscous braking due to the eddy currents occurs such as in soft ferrites, the mobility of the domain walls is not infinite. In fact, other frictional forces, such as the magnetic moment coupling, that were *drowned out* by the eddy current effects, become preponderant in this case.

1.5.1.4 Macroscopic eddy current losses

In the dynamic regime, in addition to the losses that are due to the quasi-static magnetization process with microscopic eddy currents, they also exist macroscopic eddy current losses (classical eddy current losses). These losses depend on the macroscopic electrical conductivity and also on the geometry of the considered material.

In fact, a variable magnetic field gives rise to a circulating current through the electrically conductive sample. For simple geometries, and with an unidirectional variable magnetic field, this circulation is within cross-sections of the core as illustrated in figure 1.16. Using materials with high electrical resistivity, such as ferrites, allows to reduce the classical losses. For materials, such as iron alloys, the classical way for reducing macroscopic eddy currents is to act on the geometry of the material as it is the case for laminated electrical steels. This will increase the apparent resistance in the cross-section of the lamination where the macroscopic eddy currents are circulating. A complementary technique consists in reducing the electrical conductivity of the materials, without significantly impacting the magnetic properties, by adding impurities such as Silicon in FeSi lamination or Nickel in FeNi laminations.

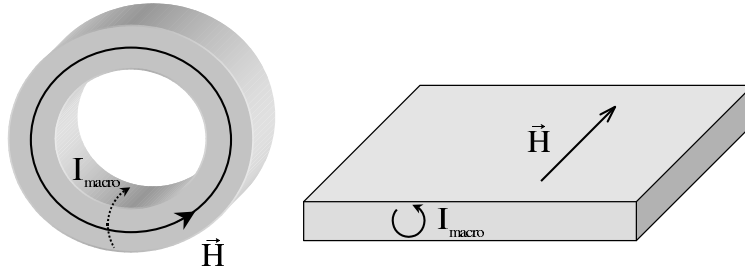


Figure 1.16: Macroscopic eddy currents in the cross-sections of simple geometries: ring core and lamination.

From an experimental point of view, in the dynamic regime, the classical losses impact the apparent hysteresis loop in a way that its coercive field increases together with a *smoothing* effect on the loop tips if the dynamic is much more higher. The significance of these effects depends on the magnetic material characteristics (physical properties and geometry). As illustration, in figure 1.17, the dynamic behaviour is emphasized with increasing frequency of the applied field.

From a global approach to the losses, and according to the loss decomposition approach proposed by Bertotti [6], the total power losses can be expressed as the sum of three contributions:

$$P_{moy} = P_{hyst} + P_{cl} + P_{exc} \quad (1.35)$$

where P_{hyst} represents the hysteresis losses, P_{cl} represents the classical eddy current losses and P_{exc} represents the contribution of *excess* losses that are associated to groups of magnetically correlated domain walls as introduced by Pry&Bean [67] and generalized by G. Bertotti *and al* in [68, 69].

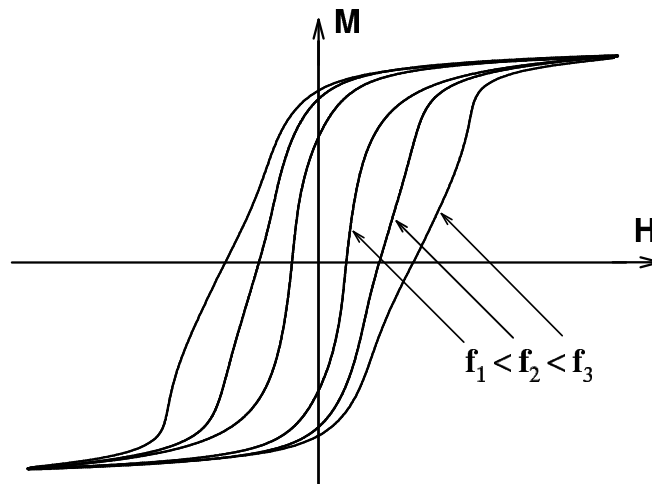


Figure 1.17: Shape modification of the apparent hysteresis loop in dynamic regime.

1.5.2 Hard magnetic materials

Historically, the use of permanent magnets in electrical engineering applications started in the 1930s with iron alloys composed of aluminium (Al), nickel (Ni) and cobalt (Co), the so-called *Alnico* magnets. Then came the *hardferrites* in the 1950s and the rare earth permanent magnets with the *SmCo* in the late 1960s till the end of the 1970s and the *NdFeB* in the 1980s [17].

As shown in figure 1.12, these permanent magnets exhibit different characteristics in terms of coercivity and remnant flux density. In addition, the maximum operating temperature is also different from one magnet type to another. Note also that the temperature effects on a magnet behaviour appear quite rapidly with regard to the usual operating temperature in electrical engineering applications, requiring then special attention when designing the device.

1.5.2.1 Physical and magnetic properties

A permanent magnet (PM) can be represented by either its $B(H)$ or $J(H)$ hysteresis loop, where $J = \mu_0 M$ stands for the magnetic polarisation. The $J(H)$ representation is the intrinsic characteristic of the PM and the corresponding intrinsic coercive field is usually written H_{cJ} . For the $B(H)$ characteristic, the coercive field is denoted H_{cB} . Moreover, for normal operating conditions, the working point of the PM lies generally within the second quadrant. Therefore, only the characteristic in this quadrant, the so-called *demagnetization curve* (see figure 1.18), is represented.

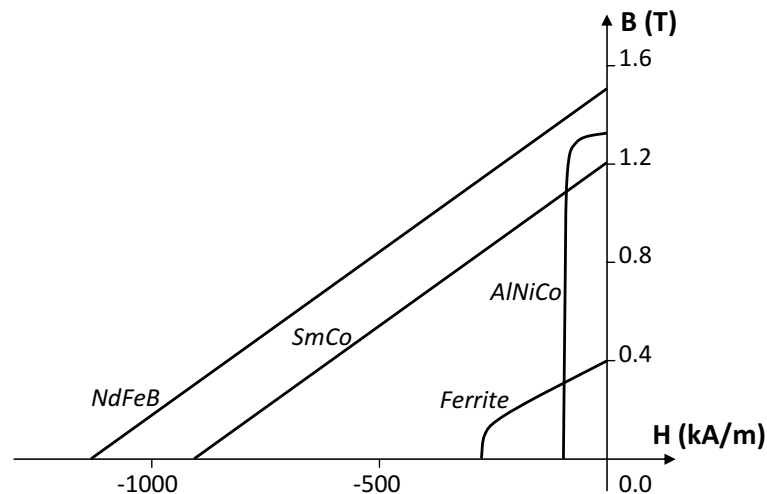


Figure 1.18: Demagnetization curves for different types of permanent magnets.

The demagnetization curve defines all the macroscopic characteristics of the PM:

- the remnant magnetic flux density B_r , that is linked to the potential *strength* of the PM,
- the intrinsic coercive field H_{cJ} that reflects the ability of the magnet to remain stable in a demagnetization field,

- the product $(BH)_{max}$ that defines the maximum potential energy density being available in the PM.

These three parameters, together with the maximum operating temperature, usually define the choice of a PM for a given application. The table 1.4 gives typical value intervals for these parameters.

Table 1.4: Typical characteristics of common permanent magnets.

Type of PM	$(BH)_{max}$ [kJ/m ³]	H_{cJ} [kA/m]	B_r [T]	T_{max} [°C]
<i>AlNiCo</i>	35-70	50-170	0.8-1.3	400- 550
Hard <i>Ferrites</i>	10-40	150-400	0.2-0.45	350
sintered <i>SmCo₅</i>	150-180	800-1500	0.8-1.0	250
sintered <i>Sm₂Co₁₇</i>	150-250	700-2000	0.9-1.1	450-550
sintered <i>NdFeB</i>	200-380	800-2500	0.9-1.4	80-220

In addition to these characteristics, other criteria can be determining in the choice of a PM for a specific application. These parameters are linked to the mechanical properties, electrical resistivity, thermal stability and oxidation resistance.

1.5.2.2 Stability of the permanent magnets

Besides their high magnetic energy density, one of the main reason for using PMs in numerous electrical devices is their ability to maintain a constant magnetic flux over a long period compared to the life cycle of the device. In modern applications, and due to economic as well as technical reasons, PMs are subjected to additional constraints that electrical machine designers must take into account. In fact, depending on the operating conditions, a PM can suffer from partial or total magnetization loss. This magnetization loss can be classified in three types:

Reversible loss

This kind of magnetization loss appears for a moderate increase of the temperature in the PM. Once this increase of temperature disappears, the PM recovers its initial magnetization state.

Irreversible loss

In this case, even if the origin of the magnetization loss disappears, the initial magnetization is not recovered. Some of these causes are:

- Significant increase of the ambient temperature,
- Local overheating of the permanent magnet due to eddy currents,
- High demagnetizing field due to the reluctance and/or external excitation field.

However, in this case, the magnetization loss can be fully recovered by a re-magnetizing process of the material. Note that it is rather difficult to achieve such operation for permanent magnets already mounted in an electrical machine.

Permanent loss

Permanent loss of magnetization results from processes over time. These are associated to a permanent change in the internal structure or metallurgical property. This is, for example, the case when the following effects occur: oxidation, radiation, annealing, exceed of the Curie temperature, mechanical shock ... Once a PM has suffered from these effects, the initial magnetization can not be restored.

In the following, the temperature effect is briefly described.

1.5.2.3 Temperature effect

The performances of permanent magnets are closely related to their hysteresis loop, particularly to their demagnetization curve. The variation of the temperature has a different impact on this curve depending on the kind of PMs. When the temperature increases the knee of the curve shifts, for most PMs, towards the origin of the $B(H)$ plane (see figure 1.19). It manifests as the decrease of the coercive field and remnant magnetic flux density. However, for hard ferrites (based on *baryum* or *strontium*, the most used in electrical engineering), the temperature increase has an opposite effect on the knee of the curve that shifts away from the origin of the $B(H)$ plane (see figure 1.20). In this case, the coercive field increases whereas the remnant magnetic flux density decreases [7].

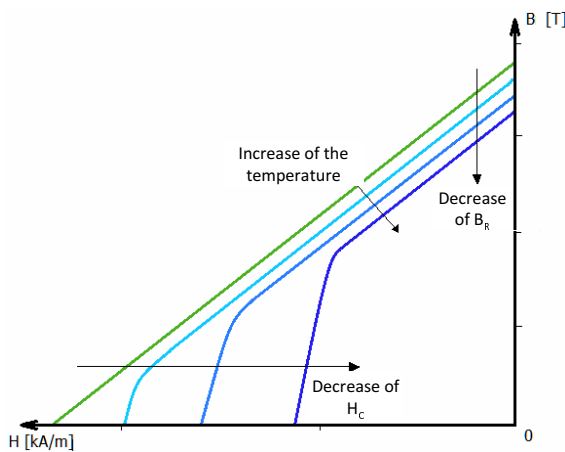


Figure 1.19: Effect of the temperature on the demagnetization curve of rare earth PMs.

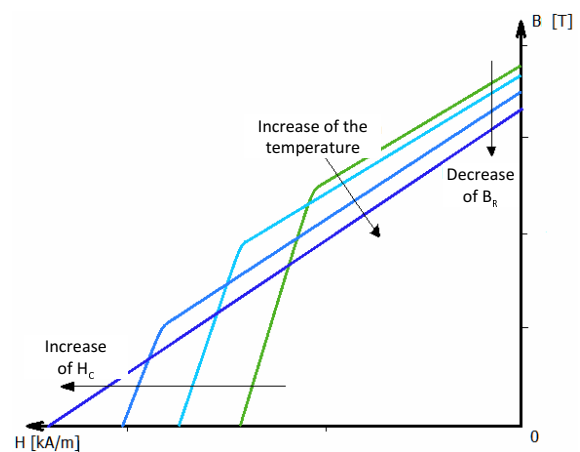


Figure 1.20: Effect of the temperature on the demagnetization curve of ferrite PMs.

Temperature coefficients for common PMs are summarized in table 1.5. It shows that, despite their good magnetic performances, $NdFeB$ magnets present the lowest maximum operating temperature as well as significant temperature coefficients for B_r and H_{cJ} . For $SmCo$ magnets, the magnetic performances are also interesting together with a good temperature resistance. In the case of $AlNiCo$ and *Ferrites* magnets, the temperature

resistance is the most interesting but their magnetic performances are rather limited compared to those of rare earth permanent magnets. It is especially the case for *AlNiCo* magnets that present high risks of demagnetization due to their low intrinsic coercive field H_{cJ} .

Table 1.5: Temperature coefficients for common permanent magnets.

Type of PM	α_{B_r} [%/°K]	$\alpha_{H_{cJ}}$ [%/°K]	T_{max} [°C]	T_{Curie} [°C]
<i>AlNiCo</i>	-0.03 to -0.02	-0.02 to 0.03	400-550	800-850
Hard <i>Ferrites</i>	-0.20 to -0.18	0.30 to 0.50	350	450
<i>SmCo</i>	-0.05 to -0.03	-0.40 to -0.15	400	700-800
<i>NdFeB</i>	-0.13 to -0.10	-0.65 to -0.50	80-220	310-370

α_{B_r} - Reversible temp. coef. of remnant magnetic flux density B_r

$\alpha_{H_{cJ}}$ - Reversible temp. coef. of intrinsic coercive field H_{cJ}

Let us consider rare earth PMs with negative reversible temperature coefficients. The influence of the temperature is illustrated in figure 1.21 in terms of the working point on the demagnetization curve. Initially, at the temperature T_1 , the working point A is determined by the intersection of the load line L and the demagnetization curve N°1. If the temperature increases up to T_2 , the remnant magnetic flux density B_r and the coercive field H_c decrease so that the new demagnetization curve N°2 is obtained. For the same load line L , the working point is now B with lower magnetic performances than initially at temperature T_1 .

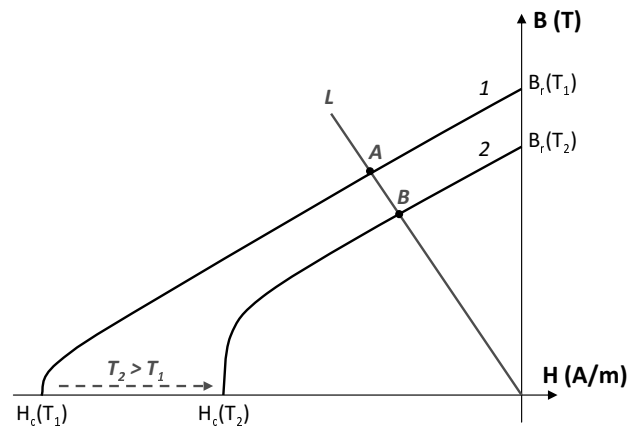


Figure 1.21: Effect of the temperature on the working point of a permanent magnet.

1.6 Conclusion

This chapter was dedicated to the ferromagnetic material properties of interest for the electrical engineer. The main idea to retain for the following chapters is that the ferro-

magnetic behaviour is linked to intrinsic parameters (composition, micro-structure ...) as well as to extrinsic parameters (frequency, temperature ...), these latter being usually associated to the operating conditions of the electrical device. The magnetic hysteresis and iron losses are characteristics that play a key role in the energy conversion process. In that context, and especially for electrical devices modelling, the experimental characterization of the material behaviour is an essential step before the development of material models. Some experimental characterization techniques that have been used and/or developed are presented in the next chapter.

2

Material characterization

The experimental characterization of magnetic materials properties is generally motivated by two main objectives: understanding of the magnetization processes and identification of material models. In electrical engineering, both of these aspects are linked as the main goal is to develop accurate magnetic material models for the design and study of electrical devices. The magnetic properties of a material can be distinguished in terms of *intrinsic* (micro-structure, magneto-crystalline anisotropy, ...) and *extrinsic* characteristics (magnetic shape anisotropy caused by the demagnetizing field, mechanical strain that can be introduced by the manufacturing process, etc). In electrical engineering, even if the intrinsic characteristics are of interest, the development of magnetic material models is mainly focused on extrinsic characteristics considerations and their impact on the intrinsic characteristics.

In the following, the basic principles for calculating the magnetic field H and magnetic flux density B are described in the case of a closed magnetic circuit. The standard techniques, used to characterize the global characteristics of soft magnetic materials, are also briefly described. For some applications or particular material problematic studies, the standard techniques can be insufficient or not adapted. Therefore, specific characterization techniques must be developed for extracting the required material information. Some specific experimental approaches developed within the frame of these activities are also presented.

2.1 Standard techniques

2.1.1 Principle

The characteristic of interest for energy conversion devices being the magnetic behaviour $B(H)$, it is mandatory to evaluate H and B as much accurately as possible. One way to achieve this goal is to use a closed magnetic circuit carrying a primary (excitation) winding, with N_1 turns, and a secondary winding, with N_2 turns. The primary winding being fed by a current I_1 , the magnetic circuit is magnetized and the secondary winding allows to measure the induced electromotive force V_2 . In addition, the sample cross-section S (assumed to be constant and perpendicular to the field lines), and mean magnetic path

length l_m are also defined (figure 2.1).

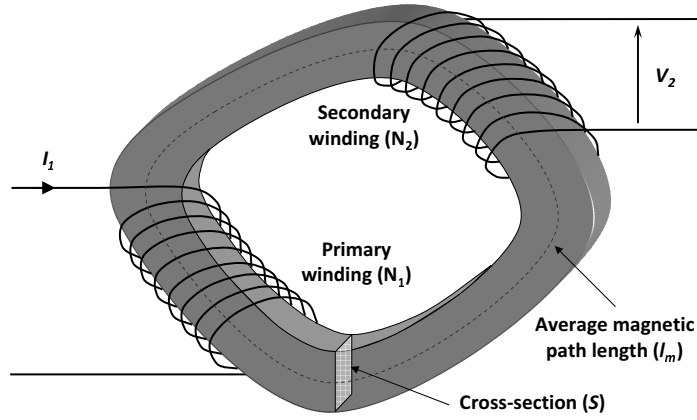


Figure 2.1: Closed magnetic circuit.

Two main hypotheses are made before considering the calculation of H and B . The first one consists in assuming the homogeneity of the magnetic fields in the cross section of the sample. The second hypothesis considers that the relative magnetic permeability μ_r of the sample is sufficiently high for channelling the magnetic flux inside the sample.

On the one hand, the magnetic field H can be calculated from the Ampere's law :

$$\oint_C \mathbf{H} \cdot d\mathbf{l} = \iint_{S_c} \mathbf{J} \cdot d\mathbf{S}_c \quad (2.1)$$

where \mathbf{J} is the current density through the surface S_c enclosed by the contour C . Considering the previously mentioned hypotheses, this contour is chosen coincident with l_m the mean path such that the magnetic field \mathbf{H} is collinear with the infinitesimal element of the contour $d\mathbf{l}$. Then, the magnetic field can be deduced from the primary current $I_1(t)$:

$$H(t) = \frac{N_1 \cdot I_1(t)}{l_m} \quad (2.2)$$

On the other hand, the magnetic flux density B can be obtained from the Faraday's law :

$$V_2(t) = N_2 \frac{d\phi(t)}{dt} \quad (2.3)$$

where ϕ is the magnetic flux assumed to be "seen" by the secondary winding without leakage flux. Then, since $B(t)$ is also assumed to be homogeneous in the cross-section, the definition of the magnetic flux $\phi(t) = N_2 \cdot S \cdot B(t)$ allows to calculate the magnetic flux density from the secondary voltage $V_2(t)$:

$$B(t) = \frac{1}{N_2 \cdot S} \int V_2(t) \cdot dt \quad (2.4)$$

2.1.2 Ring core technique

The ring core measurement technique is defined by the standard IEC 60404-6. The samples are often obtained from the stacking of several rings cut in the lamination of interest. As explained in the previous section, primary and secondary coils are wound on the sample such that all the perimeter is regularly covered. Several layers of windings can be made depending on the required magnetic field strength. In all cases, it is recommended to place the secondary winding as close as possible to the magnetic core.

The ring core measurement technique provides ideal conditions for the magnetic characterization as the average magnetic length l_m , as well as the cross-section S , can be easily controlled. Nevertheless, for this kind of sample shape, the magnetic field is radially dependent and the consideration of an average magnetic length must be regarded carefully. In order to minimize this source of error, it is also recommended that the ring core dimensions verify the condition $D_{ext}/D_{int} \simeq 1.15$.

Moreover, this measurement technique is rather limited to the characterization of isotropic magnetic properties. In fact, with a ring-shaped magnetic circuit, the magnetic flux flows through all the directions of the lamination from which the ring has been cut. Note that in the case of common non-oriented grain electrical steels, an anisotropy still exists due to the rolling process (usually between 5% and 10%) and, with the ring core technique, the apparent "average" magnetic behaviour will be measured. In the case of anisotropic magnetic properties, such as for grain oriented electrical steels, this measurement technique is clearly not adapted.

2.1.3 Epstein frame

The Epstein frame is one of most used device for the characterization of electrical steels, particularly in the industry (material producers and electrical device manufacturers). In fact, this measurement technique, as defined in the standard IEC 60404-2, must respect specific requirements and presents high reproducibility in the measurements. The frame is constituted by the association of 4 winding sets, each set consisting in a primary and secondary windings (see figure 2.2). The material samples are strips that are cut according to the standard specifications: between 280 and 320mm length and $30mm \pm 0.2mm$ width. The strips are stacked alternatively in the frame to "close" the magnetic path. In addition, it is recommended to place a weight corresponding to a 1N force on each corner in order to improve the "magnetic contact" and avoid magnetic vibrations. The magnetic field H is calculated by considering the average magnetic path length equal to 0.94m as defined by the National Metrology Institutes.

For non-oriented grain laminations, half of the strips is cut along the rolling direction whereas the other half is cut along the transverse direction. For grain oriented laminations, the samples are cut along the rolling direction in order to avoid the demagnetizing field at the samples edges. Note that, for this latter case, to characterize an arbitrary direction of a grain oriented material with the Epstein frame, a solution consists in cross-stacking the strips from one layer to another in order to obtain the lateral magnetic flux closure. Finally, the number of strips depends on the lamination thickness but is a multiple of four.

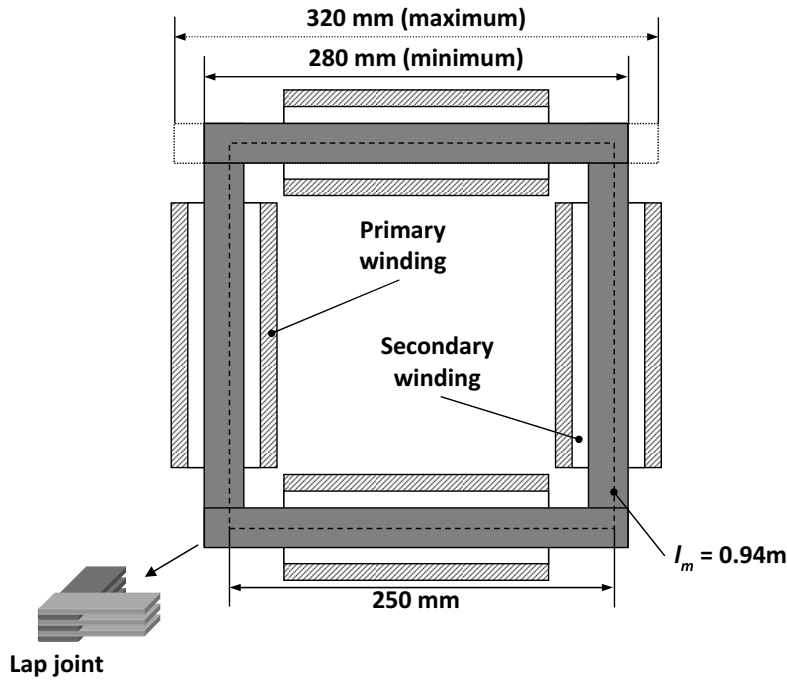


Figure 2.2: Epstein frame.

2.1.4 Single Sheet Tester

For the Single Sheet Tester (SST), the standard IEC 60404-3 describes the measurement method. In practice, the device is made of a double U-shaped magnetic circuit (yokes) that allows to magnetize the sample clamped between the yokes (see figure 2.3). The primary (excitation) and secondary (flux measure) windings are placed over the sample with the secondary being the interior winding (close to the sample). In the standard, the sample is defined with the following dimensions: 500mm minimum length and 500mm maximum width. One must note that in practice different dimensions can be used depending on the available samples. For the SST test, ideally only one sample is needed and no specific preparation is required, making this test very used. Nevertheless, the inherent air-gap that subsists between the yokes and the sample is a source of error that must be minimized as much as possible (the surfaces of the yokes in contact with the sample must be as plane as possible) and their positioning repeatable. In addition, the magneto-motive force in the yokes can be neglected if the material of the yoke is chosen accordingly (high magnetic permeability) and its section is sufficiently high with regard to the sample section. Also, the SST can be calibrated by adapting the effective magnetic path length in the sample by comparison with other characterization techniques.

2.1.5 Discussion and limits

One fundamental assumption of the standard techniques is the homogeneous magnetization of the sample. The error made with this assumption is minimized by the choice of adequate dimensions of the sample under test. In the case of the Epstein frame, the

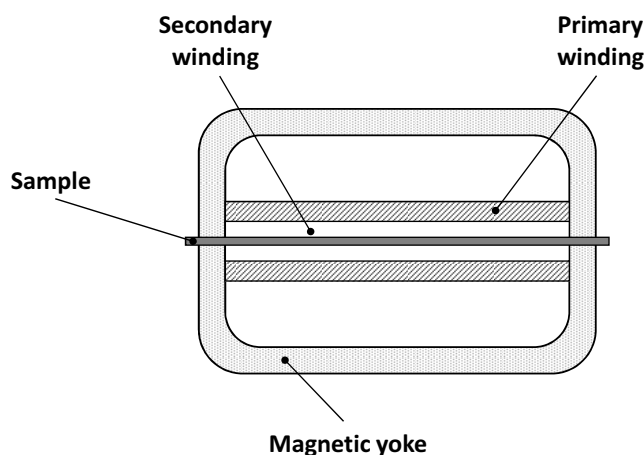


Figure 2.3: Single Sheet Tester (SST) frame.

lap joint region is highly non homogeneous and lead to a systematic error. In addition, preparation of Epstein samples requires stress relief annealing and a significant number of samples. The SST method was proposed to overcome these drawbacks (less sample preparation and fast to perform) but its result acceptance remains below the Epstein frame. Some studies have been conducted in order to evaluate the relationship between the Epstein frame and the SST measurements [8,9]. These works emphasize that a systematic error exists for both characterization techniques and insist on the statistical approach for comparison purposes. In addition, there are still issues that must be clarified with the error sources linked to the Epstein frame lap joints and the yoke of the SST.

In [10], an international comparison is performed for SST and Epstein measurements on grain-oriented electrical steels. The aim of this study was to test the degree of reproducibility of the SST method with regard to the Epstein method. Results showed that the good reproducibility, and its simple practical implementation, make the SST method a good candidate for becoming a reference method for the specifications of grain-oriented alloys.

Finally, even if the Epstein frame is usually considered as a reference, some works [11] have been interested in the relevancy of the magnetic path length such as defined by the standard. In fact, some studies showed that this mean path length should not be considered constant, especially when different grades of materials, and non-standard excitation conditions (flux densities and frequency), are involved. Significant errors can be introduced in the measured losses and magnetic permeability [12–14].

Nevertheless, in a more general way, these standard techniques are mostly useful for quality monitoring in the industry and, in a less extent, for the development of material models for engineering purposes. When specific specific tests and studies are required, such as the impact of the manufacturing process, one must, at least, adapt these characterization methods or develop a dedicated characterization device.

2.2 Specific approaches

The development of more and more efficient devices requires to study with more accuracy the magnetic material properties and their evolution under external constraints. In that context, the standard methods can be rapidly limiting and specific approaches must be developed. For instance, the effect of the cutting on laminations can be very significant on small electrical devices with typical dimensions in the lamination plane of few millimetres. Besides, even for devices with higher dimensions, this effect affects the air-gap region behaviour in rotating electrical machines.

There exist also different contexts of magnetic material characterization that require specific approaches. For example, the on-line quality monitoring of complex shaped massive magnetic pieces can not be performed by classical techniques. A non-destructive measurement approach is then needed.

Some specific devices developed for the characterization of magnetic materials, related to these problematics, are presented in the following. In addition, a technique for characterizing low permeability materials and a setup for ferrites ring core characterization are presented.

2.2.1 Cutting effect on stator teeth of slinky stators

Claw pole generators are constituted of a laminated stator and a massive rotor. To reduce the cost of manufacturing and waste, the stator is made from a single punched lamination strip that is rolled up in a spiral (slinky) and welded. Additional manufacturing steps are also involved, such as the pressing and machining, that globally impact the magnetic properties of the lamination. In the particular case of the punching process, the stator teeth are a critical region for the study of the manufacturing process impact. In fact, regarding the width of the teeth, typically a few millimetres, the magnetic behaviour in the edges of the teeth is expected to be significantly modified. This is a key point for the edge near the air-gap where the deterioration of the magnetic permeability can lead to a decrease of the magnetic flux flowing from the stator to the rotor.

In the literature, experimental approaches for studying the cutting effect on magnetic properties have been performed by using the standard techniques. In [15] the authors studied the impact of the number of cutting edges on the magnetic behaviour and iron losses of laminations strips (width = 80mm). The samples, which initial geometry was obtained from a cutting by electrical discharge machining, are characterized with a single sheet tester. The procedure consists in cutting the samples by guillotine for different number of cutting edges (0 to 42). The measurements showed a significant decrease in the maximum permeability (divided by 3 in this case) and also an increase (up to 70% at low frequency) in the iron losses for a wide range of excitation frequencies. In [16], a local investigation of the punching effect on electrical steels has been performed. The micro-indentation technique was used to extract the micro-hardness which is converted into an equivalent plastic strain due to uni-axial tensile stress. Then, from measurements on a single sheet tester bench equipped with a tensile stress device, a magnetic model, including the plastic strain parameter, is proposed to study the magnetic behaviour of the cutting edges of electrical machine stator teeth.

In the present work, the study of the punching impact on the slinky stator teeth has been realized on teeth samples issued from the fabrication chain. The considered teeth samples are obtained just after the punching step without the rolling process of the lamination strip (that obviously also impacts the teeth). In our case, assessment of the magnetic properties degradation is performed by direct measurements on the teeth. The principle of the measurement presented in section 2.1.1 is applied to the teeth as illustrated in figure 2.4.

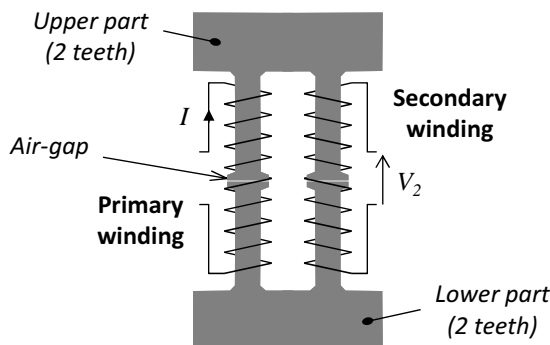


Figure 2.4: Schematic of the teeth magnetic characterization.

Two difficulties arise from such topology of the magnetic core. The first one is related to the geometrical parameters (cross-section and magnetic path length) that are not constant along the path of the magnetic flux. Therefore, to avoid any additional error in estimating these parameters, the physical quantities reflecting the magnetic behaviour of the material, that is to say the Ampère-turns (AT) NI in the primary winding and the magnetic flux Φ in the secondary winding, are used. The second aspect is the existence of a parasitic air-gap at the joint between the upper and lower teeth. To estimate its influence, two sets of additional samples are prepared from the same lamination grade: the first set consists in a single core (without air-gap) and the second one is constituted of the upper and lower parts with the parasitic air-gap (see figure 2.5). In order to neglect the effect of the cutting process, both sets are cut using wire electrical discharge machining (EDM).

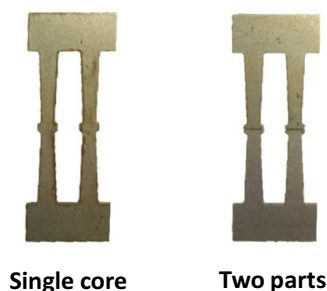


Figure 2.5: Test samples for the air-gap sensitivity.

In figure 2.6, the measured hysteresis loops at $50Hz$ are illustrated for 3 different levels of the magnetic flux and for both configurations of the EDM samples. As expected, the effect of the parasitic air-gap is clearly visible for the magnetic core made of two parts for

which the apparent magnetic permeability is lower. In figure 2.7, the punched samples are compared, for the same level of the magnetic flux density, with the EDM samples. This figure emphasizes two aspects for the punched samples: the significant degradation of the apparent magnetic permeability and the increase of the hysteresis loop area, that is to say the iron losses. As the difference observed between the EDM samples (effect of the parasitic air-gap) is negligible in comparison with the difference between the EDM and punched samples, this result shows clearly the degradation of the magnetic properties due to the punching process.

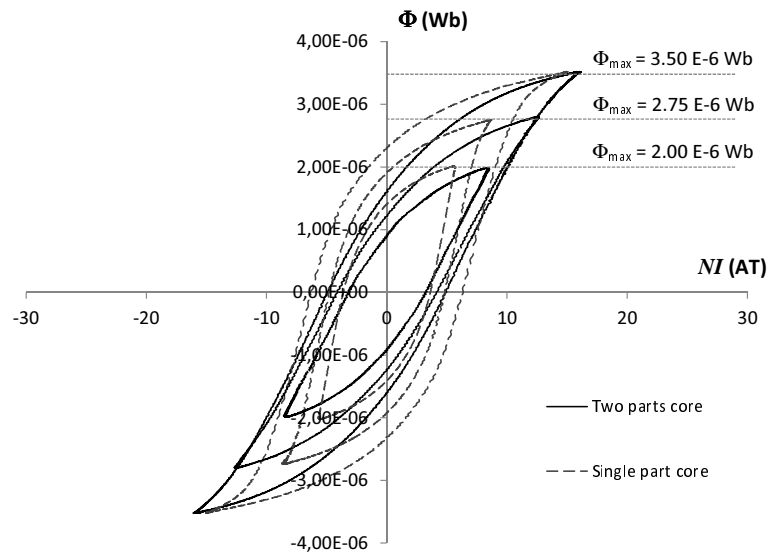


Figure 2.6: Comparison of the EDM samples "Single core" and "Two parts core": measured hysteresis loops at 50Hz.

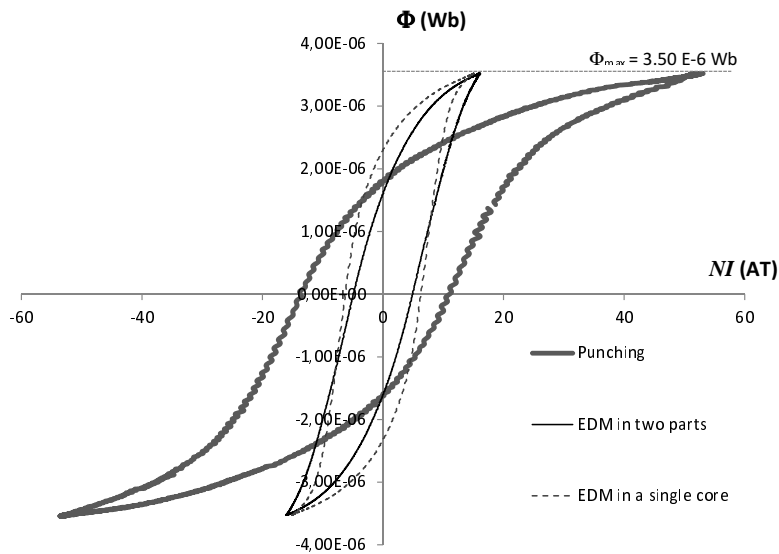


Figure 2.7: Comparison of the punching and EDM cutting processes: measured hysteresis loops at 50Hz.

This aspect is emphasized in the summarizing graph in figure 2.8 where the area of the hysteresis loop is reported for all samples and up to 600Hz . A quite constant gap is observed for the whole frequency range between the EDM samples cut in a single core and the EDM samples cut in two parts. The most interesting result is that this gap remains lower than the one existing between, on the one hand, both EDM sample types and, on the other hand, the punched samples. Moreover, the slope of the surface area evolution remains quite similar for all samples meaning that the eddy current losses are similar for all samples as well. Finally, the observed gap between the EDM samples and the punched samples can be directly associated to the degradation of the quasi-static hysteresis behaviour that is obtained when the frequency tends to zero.

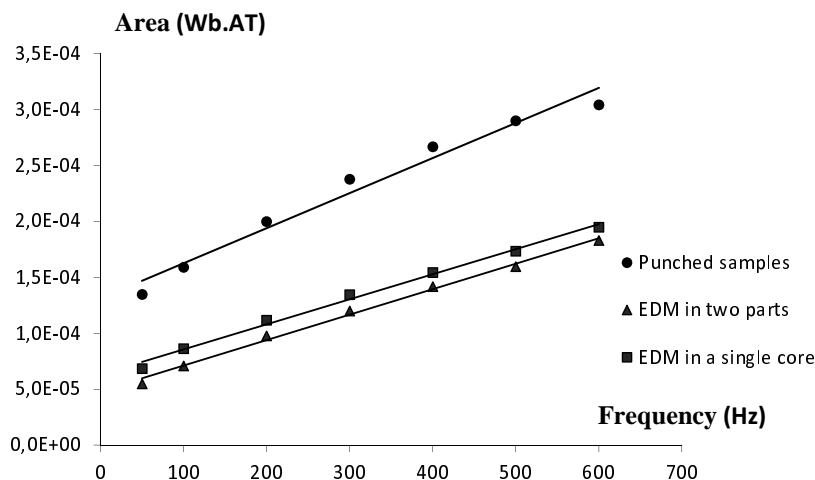


Figure 2.8: Frequency evolution of the hysteresis loop area for the punching and EDM samples ($\Phi_{max} = 3.5 \times 10^{-6}\text{Wb}$).

2.2.2 Electrical conductivity in non-trivial geometries⁶

2.2.2.1 Proposed approach

In the same way as the punching effect on laminations, the manufacturing process of massive magnetic parts influences the properties of the materials. This is the case of forged rotors in claw pole alternators for which it is preferable to perform a characterization on the manufactured part rather than on the raw material. A first approach consists in extracting adequate samples for standard characterizations but it remains destructive for the magnetic part. Then, when non-destructive testing is required, a specific characterization approach must be developed.

In the case of the claw pole rotor, its complex geometry is not adapted for the classical conductivity measurement techniques, such as the four-points method [17] usually applied on samples with standard shapes like a bar or a cylinder. A solution, presented hereafter, consists in combining both the experiment and the numerical calculation to obtain a quantitative estimation of the electrical conductivity.

⁶The presented results are part of the PhD Thesis of Laure Arbenz.

The experimental test consists in measuring the electric potential drop U between two points when a DC-current I is injected in the material. Obviously, the electric response of a material, as the geometry is not regular (bar, cylinder ...), depends on the electrical conductivity σ and also on the location of the measuring points. Then, to link the electrical response to the intrinsic material characteristics, the experimental device is modelled in 3D-FE. From this modelling, simulations, for different locations of the measuring sensor, allow then to extract the link between the electrical conductivity and the sensor response. Moreover, considering that the electrical conductivity is constant in the vicinity of the measuring points, the response U is linear with $1/\sigma$ and then only one calculation point is necessary for each sensor location \mathbf{x} to obtain the law $\sigma = f(U, \mathbf{x})$.

2.2.2.2 Numerical study of the sensor

First, to model the measurement process, the geometrical aspects of the sensor were studied by 3D-FE analysis. The aim is to adapt the sensor to the studied geometry by optimizing the distance between the measuring points and also to investigate the main sources of error, especially the points alignment and sensor positioning accuracy.

The simulated experiment is the measure of the electrical resistance along one claw when injecting a 10A DC-current through the external points of the sensor (see figure 2.9). The simulation results are reported in figure 2.9 where $s(mm)$ is the distance between the external and internal points and $a(mm)$ is the distance between the internal points. The evolution of the resistance R , calculated between the internal points, presents a fast decreasing tendency for low values of s and a quite 'stable' behaviour for higher values of s . In that case, the measured value is less sensitive to a variation of a and s . For the purpose of the experiment, one constraint is to perform a measure as much local as possible, leading then to small values of s and a . Nevertheless, limitations exist regarding the level of the measured signal that will drop when a and s decrease and also the practical realization aspects that require the contact diameter to be sufficiently small regarding the distance between the contact points [17]. In our case, the geometrical choice for the sensor is $a = s = 6mm$.

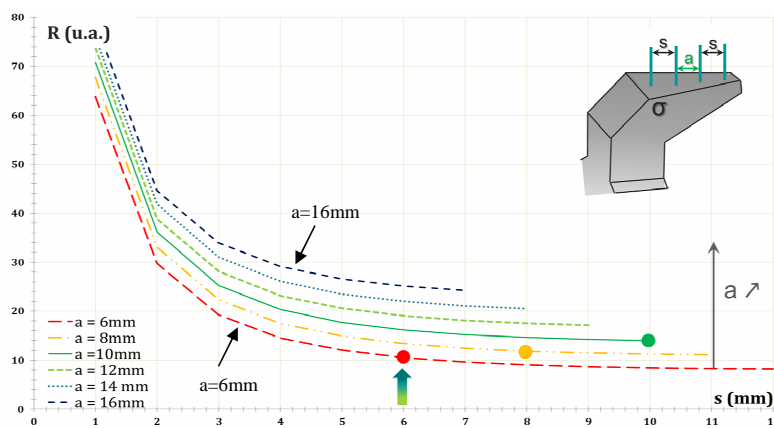


Figure 2.9: Simulated resistance between the internal points depending on geometrical parameters of the sensor.

In a second step, the influence of the misalignment of the four points is studied. From the nominal parameters $a = s = 6\text{mm}$, each point is independently moved in the direction transverse to the points alignment. For each point, two positions $\pm 0.5\text{mm}$ are considered on either side of the point alignment. The 16 combinations have been simulated and the most significant error, with regard to the nominal sensor, is about 1%. This value is very satisfactory regarding the experimental uncertainties.

Even for well aligned sensor points, it is necessary to verify the impact of the sensor positioning on the claw. Therefore, the longitudinal and transverse positioning of the sensor on the claw is analysed through FE simulations. In figure 2.10, the simulation results show that, depending on the longitudinal position on the claw, the variation of the resistance can reach up to 40% when positioning the sensor from the bottom (2mm) to the tip of the claw (14mm). A similar study is performed for the transverse positioning of the sensor as illustrated in figure 2.11. In that case, the variation of the resistance is less significant but reaches 5% between the center and the lateral position of the sensor as shown in figure 2.11.

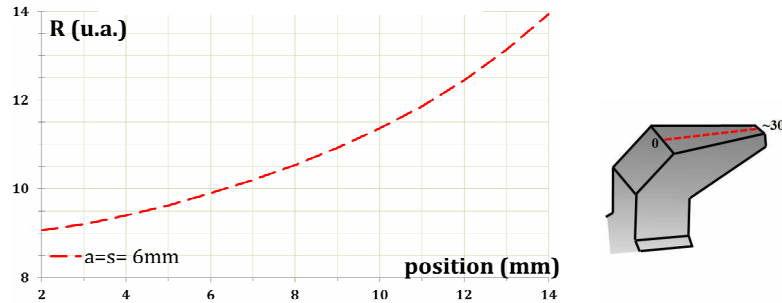


Figure 2.10: Resistance versus the longitudinal position of the sensor.

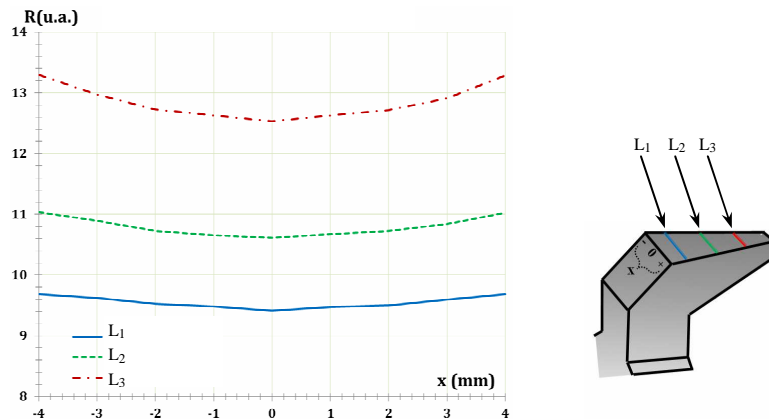


Figure 2.11: Resistance versus the transverse position of the sensor.

These results emphasize that the experimental positioning of the sensor must be carried out with accuracy in order to have a quantitative estimation of the electrical conductivity. Once the experimental device has been developed, a reference test was performed in order to validate the proposed approach combining the experiment and the FE calculations.

2.2.2.3 Application of the proposed approach

To validate the proposed approach, a reference claw pole rotor, made from machining in a homogeneous steel billet, is considered. In fact, for the validation purpose, it is necessary to avoid studying a forged piece in which a spatial variability of the electrical conductivity may exist. The geometry of the claw pole is given in figure 2.12. The experimental protocol consists in measuring, for a given position of the sensor, the resistance on 3 claws as indicated in the figure. Then, the corresponding electrical conductivity is deduced from the FE calculation as explained in section 2.2.2.1.

In a second step, 3 samples with regular and well known geometry (cylinders) are extracted from the claws. From these samples, the electrical conductivity σ is deduced by measuring the resistance R with the same sensor. The classical analytical expression is then used: $\sigma = \frac{l}{RS}$, where l is the length between the internal points and S the section of the sample.

Note that, for all the measurements, the samples were put in a temperature chamber in order to control the temperature around 45°C . The resistance is measured once the thermal steady state is reached.

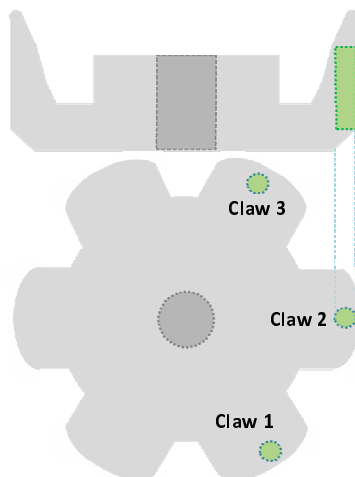


Figure 2.12: Studied claw pole rotor and extracted samples.

The obtained results are summarized in table 2.1. It is observed that the values of the electrical conductivity, obtained from the proposed method and the classical approach, are in good agreement. This result allow then to validate the proposed non-destructive approach that can be applied to forged claw poles in the context of the study of the manufacturing process impact.

2.2.3 Identification procedure for low permeability magnetic materials

In some cases, it is not necessary to develop a complex non-linear model to represent the behaviour of a magnetic material. This is the case for permanent magnets (PMs), such

Table 2.1: Measured resistance and deduced electrical conductivity for the reference material.

		Resistance (in a.u.)	Conductivity (in a.u.)
Proposed approach	Claw 1	76	1.20
	Claw 2	78	1.16
	Claw 3	76	1.19
Classical approach	Sample 1	196	1.20
	Sample 2	197	1.20
	Sample 3	197	1.20

as rare earth and ferrites, that are often used in electrical machines, providing the demagnetizing field and temperature are such that the operating point remains in the linear part of the demagnetization curve (see section 3.2.4). The point is then to determine, in this linear part, the magnetic permeability of the PM and also its electrical conductivity which play an important role when operating at high frequency. In the following, a simple experimental technique, combined with FE calculation, is presented for the determination of these both quantities.

2.2.3.1 Principle of the method

The proposed procedure is based on the consideration that the measurement of the impedance of an electrical load versus the frequency can be done accurately. Then, from the variation of the impedance induced by the introduction of a material sample inside a coil, it is possible to extract the material properties. According to this measured variation, and using a field calculation code, an equivalent conductivity of the material sample is deduced from the best fitting results for the frequency behaviour of the considered material.

Experimental procedure

The system used for the frequency identification is composed of a coil surrounding a PVC tube. Inside this one, the material sample is placed (see figure 2.13).

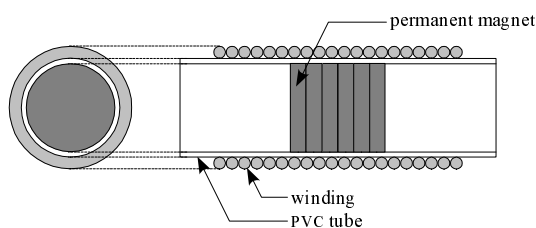


Figure 2.13: Geometry of the studied system.

The experimental set up is composed of a coil connected to an impedance analyser (HP 4294A) that measures the parameters of the equivalent electric circuit, which is

considered to be a resistance in series with an inductance. A two steps measurement has been achieved, one with only the coil and the other with the material sample inside the coil. For the coil alone, R_{exp}^0 and L_{exp}^0 are defined as the equivalent resistance and inductance values. These parameters are denoted R_{exp}^m and L_{exp}^m when the material sample is placed inside the coil. Measurements are achieved in a given frequency range, depending on the considered material. Then, the influence of the material is accounted by considering the quantities ΔR_{exp} and ΔL_{exp} such as :

$$\begin{aligned}\Delta R_{exp} &= R_{exp}^m - R_{exp}^0 \\ \Delta L_{exp} &= L_{exp}^m - L_{exp}^0\end{aligned}\tag{2.5}$$

Finite element procedure

The numerical model is a 2D-FE axisymmetric problem. The main assumption is that the material subjected to an alternating magnetic field has the same behaviour as an homogeneous media with constant magnetic permeability μ and electrical conductivity σ . The sample is then modelled by a unique homogeneous medium where the eddy currents are oriented in a direction perpendicular to the plane (r, z) in figure 2.14. In addition, the symmetry of the system allow to model only half of the system (see figure 2.14).

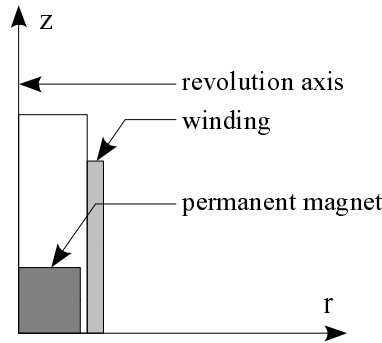


Figure 2.14: Modelled device with the sample inside the coil.

Besides, as the material behaviour law is considered linear, a time harmonic magneto-dynamic formulation can be used. The FE mesh of the numerical problem is made of 31 390 elements. The current is imposed in the coil that is considered as an ideal conductor. Then, and for each considered frequency, the FE analysis allows us to compute the linkage flux Φ of the coil such that:

$$\Phi = \phi_r + j\phi_{im}\tag{2.6}$$

where ϕ_r is the real part and ϕ_{im} the imaginary part of the flux. If we consider the coil alone, i.e. without the magnets inside the tube, there is no phase lag between the magnetic flux and the current I_{theo} flowing through the winding. Then $\Phi = \phi_r$ and we can define the inductance L_{theo}^0 as:

$$L_{theo}^0 = \frac{\phi_r}{I_{theo}}\tag{2.7}$$

The resistance R_{theo}^0 of the coil is assumed to be equal to zero as the losses in the winding are neglected (ideal conductor). At the opposite, if we denote Φ^m the magnetic flux in presence of the permanent magnets, eddy currents lead to a phase lag between the magnetic flux Φ^m and the current I_{theo} . Hence, we have:

$$\Phi^m = \phi_r^m + j\phi_{im}^m \quad (2.8)$$

with ϕ_{im}^m not equal to zero. Then, we can define an equivalent inductance and an equivalent resistance in presence of the PM:

$$\begin{aligned} L_{theo}^m &= \frac{\phi_r^m}{I_{theo}} \\ R_{theo}^m &= \frac{\omega\phi_{im}^m}{I_{theo}} \end{aligned} \quad (2.9)$$

In the same way as in 2.2.3.1, we consider the quantities ΔR_{theo} and ΔL_{theo} :

$$\begin{aligned} \Delta R_{theo} &= R_{theo}^m - R_{theo}^0 \\ \Delta L_{theo} &= L_{theo}^m - L_{theo}^0 \end{aligned} \quad (2.10)$$

Then, if the permanent magnets dynamic behaviour can be modelled by its magnetic permeability μ and electrical conductivity σ , the frequency evolutions of ΔR_{theo} and ΔL_{theo} should be the same as ΔR_{exp} and ΔL_{exp} respectively. In the next section, we propose a validation test for the procedure.

Validation of the procedure

The validation has been carried out by using a material which electrical conductivity is well known. An aluminium cylinder is chosen with $\sigma = 25 \times 10^6 (\Omega.m)^{-1}$ and the magnetic permeability is taken equal to the one of the vacuum. This cylinder is placed inside the coil instead of the permanent magnets presented in figure 2.13. First, the coil is characterized alone and the measurements obtained from the impedance analyser show a constant inductance ($L_{exp}^0 = 47.5 \mu H$) whereas the resistance increases, due to the skin and proximity effects that occur in the winding at high frequencies (see figure 2.15). This variation becomes significant above $20kHz$ and below this frequency the resistance can be considered to be constant. Thus, assuming that the winding is an homogeneous medium flowed by a uniform current density is correct.

In a second step, the evolutions of the coil inductance and resistance versus the frequency are measured when the aluminium cylinder is inside the coil. Then, the evolutions of ΔR_{exp} and ΔL_{exp} have been calculated. The same steps have been carried out by FE analysis, and evolutions of ΔR_{theo} and ΔL_{theo} have been calculated. For the coil alone, the calculated inductance is constant and equal to $L_{sim}^0 = 47 \mu H$, that is very close to the measured one. The comparison between calculated and measured variations of the resistance and the inductance are reported on figures 2.16 and 2.17 respectively.

Results show good agreement between measurements and FE calculation. We can note an increase of ΔR^{Al} . This is the consequence of the eddy currents which are induced

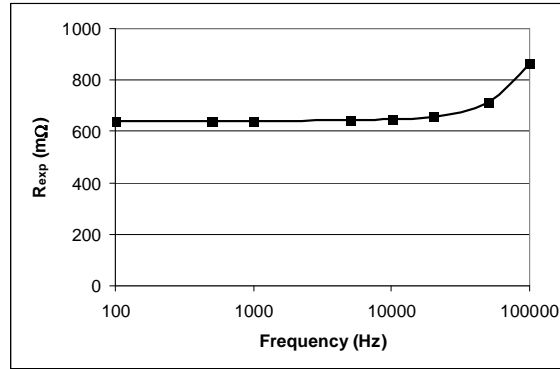


Figure 2.15: Winding resistance versus the frequency for the only coil.

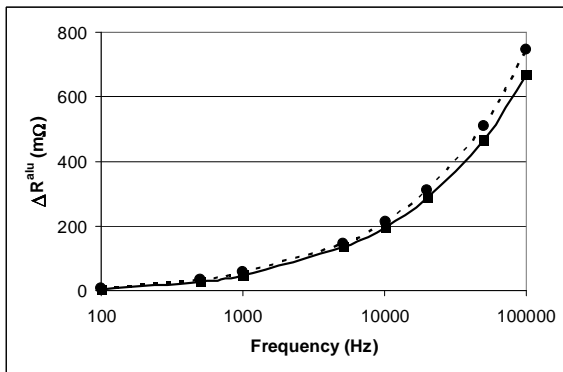


Figure 2.16: Evolutions of ΔR^{Al} obtained from calculation (solid line) and measurements (dashed line).

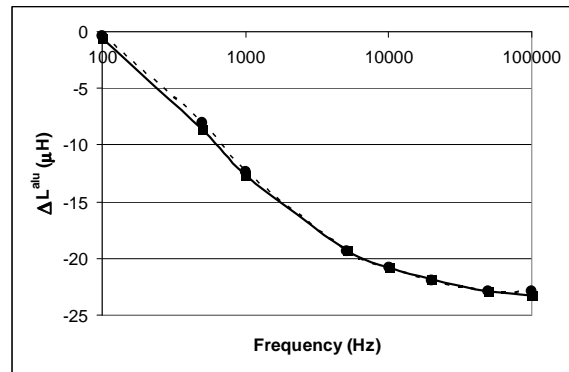


Figure 2.17: Evolutions of ΔL^{Al} obtained from calculation (solid line) and measurements (dashed line).

in the aluminium cylinder by the magnetic field. Moreover, the inductance variation from 100Hz to 100kHz is greater than 50%. It is due to the eddy currents that create a magnetic field which opposes the applied field so that the linkage flux decreases inside the coil. The error observed between measurements and FE calculations is less than 10% at 100kHz . This can be explained by the simplified hypothesis used to model the system. In fact, in the experimental case, there is an induced magnetic field due to eddy currents which influences the excitation winding. It is not the case in the numerical model as we impose a homogeneous current density in the winding that is considered with a null conductivity. Moreover, the numerical error due to the discretization also exists.

Consequently, this example validates the approach if the material inserted into the coil can be modelled using constant conductivity σ and permeability μ . In the following, the approach is applied to samples of permanent magnets and magnetite powder.

2.2.3.2 Application to rare earth NdFeB permanent magnets

The *NdFeB* permanent magnets to be identified are reported in table 2.2 with their geometrical and physical characteristics.

Table 2.2: Geometrical and physical characteristics of the studied permanent magnets given by the manufacturer

Permanent magnet	Diameter (mm)	Height (mm)	B_r (Tesla)	H_c (kA/m)	σ ($\Omega.m$) ⁻¹
BREMAG 10 (sintered)	15	5	0.825	540	0.666×10^6
BREMAG 27 (bonded)	15	3	1.050	800	0.714×10^6

Anisotropic sintered NdFeB magnets (BREMAG 10)

A sample of sintered permanent magnet is coated with a thin layer of nickel of about 15 μm . As this material is electrically conductive with $\sigma_{Ni} = 14.62 \times 10^6$ ($\Omega.m$)⁻¹, a FE calculation has been carried out in order to estimate the influence of the nickel coating in the range of the considered frequencies. By considering the calculated evolutions of ΔR and ΔL for a single sample of permanent magnet with and without the nickel layer, we have observed a weak influence (less than 5%) of the nickel layer. This one is then neglected in the following FE calculations.

A stack of ten samples of sintered NdFeB magnets, as presented in figure 2.13, is modelled by an unique volume of material with conductivity σ and permeability μ . First, we have measured the evolution of ΔR_{sint}^{exp} and ΔL_{sint}^{exp} . Then, an optimization procedure is performed to minimize the least square error between ΔR_{sint}^{exp} and ΔR_{sint}^{sim} , as well as the least square error between ΔL_{sint}^{exp} and ΔL_{sint}^{sim} with the conductivity and the permeability as variables. The identification procedure gives $\sigma_{sint} = 0.714 \times 10^6$ ($\Omega.m$)⁻¹ and $\mu = 1.09\mu_0$. In figures 2.18 and 2.19, both evolutions of ΔR_{sint} and ΔL_{sint} are illustrated.

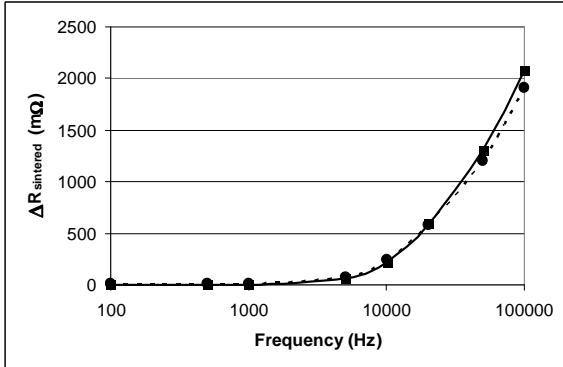


Figure 2.18: Solid line gives the evolution of ΔR_{sint} obtained from calculation using $\sigma_{sint} = 0.714 \times 10^6$ ($\Omega.m$)⁻¹ and $\mu_r = 1.09$ along the z axis. Dashed line gives the measurements.

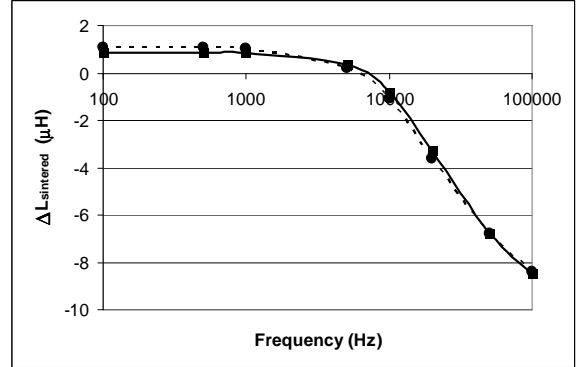


Figure 2.19: Solid line gives the evolution of ΔL_{sint} obtained from calculation using $\sigma_{sint} = 0.714 \times 10^6$ ($\Omega.m$)⁻¹ and $\mu_r = 1.09$ along the z axis. Dashed line gives the measurements.

A similar behaviour of the ΔR_{sint} evolution is observed between the calculation and the measurement. Moreover, the permanent magnet presents a relative magnetic permeability different from the unit along the z axis in order to represent correctly the measurement. In fact, ΔL_{sint} is very sensitive to the permeability and a significant gap could appear

regarding the experimental evolution if we consider the vacuum magnetic permeability in the PM. Then, it can be concluded that, in the considered frequency range and for low levels of the magnetic flux density, this kind of permanent magnet can be well represented by the model.

Anisotropic bonded NdFeB magnets (BREMAG 27)

The same identification procedure was applied for the bonded NdFeB magnets. The obtained electrical conductivity and relative magnetic permeability are respectively $\sigma_{bonded} = 0.019 \times 10^6 (\Omega.m)^{-1}$ and $\mu_r = 1.22$ along the z axis. Evolutions of ΔR_{bonded} and ΔL_{bonded} are given in figures 2.20 and 2.21.

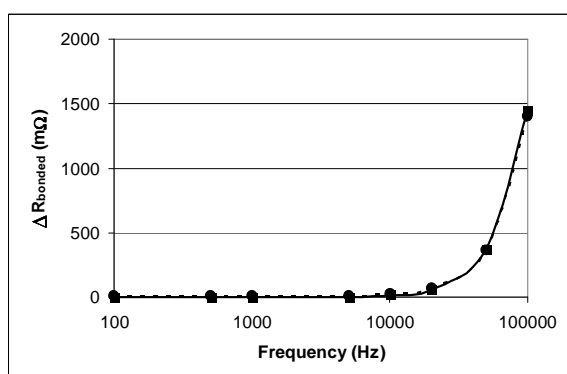


Figure 2.20: Solid line gives the evolution of ΔR_{bonded} obtained from calculation using $\sigma_{bonded} = 0.019 \times 10^6 (\Omega.m)^{-1}$ and $\mu_r = 1.22$ along the z axis. Dashed line gives the measurements.

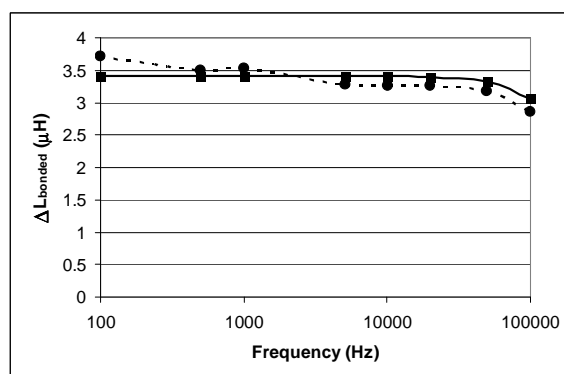


Figure 2.21: Solid line gives the evolution of ΔL_{bonded} obtained from calculation using $\sigma_{bonded} = 0.019 \times 10^6 (\Omega.m)^{-1}$ and $\mu_r = 1.22$ along the z axis. Dashed line gives the measurements.

If we consider the evolution of ΔR_{bonded} , the calculation gives results very close to the measurements. At the opposite, the evolution of ΔL_{bonded} shows a behaviour that is globally correct but with an under-estimated calculated value below about $3kHz$ and over-estimated above this same frequency. Nevertheless, the gap between calculation and measurement is less than 8% in these both regions. Finally, in the same way as the previous kind of magnet, we can consider the magnet to be correctly represented in this frequency range for low levels of magnetic induction.

2.2.3.3 Application to a magnetite powder

Samples

In the context of a non-destructive testing (NDT) study [18], the challenge was to test the procedure for a magnetic powder material that is found as deposits in heat exchangers of a nuclear plant. Four samples of magnetite powders are characterized in the same way as the PMs previously as shown in figure 2.22. To investigate the influence of the density and composition of the powder (mass fraction of magnetite) on its global magnetic behaviour, different combinations of these two parameters have been considered (see table 2.3). All

Table 2.3: Characteristics of the magnetite samples

Sample	Mass fraction	Density (g/cm^3)
1	95%	5
2	70%	5
3	70%	2.5
4	70%+10% copper	5

Table 2.4: ΔL^{exp} and ΔR^{exp} values in the frequency range $15kHz$ to $200kHz$

Sample	ΔL^{exp} (μH)	ΔR^{exp} ($m\Omega$)
1	3.11	from 1.0 to 3.5
2	1.55	from 0.2 to 1.5
3	1.25	from 0.6 to 1.8
4	1.65	from 1.4 to 3.0

samples are mixed with a non magnetic and non conducting material except for the 4th sample that includes also copper (10% of the mass fraction).



Figure 2.22: Magnetite sample and excitation coil

Identification of the parameters

The identification procedure has been carried out in the frequency range of the eddy current NDT, that means from $15kHz$ to $200kHz$. For all samples, the measured evolution of ΔL^{exp} is relatively constant in the considered frequency range (see table 2.4), that justifies the hypothesis on a constant magnetic permeability in the numerical model of the system. At the opposite, the measured evolution of ΔR^{exp} , due to the skin and proximity effects, presents a small linear increase (see table 2.4) in the same frequency interval. These both effects are taken into account in the numerical model by modelling the real geometry of the winding, i.e. by modelling each turn.

Results of the inverse problem resolution are presented in table 2.5. One can observe that the magnetic permeability is within the range of what can be found in the literature [19]. The most important value is obtained for the sample 1, for which the mass fraction of magnetite and density are the highest. For the other samples, which have the same mass fraction of magnetite, samples 2 and 4 have, as expected, the most important magnetic permeability as they present the highest density.

Table 2.5: Results for magnetic permeability and electrical conductivity identification

Sample	Relative magnetic permeability	Electrical conductivity (S/m)
1	2.64	78
2	1.81	49
3	1.66	71
4	1.86	115

When considering the electrical conductivity, this one lies within the range 49 to $115S/m$, which is lower than the solid magnetite values [20] (between few hundreds to $10^5S/m$). This can be explained by the fact that, in the present case, the magnetite is powdered and not in a massive state. For the sample 4, the apparent electrical conductivity is more important relatively to the other ones, as this sample includes copper.

Validation of the identified magnetic permeability

One way to verify the values of the magnetic permeability is to measure the magnetic force exerted by a permanent magnet on the magnetite samples. The principle of the experiment is presented in figure 2.23. The experimental device is modelled in 2D-FE using the previously determined magnetic permeability for the magnetite powders. The calculated force is then compared with the measured one (see table 2.6). Good agreement is observed between experiment and calculation, confirming the magnetic permeability values of the studied samples. Note that, from these values of the magnetic permeabilities, the NDT study [18] has shown that, for the specific tested device, the magnetic permeability has the most impacting effect on the NDT sensor response whereas the electrical conductivity has no significant impact. This imply that the magnetite powder involved in the tested device must be characterized with accuracy regarding its magnetic permeability whereas no special care has to be taken for the electrical conductivity identification.

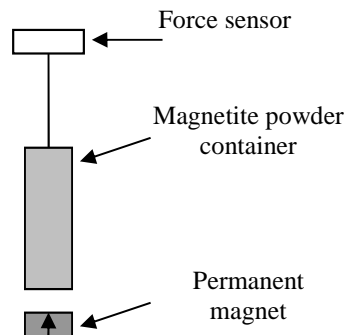


Figure 2.23: Principle of the force measurement device

Table 2.6: Comparison between measured and calculated forces on magnetite samples

Sample	Experimental force (mN)	Simulated force (mN)
1	39	41
2	24	24
3	22	20
4	26	25

2.2.4 Magnetization loss in permanent magnets⁷

2.2.4.1 Motivation

When studying and/or designing electrical machines with permanent magnets (PM), it is of importance to be able to predict any risk of magnetization loss in the PM. In the same way as the impact of the manufacturing processes, it is more and more crucial to include such aspect in the numerical models. In fact, the improvement of the performances and energy efficiency with the lowest cost and weight, lead the designers of electrical machine to limit the amount of materials (copper, lamination, permanent magnets ...). Therefore, electrical machines often operate at the limits of the material performances. In the case of sintered rare earth *NdFeB* PM, used in various types of electrical machines and devices because of their high power density, one of the most critical constraint in operation is the temperature. In fact, as the electrical conductivity of these magnets is moderate, the eddy current loss due to space and time harmonics cannot be neglected [21] as well as the associated temperature increase in the PM. Even if the coercive field is rather high at the ambient temperature (usually above $800kA/m$), due to their high temperature coefficients of remnant magnetic flux density and coercive field [22], the heating of the PM can lead to an irreversible demagnetization. For instance, for typical *NdFeB* PM, the coercive field drops drastically around $200kA/m$ at $180^{\circ}C$. An accurate description and model of the magnetic behaviour law of the PM are required in order to predict any demagnetization that will impact their performances. Besides, to validate the model of the PM demagnetization (presented in section 3.2.4), it is also required to develop adapted experimental devices.

2.2.4.2 Experimental device

The developed experimental device (see figure 2.24) is made of a magnetic circuit with a fixed part and a mobile part. The fixed part is wound with two excitation coils and the mobile part allows to adjust the air-gap between the PM and the fixed part. The entire device is build so that it can support up to $200^{\circ}C$.

To model such device, for the validation of the PM demagnetization model, the experimental parameters must be well known. In addition to the geometry and electrical parameters, the other parameters are related to the magnetic behaviour laws (lamination and PM), electrical conductivity of the PM and losses in the laminations. For the magnetic behaviour laws, the laminations were characterized with the Epstein frame, in a wide

⁷The presented results are part of the PhD Thesis of Radu Fratila.

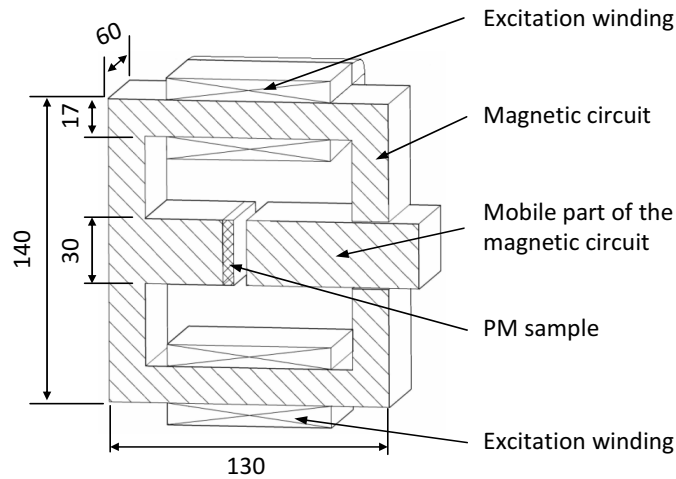


Figure 2.24: Experimental PM device (dimensions in *mm*).

range of excitation frequency (up to 600Hz) in order to extract the iron loss model parameters (presented in section 3.3) and the average $B - H$ curve. The PM behaviour law in the second quadrant was characterized with a Pulsed Field Magnetometer at different temperatures, from the ambient up to 180°C . In addition, the electrical conductivity of the PM was also characterized using the *contact-less* technique presented in section 2.2.3. As a first approach, for determining the impact of the operating conditions on the PM magnetization, the device was instrumented with Hall sensors. These sensors (H_1, H_2, H_3, H_4) were placed at specific locations, as illustrated in figure 2.25, in order to measure the component of the magnetic flux density that is normal to the surface of the PM in the air-gap. In addition, three temperature sensors were added to the experimental device: one for measuring the ambient temperature and two in contact with the PM.

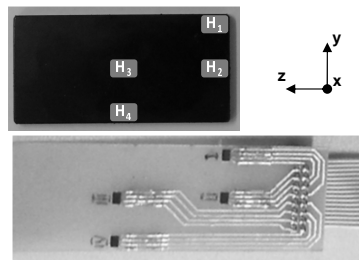


Figure 2.25: Hall sensor locations and experimental board.

To emphasize the effect of the local magnetization loss process, two experimental tests are illustrated in figure 2.26. On the one hand, in figure 2.26a, the frequency and excitation current were set so that, in a global way, the operating point of the PM remains in the linear region of the PM behaviour law. At the other hand, in figure 2.26b, the frequency was increased by keeping the same excitation current in the windings. In this case, the magnitude of the magnetic field variation remains globally the same but with a higher excitation frequency that leads to more significant eddy current losses. This impacts the PM behaviour law that is shifted, due to the temperature increase, towards

the origin of the BH plane. These measurements reveals that the PM does not suffer from magnetization loss at location H_1 with an average value of magnetic flux density that remains around $0.37T$. At the opposite, in the center of the PM at location H_3 , the magnetization loss is significant with a decrease of the average magnetic flux density from $0.46T$ to $0.34T$. The behaviour of the working point at higher temperature is illustrated in figure 2.27. During the alternative excitation, the load line will go back and forth along the vertical axis. For the same magnitude of alternative magnetic flux density, the higher the temperature is, the higher the risk of demagnetization is.

These results will be further discussed and analyzed in section 3.2.4 where the modelling of the magnetization loss is presented.

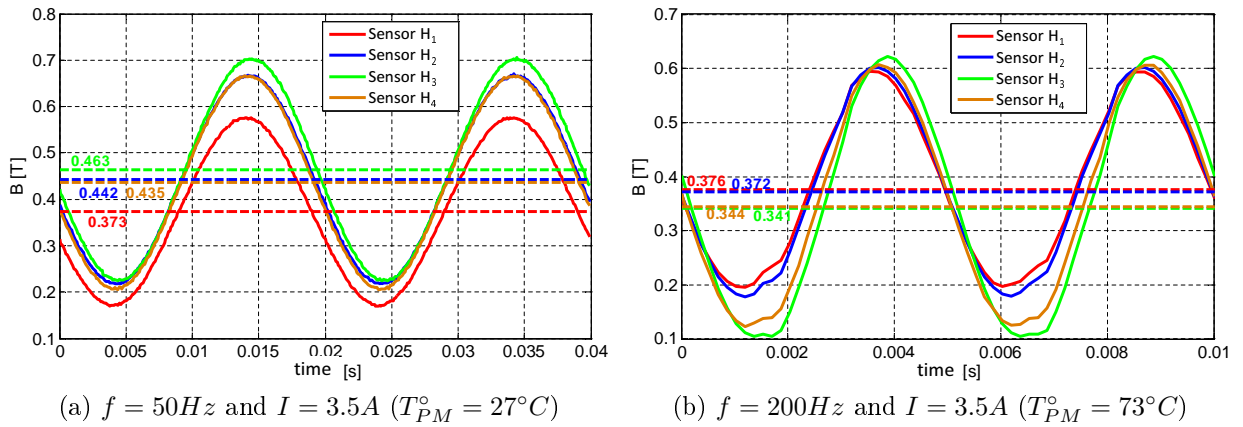


Figure 2.26: Measured magnetic flux density with sensors H_1 to H_4 . Case (a): no magnetization loss. Case (b) : magnetization loss

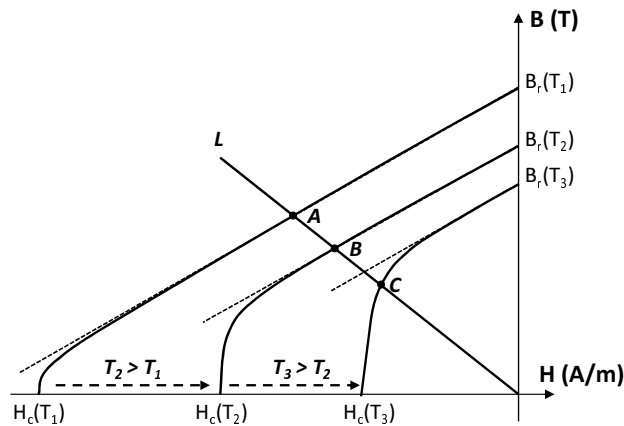


Figure 2.27: Illustration of the working point in a PM, depending on the temperature.

2.2.5 Magnetic characterization in High Frequency for EMI filters⁸

2.2.5.1 Context of the study

The design of Electro-Magnetic Interference (EMI) filters requires an accurate model representing of each component of the filter. This is essential to reduce the uncertainty on the behaviour of the filters under specific operating conditions. In particular, the inductive components are in part responsible for the High Frequency (HF) behaviour of the EMI filter. These are made from magnetic materials(usually ferrites) that can be subjected to different magnetization levels during the operating conditions. Usually, the data-sheets of these materials provide the complex magnetic permeability (CMP) curves that allow calculating the inductance from the real part and the losses (damping effect) from the imaginary part of the CMP [23]. However, this CMP information is limited to a small-signal characterization process, usually with an impedance analyzer, where the applied current to magnetize the material reaches milliamps as maximum [24]. Then, the measurement is typically in the Rayleigh zone, which does not always correspond to the real operating conditions of the material. In fact, most of the inductor models are based on small-signal levels [25, 26] and consequently, the non-linear effects of the material are not taken into account.

The non-linear behaviour of the material is linked to various parameters such as the applied current, frequency, temperature and intrinsic material properties. When characterizing the impedance of the inductor in a large frequency range, typically above $1MHz$ for ferrites, the real component of the CMP exhibits negative values. This behaviour has been explained by a capacitive effect associated to the magnetic core of the inductor [27], and has also been observed in [28] by hysteresis loop measurement. Therefore, in the following, the notion of material capacitance C_m has been introduced to represent the material behaviour with more accuracy.

2.2.5.2 Model of the experimental setup

Regarding the experimental characterization of the material behaviour law, there exist works that deal with the measurements of hysteresis loops in HF ranges (up to 100 kHz) such as in [29, 30]. In these works the two winding configuration is basically proposed. However, the HF effects in the measurement setup are not usually addressed. Therefore, to obtain an adequate model for the high frequency behaviour of non-linear inductors, a specific experimental procedure has been developed for characterizing ring cores up to $1MHz$, as shown in figure 2.28.

The proposed approach consists in using a single turn of flat copper ribbon (STFC). The advantages of this structure are: no magnetic coupling with a secondary winding, no inter-turns capacitances and no proximity effect. Nevertheless, it must be noted that the calculation of the magnetic flux density must be performed from the primary voltage that also includes the resistive component. Another aspect is that, at the opposite to low frequency characterization, the approach requires to identify the parameters associated

⁸The presented results are part of the PhD Thesis of Carlos Cuellar.

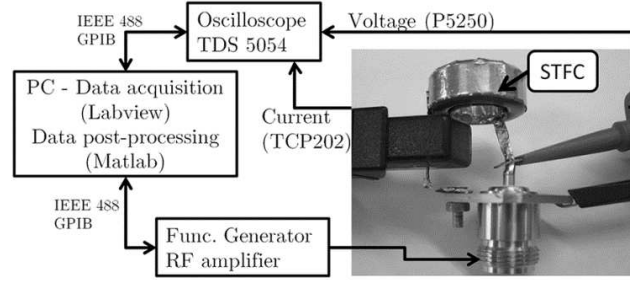


Figure 2.28: Experimental setup for the characterization of ring core using a single turn flat coil.

to each element in the experimental setup, such as parasitic capacitances, that influences the measurement. To illustrate these parameters, the equivalent circuit of the setup configuration is given in figure 2.29.

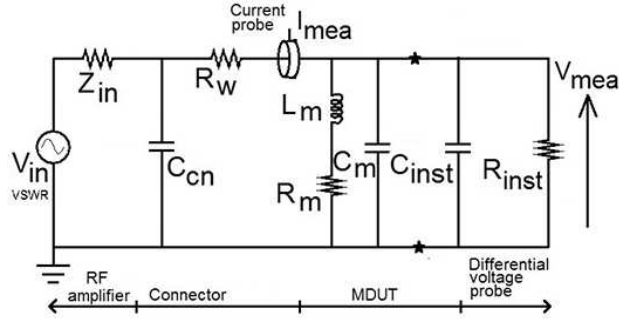


Figure 2.29: Equivalent circuit of the setup configuration.

The power source is represented by the voltage source V_{in} and the series impedance Z . The N-connector, between the power source and the flat copper ribbon, is represented by a capacitance C_{cn} and the copper resistance is R_w . The ring core under test is represented with the inductive L_m and loss R_m elements connected in series. The additional element in parallel corresponds to the material capacitance C_m (dielectric effect) mentioned previously. The circuit branch $L_m - R_m - C_m$ represents the magnetic material under test (MDUT). Finally, the voltage-differential probe is also represented by its capacitance C_{inst} and resistance R_{inst} .

2.2.5.3 Identification procedure of the equivalent circuit parameters

First, the parasitic capacitance C_{cn} of the N-connector is identified from the measurement to be about $1.5pF$ and confirmed by an electrostatic study based on a Finite Element model ($1.46pF$). The copper resistance R_w is identified from an impedance analyzer measurement, without the ring core, and is found to be about $30m\Omega$.

Regarding the differential voltage probe, its resistance R_{inst} is equal to $8M\Omega$. For the capacitance C_{inst} , two tests have been performed. The first one is carried out with the impedance analyzer and gave a value of $4pF$. The second test was realized with the open-circuit configuration in order to measure the RF output voltage. The open-circuit

measurement was made by the differential voltage probe connected in parallel to the amplifier output, and the current probe clamped on one phase of the voltage probe. The voltage and current signals are measured and the impedance of the open-circuit measure gave a value of about $6pF$ where $1.5pF$ is the contribution from the N-connector, leading then C_{inst} to a value of $4.5pF$.

For the current measurement, usually experimental devices include a shunt-resistor as a current sensor. In the present work, a $20m\Omega$ shunt has been tested and compared with measurements obtained from a current probe. It has been observed, in the shunt configuration, that a coupling capacitance appears between the shunt and the ring core under test that impacts the measurement close to $1MHz$. Moreover, the shunt voltage measure requires an extra voltage probe, increasing the parasitic elements in the circuit. That is why, for the present work, a current probe with a bandwidth is of $50MHz$ is used.

Finally, to estimate the capacitance C_m associated to the material, the frequency resonance linked to the material can be used as detailed in [27]. This frequency resonance is obtained from the impedance measurement of the ring core as illustrated in figure 2.30. Then, the material capacitance is deduced from the analytical expression (2.11) where μ_i is the initial permeability of the material, f_m the frequency of resonance ($\sim 1MHz$ here) and N the number of turns ($N = 1$ here). The parameters D_i , D_e , H_g are linked to the geometry of the ring and are, respectively, the internal and external diameters and height. The resulting material capacitance is found to be about $400pF$.

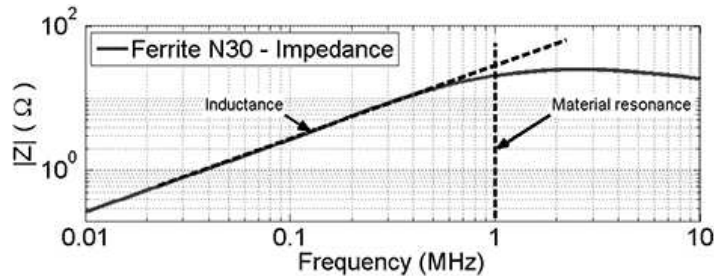


Figure 2.30: Impedance evolution for a N30 ferrite ring core inductor (resonance occurs near $1MHz$).

$$C_m = \frac{1}{4\pi\mu_0\mu_i N^2 (2\pi f_m)^2} \left[\frac{\pi(D_e + D_i)}{H_g(D_e - D_i)} \right] \quad (2.11)$$

Knowing all these parameters, and from the measured voltage and current, the $B-H$ loops of the ring core can be easily deduced in a post-processing step allowing to extract the voltage and current corresponding to the circuit branch $L_m - R_m$. The classical expressions (2.4) and (2.2) are used to calculate the B and H quantities. Note here that L_m and R_m are non-linear parameters.

To illustrate the proposed approach, the measured and identified hysteresis loops with the Jiles-Atherton model (presented in section 3.2.3) are given in figure 2.31 for the frequency $20kHz$ that is considered as a *low* frequency for the N30 ferrite material. Then, to test the robustness of the identified model and validating the experimental approach, a procedure consisting in using the model for arbitrary frequencies (without re-identifying

its parameters) and comparing the results with the experiment is performed. Results are illustrated in figure 2.32 for frequencies up to 1MHz and are in good agreement between the model and the experiment. This allows to validate the proposed approach, at least for the considered type of material.

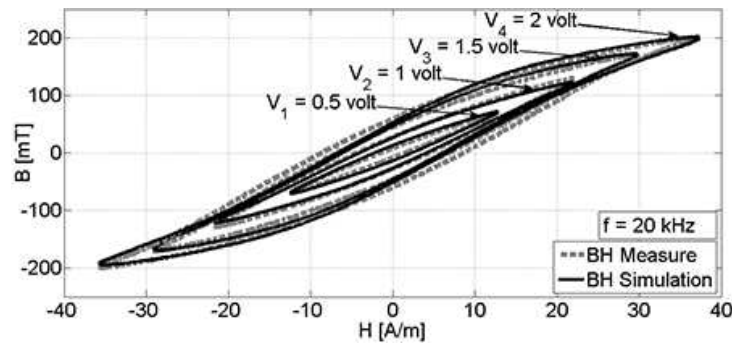


Figure 2.31: Measured and identified hysteresis loops for a N30 ferrite.

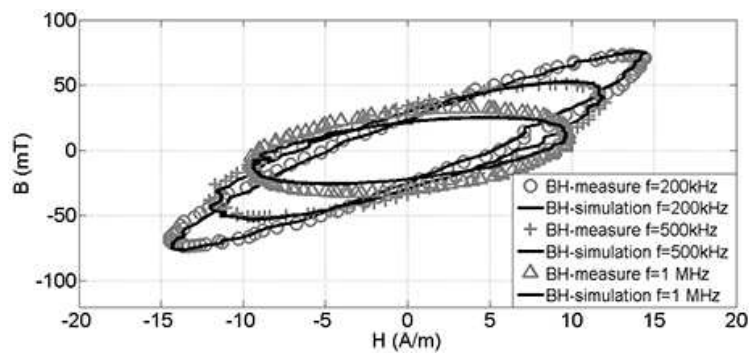


Figure 2.32: Hysteresis loops of N30 ferrite for frequencies of 200kHz , 500kHz and 1MHz .

The model was further applied to an EMI filter with DC-bias current, to emphasize the usefulness of such model, and compared with the experiment with very satisfactory results [31].

3

Materials and numerical modelling

3.1 General context of the numerical modelling

3.1.1 Mathematical model

Once the experimental step consisting in the characterization of the magnetic material properties has been achieved, the study of an electrical device requires models for the material behaviour. Actually, one of the most accurate techniques for modelling the electromagnetic phenomena is the Finite Element (FE) method. This is why we mainly develop models of ferromagnetic material which are adapted for FE analysis. Obviously, these material models should be accurate and remain fast to compute within the frame of the FE calculation. Also, the associated memory requirements should be limited in order to not penalize the FE model.

First, the mathematical model, from which the numerical model is build, is presented. In particular, the main mathematical formulations used for solving a classical electromagnetic problem in low frequency are detailed.

3.1.1.1 Maxwell's equations

Let us consider an electromagnetic problem associated to a domain \mathcal{D} that is contractible and, in practice, of finite size and with a boundary Γ . The Maxwell's equations defining the electromagnetic phenomena in \mathcal{D} are written such as:

$$\mathbf{curl}\mathbf{E} = -\frac{\partial\mathbf{B}}{\partial t} \quad (3.1)$$

$$\mathbf{curl}\mathbf{H} = \mathbf{J} + \frac{\partial\mathbf{D}}{\partial t} \quad (3.2)$$

where \mathbf{E} and \mathbf{D} are the electric field and induction vectors, \mathbf{H} and \mathbf{B} the magnetic field and flux density vectors, \mathbf{J} the current density vector. In low frequency electrical engineering applications, the Magneto Quasi Static (MQS) approximation is usually considered, that is to say the displacement currents are neglected. In that condition, the term $\partial_t\mathbf{D}$ is omitted in equation (3.2) that becomes:

$$\mathbf{curl}\mathbf{H} = \mathbf{J} \quad (3.3)$$

3.1.1.2 Behaviour laws

Equations (3.1) and (3.2), in which four quantities are involved, are not sufficient to describe the electromagnetic problem. Therefore, to account for specific characteristics of a system (different materials), two constitutive relationships are introduced so that the vectors (\mathbf{E} , \mathbf{B} , \mathbf{H} and \mathbf{J}) are linked. The magnetic induction \mathbf{B} (resp. \mathbf{J}), depends not only on the magnetic field \mathbf{H} (resp. \mathbf{E}), but also on other parameters such as, for example, the temperature T . Both constitutive relationships can be written in the following general way:

$$\mathbf{B} = \mathbf{f}(\mathbf{H}, t, T, \dots) \quad (3.4)$$

$$\mathbf{J} = \mathbf{g}(\mathbf{E}, t, T, \dots) \quad (3.5)$$

where t is the time. Usually, the material models are considered stationary, i.e. not time dependent and the parameters like the temperature T are often supposed to be constant. Moreover, whereas the magnetic constitutive relationship can be non-linear, the electric constitutive relationship is often considered with a linear behaviour. Under these assumptions, and neglecting the hysteresis phenomenon in the magnetic materials, the constitutive relationships can be written:

$$\mathbf{B} = \mathbf{f}(\mathbf{H}) \quad (3.6)$$

$$\mathbf{J} = \sigma\mathbf{E} \quad (3.7)$$

Both constitutive relationships can be determined from macroscopic measurements.

3.1.1.3 Boundary conditions

To impose the unicity of the mathematical model grouping equations (3.1) and (3.3) together with the relationships (3.6) and (3.7), it is necessary to define time and spatial boundary conditions associated to the fields.

Time boundary conditions are fixed by the initial distribution of the magnetic fields. Regarding the spatial boundary conditions, these are defined on the boundary Γ of the domain of study \mathcal{D} (figure 3.1).

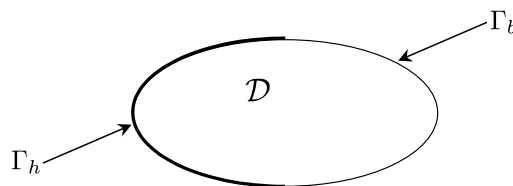


Figure 3.1: Domain of study.

The boundary Γ is decomposed into Γ_b and Γ_h verifying $\Gamma = \Gamma_b \cup \Gamma_h$ and $\Gamma_b \cap \Gamma_h = \emptyset$. The boundary conditions on the magnetic field and magnetic induction are often set to be homogeneous:

$$\mathbf{H} \wedge \mathbf{n}|_{\Gamma_h} = \mathbf{0} \quad (3.8)$$

$$\mathbf{B} \cdot \mathbf{n}|_{\Gamma_b} = 0 \quad (3.9)$$

with \mathbf{n} is the unit normal vector to the boundary Γ .

Combining, on the one hand, (3.3) and (3.8) and, on the other hand, (3.1) and (3.9), the resulting boundary conditions are obtained :

$$\mathbf{J} \cdot \mathbf{n}|_{\Gamma_h} = 0 \quad (3.10)$$

$$\mathbf{E} \wedge \mathbf{n}|_{\Gamma_b} = \mathbf{0} \quad (3.11)$$

3.1.2 Formulations

To solve the system of equations, potential formulations can be used [32]. In the following, these formulations are introduced in the:

- *magnetostatic* case, where the current density \mathbf{J} is supposed to be known. The studied problem can include ferromagnetic materials with no electrical conductivity.

- *magnetodynamic* case, where eddy currents in conductive materials can not be neglected.

3.1.2.1 Magnetostatic formulations

In that kind of formulation, the source current density \mathbf{J}_0 in inductors is supposed known and homogeneous. The system of equations to be solved is:

$$\mathbf{curl} \mathbf{H} = \mathbf{J}_0 \quad (3.12)$$

$$\mathbf{div} \mathbf{B} = 0 \quad (3.13)$$

where (3.13) is obtained from (3.1). In addition, the boundary conditions (3.8) and (3.9) together with the behaviour law (3.6) are considered.

To solve such system, potentials are generally introduced: the magnetic scalar potential Ω formulation and the magnetic vector potential \mathbf{A} formulation.

Magnetic scalar potential formulation

To account for the inductors with a known current density \mathbf{J}_0 , a source field \mathbf{H}_s is introduced such that:

$$\begin{aligned} \mathbf{curl} \mathbf{H}_s &= \mathbf{J}_0 \\ \text{with } \mathbf{n} \wedge \mathbf{H}_s|_{\Gamma_h} &= \mathbf{0} \end{aligned} \quad (3.14)$$

As $\mathbf{curl}(\mathbf{H} - \mathbf{H}_s) = \mathbf{0}$, a magnetic scalar potential Ω can be found such that:

$$\mathbf{H} = \mathbf{H}_s - \mathbf{grad} \Omega \quad (3.15)$$

Different methods can be used to determine the source field, either analytically or by numerical techniques [33]. The magnetic scalar potential formulation to solve is then:

$$\begin{aligned} \mathit{div} [\mathbf{f}(\mathbf{H}_s - \mathbf{grad} \Omega)] &= 0 \\ \text{with } \mathbf{n} \cdot [\mathbf{f}(\mathbf{H}_s - \mathbf{grad} \Omega)]|_{\Gamma_b} &= 0 \\ \text{and } \Omega|_{\Gamma_h} &= 0 \end{aligned} \quad (3.16)$$

Magnetic vector potential formulation

From (3.13), the magnetic induction \mathbf{B} can be derived from a vector potential \mathbf{A} such that:

$$\mathbf{B} = \mathbf{curl} \mathbf{A} \quad (3.17)$$

Associating equations (3.12) and (3.17), the magnetic vector potential formulation is obtained:

$$\begin{aligned} \mathbf{curl}[\mathbf{f}^{-1}(\mathbf{curl} \mathbf{A})] &= \mathbf{J}_0 \\ \text{with } \mathbf{n} \wedge [\mathbf{f}^{-1}(\mathbf{curl} \mathbf{A})]|_{\Gamma_h} &= \mathbf{0} \\ \text{and } \mathbf{n} \wedge \mathbf{A}|_{\Gamma_b} &= \mathbf{0} \end{aligned} \quad (3.18)$$

The curl of a gradient is identically zero, then any arbitrary function which can be expressed as the gradient of a scalar function may be added to \mathbf{A} . Therefore, a gauge condition, such as, for example, the Coulomb gauge in equation (3.19), must be added in order to assure the unicity of \mathbf{A} .

$$\mathit{div} \mathbf{A} = 0 \quad (3.19)$$

3.1.2.2 Magnetodynamic formulations

In electrical engineering, the magnetodynamic is the study of non stationary electromagnetic phenomena. This is particularly the case when the studied system is made of electrically conductive materials where eddy currents can not be neglected. The equations representing such problem are:

$$\mathbf{curl}\mathbf{E} = -\frac{\partial\mathbf{B}}{\partial t} \quad (3.20)$$

$$\mathbf{curl}\mathbf{H} = \mathbf{J} + \mathbf{J}_0 \quad (3.21)$$

where \mathbf{J} is the eddy current density vector.

The constitutive relationships (3.7) and (3.6), together with the boundary conditions (3.8) to (3.11), are also added to the system of equations. In the following, the magnetodynamic formulations are detailed for electrically conductive regions.

Electric potential formulation \mathbf{A} - φ

From the definition of the vector potential (3.17), equation (3.20) becomes:

$$\mathbf{E} = -\left(\frac{\partial\mathbf{A}}{\partial t} + \mathbf{grad}\varphi\right) \quad (3.22)$$

where φ is the electric scalar potential.

Combining this result with equation (3.21) and the relationship (3.7), the electric potential formulation is obtained:

$$\mathbf{curl}[f^{-1}(\mathbf{curl}\mathbf{A})] + \sigma\left(\frac{\partial\mathbf{A}}{\partial t} + \mathbf{grad}\varphi\right) = \mathbf{0} \quad (3.23)$$

Magnetic potential formulation \mathbf{T} - Ω

The electric vector potential \mathbf{T} is defined such as $\mathbf{curl}\mathbf{T} = \mathbf{J}$ and introduced in equation (3.21) so that:

$$\begin{aligned} \mathbf{H} &= \mathbf{T} + \mathbf{H}_s - \mathbf{grad}\Omega \\ &\text{with } \mathbf{curl}\mathbf{H}_s = \mathbf{J}_0 \end{aligned} \quad (3.24)$$

where Ω is the magnetic scalar potential defined in section 3.1.2.1.

Finally, from equations (3.24) and (3.20), the magnetic potential formulation can be written:

$$\mathbf{curl}\left(\frac{1}{\sigma}\mathbf{curl}\mathbf{T}\right) + \frac{\partial f(\mathbf{T} - \mathbf{grad}\Omega)}{\partial t} = \mathbf{0} \quad (3.25)$$

It must be noted that, depending on the considered mathematical formulation of the problem, one has to use a material model with the magnetic field H as the input variable (for the magnetic potential formulation) or a material model with the flux density B as the input variable (for the electric potential formulation). Therefore, both types of models will be presented. Hereafter, two numerical schemes used to implement the non-linear behaviour in the FE method are presented.

3.1.3 Accounting for the non-linear magnetic behaviour

3.1.3.1 Fixed point method

To account for the magnetic hysteresis behaviour, it is necessary to write the formulation in a proper way. In the literature, several works have been focused in the implementation of the magnetic hysteresis in the FE method and different numerical schemes have been proposed [34–36]. One common way to implement this behaviour is the fixed point method [35]. In the case of the magnetic vector potential formulation, the magnetic behaviour law is written under the form:

$$\mathbf{H} = \mathbf{f}^{-1}(\mathbf{B}) = \nu_{FP}\mathbf{B} - \mathbf{M}_{FP}(\mathbf{B}) \quad (3.26)$$

where the reluctivity ν_{FP} is a constant and $M_{FP}(B)$ is a fictive magnetization, depending on \mathbf{B} . The vector potential formulation in equation (3.18) becomes:

$$\mathbf{curl}\nu_{FP}\mathbf{curl}\mathbf{A} = \mathbf{J}_0 + \mathbf{curl}\mathbf{M}_{FP}(\mathbf{B}) \quad (3.27)$$

This numerical scheme presents the advantage of a simple implementation but suffers from a low convergence rate and numerical instabilities when a hysteresis behaviour is involved. This issue is especially linked to a judicious choice of the value for ν_{FP} . In that context, some works have been interested in improving the efficiency of the technique, such as the ones presented in [36]. Then, the discretization with nodal shape functions of equation (3.27) using the Galerkin method leads to the following matrix system:

$$[S_{FP}][A] = [J] + [M_{FP}] \quad (3.28)$$

where $[A]$ represents the vector potential unknowns of the problem, $[S_{FP}]$ is a square matrix, $[M_{FP}]$ and $[J]$ are the vectors which take into account the magnetization \mathbf{M}_{FP} and the current density \mathbf{J}_0 . One can note that the matrix $[S_{FP}]$ is constant because the permeability ν_{FP} is constant as well. The non-linearity introduced by ferromagnetic materials are reported in the source term $[M_{FP}]$ that depends on \mathbf{B} (i.e. \mathbf{A}).

3.1.3.2 Differential reluctivity tensor

Another way to include the non-linearity, and especially the hysteresis behaviour, has been presented in [37]. The method requires the use of the differential reluctivity tensor $\|\partial\nu\|$ in the vector potential formulation given by equation (3.18). This tensor can be obtained from a vector hysteresis model, such as the vectorized Jiles-Atherton hysteresis model [38], that allows to calculate $d\mathbf{H} = \|\partial\nu\|d\mathbf{B}$. Using the Euler scheme, the previous term can be written:

$$\mathbf{H}_i = \|\partial\nu\|(\mathbf{B}_i - \mathbf{B}_{i-1}) + \mathbf{H}_{i-1} \quad (3.29)$$

Then, by incorporating this expression of the magnetic field into equation (3.18) and replacing the magnetic induction by $\mathbf{B} = \mathbf{curl}\mathbf{A}$, the vector potential formulation is written under the form:

$$\mathbf{curl} (\|\partial\nu\|\mathbf{curl}\mathbf{A}_i) = \mathbf{J}_i + \mathbf{curl} (\|\partial\nu\|\mathbf{curl}\mathbf{A}_{i-1}) - \mathbf{curl}\mathbf{H}_{i-1} \quad (3.30)$$

Note here that the i index is related to the time step. This way of including the hysteresis is very simple as it does not require to modify deeply an existing finite element procedure. The only modification is the storage of the previous time step solution of the magnetic vector potential in each element of the material with magnetic hysteresis.

3.2 Magnetic behaviour

3.2.1 Single-valued approximation

A first approach for representing the behaviour of magnetic materials in FE models is the single-valued behaviour. In most of the applications, this hypothesis is sufficient and permits a non negligible gain in the computation time. Besides the linear behaviour with constant magnetic permeability, used in practice for pre-dimensioning or for devices that do not involve magnetic saturation, the non-linear single-valued, or anhysteretic, behaviour allows to represent the saturation effects. This latter approach is commonly used in the study of electrical devices and the energy dissipation effects, associated to the magnetic hysteresis, can be taken into account in a post-processing step as it will be detailed in section 3.3. Generally, this non-linear behaviour is implemented through an analytical expression or a spline interpolation technique on experimental data points.

For the present work, the mathematical expression 3.31, originally introduced in [39], is used when a non-linear single-valued behaviour is required:

$$H = \frac{B}{\mu_0} \left[\frac{B^{2\alpha}}{B^{2\alpha} + \tau} (c - \epsilon) + \epsilon \right] \quad (3.31)$$

For the electric potential formulation, this expression can be directly applied whereas for the magnetic potential formulation, a numerical inversion is performed in order to obtain the magnetic field H as the input variable.

Nevertheless, as it will be presented in the next chapter, for some applications the hysteresis phenomenon is mandatory for an accurate modelling with the FE method. In that context, two commonly used models of the hysteresis in soft magnetic materials have been studied. The first one, the Preisach model [40], is based on phenomenological considerations on the magnetization process. The second one, the Jiles-Atherton model [41], is obtained from an energy-balance method starting from the anhysteretic behaviour.

3.2.2 Preisach model

3.2.2.1 Mathematical expression of the model

In the Preisach model, a ferromagnetic material is assimilated to a set of bistable units defined by the function $\gamma_{a,b} = \pm 1$ (Fig. 3.2 (a)). A bistable unit is characterized by a couple of switching fields (a, b) that must respect some conditions. In fact, if H_{sat}

represents the saturation magnetic field and M_{sat} the corresponding magnetization of the ferromagnetic material, when $H > H_{sat}$ all bistable units are in the positive state and the magnetization is $M = M_{sat}$. On the opposite, if $H < -H_{sat}$, all bistable units are in the negative state and $M = -M_{sat}$. Both previous assumptions define the following conditions for the couple (a, b) [42]:

$$\begin{aligned} a &\leq H_{sat} \\ b &\geq -H_{sat} \end{aligned}$$

As the hysteresis phenomenon is energetically dissipative, the condition $a \geq b$ must also be verified. These three conditions allow us to define a triangle Δ (Fig. 3.2), called the Preisach plane. Each couple (a, b) characterizing a bistable unit must belong to this plane. Finally, a ferromagnetic material is determined by a statistic distribution $p(a, b)$ of the switching field couples (a, b) belonging to the triangle Δ .

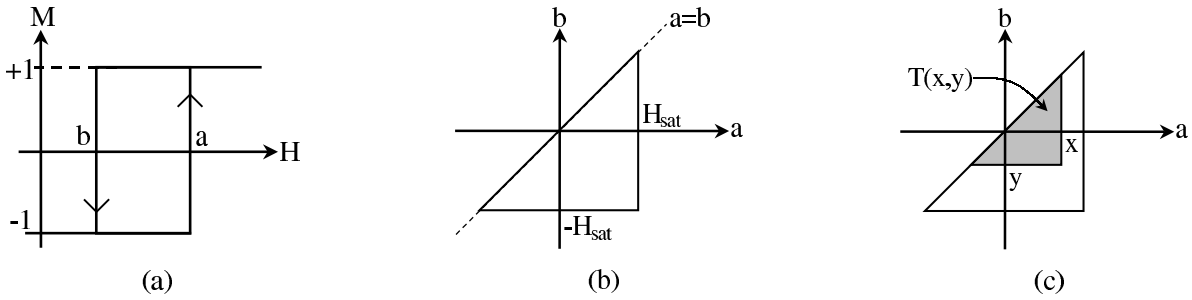


Figure 3.2: (a) Bistable unit (b) Triangle Δ (c) Triangle $T(x,y)$.

The total magnetization is then given by :

$$M = M_{sat} \iint_{\Delta} p(a, b) \gamma_{a,b} da db \quad (3.32)$$

The demagnetized state is represented by the equation $b = -a$ and the Preisach plane is split into two equal surfaces $S+$ and $S-$. $S+$ is the surface of couples (a,b) which are such that $\gamma_{a,b} = +1$ and $S-$ the surface of couples (a,b) such that $\gamma_{a,b} = -1$. For any other state of the system, the triangle Δ is split into two surfaces $S+$ and $S-$ separated by a broken line as shown in Figure 3.3. The expression (3.32) can be rearranged as :

$$M = M_{sat} \left(\iint_{S+} p(a, b) da db - \iint_{S-} p(a, b) da db \right) \quad (3.33)$$

The magnetic state of the system is totally characterized by the broken line. This latter is associated to a memory vector \mathbf{h} which includes some extrema of the excitation magnetic field H_i , i.e. some return points of the magnetic field. The memory vector coordinates must verify the following conditions:

$$\begin{aligned}
 H_0 &= 0, \quad \mathbf{h} = \{H_0, H_1, H_2, H_3, \dots, H_n\}, \\
 \text{for } i &= 1, \dots, n-1 \text{ and } d_i = H_i - H_{i-1} \\
 d_i \cdot d_{i+1} &< 0 \\
 |d_{i+1}| &< |d_i|
 \end{aligned} \tag{3.34}$$

where H_n , the last component, is the current value of the magnetic field. Using these relations, the memory vector can be easily determined. For example, the magnetic state of Figure 3.3 is given by the memory vector $\mathbf{h} = \{0, +H_{sat}, H_1, H_2, H_3\}$.

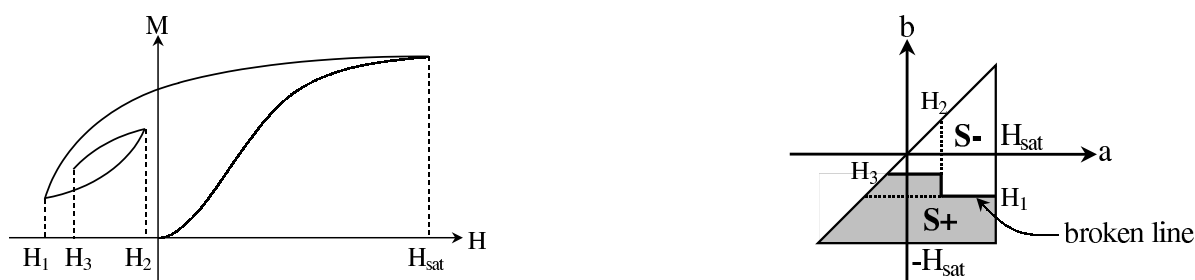


Figure 3.3: Example of a magnetization process and the corresponding surfaces $S+$ and $S-$

In these conditions, a ferromagnetic material can be fully described once its Preisach density function is known. Several methods for the determination of this function from experimental results are proposed in the literature [43–45]. All these methods require generally numerical derivation and integration, which adds extra numerical errors to experimental ones. Another solution is to identify the Preisach density function in its integral form, directly from the experiment. This form is known as the Everett function [46] defined by equation (3.35).

$$E(x, y) = M_{sat} \iint_{T(x,y)} p(a, b) da db \tag{3.35}$$

The surface $T(x, y)$ is defined by the right-angled triangle in the Preisach plane (Fig. 3.2) with (x, y) the vertex coordinates corresponding to the right angle and the hypotenuse is supported by the straight line $a = b$. The two other sides of the triangle are parallel to a and b axis, respectively. Then, if the Everett function is known, the magnetization M can be calculated from:

$$\begin{aligned}
 \text{if } H > H_m \quad M(H) &= M(H_m) + 2E(H, H_m) \\
 \text{if } H < H_m \quad M(H) &= M(H_m) - 2E(H_m, H)
 \end{aligned} \tag{3.36}$$

where H_m is the last return point of the magnetic field (the next to last value of vector h). Here, the Everett function and the magnetization M are linked by a relation which requires no numerical derivation or integration. Experimental determination of the Everett function is presented in the next section.

3.2.2.2 Identification of the Everett function

For the identification of the Everett function, the proposed method requires a set of measured centred minor hysteresis loops. From these experimental data of $M(H)$, the function $E(H_m, H)$ is determined for values of H belonging to $[-H_m, H_m]$. Figure 3.4 gives the descending part of a centred hysteresis loop and the corresponding function $E(H_m, H)$ obtained from Equation 3.36 for $H_m = 530 \text{ A.m}^{-1}$.

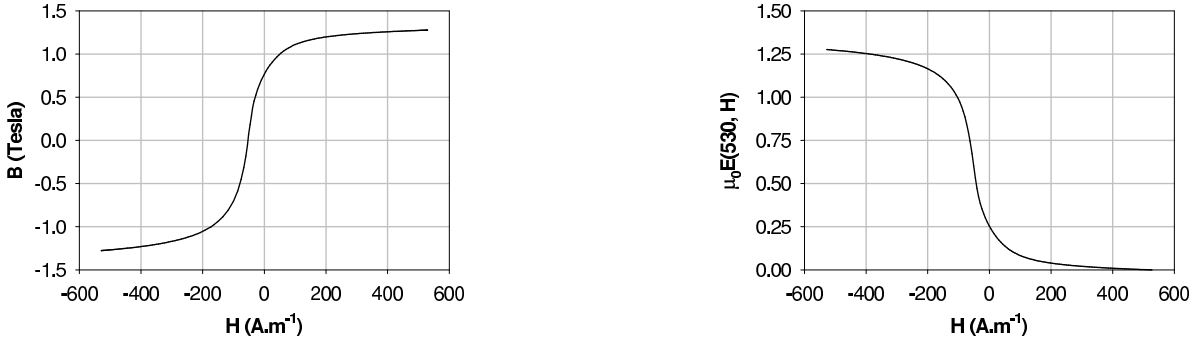


Figure 3.4: Descending part of a centered hysteresis curve and the corresponding Everett function ($M(H)$ model).

Then, from n measured centred loops ($i = 1, n$), a set of curves $E(H_{mi}, H)$ supporting the Everett function is obtained [47]. When using the model for any arbitrary point (H'_m, H') of the triangle Δ , an interpolation method is applied to the previous set of curves. This interpolation method must respect the Everett function continuity (this function is a primitive) on the whole studied domain and then for the hysteresis curves. The proposed method, already presented in [47] satisfies this condition. It is based on shape functions used to interpolate the field in 2D finite element method [48]. The expressions of these shape functions are detailed in [47].

Note that the Preisach model can also be adapted to obtain a model with the magnetic induction B as the input variable [49]. In this case, the method used for the Everett function identification is detailed in [47]. Finally, for each model $M(H)$ or $M(B)$, an Everett function $E(H_m, H)$ or $E(B_m, B)$ must be determined.

3.2.2.3 Global stress inclusion in the Preisach model

In order to take into account the effect of the mechanical stress on the hysteresis phenomenon, the Everett function can be parametrized with the stress [50]. The principle consists in identifying the Everett function in the same way as in section 3.2.2.2 but multiple times, for different applied mechanical stresses. Then, in the modelling process, to calculate the magnetisation for a given stress σ , the experimental values of stress σ_{inf} et σ_{sup} that bound σ . Values of $M_{inf}(B)$ and $M_{sup}(B)$ are calculated for, respectively, σ_{inf} and σ_{sup} from the corresponding Everett functions. As a first approach, a linear interpolation between $M_{inf}(B)$ and $M_{sup}(B)$ can be considered to calculate the desired magnetisation $M_\sigma(B)$. The procedure is summarized as follows:

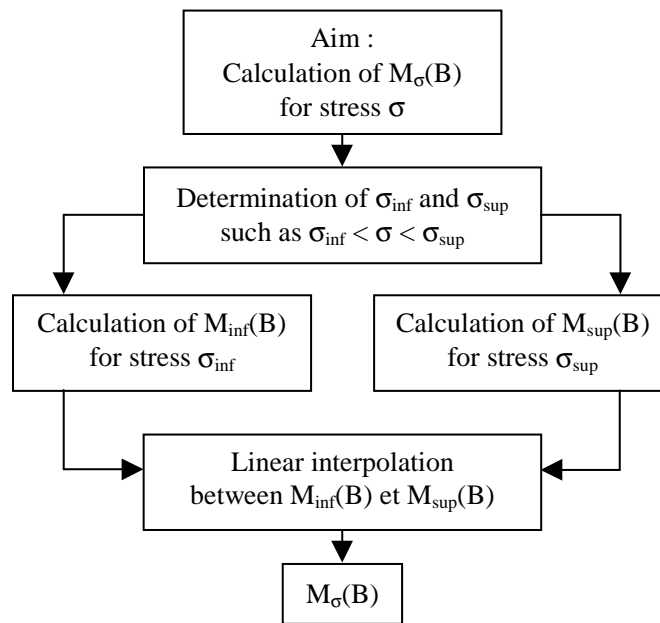


Figure 3.5: Diagram of the procedure for calculating the magnetisation.

Identification

For the identification of the model, the experiments require a specific device suitable to apply a magnetic field as well as a mechanical stress. This device, developed at the Ghent University, is derived from a small single-sheet tester, around which a mechanical yoke is constructed [50].

In Figure 3.6, the influence of the stress on the magnetic behaviour is illustrated. In the particular case of the studied sample, an improvement of the magnetic properties is observed under applied stress for $B_{max} = 0.6T$. In fact, when applying the stress, a narrower hysteresis loop and a reduction of the maximum magnetic field value for the same maximum magnetic induction value is observed.

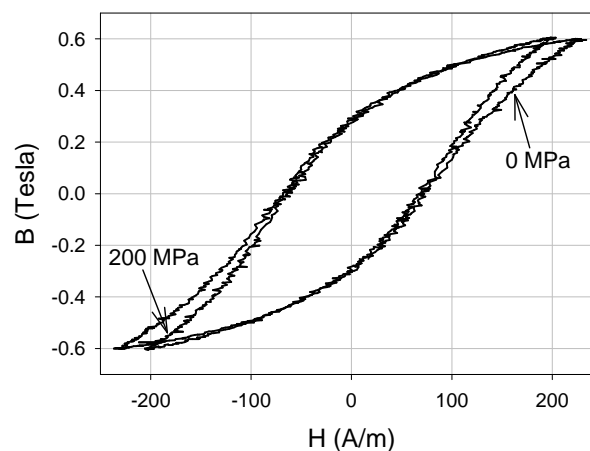


Figure 3.6: Hysteresis loops when applying stress to the sample sheet.

Testing of the model

To illustrate the proposed approach, a simple system is considered. A steel sheet sample (see figure 3.7), with variable width, has been considered in order to obtain non-uniform stress and magnetic induction. The lower left corner of the sample is fixed and the displacement in y -direction in the lower right corner is set to zero as well. A uniform tensile stress of $100MPa$ in x -direction is applied to the right edge. From a 2D Finite Element plane-stress model, with constant elasticity modulus E and Poisson coefficient ϵ , the tensile stress in x -direction is calculated. This stress, varying between 70 and $190MPa$, is depicted in figure 3.8.

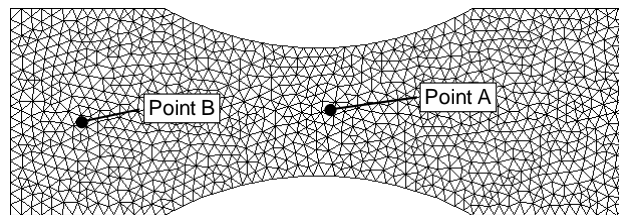


Figure 3.7: Steel sample model and Finite Element discretization.

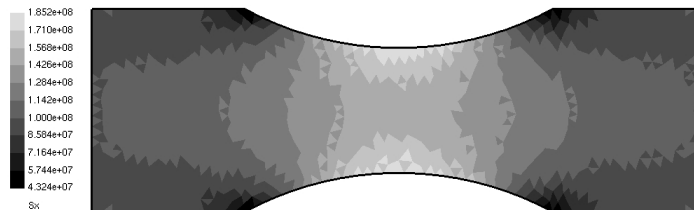


Figure 3.8: Calculated tensile stress in x -direction.

Keeping the same mesh, the magnetic equations are solved separately with a FE calculation based on the formulation presented in section 3.1.3.1. The magnetic flux is straightforwardly imposed through the sample in the x -direction by means of Dirichlet boundary conditions on the lower and upper edges of the sample. In this example, it is assumed that the magnetic behaviour of the steel sheet is only influenced by the uni-axial stress along the x -direction. This is verified by the stress along the y -direction is always, at least, 10 times lower than that along the x -direction. To illustrate the impact of the tensile stress on the calculated magnetic behaviour, two elements, denoted by A and B in figure 3.7, are considered. In figure 3.9, the hysteresis loops obtained at points A and B are given.

One can note that, when the steel sheet is under stress, the magnetic behaviour is improved as previously indicated.

3.2.3 Jiles-Atherton model

3.2.3.1 Expression of the static model

The original Jiles-Atherton (J-A) model presented in [41] gives the magnetization M versus the external magnetic field H . This model is based on the magnetic material

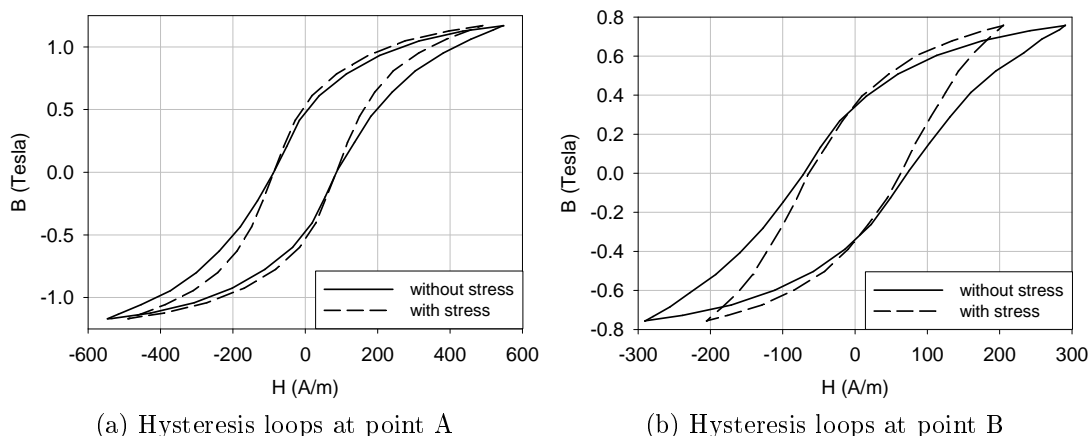


Figure 3.9: Comparison of the hysteresis loops at points A and B with and without tensile stress impact consideration

response without hysteresis losses, that is to say the anhysteretic curve $M_{an}(H)$ that can be described by the Langevin expression (1.13) introduced in chapter 1. The quantity $H_e = H + \alpha M$ is defined as the effective field experienced by the magnetic domains, with H the external applied magnetic field and α the mean field parameter representing the inter-domain coupling:

$$M_{an}(H) = M_{sat} \left[\coth \left(\frac{H_e}{a} \right) - \left(\frac{a}{H_e} \right) \right] \quad (3.37)$$

This anhysteretic magnetization represents the effects of moment rotation within domains but does not take into account the losses induced by domain wall motions. Then, by considering rigid and planar domain walls, the energy dissipated through pinning sites during a domain wall displacement is calculated [41]. The expression of the magnetization energy is obtained under the assumption of a uniform distribution of pinning sites. The magnetization energy is assumed to be the difference between the energy which would be obtained in the anhysteretic case minus the energy due to the losses induced by domain wall motions. Consequently, after some algebraic operations, the differential susceptibility of the irreversible magnetization M_{irr} can be written as:

$$\frac{dM_{irr}}{dH_e} = \frac{(M_{an} - M_{irr})}{k\delta} \quad (3.38)$$

where the constant k is linked to the average pinning site energy. The parameter δ takes the value $+1$ when $\frac{dH}{dt} > 0$ and -1 when $\frac{dH}{dt} < 0$ with respect to the force which opposes variations of the magnetization. However, during the magnetization process, domain walls do not only jump from one pinning site to another: to a certain extent, they can be seen as flexible and can bend when being held on pinning sites. In that context, the domain wall bending is associated to reversible changes in the magnetization process. Then, by some physical energy assumptions on the domain wall bending, the obtained reversible magnetization is linearly dependent on $M_{an} - M_{irr}$ [41].

$$M_{rev} = c(M_{an} - M_{irr}) \quad (3.39)$$

where the reversibility coefficient c belongs to the interval $[0, 1]$. Assuming that the total magnetization is the sum of the reversible and irreversible components, we have the following expression:

$$M = M_{rev} + M_{irr} \quad (3.40)$$

with M_{irr} and M_{rev} defined by (3.38) and (3.39). Using (3.40) and (3.39) we can write:

$$M = M_{irr} + c(M_{an} - M_{irr}) \quad (3.41)$$

Then, by differentiating this equation with respect to H , the total differential susceptibility of the system is given by the following expression which has already been presented in [41]:

$$\frac{dM}{dH} = \frac{(1 - c)\frac{dM_{irr}}{dH_e} + c\frac{dM_{an}}{dH_e}}{1 - \alpha c\frac{dM_{an}}{dH_e} - \alpha(1 - c)\frac{dM_{irr}}{dH_e}} \quad (3.42)$$

This differential equation represents the model that gives the magnetization as a function of the magnetic field H , where M_{an} is given by (3.37). The model can also be adapted with the magnetic flux density B as input [51]. As for the previous model, and using the fact that $B_e = \mu_0 H_e$, equation (3.41) is differentiated with respect to B :

$$\frac{dM}{dB} = \frac{(1 - c)\frac{dM_{irr}}{dB_e} + c\frac{dM_{an}}{dB_e}}{1 + \mu_0(1 - c)(1 - \alpha)\frac{dM_{irr}}{dB_e} + \mu_0 c(1 - \alpha)\frac{dM_{an}}{dB_e}} \quad (3.43)$$

In both cases, five parameters α, a, k, c and M_s have to be determined from experimental results. It is important to notice that the J-A parameters are theoretically the same whether B or H is the input of the model. At the opposite, the Preisach model requires the determination of two independent functions $E(H_m, H)$ and $E(B_m, B)$. The physical meaning of the five parameters are presented in Table 3.1.

Table 3.1: Physical properties of model parameters α, a, k, c, M_s .

Parameter	Physical property
α	Linked to domain interaction
a	Shape parameter for M_{an}
k	Linked to hysteresis losses
c	Reversibility coefficient
M_{sat}	Saturation magnetization

3.2.3.2 Parameter identification

An identification procedure from experimental data has been described in [52]. After mathematical developments using equations (3.37), (3.38) and (3.41) for some specific points of the hysteresis loop, the implicit expressions of the five parameters are obtained. These depend on measured data which are:

- H_c and M_r the coercive magnetic field and the remnant magnetization,
- M_{sat} the saturation magnetization,
- χ'_{ini} and χ'_{an} the normal and the anhysteretic differential susceptibilities,
- χ'_c and χ'_r the coercive and remnant differential susceptibilities.

Determination of parameters c, a, k and α requires an iterative procedure presented in [52]. This method is numerically sensitive and does not systematically converge. A slightly different procedure can be used: first an objective function F_{obj} is defined such as:

$$F_{obj} = \int_0^T [M_{exp}(t) - M_{J-A}(t)]^2 . dt \quad (3.44)$$

where $M_{exp}(t)$ is the experimental magnetization and $M_{J-A}(t)$ the calculated one, obtained with the same periodic excitation field $H(t)$ with a period T . The data $(H(t), M_{exp}(t))$ corresponds to the major hysteresis loop. The following procedure is used to calculate the five parameters.

1. systematic choice of α_i in the interval $[\alpha_{min} , \alpha_{max}]$ by steps $\Delta\alpha$,
2. calculation of a_i, c_i, k_i from experimental data $(H_c, M_r, M_{sat}, \chi'_{ini}, \dots)$,
3. calculation of the objective function F_{obj}^i ,
4. back to **1.** until $\alpha_i = \alpha_{max}$,
5. determination of $(\alpha_j, a_j, c_j, k_j)$ using $F_{obj}^j = \min(F_{obj}^i)$

The choice of the interval $[\alpha_{min} , \alpha_{max}]$ depends on the materials. But, it can be chosen sufficiently large because this procedure is relatively fast. This first algorithm gives a good estimation of the parameter values but these can be still improved. In a second step, an optimisation procedure can be applied to minimize the objective function F_{obj} by modifying independently the five parameters without any constraint. The minimization is carried out considering a set of centred hysteresis loops and not only the major hysteresis loop. Numerical tests have shown that the second step does not lead always to good results without the first step. In fact, this latter enables us to have a set of parameters close to the best solution (in the sense of the chosen objective function) which makes easier the convergence of the optimization procedure.

3.2.3.3 Time dependent extension of the model

Energy balance

D.C. Jiles has proposed an extension of the $M(H)$ J-A static hysteresis model to take into account the dynamical contributions when the skin effect is higher than the lamination thickness [53]. The obtained model requires the calculation of a 4th order polynomial equation with variable $(dM/dH)^{\frac{1}{2}}$.

We propose to rewrite this time dependent model with B as the input variable [54] for an adapted FE implementation in the magnetic vector potential formulation. Starting from the same assumptions, the energy balance is written by adding both dynamical contributions (eddy current and excess losses) to the static energy balance. In the case of a uniform penetration of the field in the material, the instantaneous eddy current power loss contribution can be written as the time derivative of the associated energy dissipation W_{EC} :

$$\frac{dW_{EC}}{dt} = \frac{d^2}{2\rho\beta} \left(\frac{dB}{dt} \right)^2 \quad (3.45)$$

where ρ is the electrical resistivity of the material, d and β are parameters linked to the geometry of the sample [53]. In the case of a steel sheet with a thickness e , these parameters are such that $d = e$ and $\beta = 6$.

For the second contribution, it is assumed that the energy associated to the excess losses is given by the expression proposed by G. Bertotti [6] and used by D.C. Jiles in [53]:

$$\frac{dW_{EXC}}{dt} = \left(\frac{GdwH_0}{\rho} \right)^{\frac{1}{2}} \left(\frac{dB}{dt} \right)^{\frac{3}{2}} \quad (3.46)$$

where w is the steel sheet width. The other parameters are G , a dimensionless constant ($G = 0.1356$), and H_0 a parameter linked to the internal potential experienced by domain walls [53].

The energy balance of the static hysteresis model is given by:

$$\mu_0 \int M_{an} dH_e = \mu_0 \int M dH_e + \mu_0 k \delta \int \frac{dM}{dH_e} dH_e - \mu_0 k \delta c \int \frac{dM_{an}}{dH_e} dH_e \quad (3.47)$$

where $H_e = H + \alpha M$ is the effective field experienced by the domain wall [41]. Then, by adding the contribution of the eddy current (3.45) and excess losses (3.46), the new energy balance becomes:

$$\begin{aligned} \mu_0 \int M_{an} dH_e = & \mu_0 \int M dH_e + \mu_0 k \delta \int \frac{dM}{dH_e} dH_e - \mu_0 k \delta c \int \frac{dM_{an}}{dH_e} dH_e \\ & + \int \frac{d^2}{2\rho\beta} \left(\frac{dB}{dt} \right)^2 dt + \int \left(\frac{GdwH_0}{\rho} \right)^{\frac{1}{2}} \left(\frac{dB}{dt} \right)^{\frac{3}{2}} dt \end{aligned} \quad (3.48)$$

Moreover, using the fact that:

$$\begin{aligned}\left(\frac{dB}{dt}\right)^2 dt &= \left(\frac{dB}{dt}\right) \left(\frac{dB}{dH_e}\right) dH_e \\ \left(\frac{dB}{dt}\right)^{\frac{3}{2}} dt &= \left(\frac{dB}{dt}\right)^{\frac{1}{2}} \left(\frac{dB}{dH_e}\right) dH_e\end{aligned}$$

and by differentiating versus H_e and multiplying by (dH_e/dB) , the following expression is obtained:

$$\begin{aligned}\mu_0 M_{an} \left(\frac{dH_e}{dB}\right) &= \mu_0 M \left(\frac{dH_e}{dB}\right) + \mu_0 k \delta \frac{dM}{dB} - \mu_0 k \delta c \left(\frac{dM_{an}}{dH_e}\right) \left(\frac{dH_e}{dB}\right) \\ &\quad + \left(\frac{d^2}{2\rho\beta}\right) \left(\frac{dB}{dt}\right) + \left(\frac{GdwH_0}{\rho}\right)^{\frac{1}{2}} \left(\frac{dB}{dt}\right)^{\frac{1}{2}}\end{aligned}\quad (3.49)$$

Using $H_e = H + \alpha M$ and $B = \mu_0(H + M)$, we have $B = \mu_0[(H_e - \alpha M) + M]$ and consequently:

$$\frac{dH_e}{dB} = \frac{1}{\mu_0} + (\alpha - 1) \frac{dM}{dB}\quad (3.50)$$

The expression (3.49), after some algebraic re-arrangement of terms (dM/dB) , becomes:

$$\begin{aligned}\frac{dM}{dB} \left[\mu_0(\alpha - 1) \left(M - k\delta c \frac{dM_{an}}{dH_e} - M_{an} \right) + \mu_0 k \delta \right] &+ \left(M - M_{an} - k\delta c \frac{dM_{an}}{dH_e} \right) \\ &+ D_1 \left(\frac{dB}{dt}\right) + D_2 \left(\frac{dB}{dt}\right)^{\frac{1}{2}} = 0\end{aligned}\quad (3.51)$$

with D_1 and D_2 two parameters which can be expressed from physical properties of the material:

$$D_1 = \left(\frac{d^2}{2\rho\beta}\right) \text{ and } D_2 = \left(\frac{GdwH_0}{\rho}\right)^{\frac{1}{2}}\quad (3.52)$$

The five parameters α , a , k , c and M_{sat} are the same as in the static model. The differential equation (3.51) is solved using the implicit Euler scheme.

Testing of the model

The model is tested on a 3%FeSi lamination with thickness 0.5mm. Parameters α , a , k , c and M_{sat} are identified from major loops at low frequency (0.5 Hz) [47]. Parameters D_1 and D_2 , related to the dynamic effects, are calculated from an optimization procedure using several hysteresis loops for different magnitudes of excitation and different frequencies. The presented experimental results are obtained under sinusoidal excitations. In Figure 3.10 some experimental loops are compared with calculated loops for different frequencies and for a magnetic flux density $B_m = 1.2T$.

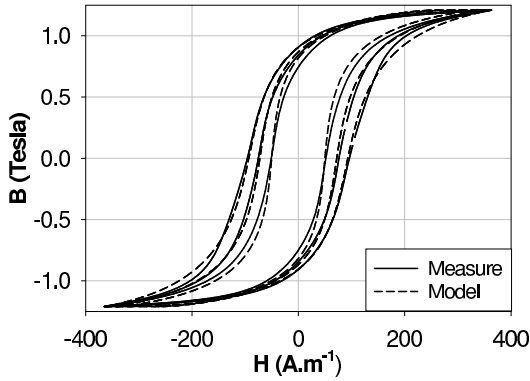


Figure 3.10: Measurements (solid lines) and prediction of the model (dashed lines) at frequencies 1, 50 and 100 Hz.

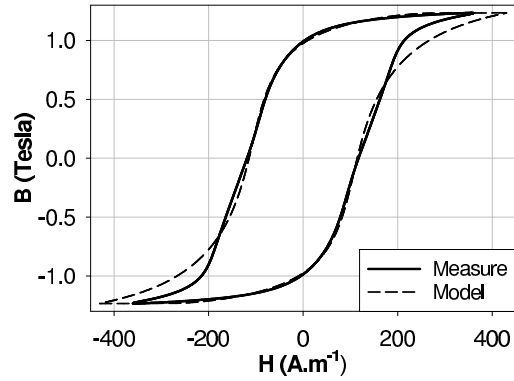


Figure 3.11: Measurement (solid line) and prediction of the model (dashed line) at frequency 200 Hz.

Considering the assumptions of the model, results are satisfactory below 200 Hz. Above this frequency, the gap between the experiment and simulation becomes significant (figure 3.11). In fact, above 200 Hz, due to the skin effect, the magnetic field can not be considered uniform in the steel sheet section.

Table 3.2: Comparison between calculated and measured hysteresis losses under sinusoidal excitation for $B_m = 1.2$ Tesla.

Frequency (Hz)	1	50	100	200
Measured losses (W/kg)	3.27×10^{-2}	2.25	5.66	14.2
Calculated losses (W/kg)	3.29×10^{-2}	2.24	5.64	15.5

The evaluation of the global losses from the model is also satisfactory (Table 3.2) in the case of sinusoidal excitation for frequencies lower than 200 Hz. This kind of model is well adapted for field calculation to study devices supplied under industrial frequencies (0-60 Hz).

3.2.3.4 About minor loops in the J-A model

Although the original J-A model is able to represent a wide range of major hysteresis loops, in particular those of soft magnetic materials, it can produce non-physical minor loops. This is inherent to the model construction that does not account for the magnetic memory property like the Preisach model does. Therefore, several works in the literature were proposed to overcome this issue [55–57]. But the proposed techniques are either quite inapplicable in finite elements procedures, such as the technique in [55] where the event of a minor loop must be known *a priori*, or either complexify the original model by additional identification procedures, such as in [56] where scaling factors are added in the main equation of the model or in [57] where different parameter sets must be identified to represent the major and minor loops.

A simpler modification is proposed here to improve the minor loop representation by adding a single parameter in the model [58]. The methodology consists in limiting the variation rate of the magnetization by introducing an additional dissipative factor R into the model equations. This dissipative factor is associated to the irreversible magnetization in order to limit its variation rate. In practice, this dissipative factor allows to limit the transient state, bringing the total magnetization to its stable trajectory more quickly. For the model $M(B)$, the irreversible contribution is modified such as:

$$\frac{dM_{irr}}{dB_e} = \frac{(M_{an} - RM_{irr})}{\mu_0 k \delta} \quad (3.53)$$

This additional parameter can be identified from an experimental set of centred loops and is dependent on the level of the magnetic flux density where the turning points occur. During the use of the model, the parameter R can be then correctly adapted by monitoring, for example, the parameter δ in the J-A model. The five other parameters remain unchanged.

An illustration of the proposed modification, where the original model behaviour is given in figure 3.12 and the modified one is illustrated in figure 3.13.

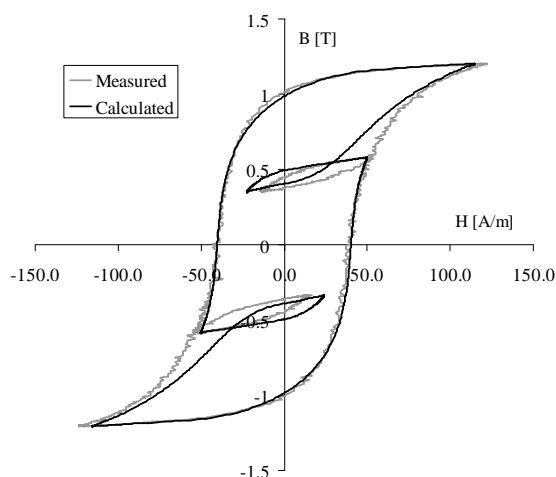


Figure 3.12: Asymmetric minor loops in the original J-A model

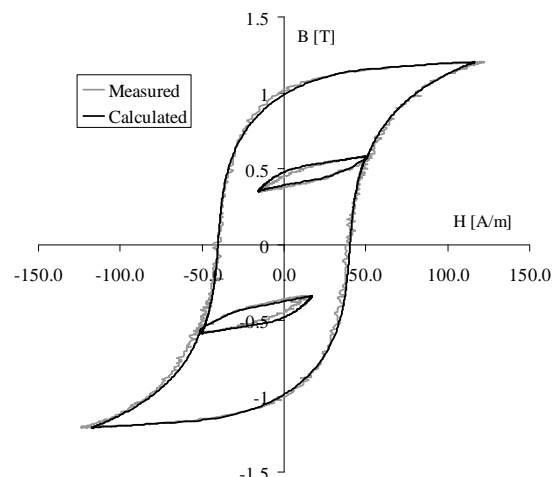


Figure 3.13: Asymmetric minor loops in the modified J-A model

The Preisach and Jiles-Atherton hysteresis models have been implemented in the FE method with the numerical schemes presented in section 3.1.3. To illustrate the contribution of the hysteresis phenomenon during the numerical resolution of a physical problem, different studies of electromagnetic devices will be detailed in the next chapter in sections 4.1.1, 4.2.1 and 4.2.2.

3.2.4 Magnetization loss model for permanent magnets

As mentioned in section 1.5.2 of chapter 1, PMs can be subjected to magnetization loss due to operating constraints in electrical devices. The design of such devices requires

then a model of PM able to account for an eventual magnetization loss due to temperature and/or demagnetizing field. Such model is proposed in the following along with its implementation in the FE method.

3.2.4.1 Problematic

The electrical conductivity of PMs is moderate but modern applications require variable speed drives that are mostly based on power electronics converters. In that context, the eddy current losses in PMS, due to space and time harmonics, cannot be neglected [21]. As previously mentioned in section 2.2.4, these losses may cause a significant heating of the PM and lead to an irreversible demagnetization, especially in the case of *NdFeB* magnets, which have high temperature coefficients of remnant magnetic flux density and coercive field [22]. Therefore, it is necessary to use an accurate description of the magnetic behaviour law of the PM in order to predict any demagnetization that will impact their performances.

In the context of the FE modelling approach, the magnetic operating conditions of electrical devices can be obtained with accuracy. For the PMs, these conditions are directly linked to the electrical device structure and supply characteristics. When designing, for example, a high performance permanent magnet synchronous machine, with rare earth PMs, the demagnetizing field and the operating temperature are critical parameters in the design process. Indeed, as illustrated in the example of section 2.2.4, if high temperature conditions are combined with a large demagnetizing field, full demagnetization can occur.

Different works have been carried out for the investigation of eddy current losses in PMs, by analytical or FE methods [21, 22]. To predict magnetization loss, due to the temperature, different techniques have been discussed in the literature. Zhou *et al.* [59] presented a linearised demagnetization model of the PM that takes into account the temperature and the associated demagnetization effects. Ruoho *et al.* [60] proposed a non-linear PM exponent function model to highlight the effects of PM magnetization loss under the effect of temperature derived from a simple network thermal resistances. Other works have been interested in implementing hysteresis models, as proposed by Xie *et al.* [61], to describe the behaviour of PMs in electrical machines. Such approach is of interest if the PM behaviour law exhibits minor loops in the recoil curves that lead to additional losses. Nevertheless, the non-linear numerical scheme used to solve the FEM problem must be robust when hysteresis is considered.

The non-linear model of the partial magnetization loss in *NdFeB* magnets presented in the following has been developed and implemented in the FEM. The model takes into account the heating of PMs induced by the eddy current losses and require to solve a coupled magneto-thermal problem.

3.2.4.2 Permanent magnet model

Magnetization loss model

The demagnetization $B-H$ curves of a PM for two temperatures are shown in figure 3.14. The initial magnetic state of the PM is given by the intersection of the load line L and the initial temperature demagnetization curve (curve 1 at T_1). For this temperature, the

operating point is given by the point A. For a temperature $T_2 > T_1$, as already mentioned in section 1.5.2 of chapter 1, the remnant magnetic flux density B_r and the coercive field H_c shift towards the origin. For a sufficiently high temperature, the demagnetization curve presents a knee point in the second quadrant of the $B - H$ plane (point K in figure 3.14).

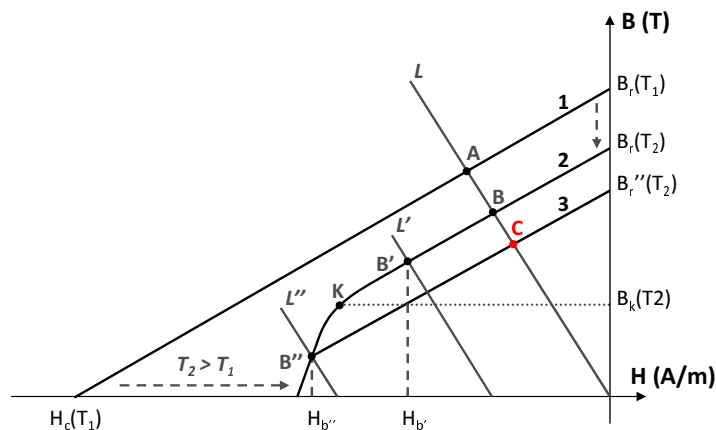


Figure 3.14: Model of the magnetization loss process in a permanent magnet.

The demagnetization process can be separated into two distinct contributions:

- a reversible part (above the knee point K) where the applied demagnetization field lead to the operating point of the magnet defined by B' (intersection of the load line L' and the demagnetization curve 2). If the demagnetization field is reduced to zero the operating point of the magnet will return to the operating point B .
- an irreversible part (below the knee point K) where the applied demagnetization field lead to the operating point of the magnet given by B'' (intersection of the load line L'' and the curve 2). If the demagnetization field is decreased to zero, the operating point of the magnet is now C . This point is determined by the intersection of the original load line L and the recoil curve 3 of the PM [62].

In this model, the partial and irreversible magnetization loss of the magnet occurs when the operating point goes below the knee of the $B - H$ curve. It is also assumed that the recoil curve has the same slope as the reversible region of the PM.

Behaviour model

The proposed PM behaviour model is based on the expression (3.31), originally used for the approximation of the anhysteretic behaviour law in soft magnetic materials as mentioned in section 3.2.1. The modified expression (3.54) is used for identifying the demagnetization curves of the PM [63].

$$H = \frac{B}{\mu_0} \left[\frac{B^{2\alpha}}{B^{2\alpha} + \tau} (c - \epsilon) + \epsilon \right] - H_c \quad (3.54)$$

In this expression, α , ϵ , τ and c are parameters that have to be determined by a fitting procedure with the experimental data. The remnant magnetic flux density B_r is numerically identified when the magnetic field H is zero.

Fitting procedures with experimental data have shown that, on the one hand, the parameter α and the coercive field H_c are temperature dependent following a polynomial function of the third order. On the other hand, parameters c , τ and the remnant magnetic flux density B_r depend on the magnetic flux density B_k that corresponds to the knee point K (see figure 3.14). This dependency is described by the function $g(B_k(T))$ given in equation (3.55), where $B_k(T)$ is linearly dependent on the temperature. One must note that the parameter ϵ remains constant.

$$g(B_k(T)) = b_0 + b_1 B_k(T) + b_2 B_k^2(T) + b_3 B_k^3(T) \quad (3.55)$$

Therefore, when a PM is subjected to a demagnetizing field, the calculation procedure consists in checking if the operating point is below the knee for a given temperature. If so, a recoil line is generated according to the parameter identification of expression (3.54), to replace the original demagnetization curve. An example of the measured and identified demagnetization curves for a *NdFeB* magnet is illustrated in figure 3.15.

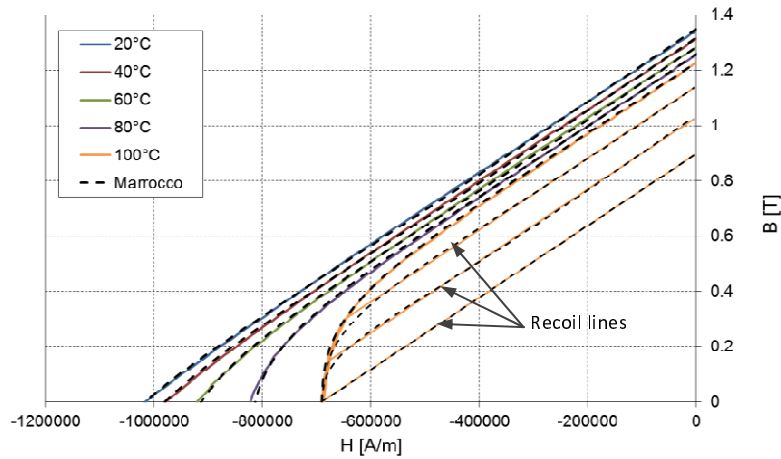


Figure 3.15: Fitting of expression (3.54) with the measured data for a *NdFeB* magnet.

Numerical testing of the model

To investigate the demagnetization loss of PMs under the influence of various demagnetization effects (geometry, demagnetization field, temperature), a FE magneto-thermal procedure is adopted according to figure 3.16. The coupling of the magnetic and thermal problem is realized by a weak coupling, i.e. both problems are independently and iteratively solved. From an initial electromagnetic FE model calculus, the eddy current losses P_{EC} and copper losses P_{Cu} are inserted in the FE thermal model to calculate the temperature distribution.

Next, the demagnetization curves associated to each element of the magnet are deduced from the temperature map in the magnet and inserted in the electromagnetic model

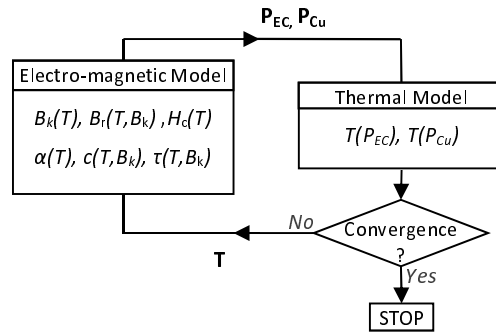


Figure 3.16: Magneto-thermal sequence.

that is solved again in order to obtain the new state of the magnet. This sequence is repeated until no temperature variation is observed between two consecutive sequences.

Testing of the model

The model has been implemented in the FEM for both the electric and magnetic formulations and tested for the device presented in section 2.2.4. The PM with the characteristics presented in figure 3.15 is considered in the simulation with an air-gap set to $5mm$. Each coil was fed by a $3.5A$ current at $400Hz$. In figure 3.17, the eddy current density in the PM as well as the steady state temperature and remnant magnetic induction are shown for both formulations.

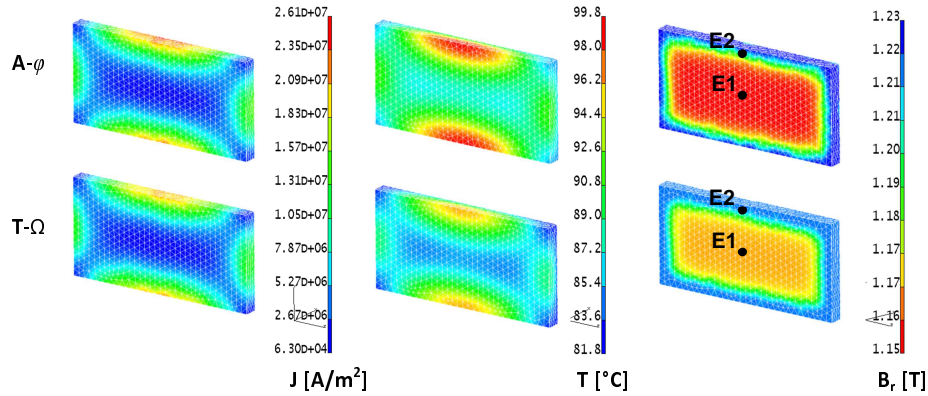


Figure 3.17: From left to right: eddy current density, temperature and remnant magnetic induction.

One can note that, despite a higher temperature on its periphery, the PM suffers from magnetization loss mainly in the centre. This aspect will be further discussed in the next Chapter, section 4.2.3, where the experimental aspect is presented.

3.3 Iron loss models

Accounting for the iron losses in electrical machines is a crucial step during the design process. This can be achieved by accounting, in the numerical model, for the magnetic

hysteresis and other energy dissipation processes, such as macroscopic eddy currents, during the energy conversion. Different approaches have been proposed in the literature for the numerical implementation of the hysteresis behaviour in FE analysis [34, 36, 37]. Simulation results are often obtained for simple devices, generally in the bi-dimensional approach. Even in these cases, the numerical convergence is not always verified and the generalization of these approaches must still be verified.

From a practical point of view, electrical machine designers need to estimate the iron losses within an acceptable interval of uncertainty and, most importantly when optimization procedures are involved, the computation time must remain acceptable. That is why, loss calculation procedures *a posteriori* to the FE calculation are also employed. One very effective approach is the Loss Surface Model [64] where the magnetic field H is determined, from the experiment, as a surface response depending on the level of the magnetic flux density and its rate of change. Other analytical models, derived from the models of Steinmetz [65], Jordan [66] (separation of hysteresis and classical eddy current losses) and Pry&Bean [67] (introduction of the excess losses). Most of the used analytical models are based on Bertotti's loss separation approach [68, 69] and the model of Fiorillo&Novikov [70]. However, these approaches lie on the essential hypothesis that the energy dissipation has a negligible impact on the electromagnetic field distribution in the electrical machine and, consequently, on its operating conditions.

Three categories of the iron loss models can be then considered:

- hysteresis models included in the FE models,
- experimental surface mapping of the losses and post-processing calculation,
- analytical expressions and post-processing calculation.

The analytical approach is one of the most employed as it allows:

- the use of only the anhysteretic curve in the FE calculation (fast and proved robustness of the numerical calculation),
- an easy and fast identification procedure of the model parameters (limited amount of experimental data),
- the ease of a post-processing implementation.

Nevertheless, some drawbacks must be kept in mind:

- during the resolution of the FE problem, the frequency effects (skin effect for instance) are not taken into account in the laminations. The magnetic fields used in post-processing suffer then from some modelling errors.
- the single-valued behaviour law (anhysteretic) is intrinsically without energy dissipation and the impact on the magnetic field distribution is not accounted for.

- the non-centred minor loops are not correctly accounted for with an anhysteretic behaviour law (the incremental permeability is different from the differential one). In this case, the post-processing must be performed with precaution.

These drawbacks, lead to the development of hybrid approaches [71]. The static hysteresis phenomenon is accounted for during the FE resolution and other dissipation processes (classical eddy current and excess losses) are calculated in the post-processing. Note that, as mentioned previously, the implementation of the hysteresis in the FE requires a robust numerical scheme, especially in 3D FE, to assure the convergence. Besides, the hysteresis model must also be sufficiently accurate to represent the behaviour of non-centred minor loops.

As presented in section 1.5.1, the classical approach consists in considering three contribution to the total losses: the *hysteresis*, *classical* (eddy currents) and *excess* losses.

Hysteresis losses

As mentioned in section 1.5.1.1, the hysteresis (or static) losses are associated to the Bloch wall motion, a process that is mainly irreversible with a lag between the magnetic field H and the magnetic induction B . The surface area of the hysteresis loop is associated to the energy dissipation per unit volume for one period of the alternating field. The total power loss per unit volume is calculated from equation (1.29). Moreover, when harmonics are involved in the excitation field, non-centred minor loops can appear with the main centred loop, as illustrated in figure 3.18. These non-centred minor loops lead to additional losses, also associated to their surface area.

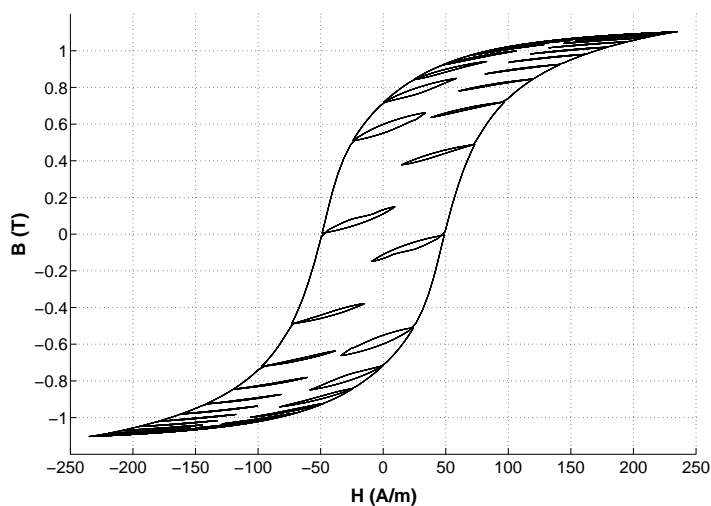


Figure 3.18: Main hysteresis loop including non-centred minor loops.

These losses can be obtained from a hysteresis model, such as the ones presented in section 3.2, or from analytical expressions.

Classical eddy current losses

Considering an infinite lamination of thickness d , and of electrical conductivity σ , submitted to a sinusoidal magnetic induction with period T , the classical eddy current losses (W/m^3) are given by:

$$P_{cl} = \frac{\sigma d^2}{12} \frac{1}{T} \int_0^T \left(\frac{dB(t)}{dt} \right)^2 dt \quad (3.56)$$

Excess losses

This losses have been described by G. Bertotti [6] as the interaction of domain walls that lead to localized eddy currents in the vicinity of the domain walls. This phenomenon can be considered homogeneous over the material volume and is strongly dependent on the frequency of the excitation field. Fiorillo&Novikov have shown [70] that the average excess losses (W/m^3) for a lamination can be expressed as:

$$P_{exc} = \sqrt{\sigma G V_0 S} \frac{1}{T} \int_0^T \left| \frac{dB(t)}{dt} \right|^{1.5} dt \quad (3.57)$$

where G is a friction coefficient between the magnetic domain, V_0 is a parameter characterizing the statistical distribution of the local coercive field and S is the cross section of the laminated material.

Rotational losses

In electrical device, especially when multiple phase excitation fields are involved, the resulting magnetic field is not always uni-directional, that is to say alternating along the same direction. For instance, in the stator yokes of electrical machines and T-joint of transformers, the combination of three-phase excitation fields lead to localized rotating magnetic induction. In general, in these regions, the tip of the magnetic induction describes a more or less ellipsoidal shape and even circular. In practice, it is observed that the losses associated to this behaviour, named *rotational losses*, are much more greater than the alternating ones for the same magnitude of the magnetic induction. In figure 3.19, an illustration of such behaviour is given.

The particular behaviour of the rotational losses when reaching the saturation of the material can be explained by the fact that, at low magnitudes of magnetic flux density, the losses are the consequence of domain wall motion. At higher magnitudes of the magnetic flux density, there are less domain walls, leading then to a drop of the associated losses. There remain only the losses associated to the eddy currents.

In the quasi-static case, if we consider a rotating magnetic field \mathbf{H} of constant magnitude, the associated rotational losses can be written [72]:

$$P_{rot} = \frac{1}{T} \int_0^T |\mathbf{H}| \cdot |\mathbf{B}| \sin \delta d\theta \quad (3.58)$$

where δ is the phase lag between \mathbf{B} and \mathbf{H} , θ is the angle between \mathbf{H} and a reference direction.

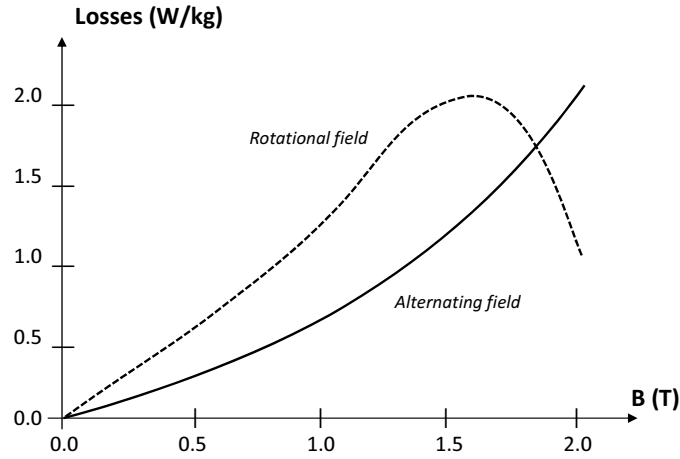


Figure 3.19: Illustration of rotational and alternating losses.

In practice, for low magnetic fields and non-oriented grain laminations, the rotational losses are usually about twice the ones observed under alternating field [72, 73]. That is why, under these conditions, the rotating losses can be assimilated to the sum of the losses obtained from the two directions (minor and major) corresponding to the general case of an ellipsoidal loci of the magnetic induction. When reaching higher values of the magnetic induction, the rotational losses must be corrected by a factor accounting for the behaviour observed in figure 3.19.

3.3.1 Analytical loss models

In a general way, from the expressions of the different loss contributions (1.29), (3.57), (3.56), and considering that the hysteresis losses depend only on the extrema of the magnetic field and follow a power law of the magnetic flux induction, the total power loss can be written:

$$P_{tot} = k_h f B_m^\alpha + \frac{k_{cl}}{2\pi^2 T} \int_0^T \left(\frac{dB(t)}{dt} \right)^2 dt + \frac{k_{exc}}{8.764 T} \int_0^T \left| \frac{dB(t)}{dt} \right|^{1.5} dt \quad (3.59)$$

where k_h , k_{cl} and k_{exc} are coefficients associated to the physical characteristics of the material. The previous expression is valid under a certain number of conditions, especially for symmetric excitation fields and negligible skin effect. Moreover, in saturated operating conditions, the losses are not always well represented by this expression. Several works exist in the literature on how to improve this expression [74, 75], either empirically or from physical considerations.

To identify the parameters involved in expression (3.59), it is interesting to see that under an alternating sinusoidal magnetic induction, the total power loss can be expressed as a function of the peak magnetic flux density B_m :

$$P_{tot} = k_h f B_m^\alpha + k_{cl} f^2 B_m^2 + k_{exc} f^{1.5} B_m^{1.5} \quad (3.60)$$

It is then easy to extract the parameters from measurements obtained with standardized characterization techniques (Epstein frame or single sheet tester). The identification of the parameters is usually performed, in a first step, by the determination of k_h and α from measurements in quasi-static conditions (typically below $1Hz$), where the *dynamic* contributions can be neglected. Then, from experimental data at higher frequencies, the parameters k_{cl} and k_{exc} are determined.

To consider non-symmetric magnetic flux densities (extrema values are not symmetric), the term B_m in the hysteresis loss contribution, can be replaced by $\Delta B/2$ in expressions (3.59) and (3.60). Obviously, it is not physically correct but it aims at reducing, to a certain extent, the error for the hysteresis loss calculation.

3.3.2 Minor loops surface response model⁹

When non-centred minor loops are involved in the excitation field, such as in the case of a Pulsed Width Modulation (PWM) supply, post-processing approaches usually consider the decomposition of the excitation field to extract the minor loops and their associated losses. A commonly used approach is the one proposed by J. Lavers *et al.* [76]:

$$P_{tot} = k_h f B_m^\alpha \left(1 + \frac{c}{B_m} \sum_{i=1}^n \Delta B_i \right) \quad (3.61)$$

where c is a parameter that must be identified from the experiment and ΔB_i is the reversal in the magnetic induction, in the positive half cycle of the waveform, of the i^{th} non-centred minor loop. In its work, J. Lavers found that, for a broad range of materials, the parameter c takes values between 0.6 and 0.7. The use of a constant parameter, typically $c = 0.6$, relies on the fact that the losses associated to a non-centred minor loop, with a given ΔB , remain the same whatever the location of this minor loop on the major loop. This is not always verified, as in the region of the major hysteresis loop where the slope changes drastically and, especially, when the material is highly saturated.

To overcome this limitation, a simple model that takes into account the position and the size of the non-centred minor loops is proposed. It consists in replacing the contribution of the minor-loop losses in (3.61) by a loss function $P(\Delta B, B_{av})$ that depends on the magnitude and offset of the non-centred minor loops:

$$P_{tot} = k_h f B_m^\alpha + f \sum_{i=1}^m P_i(\Delta B_i, B_{av,i}) \quad (3.62)$$

where m is the number of non-centred minor loops in a period and B_{av} the mean value of the minor loop (offset). The loss function $P_i(\Delta B_i, B_{av,i})$ can be determined from the experiment. In the work presented in [77], the author proposed a methodology to measure such loops under PWM and DC bias ripple voltage. Another way, that has been adopted here, is to use a hysteresis model. The Preisach model presented in section 3.2.2.1 has been chosen to illustrate the approach. From a set of centred experimental hysteresis loops, the Everett function is identified following the procedure described in section 3.2.2.2. Then, the asymmetric minor loops generated by this model, as illustrated in figure 3.20, have

⁹The presented results are part of the PhD Thesis of Mircea Fratila.

been validated with the experiment. This validation has been performed for different ΔB and B_{av} of the asymmetric minor loops.

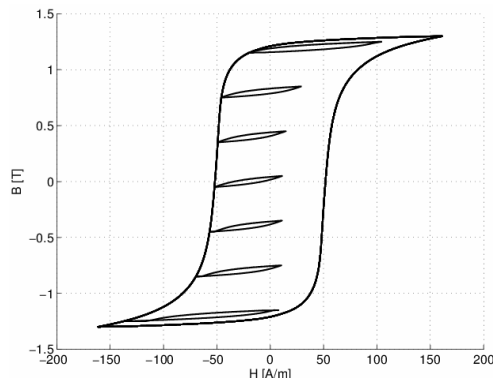


Figure 3.20: Minor loops obtained with the static Preisach model.

Then, from the simulated minor loops, the surface response $P(\Delta B, B_{av})$ is identified and compared with the classical approach proposed by J. Lavers in figure 3.21. It can be seen that the J. Lavers method is globally over-estimating the losses associated to non-centred minor loops, except for the saturation where it under-estimates the losses. Both methods are also compared in the case of an excitation signal including a 11th rank harmonic content with 10% and 20% of the fundamental magnitude. Results are shown in figure 3.22 where the J. Lavers method is always over-estimating the losses when compared to the proposed approach.

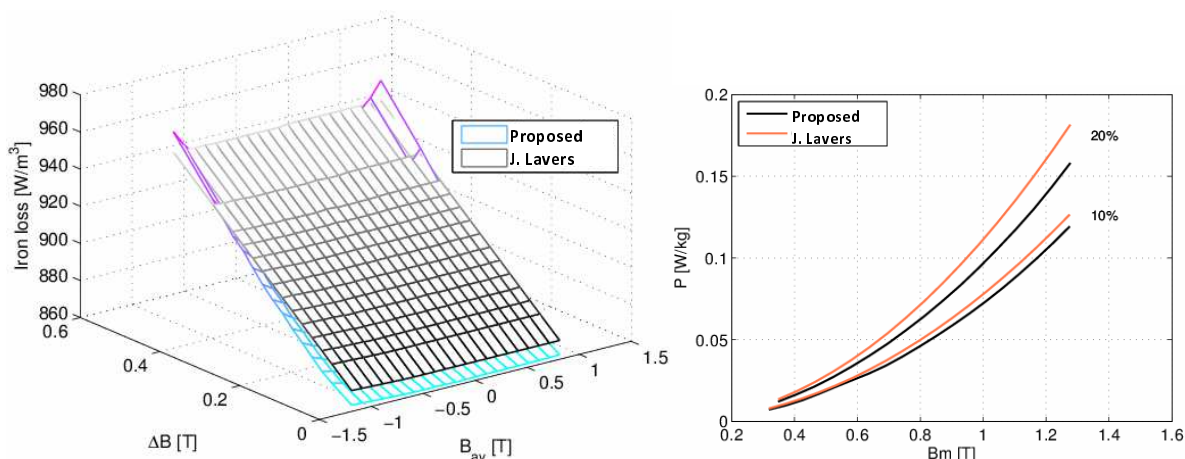


Figure 3.21: Comparison between the proposed model and the one proposed by J. Lavers [76].

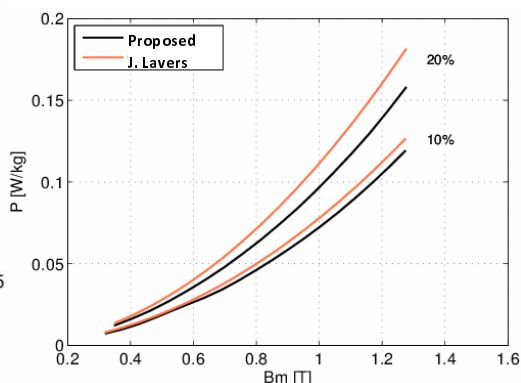


Figure 3.22: Non-centred minor loops losses versus the maximum flux density: excitation field with 10% and 20% of the 11th rank harmonic.

3.4 Probabilistic approach¹⁰

3.4.1 Context and definitions

3.4.1.1 Motivation

To improve the accuracy of electrical devices modelling, a better knowledge and representation of the material properties is required. This is why many research studies are focused on the improvement of iron losses and magnetic behaviour models [78–81]. These models are of interest when the input parameters of the modelling procedure, such as the geometry and material properties, are assumed to be well known. However, this approach can reveal itself insufficient as the manufacturing of an electrical machine, from the cutting of laminations till the final magnetic core shape, requires several industrial processes that might significantly impact the geometry and magnetic properties. Regarding the material properties, these processes may introduce residual stresses that modify the magnetic behaviour and iron losses of the considered material [82–84]. In particular, the magnetic properties of electrical steels are generally modified, either locally or globally. Moreover, for a given set of material samples, the impact of these processes is not necessarily uniform and can lead to a significant variability in the material properties. Most of the works investigate only the relationships between the magnetic properties and mechanical stresses and do not emphasize the variabilities that can be introduced. The work presented in [85], reported that the vector magnetic property of the electrical steel sheet depends on the mechanical stress and the direction of the magnetic field excitation. Moreover, in [86] the authors describe a method for detecting stress on the surface of magnetic materials from Barkhausen emission measurements. These results are interesting as they emphasize the impact of mechanical stress on the local magnetic properties.

Nevertheless, the mechanical stress induced by the manufacturing process is not necessarily well known and not the same for all samples issued from the production chain. This is due, for example, to the wear of the cutting tool or to a deviation with time in the process parameters. Therefore, it is of interest to have a probabilistic approach in order to account for the uncertainties introduced by the manufacturing process on the magnetic behaviour and iron losses.

3.4.1.2 Definitions

Generally speaking, a probabilistic modelling approach aims to investigate uncertainties on the input parameters of a model, and then to study their impact on the output(s) of the model [87–93]. The proposed common scheme for dealing with uncertainties using a probabilistic model relies upon three steps, namely the definition of the mathematical model of the physical system, the probabilistic characterization and modelling of the uncertainties on the model parameters and the propagation of these uncertainties through the model [90]. Note that this kind of modelling approach is similar to those found in the field of fatigue crack growth in mechanical probabilistic modelling [91].

¹⁰The presented results are part of the PhD Thesis of Rindra Ramarotafika.

Choice of the deterministic model

The development of a probabilistic model for a physical behaviour, subjected to uncertainty, requires the knowledge of the behaviour in a deterministic case. First, it is necessary to identify the parameters of such deterministic model. Let us consider n experimental observations $\mathbf{Y} = (y_1, y_2, \dots, y_n)$ at the points $\mathbf{X} = (x_1, x_2, \dots, x_n)$ (these observations can be, for instance, the magnetic flux densities B at different magnetic fields H for a material sample). Among the available models candidates for representing the physical behaviour, and for the set of experimental observations, a given model G can be written $\mathbf{Y} = G(\mathbf{X}, \mathbf{P})$ where $\mathbf{P} = (p_1, p_2, \dots, p_m)$ is the vector of the model parameters. The identification can be carried out by minimizing the objective function based on the least square error calculation:

$$\delta = \sum_{i=1}^n (y_i - G(x_i, \mathbf{P}))^2 \quad (3.63)$$

To test the accuracy of the parameter identification, or to choose among available deterministic models, the coefficient of determination R^2 can be determined:

$$R^2 = 1 - \frac{\delta}{\sum_{i=1}^n (y_i - \bar{y})^2} \quad (3.64)$$

where \bar{y} is the mean of the experimental observations. An ideal model that matches perfectly the measurement would give a coefficient equal to 1. In practice, this coefficient increases with the increase of the number of parameters in the model. Moreover, it is also sensitive to outliers in the measurements. Therefore, an adjusted coefficient of determination is also defined in order to account for the number q of parameters in the model:

$$R_a^2 = 1 - \frac{n-1}{n-q-1} (1 - R^2) \quad (3.65)$$

This adjusted coefficient of determination allows then to evaluate the behaviour of a deterministic model for the experimental points that have been used for the identification. It can also be used, in a first approach, for the justification of a deterministic model choice.

Nevertheless, this coefficient can not verify the adequacy of the model if a new set of experimental points is available for the same studied device (without re-identifying the model). For this new set of p additional experimental observations, and without any new identification of the model, a prediction error, or mean squared error, can be defined such that:

$$\delta_p = \frac{1}{p} \sum_{j=1}^p (y_j - G(x_j, \mathbf{P}))^2 \quad (3.66)$$

The model can be then qualified as highly predictive if low values of δ and δ_p are obtained. Note that, in the case of a low error value δ and a large error δ_p , the considered model is over-fitted and presents a bad predictive behaviour. In that context, the cross-validation technique (CVT) [94, 95] can be applied for several models in order to select

the one that is most adapted with the experimental observations. The CVT approach consists in splitting the available data into two subsets: one subset is used for the analysis (training set) and the second subset allows to validate the analysis (testing set).

Let us consider a set of experimental observations of size n such as, for example, the experimental $B - H$ points obtained on a given material sample, with the magnetic flux densities B_i corresponding to the magnetic fields H_i ($i = 1 \dots n$). The principle of the method is as follows:

- divide the experimental observations into K equally sized subsets
- identify the parameters of the model for the $K - 1$ subsets, excluding the K^{th} subset
- determine the prediction error $(\delta_p)_k$ from (3.66) for the K^{th} subset
- repeat the steps for all subsets $k = 1, 2, \dots, K$ and finally determine the global prediction error of the CVT from 3.67

$$\delta_{CVT} = \frac{1}{K} \sum_{k=1}^K ((\delta_p)_k)^2 \quad (3.67)$$

Finally, the deterministic model that can be retained would present an adjusted coefficient of determination R_a^2 close to 1 and a low global error δ_{CVT} obtained from the CVT approach.

Probabilistic modelling of the model parameters

It is now assumed that a deterministic model $y = G(p_1, p_2, \dots, p_m)$ has been chosen from the previously detailed approach. The next step consists in identifying the parameters (p_1, p_2, \dots, p_m) for a set of l experimental trajectories (*i.e.* for a set of l samples in our case). A trajectory will then corresponds to, for example, the $B - H$ data points obtained on a sample. The model parameters, identified on the l trajectories, are defined by a matrix $(\mathbf{P}_1, \mathbf{P}_2, \dots, \mathbf{P}_m)$ of size $l \times m$. The aim is to develop a probabilistic model that accounts for the dispersion of the parameters. In practice, for the observations of a given parameter $(p_i^1, p_i^2, \dots, p_i^l)$ of the random variable \mathbf{P}_i , a statistical inference is performed for the determination of the underlying statistical model that can represent the distribution of the observations.

Two approaches can be considered:

- Parametric approach: it consists in proposing a parametric distribution $f(\mathbf{P}_i, \zeta)$ (normal, log-normal ...) that can model the observations. The vector of parameters ζ (mean, standard deviation ...) describing the probability distribution can be identified, for instance, by the method of moments.
- Non-parametric approach: there is no hypothesis on the probability distribution associated to the random variable \mathbf{P}_i . In that case, the kernel density estimation is used to estimate the probability distribution of the random variable [96].

Regarding the parametric approach, the choice of the probabilistic model must be validated by statistical tests for the goodness of fit. The objective is to test a *null hypothesis* H_0 that states the correct representation of the observations with the proposed probability distribution function. In practice, the distance between the empirical and theoretical cumulative distribution functions (CDF) is evaluated. The H_0 hypothesis is rejected if the calculated distance is greater than a given critical threshold corresponding to a risk $\alpha\%$. The decision is made from the determination of the *p-value*, also called critical probability. This can be achieved by the Kolmogorov-Smirnov test (KS-test). If the *p-value* is found lower than the risk $\alpha\%$, the H_0 hypothesis must be rejected.

Note that the dependency, or correlation, between the parameters must also be considered in the probabilistic model construction. This can be done through the calculation of the covariance which is a way to measure how much two variables change together. The intensity of dependency between the random variables can be calculated from the linear *Pearson* correlation coefficient:

$$r_p = \frac{Cov(\mathbf{P}_1, \mathbf{P}_2)}{\sigma_{P_1} \sigma_{P_2}} \quad (3.68)$$

where σ_{P_1} and σ_{P_2} are the standard deviations of observations \mathbf{P}_1 and \mathbf{P}_2 . The *Pearson* coefficient is adapted to random parameters $(\mathbf{P}_1, \mathbf{P}_2)$ that follow a bivariate normal distribution. However, if the correlation is monotonous but non-linear, the *Pearson* coefficient gives information on the existence of a correlation between the parameters but represents badly the intensity.

In the case of non-linear and monotonous correlation, the *Spearman's* rank correlation coefficient is more adapted. Moreover, its advantage is also the non-parametric hypothesis of the parameter distribution, *i.e.* it does not rely on the hypothesis of a bivariate normal distribution for the parameters $(\mathbf{P}_1, \mathbf{P}_2)$. This coefficient is calculated from the ranks of the observations, meaning that, for the parameter \mathbf{P}_1 , the observations p_1 are sorted by ascending order, ranking from 1 to l (size of the parameter \mathbf{P}_1).

$$\rho_s = \frac{\sum_{i=1}^l (R_i - \bar{R})(S_i - \bar{S})}{\sqrt{\sum_{i=1}^l (R_i - \bar{R})^2} \sqrt{\sum_{i=1}^l (S_i - \bar{S})^2}} \quad (3.69)$$

where R_i (resp. S_i) is the rank of the observation p_i of \mathbf{P}_1 (resp. \mathbf{P}_2) and \bar{R} (resp. \bar{S}) is the mean of the ranks of \mathbf{P}_1 (resp. \mathbf{P}_2).

Uncertainty propagation

The probabilistic model $\mathbf{Y} = G(\mathbf{P}_1, \mathbf{P}_2, \dots, \mathbf{P}_m)$ is now defined with the marginal probability distribution functions associated to each parameter \mathbf{P}_i .

To verify the global adequacy of the probabilistic model, numerical tests, known as uncertainty propagation, are performed. This consists in propagating uncertainties carried by the parameters \mathbf{P}_i through the model G . This approach aims at validating the hypothesis made on the probability distribution of the input parameters \mathbf{P}_i .

Several approaches exist in the literature for propagating uncertainties through a model: the interval arithmetic technique [97], the Taylor series decomposition [98] or the polynomial chaos expansion [99, 100]. The most natural way for propagating the uncertainties is the Monte Carlo method which is well adapted for the generation of samples according to the probability distribution function of the input parameters. Its simplicity of implementation and applicability to any kind of model makes the Monte Carlo method a good candidate for such purpose. However, the accuracy of the Monte Carlo method depends highly on the number of generated samples N and its convergence rate is rather slow ($\frac{1}{\sqrt{N}}$). In fact, several thousands of samples are usually necessary for a satisfactory accuracy on the probability distribution function. But, this method still remains interesting if the tested model includes few parameters and is fast to evaluate.

A matrix of size $m \times N$ is build from the generation of N samples, according to the identified distribution functions, for each of the m parameters of the model. The deterministic model G is then evaluated N times leading to an output sample of the model \mathbf{Y} of size N from which the statistical moments (mean, standard deviation ...) and probability distribution functions of the output quantities can be calculated.

Usually, the input parameters $\mathbf{P}_1, \mathbf{P}_2, \dots, \mathbf{P}_m$ are supposed independent and represented by their marginal probability distribution functions. This hypothesis can lead to inaccuracies in the statistical analysis of the model outputs. In [101], it is recommended to account for the correlation structure of the input parameters, especially when the coefficient of correlation reaches about 0.7. Accounting for the correlation structure has been extensively studied in the statistical research domain and also in modern engineering. The method proposed by Iman and Conover [102–104] allows to create an artificial dependence structure of the components in a vector \mathbf{P} . This dependency is expressed through the *Spearman's* rank correlation coefficient (3.69) with the advantage of preserving the marginal distribution of each component.

3.4.2 Illustration with the iron loss variability modelling

To illustrate the probabilistic modelling approach, the magnetic properties of twenty eight slinky stators (SS), used in claw-pole alternators, are investigated. Studying this kind of stator is of interest as the manufacturing process, consisting in a long strip of steel lamination that is progressively punched and rolled up in a spiral way, has a noticeable impact on the magnetic properties. Also, it is expected to observe a certain level of variability. From experimental data obtained on the SS samples [105], the iron loss and magnetic behaviour experimental distributions are identified and modelled.

3.4.2.1 Iron loss model and probabilistic modelling of the parameters

For the experimental characterization, the excitation is sinusoidal and symmetric. Therefore, in that simple case, the loss model is considered with the equation (3.60). To identify the parameters ($k_h, \alpha, k_{cl}, k_{exc}$), the minimization of the objective function (3.63) is applied to iron losses measured for several magnetic flux densities and frequencies (between

5Hz and 200Hz).

The experimental data are split into two sets: a modelling subset for the probabilistic model identification and a test subset to validate the model. The quasi-static loss parameters k_h and α are identified from the measurements at 5Hz. The parameters k_{cl} and k_{exc} are deduced from measurements at higher frequencies. All parameters are identified for the stator samples of the modelling subset. The probabilistic modelling is considered within the frame of the parametric approach with the following considerations:

- the candidate probability density functions are the normal, log-normal and uniform distributions,
- the KS-test is applied in order to find the best probability density functions for the parameters

The p -values, obtained from the KS-test for the three probability density functions, are reported in table 3.3. In this table, it is observed that the H_0 hypothesis is not rejected, at a risk of 5%, for the normal and log-normal distributions and for all parameters. The uniform distribution is not rejected only for the parameter α . Therefore, regarding the resulting p -values, the KS-test allows to choose, on the one hand, the normal distribution for k_h and k_{exc} and, on the other hand, the log-normal distribution for α and k_{cl} .

Table 3.3: p-values of the KS-test at a risk of 5% for the three candidate distributions.

	k_h	α	k_{cl}	k_{exc}
Normal law	0.63	0.73	0.6	0.89
Log-normal law	0.53	0.75	0.82	0.75
Uniform law	0.0	0.6	0.0	0.0

The histograms and probability density functions for all parameters are reported in figure 3.23.

As the marginal distributions of the parameters do not all follow a normal distribution, their inter-dependence is quantified by the *Spearman's* rank correlation coefficients. The corresponding correlation matrix, reported in table 3.4, shows that the parameters are inter-dependent and, especially, the dynamic loss parameters k_{cl} and k_{exc} . To account for these correlations, the Iman-Conover method is employed [102–104]. This method allows to create, from the *Spearman's* rank correlation coefficients, an artificial dependence structure between the parameters of a vector \mathbf{P} by keeping unchanged their marginal distributions.

3.4.2.2 Validation of the statistical model

From the identified marginal distributions, $N = 100.000$ samples are generated, for each parameter of the model, by the Monte-Carlo method. The sample matrix ($N \times 4$) and

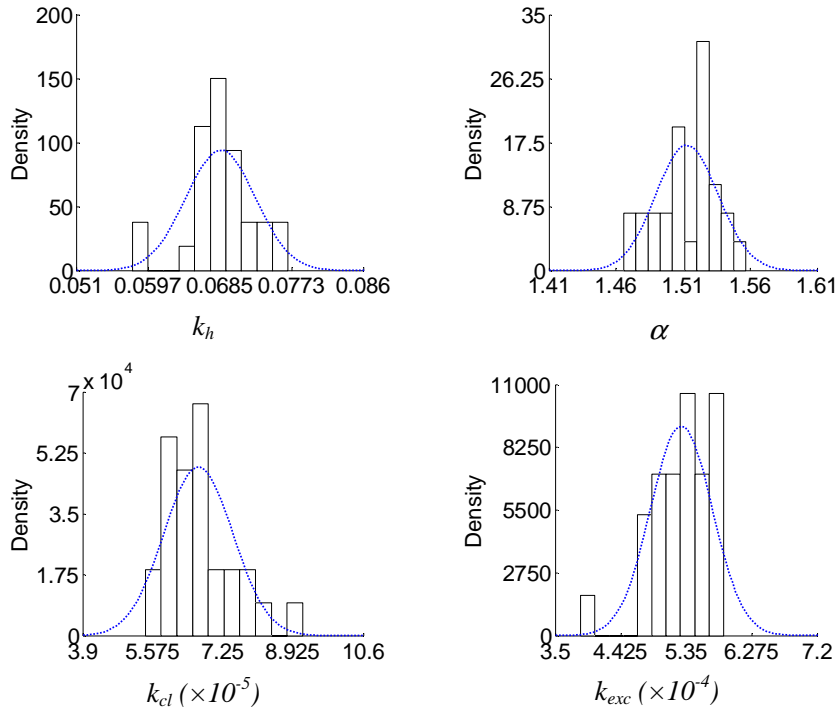


Figure 3.23: Probability density for the loss model parameters.

Table 3.4: Rank correlation matrix for the loss parameters.

	k_h	α	k_{cl}	k_{exc}
k_h	1.0	0.273	-0.248	0.0286
α	0.273	1.0	-0.336	0.424
k_{cl}	-0.248	-0.336	1.0	-0.519
k_{exc}	0.0286	0.424	-0.519	1.0

the rank correlation matrix in table 3.4 are employed with the Iman-Conover method to build a new sample matrix that respects the parameter dependence structure.

The losses for different levels of B_{max} at 50Hz are calculated from this new sample matrix. The cumulative distribution functions (CDFs) for the experimental and calculated points are illustrated in figure 3.24 for 2 levels of B_{max} .

The two samples KS-test is applied to test the null hypothesis H_0 , stating that the simulated and experimental CDFs are issued from the same continuous distribution at a risk of 5%. For the whole level of B_{max} , the p -values are between 0.17 and 0.5, allowing then not rejecting the null hypothesis at a risk of 5%.

The Confidence Interval (CI) can also be calculated to verify the probabilistic aspect of the identified statistical model. The CI verifies that, at a known probability, it is possible to find the real value within specified limits. For the present case, the 95% CI is calculated from the simulated realizations to verify that the experimental trajectories

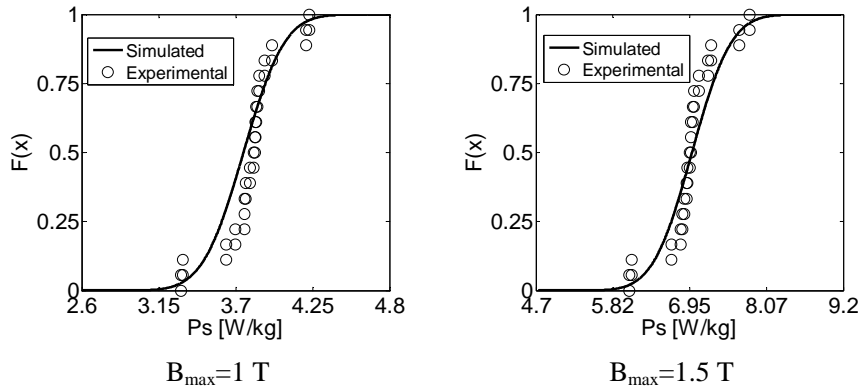


Figure 3.24: Experimental and predicted CDFs of the losses for two levels of B_{max} at $50Hz$.

(modelling subsets) lie within the CI limits as reported in figure 3.25. In the same way, the CVT is applied with the test subsets that lie within the 95% CI as illustrated in figure 3.26. All these criteria allow to validate, to a certain extent, the probabilistic model of the iron losses and the associated variability for the considered samples.

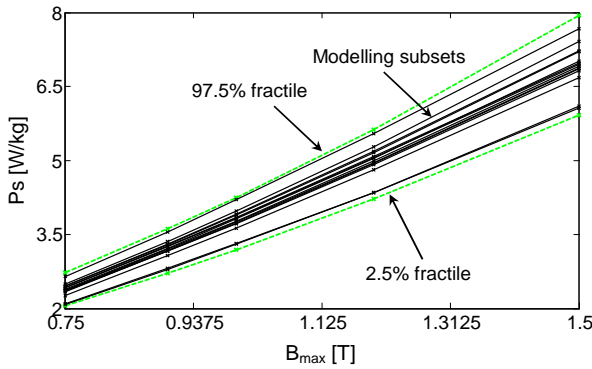


Figure 3.25: 95% confidence interval obtained from the model for the iron losses at $50Hz$ and modelling subsets (23 experimental trajectories).

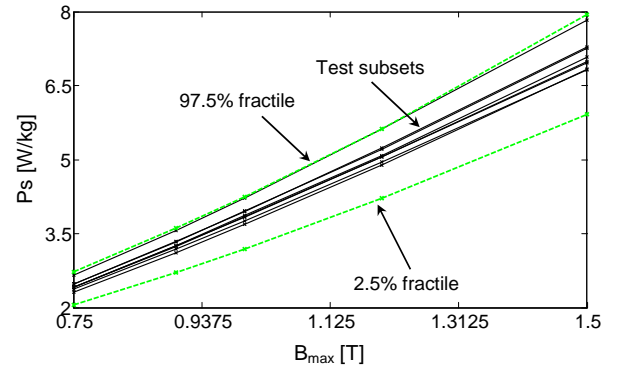


Figure 3.26: 95% confidence interval obtained from the model for the iron losses at $50Hz$ and test subsets (5 experimental trajectories).

4

Magnetic material characterization and applications

This chapter is dedicated to the illustration of magnetic material characterization and modelling within the context of electrical engineering applications. These are divided into two categories, qualified here as conventional and non-conventional applications. For each of these applications, the whole procedure for modelling the device is presented, from the material model to the validation of the FE numerical model. The proposed modelling approaches are also validated by comparison of the simulated device characteristics with the experiment.

For the conventional applications, a three phase transformer is studied, with a particular focus on the inrush currents, with the account of the hysteresis behaviour in FE. The second application deals with the calculation of stray load losses in an induction motor using pots-processing iron loss calculation.

For the non-conventional applications, three devices are studied. The first one is an hysteresis motor for which the magnetic hysteresis must be taken into account for its numerical simulation. The second device is a magneto-rheological brake that exhibits a hysteresis in the braking torque. The FE method approach is employed to investigate the origin of this hysteresis behaviour. Finally, the model of magnetization loss model in PMs, presented in the previous chapter, is applied to a dedicated experimental device and compared with the experiment in order to evaluate the accuracy of the proposed model.

4.1 Conventional applications

4.1.1 Three phase transformer and inrush current

For this specific study, the implementation in 2D-finite elements of the vectorized Jiles-Atherton hysteresis model [38] has been performed with the method based on the *differential reluctance tensor* described in section 3.1.3 and detailed in [37]. To test the robustness of such implementation, a three-phase transformer was tested under inrush current conditions when powered on.

4.1.1.1 Studied device and numerical model

The experimental device used for the validation of the proposed approach [37] is a three phase transformer of $2kVA$. Its geometry (studied domain) and electrical characteristics are given, respectively, in figure 4.1 and table 4.1. The magnetic core is made of FeSi electrical steel laminations which thickness is $0.5mm$.

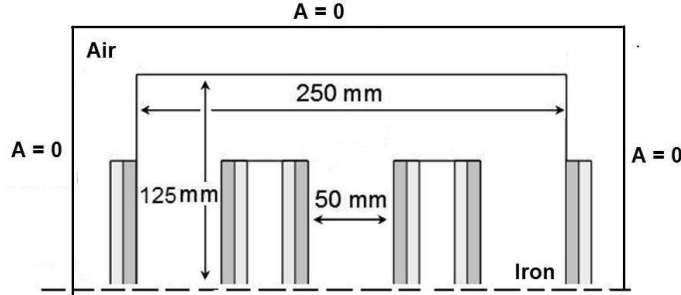


Figure 4.1: Geometry of the studied transformer.

Table 4.1: Electrical characteristics of the transformer.

	Primary winding	Secondary winding
Voltage (V)	400	230
Number of turns	403	227
Resistance (Ω)	0.89	0.38

In the no-load case, the absorbed power in the transformer is due to resistive losses in the primary windings and iron losses that occur in the magnetic core. As the resistive losses are negligible in regard to the iron losses (less than $0.1W$ per phase) one can consider the absorbed power to be only the iron losses. The measured losses for $f = 25Hz$ and $V = 127V$ at the primary windings, are about $20.2W$.

The vector hysteresis model parameters, identified with a Single Sheet Tester on samples cut along the rolling and transverse directions, are presented in table 4.2.

Table 4.2: Jiles-Atherton model parameters.

	Rolling direction	Transverse direction
M_{sat}	1.32×10^6	1.309×10^6
k	291.89	205.64
c	0.646	0.611
a	173.54	80.95
α	3.41×10^{-4}	1.47×10^{-4}

The 2D FE calculation was carried out with a mesh constituted of 700 first-order triangular elements. Besides, the Dirichlet and Neumann boundary conditions were

suitably imposed in all outer boundaries of the domain, as shown in figure 4.1. The presented three-phase transformer model is developed for no-load conditions considering coupling between the field and the voltage equations.

4.1.1.2 Results

The transient inrush currents were calculated for the transformer at no-load condition for rated sinusoidal three-phase voltages. In figures 4.2, 4.3 and 4.4, the measured and inrush currents are shown for, respectively, phases A, B, and C when the transformer is initially demagnetized (no remnant magnetic flux density). The powering on of the transformer corresponds to the maximum of the voltage in phase A.

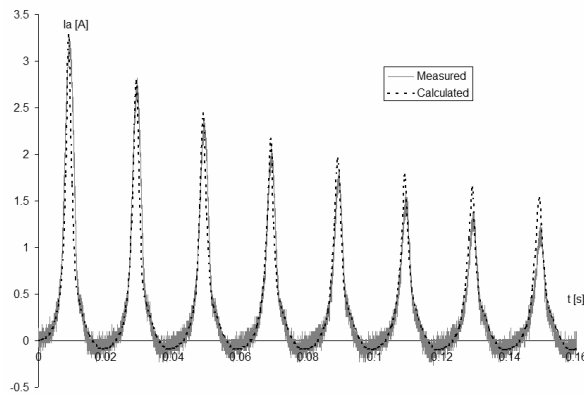


Figure 4.2: Measured and calculated inrush currents for phase A.

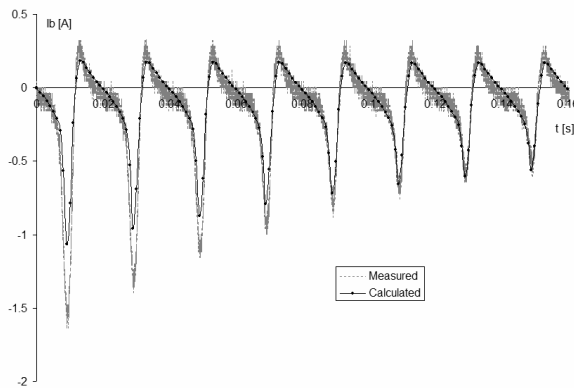


Figure 4.3: Measured and calculated inrush currents for phase B.

The comparison of these three figures shows that the FE model is able to represent with accuracy the inrush currents waveforms. In these curves, the amplitudes, oscillatory damping and distortion of calculated curves are close to the measured ones. The DC transient components, as well as the other harmonic content, are present. Numerically, the error between the maximum currents peaks is close to 4% and the phase error is negligible. One interesting aspect emphasized in such study is the local rotating magnetic

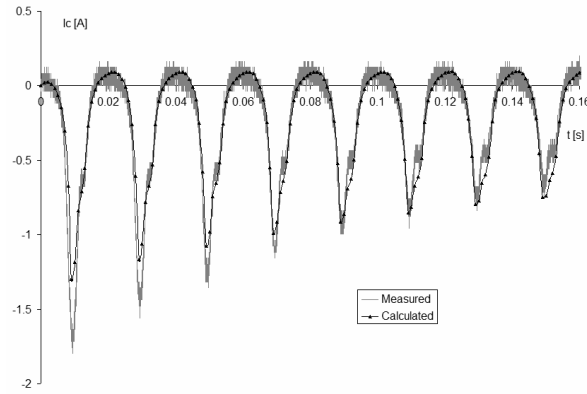


Figure 4.4: Measured and calculated inrush currents for phase C.

field that occurs in the T-joint of the transformer. In figures 4.5 and 4.6, the transient magnetic induction and field loci, occurring in the T-joint of the transformer, are shown.

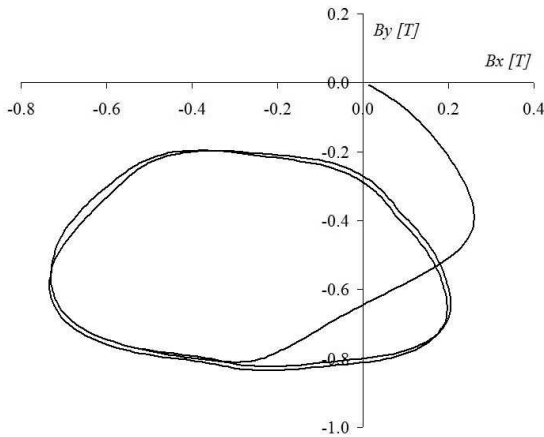


Figure 4.5: Locus of the calculated transient magnetic induction in the T-joint.

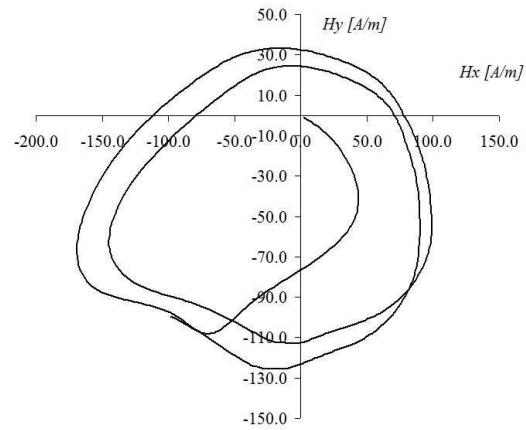


Figure 4.6: Locus of the calculated transient magnetic field in the T-joint.

The rotational flux observed in the previous figures is of importance as it can lead, depending on the level of magnetization, up to 2 times the losses under an alternating flux with the same magnitude [72]. Once the steady state currents are obtained, the gap between the measured and calculated losses is about 5%.

Finally, the model is also tested under the condition of a residual flux in the magnetic core when the transformer is powered on. This is performed by powering off the transformer at an arbitrary time (at 0.006s) during the steady state operation. Some residual flux is kept in the transformer before re-powering on few milliseconds later (at 0.026s). The inrush currents occurring in that condition are illustrated in figure 4.7.

One can observe that the inrush currents, in that particular case, are much more severe with the chosen residual flux. In fact, depending on the initial magnetic state of the core and the power-on time, the profile of the inrush currents may vary significantly. From the numerical aspect, the convergence is reached with an average of 5 non-linear iterations by time step.

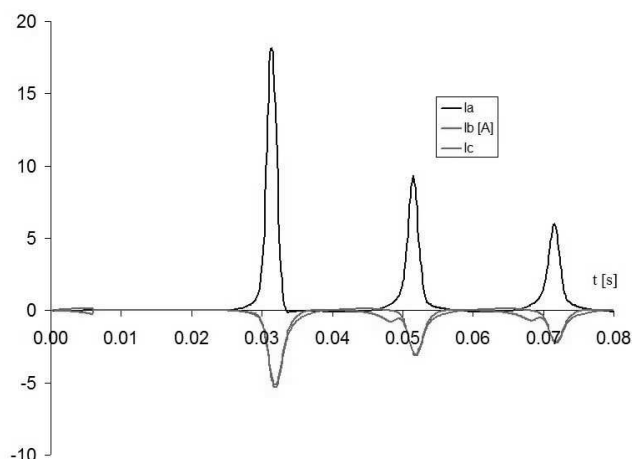


Figure 4.7: Calculated inrush currents with residual flux in the transformer core.

4.1.2 Study of the stray load losses in an induction motor¹¹

4.1.2.1 Definitions

Definition of the Stray Load Losses

Usually, the iron losses of an induction motor are measured at no-load conditions and considered to be the same when the motor is operating at load. But, in practice, there are phenomena appearing on load that increase the iron losses. The physical origins of these extra losses, or *Stray Load Losses* (SLL), is the same as the ones observed at no-load and can be linked to the increase of the losses associated to the fundamental frequency and high frequency components. In the first case, these are eddy current losses in the stator due to stator slot leakage flux, end-region losses in copper and metallic parts. For the high frequency components, the losses are linked to induced losses in the rotor due to the *m.m.f.* harmonics produced by the stator currents as well as to the induced losses in the stator due to rotor *m.m.f* harmonics. The impact of such losses on the operating conditions of the induction motor is the heating, the torque loss and the efficiency decrease [106].

To determine the SLL, they exist experimental procedures, such as the one described by the *IEEE standard 112-method B* test [107] that employs a power balance procedure. The SLL are obtained from the difference observed between, on the one hand, the total losses at load P_{tot} and, on the other hand, the sum of the iron P_{iron} and mechanical P_{mec} losses at no-load together with the stator P_{J-stat} and fundamental rotor $P_{J-fund-rot}$ Joule losses determined at load.

$$P_{SLL} = P_{tot} - (P_{iron} + P_{mec})_{NoLoad} - (P_{J-stat} + P_{J-fund-rot})_{Load} \quad (4.1)$$

From this definition, and by decomposing each loss term as proposed in [108], the SLL can be regarded as the *difference between the total losses of the machine on load and the losses determined at no-load* for the iron core, eddy current in the end-region and harmonic eddy current in the rotor cage (see equation 4.2).

¹¹The presented results are part of the PhD Thesis of Jalal Cheyrtani.

$$P_{SLL} = \left(P_{core}^{Load} - P_{core}^{NoLoad} \right) + \left(P_{End}^{Load} - P_{End}^{NoLoad} \right) + \left(P_{CageHarm}^{Load} - P_{CageHarm}^{NoLoad} \right) \quad (4.2)$$

where P_{core} , P_{End} and $P_{CageHarm}$ are, respectively, the iron core losses, end-region eddy current losses and cage harmonic eddy current losses.

Loss calculation

The proposed approach consists in using the 3D-FE Method (3D-FEM), in magnetodynamic, for the calculation of each component of the SLL that has an electromagnetic origin, which is not achievable by the experiment. From the 3D-FEM calculation, the iron losses are determined in post-processing with the loss model in equation 3.59 and the harmonic eddy current losses in the rotor cage are calculated from the following expression:

$$P_{CageHarm} = \sum_{cage} \rho |J_0|^2 + \sum_{n=1}^N \sum_{cage} \rho \frac{|J_n|^2}{2} \quad (4.3)$$

where J_0 is the average current, J_n the magnitude of the n^{th} harmonic and ρ the electrical resistivity.

4.1.2.2 Studied machine

The 3D geometry of the studied high power induction motor is illustrated in figure 4.8. The end-region parts, such as the end-winding, housing and clamping plates are also included in the model. The machine is discretized with a finite element mesh constituted of about 684 000 tetrahedral and prismatic elements. The mesh accounts for the skin depth of the rotor bars and the rotor rotation.

Regarding the magnetic material, and according to the motor manufacturer, both stator and rotor are made from the same non-oriented electrical steel grade. The magnetic characteristics of the rotor and stator steel along with the iron loss coefficients are identified for different levels of the maximum magnetic flux density and for different frequencies. The simulations are performed at no-load, locked rotor and rated load conditions, using the time-domain electromagnetic finite element simulations with *code_Carmel*. For no-load and load conditions, the motor is fed by sinusoidal rated voltages while for locked rotor conditions it is fed by sinusoidal voltages corresponding to the rated current. Moreover, all global and local results are calculated for the last electrical period once the steady-state is reached.

4.1.2.3 End-region parts losses

Different simulations at no-load, locked rotor and load conditions are performed to calculate the eddy current losses in each part of the end-region. The comparison of these losses is shown in table 4.3.

- At no-load condition, only the stator clamping plate losses are significant because the primary current is low in comparison with the rated primary current.

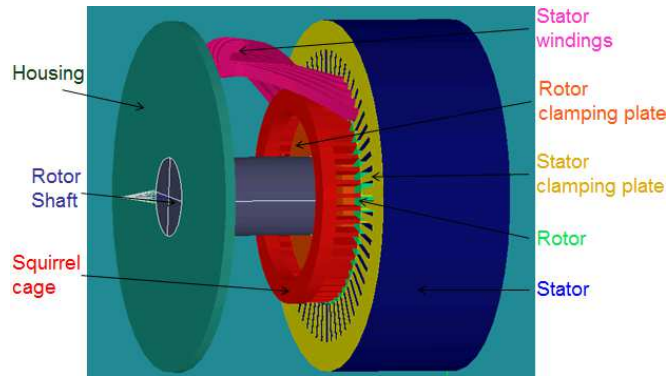


Figure 4.8: Geometry of the studied induction motor.

- At rated load condition, the variation of the rated primary current in the end-windings lead to the increase of the stator clamping plate and housing losses. However, as the rated slip is low, the fluxes at the rotor clamping plate and shaft rotate at almost the same speed of the primary fluxes. Thus, the variation of the fluxes and eddy current losses are minimal.
- At locked rotor, in addition to the rated primary current in the end-windings, the eddy currents in the squirrel cage and the variation between the primary and secondary fluxes are maximal. This leads to a significant increase in eddy current losses in the end-region parts.

Table 4.3: Eddy current losses in end-region parts.

End-region parts	No-load [W]	Load [W]	Locked rotor [W]
Stator clamping plate	12.5	23.77	16.04
Rotor clamping plate	0.15	0.69	22.08
Housing	1.52	11.0	37.76
Rotor shaft	0.04	0.06	45.29

4.1.2.4 Stray Load Losses calculation

From the loss calculation results obtained for the iron core, end-region and harmonic eddy current for both no-load and load conditions, the SLL can be calculated with the approach described in section 4.1.2.1.

First, let us plot the experimental and calculated iron losses at no-load condition with rated voltages as shown in figure 4.9. The difference between the experiment and the calculation is about 12%, which is a satisfactory result regarding the measurement uncertainties and numerical errors. Moreover, it can be noticed that the main part of the calculated iron losses is constituted of the stator and rotor core losses (90%). The harmonic cage losses are less important and are essentially due to the stator slot harmonics. Finally, the end-region losses are negligible when compared with the total iron losses.

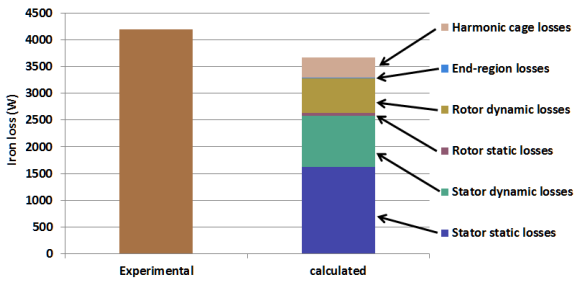


Figure 4.9: Experimental and calculated iron losses at no-load condition.

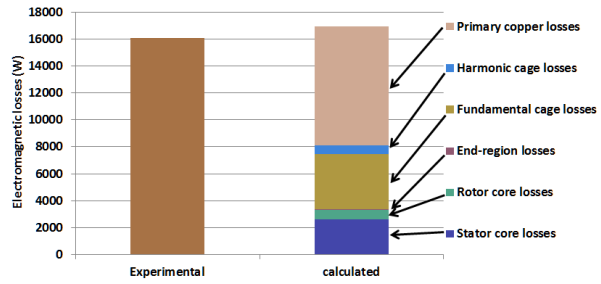


Figure 4.10: Experimental and calculated electromagnetic losses at load condition.

Regarding the rated load simulation, figure 4.10 shows the comparison with the experiment. The difference between the simulation and experiment is up to 5% where the calculated electromagnetic losses are mainly linked to the primary copper losses (52%). The harmonic cage losses are almost multiplied by two in comparison with the no-load condition. This is due to the increase of the stator slot harmonics at load condition, representing 15% of the total eddy current cage losses. However, as in the case of no-load condition, the end-region losses are negligible in comparison with the total rated load ones.

Finally, from both results at no-load and rated load simulations, the SLL can be deduced and compared with the experimental results using the *IEEE standard 112-method B* test, as shown in figure 4.11. The main part of the SLL is the consequence of the eddy current harmonic loss increase in the rotor cage (80%) due to the increase of the stator slot harmonics at load. Moreover, even if the end-region losses are negligible at no-load and load conditions, compared with the total losses, the increase of these losses is non-negligible since they represent 6% of the total stray load losses.

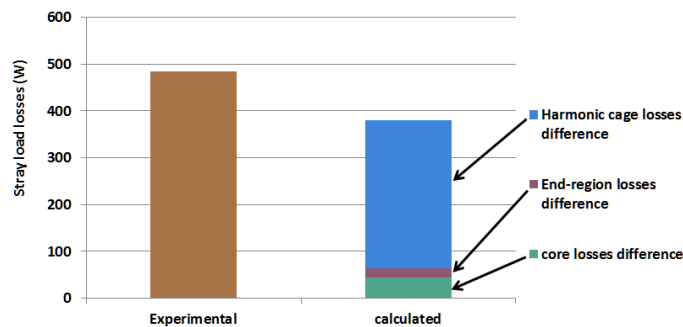


Figure 4.11: Experimental and calculated Stray Load Losses.

This results shows that, despite the complex representation of all 3-D magnetic phenomena contributing to the SLL and the measurement uncertainties, the calculated SLL are satisfactory regarding the experimental ones.

Another aspect must also be emphasized regarding the ratio of SLL to the input power for the studied electrical machine. In fact, the measured SLL, as well as the calculated ones, are up to 0.1% compared with the total input power. This is rather low when compared with the *60034-3 standard* that estimates the SLL up to 0.5% of the input

power for high power induction machines. However, this rate exceeds the real value and, in addition, considers both the skew losses and harmonic inter-bar current losses that occur in the case of skewed cage induction machines. For the studied machine, these contributions to the SLL are negligible since the squirrel cage of the considered induction machine is not skewed.

4.2 Non-conventional applications

4.2.1 Hysteresis motor

4.2.1.1 Presentation of the system

There are some systems that require the inclusion of the magnetic hysteresis in the modelling process in order to account correctly for their operating conditions. The hysteresis motor is one of such devices.

The studied motor (see figures 4.13 and 4.12) has a rotating speed of $22500rpm$. The 3-phase stator winding has 8 poles distributed in a total of 24 slots, which are totally closed. It enables to have a smooth airgap to avoid high torque ripples. The number of turns of each coil is equal to 73 and the winding is supplied by a 3-phase voltage of $19V$ with a frequency of $1500Hz$. The yoke of the stator is made of FeNi laminations in order to reduce iron losses as the nominal operating point is at $1500Hz$. In fact, this material is better adapted for high speed machines than classical FeSi sheets. The rotor is made up of thin magnetic rings of semi-hard material (Magnetoflex 35) and the stack is surrounding a yoke made of a non-magnetic material. The airgap is very thin compared with the outer diameter of the machine (ratio about $1/1000$).

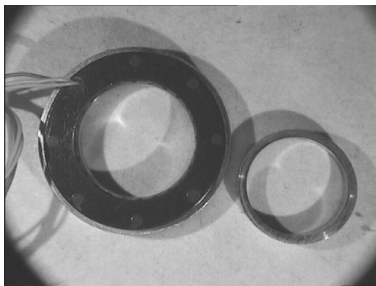


Figure 4.12: Studied motor

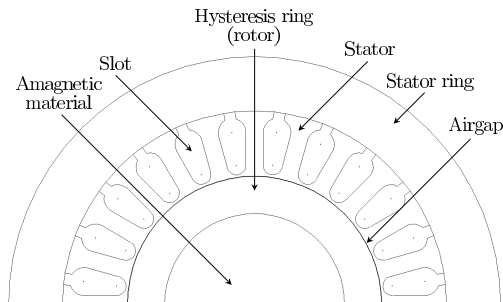


Figure 4.13: Hysteresis motor geometrical structure

4.2.1.2 Modelling of the hysteresis motor

The numerical model of the motor is a 2D-FE model with the inclusion of the magnetic hysteresis following the mathematical formulation presented in 3.1.3 with the fixed-point method. Some hypotheses are made for the FeNi laminations at the stator. The eddy currents and hysteresis effects are considered negligible at the stator and the magnetic behaviour is considered isotropic. In fact, the hysteresis loop of the FeNi material has a vary low coercive field in comparison with the characteristic loop of the Magnetoflex

material and, consequently, the hysteresis effect of the FeNi laminations has negligible impact on the electromechanical energy conversion process.

Therefore, the description the magnetic of the FeNi material is made with a single-valued function $H = H(B)$ given by the expression (3.31). In figure 4.14, the experimental and identified anhysteretic curves are illustrated.

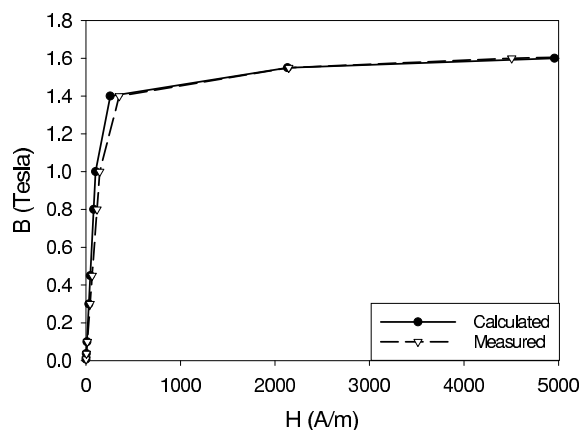


Figure 4.14: Anhysteretic curve for the stator lamination

Regarding the rotor ring material, the hysteresis effect must be accounted for. As the Magnetoflex 35 presents an average anisotropy with a preferential magnetization direction along the rolling direction. In the transverse direction, the value of the remnant magnetic flux density is 10 to 30% lower. In Table 4.4, some additional characteristics of the material are given.

Table 4.4: Physical properties of the Magnetoflex 35

Density	8.1 g/cm^3
Electrical resistivity	$0.7 \times 10^{-6} \Omega.m$
Curie temperature	$700 \text{ }^\circ C$
Remanence	$0.8 - 0.95 \text{ T}$
Coercivity	$24 - 30 \text{ kA/m}$

To limit the effects of anisotropy, the directions of the Magnetoflex-35 laminations have been shifted with respect to each other. In this configuration, the lamination stack is assumed to behave like an isotropic medium. It must also be noticed that the lamination thickness is small and the hysteresis loop is quite large (the coercive field is about 24 to 30 kA/m). Consequently, the eddy current effect does not modify much the shape of the loop. However, for a motor with a greater thickness of the hysteresis ring, the flux lines are not circumferential and rotational hysteresis occurs in the ring, which increases the iron losses and influences the torque evolution, as already presented in [109]. In this case, a vector hysteresis model is needed. In our case, the ring is thin, so the flux lines are mainly circumferential. Then, the directions of \mathbf{B} and \mathbf{H} are only slightly modified and

can be considered parallel. A relationship linking the moduli of \mathbf{B} and \mathbf{H} is then sufficient to represent the rotor ring behaviour.

Therefore, the static Jiles-Atherton model (see section 3.2.3), which is more simple to implement and faster in terms of time calculation [47], is chosen for this study. The five parameters of the model c, a, k, α and M_{sat} have been identified from only one $B(H)$ loop using an optimization procedure. The protocol used to identify the parameters of the Jiles-Atherton model is described in [47]. The obtained parameters for the Magnetoflex 35 material are given in table 4.5.

Table 4.5: Jiles-Atherton parameters for the Magnetoflex 35

c	0.25
a	$40 A/m$
k	40
α	1.0×10^{-4}
M_{sat}	$1.2 \times 10^6 A/m$

A comparison between the $B(H)$ loops used for the identification and the model is given in figure 4.15.

Finally from the 2D-FE model build with these considerations, a 2D mesh is generated with 868 triangular elements. An illustration of the magnetic flux pattern obtained in the motor is given in Figure 4.16.

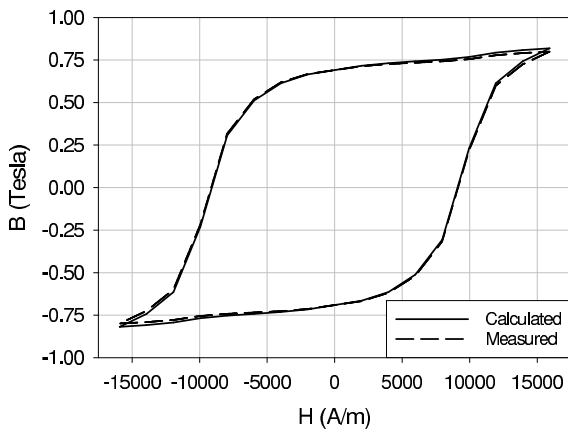


Figure 4.15: Magnetoflex 35 hysteresis loop: measurements and model

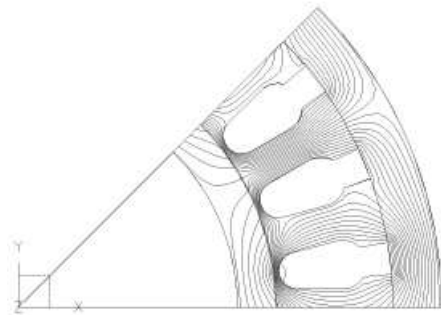


Figure 4.16: Flux pattern in the machine loop

4.2.1.3 Validation of the model

To validate the model, the experiment and simulation are compared for the torque and electrical quantities. The calculations were performed when the motor is supplied by the nominal voltage (3 phased sinusoidal voltage of 19V RMS). First, we give the characteristic for the torque versus the speed measured during a startup of the machine from

Table 4.6: Current RMS values (in Ampere) obtained by measurement and field calculation

	Measurement (synchronous speed)	Measurement (at standstill)	Calculation
I_{RMS}	322.2×10^{-3}	509.6×10^{-3}	417.5×10^{-3}
I_{h1}	322.0×10^{-3}	478.0×10^{-3}	416.9×10^{-3}
I_{h5}	4.33×10^{-3}	18.94×10^{-3}	11.27×10^{-3}
I_{h7}	1.96×10^{-3}	7.73×10^{-3}	7.18×10^{-3}

standstill to the synchronous speed (Figure 4.17). One can note a variation of the experimental torque of about 20%. The model leads to a constant torque equal to $0.72mN.m$. In fact, in the simulation, no dynamic effects are considered since eddy currents and frequency dependency of the hysteresis loop are neglected. Under these conditions, the rotor speed has no influence since the shape of the hysteresis loop depends only on the field magnitude, not on its time variation. It can be observed in figure 4.17 that the mean value of the computed torque agrees rather well with the experimental one, taking into account that this quantity is generally difficult to calculate for a machine with thin airgap (asynchronous machine, reluctance variable machine...).

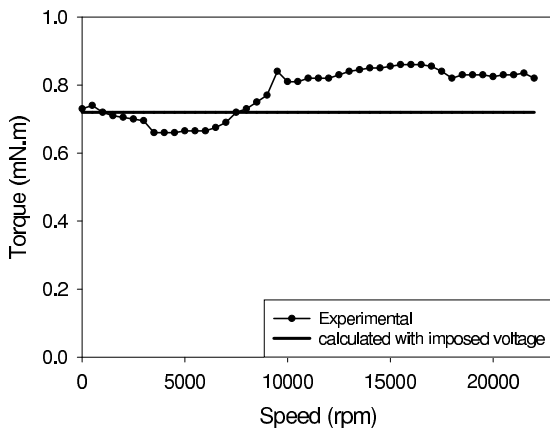


Figure 4.17: Experimental torque versus the speed during a startup

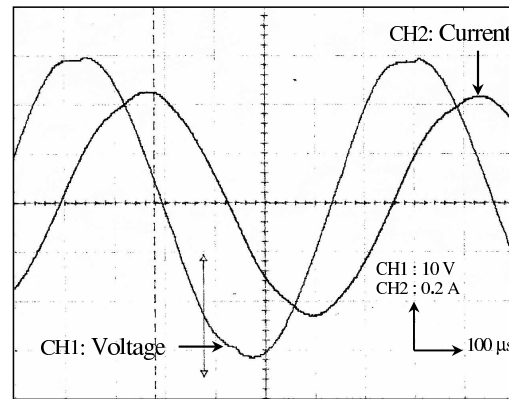


Figure 4.18: Measured current and voltage waveshapes at rated speed

The measured waveforms of the line current and voltage for synchronous speed are given in figure 4.18 and the waveforms of the calculated current is given in Figure 4.19. For more convenience, we give in table 4.6 the magnitude of the fundamental and harmonics of currents for the experiment and the calculation. The values for the experimental currents when the motor is supplied at standstill are also presented. A difference is observed between the measured currents at standstill and at synchronous speed. This is due to dynamic effects which appear mainly at standstill in the rotor.

Regarding the calculation results, also in Table 4.6, these are quite close to the experimental ones. The hypotheses made to build the model seem then to be justified for this

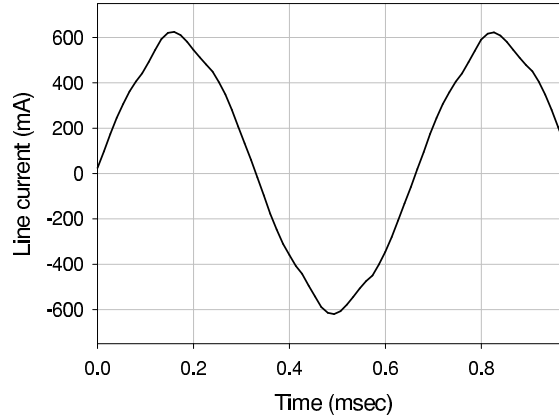


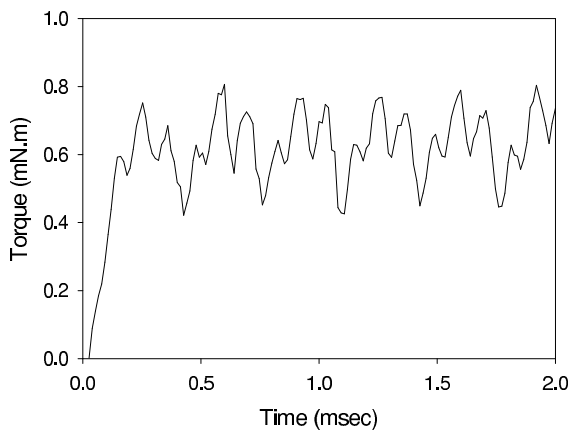
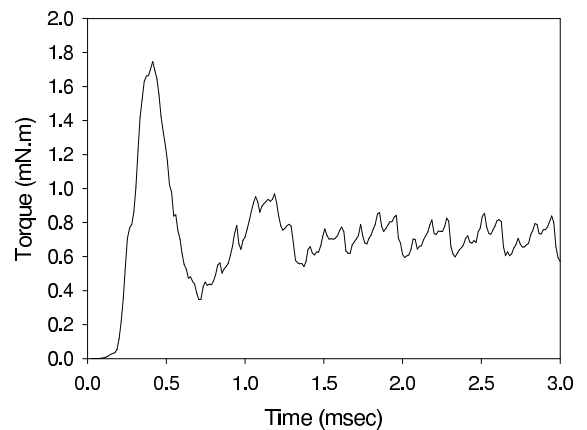
Figure 4.19: Time evolution of the line current in one phase

motor. The model can be further used to study the influence of parameters on the torque. In the following section, a comparison of the hysteresis motor features is performed when it is supplied either by imposing a sinusoidal current or by imposing a sinusoidal voltage.

4.2.1.4 Study of the motor

Torque calculation

In figures 4.20 and 4.21, results obtained for the torque by field calculation by imposing, respectively, the RMS values for the currents $I_{line} = 0.44A$ and the voltages $V = 19V$ are illustrated. Both supplies lead to similar average torque values at steady state (see table 4.7). In both cases, the semi-hard material is initially supposed to be demagnetized ($M = 0$ for $H = 0$).

Figure 4.20: Torque evolution when imposing a sinusoidal current $I_{line} = 0.44A$ Figure 4.21: Torque evolution when imposing a sinusoidal voltage $V = 19V$

When supplying by sinusoidal current (Fig. 4.20), in the first part of the curve we can see the magnetization process and in the second part the steady state when the magnitude

Table 4.7: Torque values obtained by field calculation

Calculation (imposed current)	0.65 <i>mN.m</i>
Calculation (imposed voltage)	0.72 <i>mN.m</i>

of the torque ripple is about 50% of the average torque. In Figure 4.21, when the motor is supplied by sinusoidal voltages, transient is longer than the previous case. But, the torque ripple magnitude is weaker and represents about 25% of the average torque.

Finally, the evolution of the average torque versus the current and the voltage magnitudes are also calculated (see figures 4.22 and 4.23) at steady state. We observe a quadratic evolution of the torque versus the applied current, i.e. the applied magnetic field. Nevertheless, if the current is too high, due to the magnetic saturation, the torque rate evolution versus the current becomes slower. This case cannot appear in practice as it leads to an overheating of the machine due to an excess of Joule losses.

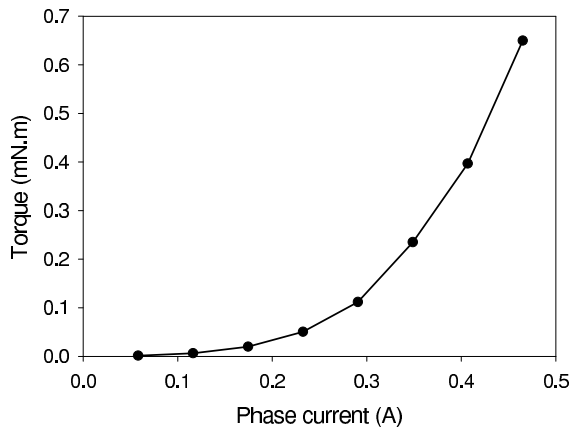


Figure 4.22: Evolution of the torque versus the supply current

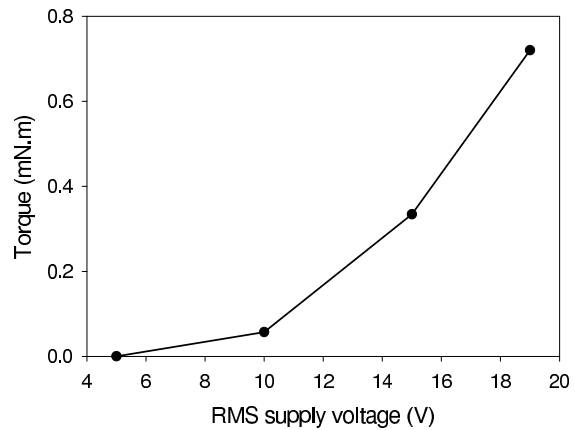


Figure 4.23: Evolution of the torque versus the supply voltage

Current waveforms when applying the voltages

The phases are coupled in delta, so the line currents are a combination of phase currents. When the supply voltage is sinusoidal, the line currents and the phase currents are not sinusoidal as seen above in section 4.2.1.3. The harmonic distortion of line currents remains small compared to the one of the current flowing the windings (see figure 4.24) which third harmonic has a magnitude of 115mA. Due to the saturation and hysteresis effects, an important circulation current appears, as shown in Figure 4.25. This circulation current lead to a reduction of the torque ripple. Indeed, it was noticed that the ripple magnitude are greater when the current is imposed with a perfect sinusoidal waveform.

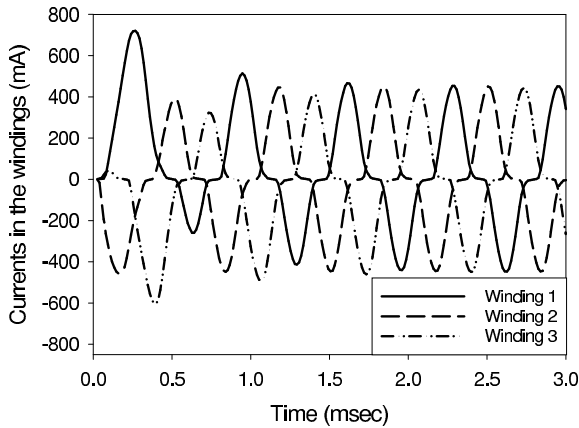


Figure 4.24: Currents in the windings when imposing the voltage

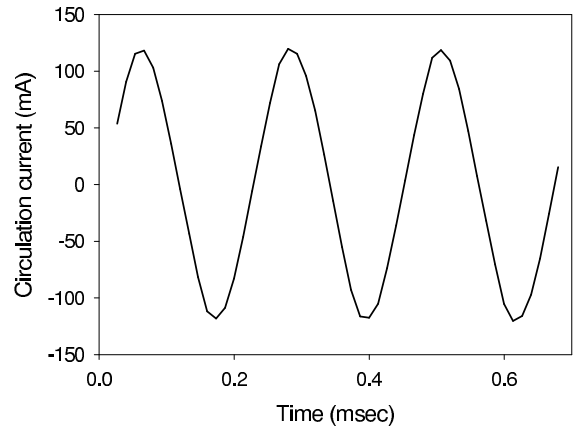


Figure 4.25: Circulation current for one fundamental period

4.2.2 Study of a magneto-rheological brake¹²

We are interested here in the use of a magneto-rheological fluid (MRF) in a braking application. The aim is to build a numerical model able to represent the particular behaviour of the MRF-brake, especially the hysteresis phenomena observed in the braking torque. The experimental aspect is first presented, then simulation results are presented for the investigation on the origin of such hysteresis phenomena in the torque evolution of the MRF-brake.

4.2.2.1 Experimental study

Preliminary notions about MRF behavior

Typically, a magneto-rheological fluid (MRF) shift from Newtonian liquids, characterized by a linear relationship between the stress τ and the shear rate $\dot{\gamma}$ (4.4) in the linear shear flow (figure 4.26), to Bingham plastics, characterised by an affine relationship (4.5) [110]. Here τ is equal to the ratio of shear force F on poles surface S and $\dot{\gamma}$ to the derivative of the velocity field v with respect to the z coordinate, which is a constant equal to the ratio between the shear velocity V and the gap height h . The coefficients η and η_p are called respectively Newtonian and plastic velocities. τ_y is called yield stress; below this stress value, a MRF behaves like a rigid body; above, it flows like a viscous fluid. Equation (4.5) represents the flow behaviour of a MRF. In the case of MRFs, τ_y depends on the magnetic field strength H . The yield stress values that can be reached are typically up to 100 kPa, which is much larger than the typical 3 kPa that can be reached with the electro-rheological fluids [111].

$$\tau(\dot{\gamma}) = \eta\dot{\gamma} \quad (4.4)$$

¹²The presented results are part of the PhD Thesis of Richard Demersseman.

$$\tau(\dot{\gamma}, H) = \text{sgn}(\dot{\gamma}) \tau_y(H) + \eta_p \dot{\gamma} \quad (4.5)$$

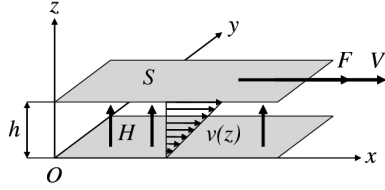


Figure 4.26: Linear shear flow with indication of the magnetic field direction

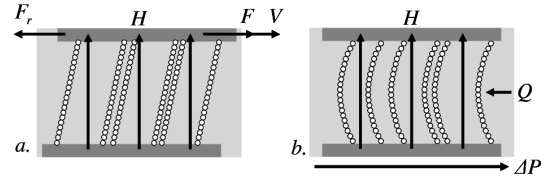


Figure 4.27: Deformation of the chains of particles in shear flow (a) and valve flow (b)

The plastic behaviour observed at macroscopic scale is the consequence of the particles behaviour at microscopic scale. When the magnetic field is applied, the particles are magnetized and aggregate to form a kind of linear ‘chains’ which links to the two pole surfaces. When a MRF is sheared (i.e., the two poles surfaces are in relative motion to each other), these chains act like springs which create an opposing force F_r to the shear force (figure 4.27.a). When a MRF is in a valve (i.e., the two poles surfaces are fixed) that experiences a pressure difference ΔP between its entry and exit, they act as hydraulic obstacles which oppose to the flow Q of the fluid (figure 4.27.b).

Mechanical and electrical design of the brake

A cross-section of the MRF brake is represented in figure 4.28. The rotor is composed of a disk mounted on a shaft supported by two single row radial contact ball bearings. The disk and the stator parts #1 and #2 are made of AISI1035 steel and, together with the MRF filling the gaps between them, compose the magnetic circuit. The shaft, the spacer, the coil core and the stator part #3 are made of aluminium. The MRF is retained inside the brake by a lip seal inserted inside the stator part #2. The used fluid is the MRF-132AD from Lord Corporation. The excitation winding supports a maximum continuous current of 1.2 A.

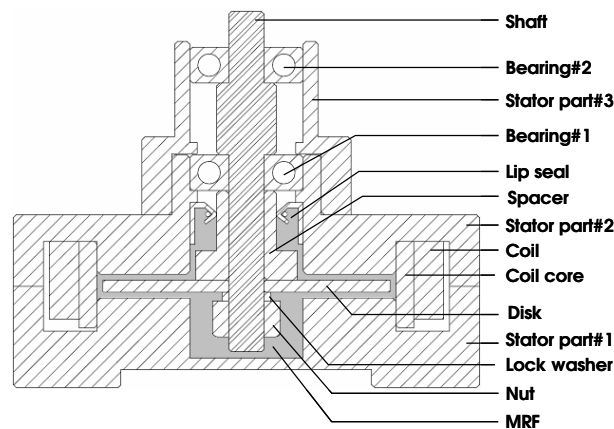


Figure 4.28: Mechanical design of the MRF brake

The design of the MRF brake is based on analytical considerations described in a previous work [112].

Description of the experimental set-up

An overview of the experimental set-up is illustrated in figure 4.29. The MRF brake is driven by a DC motor coupled to a two stages planetary gearbox with a 1 : 32 ratio. Two bellow couplings and an intermediate shaft are used to connect the gearbox to the brake. The torque is measured with a transducer which is located between the stator of the brake and the frame. For the speed feedback, a digital rotary encoder mounted at the rear of the motor housing is used. Signals are routed to a digital acquisition device data conditioning and storage. Tests were performed using two programmable DC power supplies for both the brake and the motor. The input current of the brake i_f or the speed of its shaft ω can be controlled.

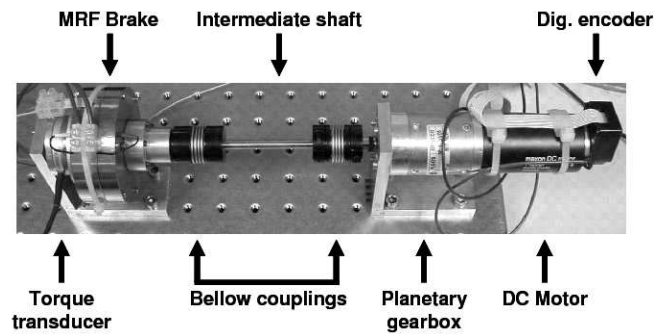


Figure 4.29: Overview of the experimental set-up

The torque transducer gives a measurement of the torque Γ exerted on the brake stator which can be divided in a torque Γ_{MR} exerted by the MRF on the inner surfaces and a total friction torque Γ_f which is the sum of the friction torques exerted by the moving elements on the stator. Γ_{MR} is the actual torque that we aim at measuring. Thus, the first step in the measurement process will be to get a plot of Γ_f as a function of ω , which can be done before filling the brake with the MRF ($\Gamma = \Gamma_f$). Then, once the brake has been filled with the MRF, for one measured value Γ at a given speed ω , the measurement of Γ_{MR} is obtained by deducing the value of Γ_f at the same speed from Γ .

In the case of the experiments presented here it is particularly important to define a ‘reference’ state for the brake, i.e. an initial state which must be, as much as possible, the same for all the experiments. In fact, because of the remnant magnetization of the magnetic circuit, the initial state may vary from one experiment to another. Therefore, the brake was demagnetised before each experiment, following the ‘classical method’ for such electromagnetic coil-core system. This method consists in feeding the coil with a low frequency sine or triangle current, which magnitude slowly decreases to zero.

Measurements results

In figure 4.30 shows the plot of the total friction torque Γ_f as a function of the speed ω . We observe a dry-friction type behaviour, with an average torque value of 1.5 N.cm.

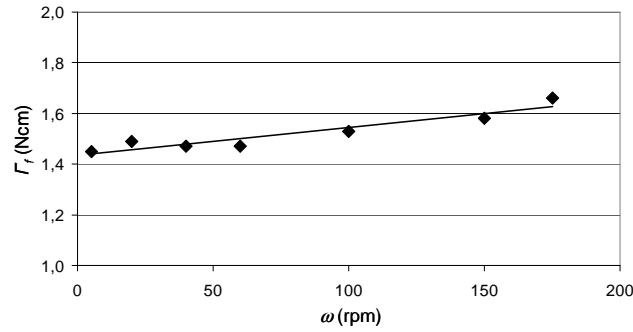


Figure 4.30: Total friction torque as a function of speed

Once the brake has been filled with the MRF, the torque Γ_{MR} is measured as a function of ω . The results are plotted in figure 4.31 for different values of i_f . The input current of the brake was sequentially increased from 0 to 1.2 A, then decreased to 0 A, with steps of 0.4 A. For each value of the current, the speed is kept constant.

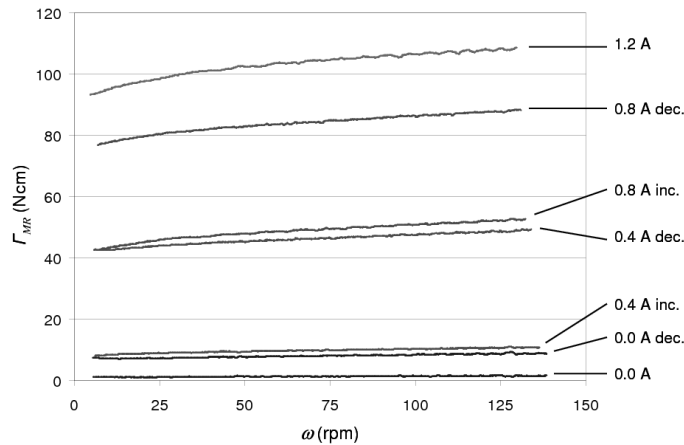


Figure 4.31: Magneto-rheological torque as a function of speed for different currents (inc. and dec. are, respectively, for the increasing and decreasing current)

In a first approximation, we can state that the typical behaviour of a MRF brake, for a given current, presents a torque that is almost constant with speed. Moreover, the figure shows that, for a given speed, the evolution of the torque is not single-valued with respect to the current. This has been already observed in [113], but no further study has been achieved concerning the origin of this phenomenon. It will be further emphasized that this phenomenon is due to the hysteresis behaviour of the ferromagnetic material used for the yoke.

Large gaps are observed between the plots obtained for $i_f = 0.4$ A and 0.8 A during the increase and the decrease of i_f . These gaps are almost 40 N.cm for both current values. To illustrate this effect, the complete hysteresis loop of Γ_{MR} as a function of i_f is represented in figure 4.32 for a constant speed of 120 rpm. To get this plot, the current applied according to the waveform in figure 4.34. This sequence was repeated twice, and the obtained loops are almost superposed, which indicates that the hysteresis loop is

stable. From this loop we can define the remnant torque Γ_{MR}^r as the torque (in absolute value) which still exists when the current is zero and the coercive current i_f^c as the current (in absolute value) for which the torque Γ_{MR} is minimum. Here we have $\Gamma_{MR}^r = 9$ N.cm and $i_f^c = 0.25$ A.

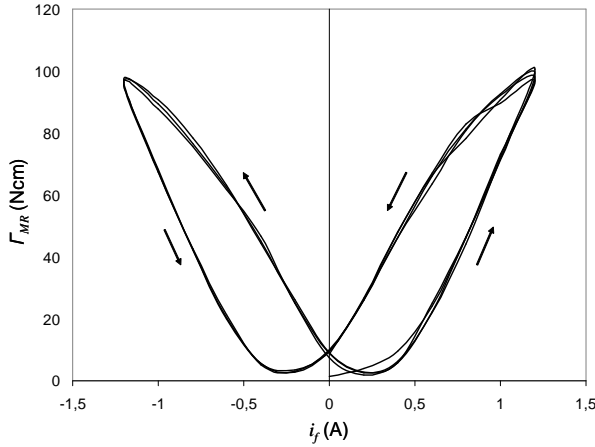


Figure 4.32: MR torque at 120 rpm with a symmetric current excitation

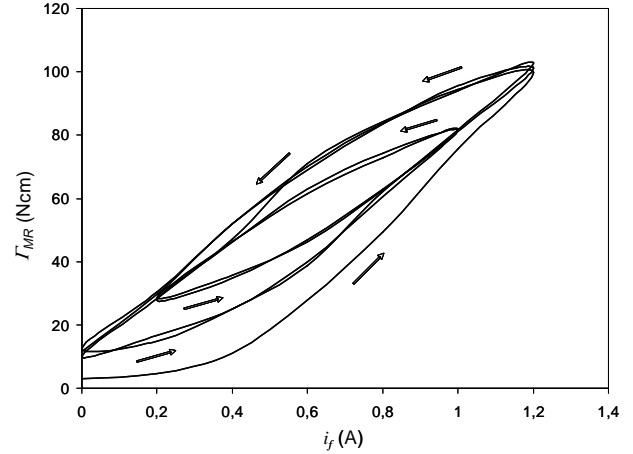


Figure 4.33: Minor loops inside the hysteresis loop of the torque at 120 rpm

In figure 4.33, the plot of Γ_{MR} is given for the same speed value and for the current sequence represented in Fig. 4.35. This sequence allows to get the plot of one minor loop inside the hysteresis loop.

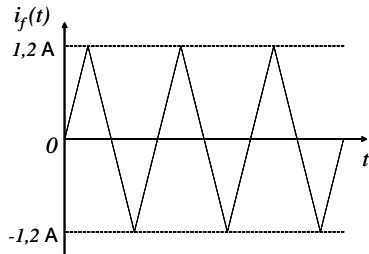


Figure 4.34: Symmetric excitation current waveform

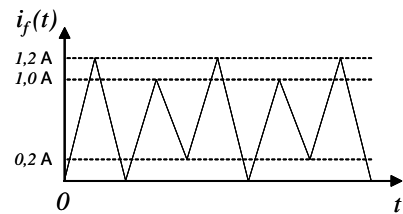


Figure 4.35: Current sequence for minor loops

4.2.2.2 Numerical model

To build the numerical model of the MRF-brake, a 2D-FE approach was considered with the account for the hysteresis phenomenon in the ferromagnetic cores. The mathematical formulation based on the fixed-point method, and presented in section 3.1.3, was applied with the Jiles-Atherton model. The simulations were carried out using both non-hysteretic and hysteretic behaviours for a comparison with the phenomena observed in the experiment and described in section 4.2.2.1.

Ferromagnetic steel and magneto-rheological fluid behaviour laws

The behaviour law of the MRF-132AD fluid provided by the manufacturer is given in figure 4.36. In order to take into account this non-linear behaviour law in the FE code, the manufacturer data are fitted to the analytical expression (3.31). The obtained coefficient are given in table 4.8.

Table 4.8: Parameters for the $H(B)$ curve used for the MRF-132AD material

ϵ	1.06×10^{-1}
c	46.69
α	5.82×10^{-1}
τ	148.33

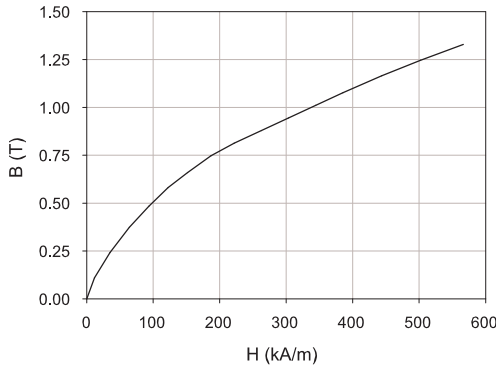


Figure 4.36: Magnetisation curve of the MRF-132AD (from Lord Corporation)

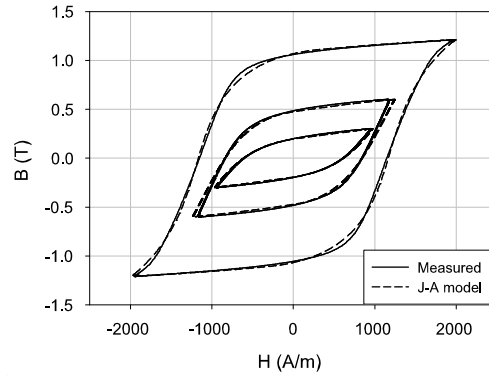


Figure 4.37: Measured and calculated hysteresis loops for the AISI1035 steel

Moreover, some measured $B(H)$ loops for the AISI1035 steel are given in figure 4.37. The parameters of the Jiles-Atherton hysteresis model were obtained from experimental measurements [47] and are given in table 4.9. As illustration, figure 4.37 shows the $B(H)$ loops obtained from the model for different magnitudes of the magnetic flux density.

Table 4.9: Parameters of the J-A model for the AISI1035 steel

α	3.15×10^{-3}	-
a	2032	[A/m]
k	1392	[A/m]
c	0.23	-
M_{sat}	1871842	[A/m]

Calculation of the torque

The studied system being axi-symmetric, the 2D FE approximation can be used. Moreover, in a first approach, the eddy currents are neglected. The 2D mesh of the system is made of 9 181 triangular elements. In figure 4.38, the modelled geometry is given with an example of a magnetic flux pattern.

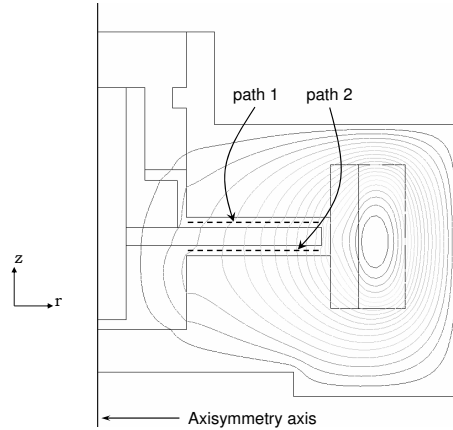


Figure 4.38: Magnetic flux lines in the 2D axisymmetric structure of the brake

The distribution of the magnetic flux density is extracted from the FE results for the air gap region where the physical phenomenon of "braking", due to the MRF, takes place. Then, to calculate the developed torque, we use the relation giving the yield stress versus the magnetic flux density $\tau_y(B)$. The expression of this function is obtained from the fitting of the manufacturer data (figure 4.39) to a polynomial expression. Then, using the magnetic field distribution obtained from the FE calculation, one can determine its component along a path in the gap between the moving and fixed parts of the brake as shown by the dashed lines in figure 4.38. These dashed lines are defined between the radii r_1 and r_2 where the particles of the MRF are supposed to line up to form chains between the moving and fixed parts of the brake. One must note that the gap between the moving and fixed parts is small enough to consider a uniform magnetic field along the (Oz) axis in these regions. The magnetic flux density is plotted at the interfaces between the MRF and the fixed part on one hand, and between the MRF and the moving part on the other hand (figure 4.40). One can observe that the magnetic field is mainly along the (Oz) axis that allows us to consider only the B_z component of the magnetic flux density for the calculation of the torque.

It is supposed that the main contribution to the global torque is due to the breaking of the chains in these regions when the shear stress reaches locally the yield stress. The torque is obtained by integrating the shear stress along the defined paths using the expression 4.6.

$$\Gamma_{MR}^i = 2\pi \sum_{k=1}^n \tau_y(B_{r_k}^i) r_k^2 (r_k - r_{k-1}) \quad (4.6)$$

with i stands for the index of the integration path, n for the number of points along a discretized path, r_k and B_{r_k} are, respectively, the radius at point k and the magnetic

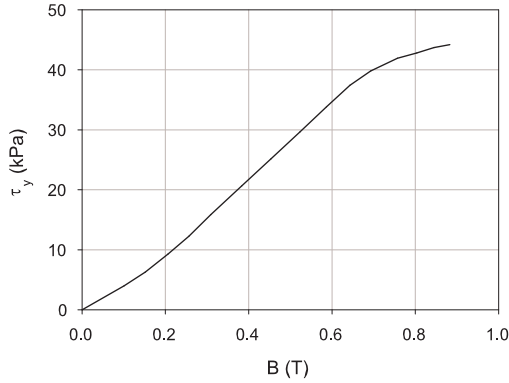


Figure 4.39: Yield stress as a function of the magnetic flux density for the fluid MRF-132AD

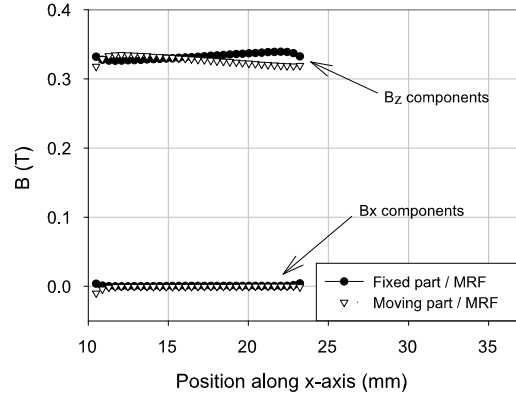


Figure 4.40: Magnetic flux density at interfaces "fixed part/MRF" and "moving part/MRF"

flux density calculated at this point. Then, as the formation of the magnetic chains take place above and below the moving part, the global torque Γ_{MR} is the summing of the integration on both paths Γ_{MR}^1 and Γ_{MR}^2 .

Calculation results

To investigate the hysteresis phenomenon in the torque evolution, calculations are considered with and without the hysteretic behaviour for the AISI1035 steel. In both cases, the MRF behaviour law will be considered non-linear and single-valued as described by equation (3.31).

In the first considered configuration, the AISI1035 steel is modelled without the hysteresis effect. The excitation current is cycled as presented in figure 4.42. Results of the calculation in these conditions are given in figure 4.41. The evolution of the torque is single-valued with respect to the current as expected. Nevertheless, due to a hysteresis effect in the torque evolution, we observe that its value is underestimated when the current decreases.

In the second configuration, to verify the influence of the hysteresis effect on the torque evolution, we now consider an hysteresis behaviour law in the AISI1035 steel. The same waveform of the current is applied and the results are given in figure 4.43. The hysteresis effect appears clearly on the torque evolution versus the current. Moreover, a good agreement is observed between the measurements and the model. In the same way, the FE calculations were performed using the waveform of the excitation current as described in figure 4.34. Results are given in figure 4.44. The results are also in good agreement with the measurements.

Finally, the numerical model, including the hysteresis behaviour in the magnetic core, show that the developed approach is very satisfactory to describe the operating of a MRF-brake. The hysteretic behaviour observed experimentally in the torque evolution versus the feeding current is clearly explained by the magnetic hysteresis existing in the solid magnetic core parts constituting the MRF-brake. Therefore, this modelling approach is

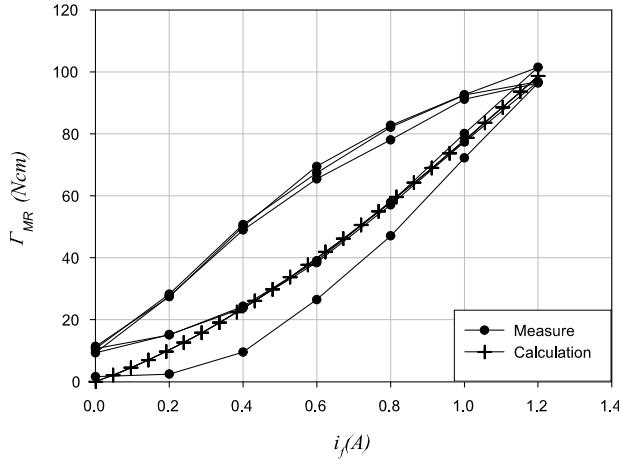


Figure 4.41: Evolution of the calculated torque without hysteresis

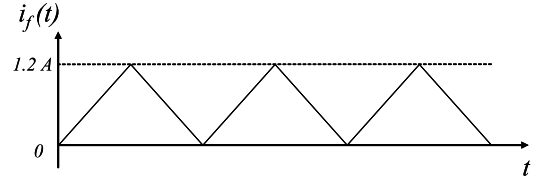


Figure 4.42: Current waveform used for the simulation and measurements

well adapted for a potential optimization study of the brake.

4.2.3 Magnetization loss in permanent magnets¹³

As described in section 3.2.4, modern applications can generate significant eddy currents in permanent magnets (PMs) due to high level of spatial and time harmonics, especially when power converters are involved. The resulting temperature increase can lead to partial, or total, magnetization loss of the PMs. In the following, the magnetization loss model presented in section 3.2.4 is validated by comparison with the experiment.

4.2.3.1 Identification of the permanent magnet model

The $B - H$ curves used to test the proposed PM model are measured with a Pulsed Field Magnetometer equipped with a heating unit. The investigated PM is a $4 \times 30 \times 30\text{mm}$ (thickness \times width \times length) sintered NdFeB magnet magnetized along its thickness. The characteristics were measured starting from 25°C up to 180°C (solid lines in figure 4.45).

The parameters of the analytical expression (3.54) are fitted with the experiment for each temperature. Results of the fitting procedure is shown by the black dashed-lines for different temperatures. Moreover for 180°C the fitted expression is shown with the associated recoil curves that are obtained following the demagnetization model described in the section 3.2.4. It can be noticed that each fitted curve matches with acceptable accuracy the corresponding measured curve.

In addition, from the parameters identified for each demagnetization curve, the polynomial evolutions describing the temperature dependence of the parameters are fitted according to the approach presented in section 3.2.4.2 of the previous chapter.

¹³The presented results are part of the PhD Thesis of Radu Fratila.

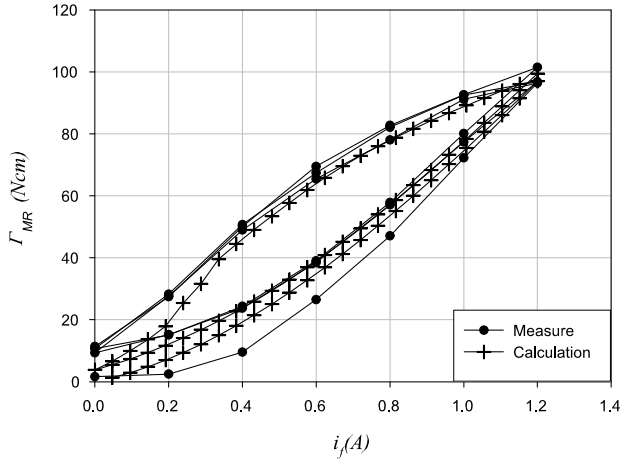


Figure 4.43: Evolution of the torque: comparison between measurement and calculation with hysteresis

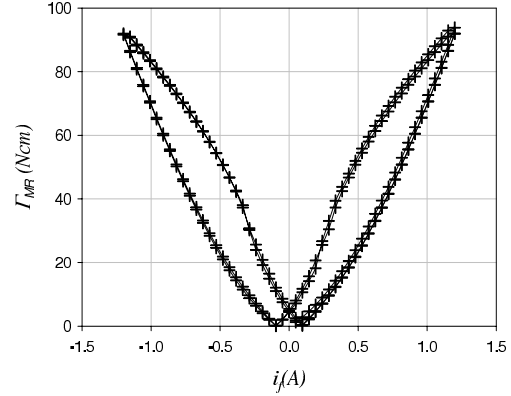


Figure 4.44: Evolution of the torque with the excitation given in Fig. 4.34

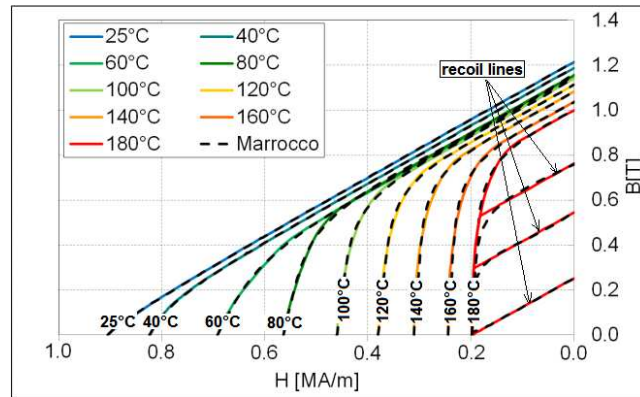


Figure 4.45: Fitting of the analytical expression (3.54) on the measured data

4.2.3.2 Studied test device

The experimental device illustrated in figure 4.46 has been designed [114] with the ability to demagnetize the permanent magnet with the increase of temperature. The experimental case, with magnetization loss in the PM such as presented in section 2.2.4, is simulated. The demagnetizing conditions are such as the air-gap is fixed to 5mm and the $NdFeB$ magnet is subjected to an alternating demagnetization field created by two coils connected in parallel and supplied by a current of 3.5A at 200Hz .

Note that, thanks to the symmetries of the device, only $1/4^{\text{th}}$ of the system is modelled with a mesh composed of 61 213 tetrahedral elements. In order to have additional comparison criteria for the validation of the model, the electromagnetic problem is solved in both electric $\mathbf{A} - \varphi$ and magnetic $\mathbf{T} - \Omega$ mathematical formulations.

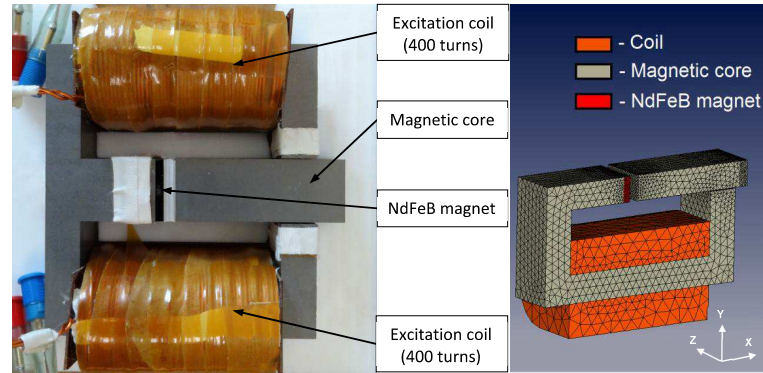


Figure 4.46: Studied device (left) and the FE model (right) of the system

4.2.3.3 Results and discussions

The aim is to investigate the magnetization loss under the combined influence of the demagnetization field created by the two coils and the temperature dissipation, due mainly to the eddy current loss in the magnet. An iterative-coupling of the electromagnetic and thermal problems is performed according to the sequential scheme illustrated in figure 3.16 in section 3.2.4.

For the steady state thermal problem, a thermal conductivity for the PM of $\lambda = 6.4W/mK$ is used. Moreover, an ambient temperature of $28^\circ C$ is imposed and the global heat transfer coefficient at the boundary of the thermal problem is fixed at $h = 10$.

First, the global temperature map obtained by simulation from both formulations is compared with the thermal image of the experimental device in figure 4.47, with a detailed temperature map of the PM in figure 4.48. A good agreement is observed regarding the distribution as well as the level of the temperature in the device where the PM temperature is about $68^\circ C$. A closer insight into the eddy current losses in the PM (see figure 4.49) shows that these losses are similar for both formulations, with the $\mathbf{T} - \Omega$ formulation giving a slightly higher loss density. This explains why the temperature of the PM is higher for this formulation (see figure 4.48).

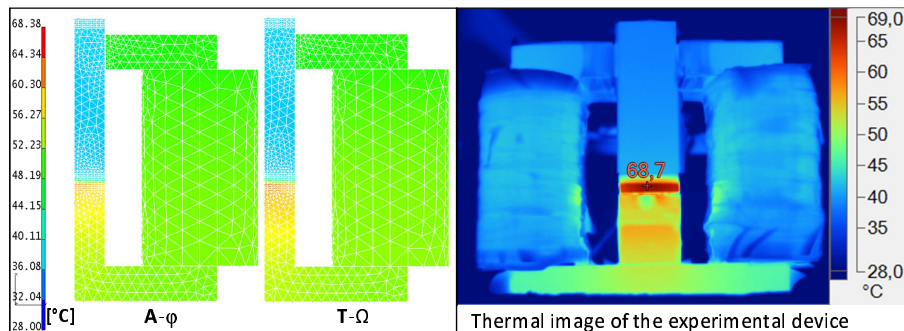


Figure 4.47: Global temperature map obtained by simulation from both formulations and experimental thermal image.

Besides, the measured temperature levels, for both locations T_1 and T_2 reported in fig-

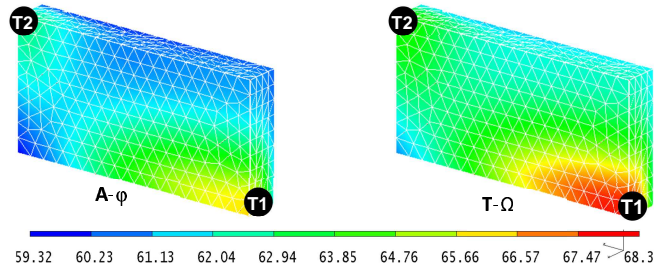


Figure 4.48: Temperature map in the PM obtained from both formulations.

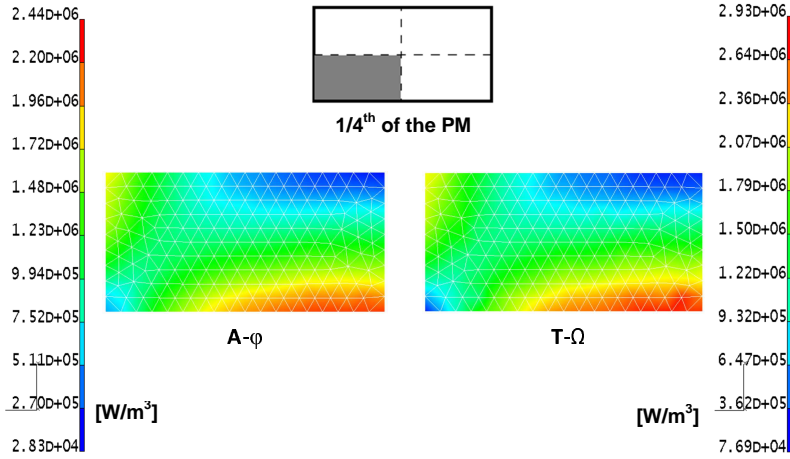


Figure 4.49: Eddy current loss density in the PM obtained from both formulations.

ure 4.48, are respectively $T_{1-exp} = 69^\circ\text{C}$ and $T_{2-exp} = 73^\circ\text{C}$. Considering the experimental uncertainties related to the temperature sensors positioning and also to the simulation errors, this result is very satisfactory.

If now we compare the Hall sensor signals of the experiment (see figure 2.25 in section 2.2.4) with the magnetic flux density obtained from the calculation, the tendency of magnetization loss is well reflected by the simulation. The table 4.10 summarizes the average values of the Hall sensor signals and magnetic flux densities of the corresponding elements in FE analysis.

Table 4.10: Average magnetic flux density in the air-gap after magnetization loss

Location	H_1	H_2	H_3	H_4
Experiment	0.376	0.372	0.341	0.344
$\mathbf{A} - \varphi$	0.359	0.418	0.355	0.397
$\mathbf{T} - \Omega$	0.399	0.388	0.358	0.407

Compared with the case without magnetization loss (see figure 2.26a in section 2.2.4), the average magnetic flux density in the centre of the PM (sensor H_3) is weaker than the magnetic flux density at the edges. this indicates a magnetization loss of 25% in that area, except for the sensor H_4 that gives a measure similar to the sensor H_3 . This

can be explained by a delicate experimental positioning of the sensor H_4 at the edge where the magnetic flux density gradient is high. Globally, the values of the average magnetic flux density obtained from the experiment and simulation results, emphasize the magnetization loss in the centre of the PM.

Regarding the magnetization loss, due to the combination of the demagnetizing field and temperature increase, the numerical model allows to analyse in detail the local behaviour as illustrated in figure 4.50. As already emphasized experimentally by the Hall sensor, the centre of the PM suffers the most from magnetization loss. A complementary illustration of this effect is given in figure 4.51 where the operating points of the elements E_1 (centre of the PM) and E_2 (edge of the PM) are given for both formulations and for the last electric period once the steady state is reached.

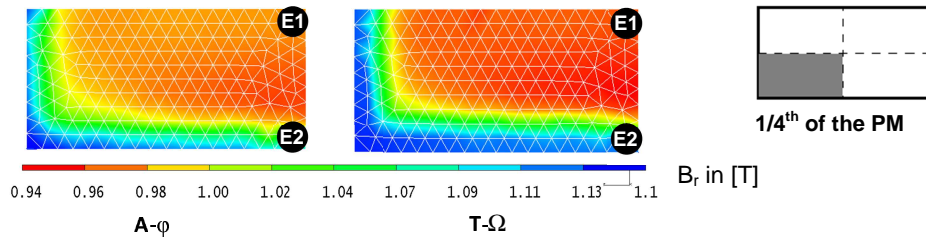


Figure 4.50: Map of the remnant magnetic flux density loss in the PM obtained from both formulations.

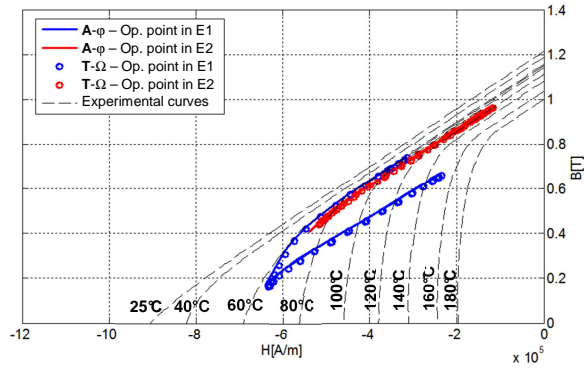


Figure 4.51: Operating points of the PM in the center (element E_1) and edge (element E_2) regions.

The element E_1 shows a significant irreversible magnetization loss with a recoil line that has been created. As the temperature in this element is about 62°C , the operating points are located on a $B(H)$ curve close to the one corresponding to 60°C . For the element E_2 , the magnetization loss is less important, even if the temperature reaches a higher level (68°C). This effect is explained by significant leakage flux that occurs at the edge of the PM (due to eddy currents), so that the element E_2 is experiencing a significantly lower demagnetizing field than the element E_1 .

Conclusion and perspectives

5.1 Conclusion

This synthesis report does not reflect all the work done since 2004, but the essence of the main research activities is reflected by the presented models, studies and application examples. As mentioned in the introduction, the background of these research activities is the "three-steps" approach of the research team, namely the model construction, the implementation in the field calculation code and the experimental validation with the operation analysis, while controlling the quality of the numerical solution. My contribution is mainly associated to the experimental characterization and model construction of the magnetic materials, together with the model implementation in the Finite Element method and also, in part, the experimental validation.

Regarding the deterministic material models, the hysteresis behaviour has been investigated for soft magnetic materials in order to be implemented in finite element modelling processes. The Preisach model was improved in a simple way in order to account for the stress in its distribution characteristic. In the same way, the Jiles-Atherton model has been extended, with limited impact on its identification procedure, to account for minor loops. Both models were implemented in the Finite Element Method and tested with success on electromagnetic devices (inrush current in a three phase transformer, hysteresis motor and magneto-rheological brake). Besides, an original approach was proposed to account for the hysteresis in inductors used for EMI filters. The interest of such approach was proved by experimental tests.

Concerning the permanent magnets, a modelling approach including demagnetizing field and thermal effects, has been proposed to account for reversible and irreversible magnetization loss. The model has been implemented in the Finite Element Method and validated by comparison with an experimental testing device.

For the probabilistic aspect in the material models, a general approach was proposed in order to identify, within a given study, the best deterministic model, the adequate distributions for its parameters and the validation of the whole identification procedure. The probabilistic tests carried out on the magnetic behaviour and iron loss models showed good agreement with the experiment. Such approach will be very useful in studying the variability in the material properties in the context of manufacturing process impact

and/or operating conditions.

The development of accurate models, depending on external stresses, such as the manufacturing process (modification of the characteristics) and operating conditions (temperature, high frequency ...), requires specific experimental devices. This is particularly the case when strong inhomogeneities exist within the material. In that context, the punching effect on stator teeth, the electrical conductivity in massive magnetic parts and the HF characterization of ring core inductors have been experimentally investigated.

5.2 Perspectives

5.2.1 Improvement and development of material models

The design of electromagnetic energy conversion devices is more and more constrained by both the evolution of efficiency standards and the competitive (cost) aspects. In addition, the application areas of such devices have been enlarged to industry domains where the robustness and safety are of importance, such as in automotive and aeronautics. These constraints require the design tools, and therefore the involved models, to be more and more accurate in the representation of the physical behaviours. To reach such accuracy, several aspects must be addressed through the improvement, and even the development, of experimental and modelling approaches. Some of these aspects, that are planned to be studied in the near future, are presented hereafter.

Multi-physic behaviour

Obviously, one of the most important aspect related to the modern applications is the involvement of other physics during the energy conversion process. This is particularly the case of devices operating in conditions where the mechanical and thermal stresses can not be neglected. As example, in the automotive domain, the traction electrical machines can reach speeds higher than $10000rpm$ and consequently the rotor is subjected to high tensile stress. In the same domain of application, the alternators have gained in terms of nominal power within a limited volume size, leading then to high thermal stresses due to the electric and iron loss densities that remain quite unchanged. In that context, and despite more efficient heat evacuation systems, it is necessary to design the device with accurate models accounting for the effect of the temperature on the magnetic materials, especially on the permanent magnets.

The development of efficient models for an implementation in the Finite Element Method will be investigated in the near future. In that context, a PhD thesis will start shortly in the area of magneto-mechanical modelling and design of electrical machines.

Ageing of materials

One aspect is usually neglected in the design process: the ageing of materials. The properties of magnetic material are obviously dependent on the mechanical and thermal stresses. But it is not obvious how these properties will change with time and with a given number of operating cycles of the device. Modern applications require a long life cycle and quite stable performance characteristics. One easy way to emphasize the interest of this

problematic is to test the performances of the device with different operating cycles, such as in the cycling tests for material fatigue. The main issue will be then to be able to link the material (electrical steel, copper ...) characteristics with the observed performances. Specific experimental devices will have to be developed, in particular the experimental protocols that allow to control the ageing of materials. Once the relevant parameters have been identified, and from experimental data, models can be build, at different scales (local, macroscopic and global). These models will be used first to assess the influence of ageing on existing devices. Moreover, the models can be introduced in design procedure to increase the robustness of electrical machine versus the ageing.

High frequency behaviour

High frequency excitations are now quite common in embedded electrical machines in automotive and aeronautics, but also in power systems with HVDC lines where high frequency power electronics converters are involved. In that conditions, despite the use of thin laminations, the electromagnetic losses will increase drastically and then lower the global efficiency. Existing magnetic behaviour and loss models are useful for the design of electrical machines but still require, especially in the case of the magnetic behaviour, improved accuracy and integration in numerical models. Another application domain is naturally power electronics where magnetic cores are widely used for high frequency filters and transformers. Specific materials (ferrites, nanocrystalline, amorphous alloys ...) are usually incorporated in these devices, but with the recent development of semi-conductors with higher capabilities of switching frequencies (*GaN* for instance), these materials can be rather limited in the frequency application domain. Therefore, either new materials should be used and/or new topologies should be investigated. In both cases, adequate models, accounting for dynamic effects and capacitive effects, must be developed.

5.2.2 Impact of the manufacturing process

Context

Till now, the research works in the field of magnetic materials for electrical devices have been mainly focused on the deterministic description of their performances. These works often considers the magnetic properties measured with standardized characterization techniques as the optimal properties when designing the electrical system. This hypothesis can be verified for large systems, where the effect of the manufacturing, especially the cutting process, can be neglected with regard to the dimensions of the devices. Nevertheless, even in such systems, the cutting may affect the magnetic behaviour of thin regions and the assembling can have an effect if it is not carefully realized because of the introduction of local stresses. In the same way, for rotating electrical machine with very small air-gaps, the degradation of the magnetic properties at the cutting edges may increase significantly the required magnetomotive force to keep the same magnetic flux density in the air-gap. Therefore, some studies focused on the impact of the cutting process (laser, punching, electrical discharge machining ...) in order to evaluate the degradation in the magnetic material properties and also the shape of the cutting edge which is not straight but inclined, modifying then the geometry of the real air-gap. But, usually, these studies do not include the cutting process parameters. For example, in the case of the punching

process, these parameters are the punch-die clearance, punch velocity, lubrication ... that will affect the quality of the cutting-edge. In addition, the tool wear, strongly linked to these parameters, will introduce a deviation of the degradation over time (essentially in the sense that the degradation becomes much more severe), especially for large series production. Note that this aspect related to the process parameters can explain why in the literature some discrepancies exist between conclusions of research works on the influence of the same process, especially when concluding on the impact significance of a given cutting process or when comparing different processes.

The perspectives presented in the following are based on the work that started few years ago (PhD Thesis of Rindra Ramarotafika) and that has opened a large field of research possibilities for the improvement of electrical machines design.

Specific characterization approaches

As mentioned in Chapter 2, standardized characterization techniques are a "starting point" for the study of magnetic materials properties. These techniques are useful when identifying, in a first approach, the parameters of iron loss and magnetic behaviour models for a global design process. Also, these techniques allow to compare different grades of materials but within the hypothesis of no impact of the cutting process or any external stress experienced in the history of the material. This is why, it is recommended to have the samples annealed before performing characterization. In that case, the *virgin* characteristic of the material, before being processed, can be measured. Different approaches have been proposed in the literature to account for the process. For instance, concerning the punching process, the approaches remain global and do not allow to extract the local behaviour law at the cutting edge, where the cutting process has modified the magnetic properties. In this region, the strain hardening (plastic deformation) and residual stress will create a strong gradient in the magnetic properties. The study of this magnetic properties degradation is usually performed by applying a mechanical stress to a lamination sample that is characterized by a technique similar to the SST. This allows to show the global impact on the lamination behaviour under tensile or compressive stress, a stress condition that is useful to know for high speed rotating machines. Few studies have used a local mechanical characterization of the cutting edge in order to evaluate the local residual stress. In that context, the link with the magnetic behaviour was made through magnetic properties measured under uniform tensile or compressive mechanical stress. But, this way of linking the magnetic properties and the mechanical stress is not really adapted as the involved mechanical operation during the punching process is associated to the shearing of the material, in the direction perpendicular to the lamination.

More generally, besides the cutting process, there are other processes involved in electrical machines manufacturing, such as the slinky stator process. This process, consisting in a single strip of lamination rolled up into a spiral way (with the rolling axis perpendicular to the lamination plane), introduces plastic and elastic deformation in the lamination and should also be studied carefully. Therefore, characterization devices accounting for the direction of the stresses must be developed in order to be able to propose adequate models. For that, existing mechanical techniques, such as the nano-indentation technique and small punch test, can be adapted with a magnetic characterization technique to ex-

tract the local properties.

In the same way, for massive magnetic parts such as forged claw poles, the experimental identification is not obvious at all. Usually, ring cores are extracted from the massive part and characterized classically. But, micro-structural observations showed that strong inhomogeneities exist within the material, due to the manufacturing process. For instance, at the interface of the material and the forging tool, a thin skin is created with a micro-structure different from the one in the volume of the material. This thin region is of importance from the magnetic point of view as it is located in contact with the air-gap where the magnetic flux flows from the rotor to the stator. Moreover, the hot forging process also leads to the alignment of the grain structure inside the material and, therefore, may introduce an anisotropic magnetic behaviour. All these aspects are planned to be experimentally investigated, for both the magnetic and electrical properties of the material. Specific experimental approaches and adequate samples geometries will be considered, together with the micro-structure and stress involved in the material.

Development of models

From the experimental data, behavioural models of the material will be developed and will depend, for instance, on the micro-structure and residual mechanical stresses. The interval of variation of the parameters of the models will have to correspond to the variations involved by the manufacturing process. In addition, the variability of the process parameters will be included in the behavioural models through probabilistic approaches, such as the ones already studied. Also, a preliminary work must be conducted on the parameters that have an impact on the operation of the end-product. In fact, there exist numerous process parameters and a sensitivity analysis must be performed in order to identify the most relevant ones.

The global aim being the modelling of the whole chain, from the process parameters to the performances of the electrical device, the material models will be the link between the metallurgical characteristics (consequence of the process parameters) and the electromagnetic properties. Moreover, the development of relevant materials models, adapted to this modelling chain, will also require specific numerical techniques. This is especially the case for taking into account the strong gradient in the magnetic properties near the cutting edge due to the punching technique. This problematic also exists in the thin skin at the surface of a hot forged magnetic piece where the micro-structure is inhomogeneous. Therefore, all the previous research perspectives will have to be conducted in collaboration, on the one hand, with researchers in the same team for the numerical implementation and design methodologies and, on the other hand, with material and manufacturing process researchers.

Bibliography

- [1] E. du Trémolet de Lacheisserie, D. Gignoux and M. Schlenker. *Magnetism: Materials and Applications*. Springer, 2005.
- [2] C.D. Cullity and B.D. Graham. *Introduction to Magnetic Materials*. Wiley-IEEE Press, 2nd Edition, 2008.
- [3] P. Brissonneau. *Magnétisme et matériaux magnétiques pour l'électrotechnique*. Edition Hermès, 1997.
- [4] L. Lliboutry. *Aimantation des aciers dans les champs magnétiques faibles*. PhD Thesis, 1950.
- [5] C. Kittel. *Introduction to Solid State Physics*. Wiley & Sons, 8th Edition.
- [6] G. Bertotti. *General properties of power losses in soft ferromagnetic materials*. IEEE Transactions on Magnetics, Vol. 24, No. 1, pp. 621-630, 1988.
- [7] R.J. Parker. *Advances in Permanent Magnetism*. Wiley & Sons, New York, NY, 1990.
- [8] J. Sievert *The measurement of magnetic properties of electrical sheet steel -survey on methods and situation of standards*. Journal of Magnetism and Magnetic Materials, Vol. 215-216, pp. 647-651, 2000.
- [9] J. Sievert and H. Ahlers. *Epstein to SST relationship - statistical rather than deterministic*. Przegląd Elektrotechniczny (Electrical Review), ISSN 0033-2097, R. 87 No 9b, 2011.
- [10] C. Appino, E. Ferrara, F. Fiorillo, L. Rocchino, C. Ragusa, J. Sievert, T. Belgrand, C. Wang, P. Denke, S. Siebert, Y. Norgren, K. Gramm, S. Norman, R. Lyke, M. Albrecht, X. Zhou, W. Fan, X. Guo and M. Hall. *International comparison on SST and Epstein measurements in grain-oriented Fe-Si sheet steel*. International Journal of Applied Electromagnetics and Mechanics, Vol. 48, No. 2-3, pp. 123-133, 2015.
- [11] Z. Cheng, N. Takahashi, B. Forghani, A.J. Moses, P.I. Anderson, Y. Fan, T. Liu, X. Wang, Z. Zhao and L. Liu. *Modeling of Magnetic Properties of GO Electrical Steel Based on Epstein Combination and Loss Data Weighted Processing* IEEE Transactions on Magnetics, Vol. 50, No. 1, 2014.

- [12] A.J. Moses. *Characterisation and performance of electrical steels for power transformers operating under extremes of magnetization conditions*. International Colloquium Transformer Research and Asset Management, Croatia, 2009.
- [13] P. Marketos, S. Zurek and A.J. Moses. *Calculation of the mean path length of the Epstein frame under non-sinusoidal excitations using the double Epstein method*. Journal of Magnetism and Magnetic Materials, Vol. 320, 2542-2545, 2008.
- [14] Z. Cheng, N. Takahashi, B. Forghani and X. Wang. *Engineering-oriented benchmarking and application-based magnetic material modeling in transformer research*. International Colloquium Transformer Research and Asset Management, Croatia, 2012.
- [15] L. Vandenbossche, S. Jacobs, F. Henrotte and K. Hameyer. *Impact of cut edges on magnetization curves and iron losses in e-machines for automotive traction*. The 25th World Battery, Hybrid and Fuel Cell Electric Vehicle Symposium & Exhibition, Shenzhen, China, 2010.
- [16] F. Ossart, E. Hug, O. Hubert, C. Buvat and R. Billardon. *Effect of punching on electrical steels: Experimental and numerical coupled analysis*. IEEE Transactions on Magnetics, Vol. 36, No. 5, pp. 3137-3140, 2000.
- [17] L.B. Valdes. *Resistivity measurements on germanium for transistors*. Proceedings of the I.R.E., Vol. 42, 1954.
- [18] K. Beddek, S. Clenet, O. Moreau, V. Costan, Y. Le Menach and A. Benabou *Adaptive method for non-intrusive spectral projection - Application on a stochastic eddy current NDT problem*. IEEE Transactions on Magnetics, Vol. 48, No. 2, pp. 759-762, 2012.
- [19] E. Petrovský, M.D. Alcalá, J.M. Criado, T. Grygar, A. Kapička and J. Šubrt. *Magnetic properties of magnetite prepared by ball milling of hematite with iron*. Journal of Magnetism and Magnetic Materials, Vol. 210, pp. 257-273, 2000.
- [20] B. Weidenfeller, M. Höfer and F. Schilling. *Thermal and electrical properties of magnetite filled polymers*. Composites Part A: Applied Science and Manufacturing, Vol. 33, pp. 1041-1053, 2002.
- [21] Y. Huang, J. Dong, L. Jin, J. Zhu and Y. Guo. *Eddy-current loss prediction in the rotor magnets of a permanent magnet synchronous generator with modular winding feeding a rectifier load*. IEEE Transactions on Magnetics, Vol. 47, No. 10, pp. 4203-4206, 2011.
- [22] A. Jassal, H. Polinder, D. Lahaye and J. A. Ferreira. *Analytical and FE calculation of eddy-current losses in PM concentrated winding machines for wind turbines*. Proceedings of Electric Machines Drives Conference (IEMDC), pp. 717-722, 2011.

-
- [23] M.L. Heldwein, L. Dalessandro and J.W. Kolar. *The three-phase common-mode inductor: modeling and design issues*. IEEE Transactions on Industrial Electronics, Vol. 58, pp. 3264-3274, 2011.
- [24] Agilent. *Agilent 16454A - Magnetic Material Test Fixture Operation and Service Manual*. Agilent technologies, 2001.
- [25] J.L. Kotny, X. Margueron and N. Idir. *High-frequency model of the coupled inductors used in EMI filters*. IEEE Transactions on Power Electronics, Vol. 27, pp. 2805-2812, 2012.
- [26] M. Kovacic, Z. Hanic, S. Stipetic, S. Krishnamurthy and D. Zarko. *Analytical wideband model of a common-mode choke*. IEEE Transactions on Power Electronics, Vol. 27, pp. 3173-3185, 2012.
- [27] C. Cuellar, W. Tan, X. Margueron, A. Benabou and N. Idir. *Measurement method of the complex magnetic permeability of ferrites in high frequency*. Proceedings of Instrumentation and Measurement Technology Conference (I2MTC), pp. 63-68, 2012.
- [28] F. Fiorillo. *Measurements of magnetic materials*. Metrologia, Vol. 47, pp. S114-S142, 2010.
- [29] V.J. Thottuvelil, T.G. Wilson and H.A. Owen Jr. *High-frequency measurement techniques for magnetic cores*. IEEE Transactions on Power Electronics, Vol. 5, pp. 41-53, 1990.
- [30] P. Nakmahachalasint, K.D.T. Ngo and V.-Q. Loc. *A behavioral model for frequency-dependent hysteresis in power ferrites*. IEEE Transactions on Magnetics, Vol. 40, pp. 1784-1790, 2004.
- [31] C. Cuellar, A. Benabou and N. Idir. *Characterization and modeling of hysteresis for magnetic materials used in EMI filters of power converters*. IEEE Transactions on Power Electronics, Vol. 29, No. 9, pp. 4911-4920, 2014.
- [32] Y. Le Menach. *Contribution à la modélisation numérique tridimensionnelle des systèmes électrotechniques: prise en compte des inducteurs*". PhD Thesis, Université des Sciences et Technologies de Lille, 1996.
- [33] Y. Le Menach, S. Clénet and F. Piriou. *Determination and utilization of the source field in 3D magnetostatic problems*. IEEE Transactions on Magnetics, Vol. 34, pp. 2509-2512, 1998.
- [34] L. Dupré, J. Gyselinck and J. Melkebeek. *Complementary finite element methods in 2D magnetics taking into account a vector Preisach model*. IEEE Transactions on Magnetics, Vol. 34, No. 5, pp. 3048-3051, 1998.

- [35] F. Ossart and V. Ionita. *Convergence of the modified fixed-point method in magnetic field problems with hysteresis*. The European Physical Journal - Applied Physics, Vol. 5, pp. 63-69, 1999.
- [36] E. Dlala, A. Belahcen, A. Arkkio. *A fast fixed-point method for solving magnetic field problems in media of hysteresis*. IEEE Transactions on Magnetics, Vol. 44, No. 6, pp. 1214-1217, 2008.
- [37] J.V. Leite, A. Benabou, N. Sadowski, Y. Le Menach, S. Clénet and P.A. Da Silva Jr. *Implementation of a vector hysteresis model in 2D finite element analysis: Study of a RSST with anisotropic sample*. International Journal of Applied Electromagnetics and Mechanics, Vol. 28, No. 1-2, pp. 41-47, 2008.
- [38] J.V. Leite, N. Sadowski, P. Kuo-Peng, N.J. Batistela and J.P.A. Bastos. *Inverse Jiles-Atherton vector hysteresis model*. IEEE Transactions on Magnetics, Vol. 40, No. 4, pp. 1769-1775, 2004.
- [39] A. Marrocco. *Analyse numérique de problèmes d'électrotechnique*. Ann. Sc. Math. Québec Vol. 1, pp. 271-296, 1977.
- [40] F. Preisach. *Über die magnetische nachwirkung*. Zeitschrift für Physik, Vol. 94, pp. 277-302, 1935.
- [41] D.C. Jiles and J.L. Atherton. *Theory of ferromagnetic hysteresis*. Journal of Magnetism and Magnetic Materials, Vol. 61, pp. 48-60, 1986.
- [42] I.D. Mayergoyz. *Mathematical models of hysteresis*. Springer Verlag, New York, 1991.
- [43] H. Debruyne, S. Clénet and F. Piriou. *Characterization and modelling of hysteresis phenomenon*. Mathematic and Computers in Simulation, Vol. 46, No. 3-4, pp 301-311, 1998.
- [44] G. Bertotti and V. Basso. *Considerations on the physical interpretation of the Preisach model of ferromagnetic hysteresis*. Journal of Applied Physics, Vol. 73, pp. 5827-5829, 1993.
- [45] G. Biorci and D. Pescetti. *Analytical theory of the behaviour of ferromagnetic materials*. Il Nuovo Cimento, Vol. 7, No. 6, pp. 829-842, 1958.
- [46] D.H. Everett. *A general approach to hysteresis. Part 4. An alternative formulation of the domain model*. Transactions of the Faraday Society, Vol. 51, pp. 1551-1557, 1955.
- [47] A. Benabou, S. Clénet and F. Piriou. *Comparison of Preisach and Jiles-Atherton models to take into account hysteresis phenomenon for finite element analysis*. Journal of Magnetism and Magnetic Materials, Vol. 261, No. 1-2, pp. 139-160, 2003.

-
- [48] O.C. Zienkiewicz and R.L. Taylor. *The Finite element method*. McGraw-Hill, London, New York, 1989.
- [49] G.S. Park, S.Y. Hahn, K.S. Lee and H.K. Jung. *Implementation of hysteresis characteristics using the Preisach model with MB variables*. IEEE Transactions on Magnetics, Vol. 29, No. 2, pp. 1542-1545, 1993.
- [50] A. Benabou, L. Vandebossche, J. Gyselinck, S. Clénet, L. Dupré and P. Dular. *Inclusion of a stress-dependent Preisach model in 2D FE calculations*. The international Journal for Computation and Mathematics in Electrical and Electronic Engineering (COMPEL), Vol. 25, No. 1, pp. 81-90, 2006.
- [51] *An inverse Jiles-Atherton model to take into account hysteresis in time stepping finite element calculations*. N. Sadowski, N.J. Batistela, J.P.A. Bastos and M. Lajoie-Mazenc. Proceedings of Compumag, Evian, France, 2-5 July, Vol. 4, pp. 246-247, 2001.
- [52] D.C. Jiles, J.B. Thoeke and M.K. Devine. *Numerical determination of hysteresis parameters for the modeling of magnetic properties using the theory of ferromagnetic hysteresis*". IEEE Transactions on Magnetics, Vol. 28, pp. 27-35, 1992.
- [53] D.C. Jiles. *Modelling the effects of eddy current losses on frequency dependent hysteresis in electrically conducting media*. IEEE Transactions on Magnetics, Vol. 30, No. 6, pp. 4326-4328, 1994.
- [54] A. Benabou, S. Clénet and F. Piriou. *Adaptation of the Frequency Dependent Jiles-Atherton Model with B as entry variable*. International Journal of Applied Electromagnetics and Mechanics, Vol. 19, No. 1-4, pp. 187-191, 2004.
- [55] D.C. Jiles. *A self consistent generalized model for the calculation of minor loops excursions in the theory of hysteresis*. IEEE Transactions on Magnetics, Vol. 28, No. 5, pp. 2602-4, 1992.
- [56] K.H. Carpenter. *A differential equation approach to minor loops in the Jiles-Atherton hysteresis model*. IEEE Transactions on Magnetics, Vol. 27, No. 6, pp. 4404-6, 1991.
- [57] F.R. Fulginei and A. Salvini. *Softcomputing for the identification of the Jiles-Atherton model parameters*. IEEE Transactions on Magnetics, Vol. 41 No. 3, pp. 1100-8, 2005.
- [58] J.V. Leite, A. Benabou and N. Sadowski. *Accurate minor loops calculation with a modified Jiles-Atherton hysteresis model*. The International Journal for Computation and Mathematics in Electrical and Electronic Engineering, Vol. 28, No. 3, pp. 741-749, 2009.
- [59] P. Zhou, D. Lin, Y. Xiao, N. Lambert and M.A. Rahman. *Temperature-Dependent Demagnetization Model of Permanent Magnets for Finite Element Analysis*. IEEE Transactions on Magnetics, Vol. 48, No. 2, pp. 1031-1034, 2012.

- [60] S. Ruoho, J. Kolehmainen, J. Ikaheimo and A. Arkkio. *Interdependence of Demagnetization, Loading, and Temperature Rise in a Permanent-Magnet Synchronous Motor*. IEEE Transactions on Magnetics, Vol. 46, No. 3, pp. 949-953, 2010.
- [61] D. Xie, W. Zhang, B. Bai, L. Zeng and L. Wang. *Finite Element Analysis of Permanent Magnet Assembly With High Field Strength Using Preisach Theory*. IEEE Transactions on Magnetics, Vol. 43, No. 4, pp. 1393-1396, 2007.
- [62] S. Ruoho, E. Dlala and A. Arkkio. *Comparison of Demagnetization Models for Finite-Element Analysis of Permanent-Magnet Synchronous Machines*. IEEE Transactions on Magnetics, Vol. 43, No. 11, pp. 3964-3968, Nov. 2007.
- [63] R. Fratila, A. Benabou, A. Tounzi and J. C. Mipo. *Nonlinear Modeling of Magnetization Loss in Permanent Magnets*. IEEE Transactions on Magnetics, Vol. 48, No. 11, pp. 2957-2960, Nov. 2012.
- [64] T. Chevalier, A. Kedous-Lebouc, B. Cornut and C. Cester. *A new dynamic hysteresis model for electrical steel sheet*. Physica B: Condensed Matter, Vol. 275, No. 1-3, pp. 197-201, 2000.
- [65] C. Steinmetz. *On the law of hysteresis*. Proceedings of the IEEE, Vol. 72, No. 2, pp. 197-221, 1984 (originally published in 1892).
- [66] H. Jordan. *Die ferromagnetischen Konstanten für schwache Wechselfelder*. Elektr. Nach. Techn., Vol. 1, p. 8, 1924.
- [67] R.H. Pry and C. P. Bean. *Calculation of the energy loss in magnetic sheet materials using a domain model*. Journal of Applied Physics, Vol. 29, No. 3, pp. 532-533, 1958.
- [68] G. Bertotti. *Physical interpretation of eddy current losses in ferromagnetic materials. I. Theoretical considerations*. Journal of Applied Physics, Vol. 57, No. 6, pp. 2110-2117, 1985.
- [69] G. Bertotti. *Physical interpretation of eddy current losses in ferromagnetic materials. II. Analysis of experimental results*. Journal of Applied Physics, Vol. 57, No. 6, pp. 2118-2126, 1985.
- [70] F. Fiorillo and A. Novikov. *An improved approach to power losses in magnetic laminations under non-sinusoidal induction waveform*. IEEE Transactions on Magnetics, Vol. 26, No. 5, pp. 2904-2910, 1990.
- [71] E. Dlala. *Comparison of models for estimating magnetic core losses in electrical machines using the Finite-Element Method*. IEEE Transactions on Magnetics, Vol. 45, No. 2, pp. 716-725, 2009.
- [72] A. Moses. *Importance of rotational losses in rotating machines and transformers*. Journal of Materials Engineering and Performance, Vol. 1, No. 2, pp. 235-244, 1992.

-
- [73] M. Enokizono, T. Suzuki, J. Sievert and J. Xu. *Rotational power loss of silicon steel sheet*. IEEE Transactions on Magnetics, Vol. 26, No. 5, pp. 2562-2564, 1990.
- [74] D. Schmidt, M. Van der Giet and K. Hameyer. *Improved iron-loss prediction by a modified loss-equation using a reduced parameter identification range*. Proceedings of SMM 20, Greece, 2011.
- [75] D. Eggers, S. Steentjes and K. Hameyer. *Advanced iron-loss estimation for nonlinear material behavior*. IEEE Transactions on Magnetics, Vol. 48, No. 11, pp. 3021-3024, 2012.
- [76] J. Lavers, P. Biringer and H. Hollitscher. *A simple method of estimating the minor loop hysteresis loss in thin laminations*. IEEE Transactions on Magnetics, Vol. 14, No. 5, pp. 386-388, 1978.
- [77] M.S. Lancarotte, C. Goldemberg and Ad.A. Penteado Jr. *Estimation of FeSi core losses under PWM or DC bias ripple voltage excitations*. IEEE Transactions on Energy Conversion, Vol. 20, No. 2, 2005.
- [78] E.Dlala, A.Belahcen and A.Arkio. *On the importance of incorporating iron losses in the magnetic field solution of electrical machines*. IEEE Transactions on Magnetics, Vol. 46, No. 8, pp. 3101-3104, 2010.
- [79] K.Yamazaki and N.Fukushima. *Iron-loss modeling for rotating machines: comparison between Bertotti's three-term expression and 3-D eddy-current analysis*. IEEE Transactions on Magnetics, Vol. 46, No. 8, pp. 3121-3124, 2010.
- [80] C. Simão, N. Sadowski, N.J. Batistela and J.P.A. Bastos. *Evaluation of hysteresis losses in iron sheets under DC-biased inductions*. IEEE Transactions on Magnetics, Vol. 45, No. 3, pp. 1158-1161, 2009.
- [81] J. Korecki, A. Benabou, Y. Le Menach, F. Piriou and J.P. Ducreux. *Hysteresis phenomenon implementation in FIT: validation with measurements*. IEEE Transactions on Magnetics, Vol. 46, No. 8, pp. 3286-3289, 2010.
- [82] W.M. Arshad, T. Ryckebush, F. Magnussen, H. Lendenmann, B.Eriksson, J. Soulard and B. Malmross. *Incorporating lamination processing and component manufacturing in electrical machine design tools*. Proceedings of Industry Applications Conference, 42nd IAS Annual Meeting, pp. 94-102, 2007.
- [83] A. Schoppa, J. Schneider and C.D. Wuppermann. *Influence of the manufacturing process on the magnetic properties of non-oriented electrical steels*. Journal of Magnetism and Magnetic Materials, Vol. 215-216, pp. 74-78, 2000.
- [84] A. Kedous-Lebouc, B. Cornut, J.C. Perrier, P. Manfé and T. Chevalier. *Punching influence on magnetic properties of the stator teeth of an induction motor,* . Journal of Magnetism and Magnetic Materials, Vol. 254-255, pp. 124-126, 2003.

BIBLIOGRAPHY

- [85] Y. Kai, Y. Tsuchida, T. Todaka and M. Enokizono. *Influence of stress on vector magnetic property under alternating magnetic flux conditions*. IEEE Transactions on Magnetics, Vol. 47, No. 10, pp. 4344-4347, 2011.
- [86] L. Mierczak, D.C. Jiles and G. Fantoni. *A new method for evaluation of mechanical stress using the reciprocal amplitude of magnetic Barkhausen noise*. IEEE Transactions on Magnetics, Vol. 47, No. 2, pp. 459-465, 2011.
- [87] Y. Liu and S. Mahadevan. *Stochastic fatigue damage modeling under variable amplitude loading*. International Journal of Fatigue, Vol. 29, No. 6, pp. 1149-1161, 2007.
- [88] W.F. Wu and C.C. Ni. *A study of stochastic fatigue crack growth modelling through experimental data*. Probabilistic Engineering Mechanics, Vol. 18, pp. 107-118, 2003.
- [89] C. Soize, E. Capiez-Lernout, J.-F. Durand, C. Fernandez and L. Gagliardini. *Probabilistic model identification of uncertainties in computational models for dynamical systems and experimental validation*. Computer Methods in Applied Mechanics and Engineering, Vol. 198, No. 1, pp. 150-163, 2008.
- [90] B. Sudret. *Uncertainty propagation and sensitivity analysis in mechanical models, contributions to structural reliability and stochastic spectral method*. HDR, Université Blaise Pascal Clermont II, 2007.
- [91] Z.A. Kotulski. *On efficiency of identification of a stochastic crack propagation model based on Virkler experimental data*. Archives on Mechanics, Vol. 50, No. 5, pp. 829-847, 1998.
- [92] R. Gaignaire, S. Clénet, O. Moreau and B. Sudret. *Current calculation in electrokinetics using a spectral stochastic finite element method*. IEEE Transactions on Magnetics, Vol. 44, No. 6, pp. 754-757, 2008.
- [93] R. Gaignaire, S. Clénet, B. Sudret and O. Moreau. *3D spectral stochastic Finite Element Method in electromagnetism*. IEEE Transactions on Magnetics, Vol. 43, No. 4, pp. 1209-1212, 2007.
- [94] P. Refaeilzadeh, L. Tang and H. Liu. *Cross-Validation*. Encyclopedia of Database Systems, pp. 532-538, 2009.
- [95] S. Arlot. *A survey of cross-validation procedures for model selection*. Statistics Surveys, Vol. 4, pp 40-79, 2010.
- [96] A.B. Tsybakov. *Introduction à l'estimation non paramétrique*. Springer Edition, 2004.
- [97] R.E. Moore, R.B. Kearfott and M.J. Cloud. *Introduction to interval analysis*. Society for Industrial and Applied Mathematics, 2009.

-
- [98] K.O. Arras. *An Introduction To Error Propagation: Derivation, Meaning and Examples of Equation*. EPFL Autonomous Systems Lab, Technical Report N° EPFL-ASL-TR-98-01 R3, 1998.
- [99] R. Ghanem and P. Spanos. *Stochastic finite elements - A spectral approach*. Springer Verlag, 1991.
- [100] R. Gaignaire. *Contribution à la modélisation numérique en électromagnétisme statique stochastique*. PhD Thesis, Arts et Métiers ParisTech, 2008.
- [101] F.C. Wu and Y.P. Tsang. *Second-order Monte Carlo uncertainty/variability analysis using correlated model parameters: application to salmonid embryo survival risk assessment*. Ecological Modelling, Vol. 177, pp. 393-414, 2004.
- [102] R.L. Iman, and W.J. Conover. *distribution-free approach to inducing rank correlation among input variables*. Communications in Statistics B11(3), pp 311-334, 1982.
- [103] X.-C. Zhang. *Generating correlative storm variables for cligen using a distribution free approach*. Transactions of the ASAE, Vol. 48, No. 2, pp. 567-575, 2005.
- [104] L. Mehrez, A. Doostan, D. Moens and D. Vandepitte. *A validation study of a stochastic representation of composite material properties from limited experimental data*. Proceedings of ISMA, 2010.
- [105] R. Ramarotafika, A. Benabou and S. Clénet. *Experimental characterization of the iron loss variability in stators of electrical machines*. IEEE Transactions on Magnetics, Vol. 48, No. 4, pp. 1629-1632, 2012.
- [106] A.A. Jimoh, R.D. Findlay and M. Poloujadoff. *Stray losses in induction machines: Part I, definition, origin and measurement*. IEEE Transactions on Power Apparatus and Systems, Vol.:PAS-104, No. 6, pp. 1500-1505, 1985.
- [107] A. Boglietti, A. Cavagnino, L. Ferraris and M. Lazzari. *Induction motor equivalent circuit including the stray load losses in the machine power balance*. IEEE Transactions on Energy Conversion, Vol. 23, No. 3, pp. 796-803, 2008.
- [108] J. Cheaytani, A. Benabou, A. Tounzi, M. Dessoude, L. Chevallier and T. Henneron. *End-Region Leakage Fluxes and Losses Analysis of Cage Induction Motors Using 3-D Finite-Element Method*. IEEE Transactions on Magnetics, Vol. 51, No. 3, 2015.
- [109] S.K. Hong, H.K. Kim, H.S. Kim and H.K. Jung. *Torque calculation of hysteresis motor using vector hysteresis model*. IEEE Transactions on Magnetics, Vol. 36, No. 4, pp. 1932-1935, 2000.
- [110] S. Genç and P.P. Phulé. *Rheological properties of magnetorheological fluids*. Smart Materials and Structures, Vol. 11, pp. 140-146, 2002.

BIBLIOGRAPHY

- [111] G. Bossis, S. Laciş, A. Meunier and O. Volkova. *Magnetorheological fluids*. Journal of Magnetism and Magnetic Materials, Vol. 252, pp. 224-228, 2002.
- [112] R. Demersseman, M. Hafez, B. Lemaire-Semail and S. Clénet. *Magnetorheological brake for haptic rendering*. Proceedings of EuroHaptics 2008, Madrid, Spain, 2008.
- [113] B. Liu, W.H. Li, P.B. Kosasih and X.Z. Zhang. *Development of a MR-brake-based haptic device*. Smart Materials and Structures, Vol. 15, pp. 1960-1966, 2006.
- [114] R. Fratila, A. Benabou, A. Tounzi and J-C. Mipo. *A combined experimental and Finite Element Analysis Method for the estimation of eddy-current loss in NdFeB magnets*. Sensors, Vol. 14, No. 5, pp. 8505-8512, 2014.